Defense Threat Reduction Agency
8725 John J. Kingman Road, MS
6201 Fort Belvoir, VA 22060-6201

DTRA-TR-10-67

TECHNICAL REPORT

Fundamental Particle Combustion Kinetics Measurement in the Shock Tube in Support of Enhanced Blast Weapons Development

July 2012

HDTRA1-07-1-0011

Nick Glumac and
Herman Krier

Prepared by:
Univ. of Illinois at Urbana-Champaign
1091 S. First Street
Suite A
Champaign, IL 61820

DESTRUCTION NOTICE:

Destroy this report when it is no longer needed.
Do not return to sender.

PLEASE NOTIFY THE DEFENSE THREAT REDUCTION AGENCY, ATTN: DTRIAC OP-ONIU, 8725 JOHN J. KINGMAN ROAD, MS-6201, FORT BELVOIR, VA 22060-6201, IF YOUR ADDRESS IS INCORRECT, IF YOU WISH THAT IT BE DELETED FROM THE DISTRIBUTION LIST, OR IF THE ADDRESSEE IS NO LONGER EMPLOYED BY YOUR ORGANIZATION.

REPORT DOCUMENTATION PAGE

Form Approved
OMB No. 0704-0188

1. REPORT DATE *(DD-MM-YYYY)*	2. REPORT TYPE	3. DATES COVERED *(From - To)*
00-07-2012	Technical Report	2006-2009

4. TITLE AND SUBTITLE
Fundamental Particle Combustion Kinetics Measurement in the Shock Tube in Support of Enhanced Blast Weapons Development

5a. CONTRACT NUMBER

5b. GRANT NUMBER
HDTRA1-07-1-0011

5c. PROGRAM ELEMENT NUMBER

6. AUTHOR(S)
Nick Glumac
Herman Krier

5d. PROJECT NUMBER

5e. TASK NUMBER

5f. WORK UNIT NUMBER

7. PERFORMING ORGANIZATION NAME(S) AND ADDRESS(ES)
Office of Sponsored Programs & Research Admin
1091 S. First Street Suite A
Champaign, IL 61820

8. PERFORMING ORGANIZATION REPORT NUMBER

9. SPONSORING/MONITORING AGENCY NAME(S) AND ADDRESS(ES)
DTRA-R&D Enterprise
8725 John J. Kingman Rd.
Fort Belvoir, VA 22060

10. SPONSOR/MONITOR'S ACRONYM(S)
DTRA

11. SPONSOR/MONITOR'S REPORT NUMBER(S)
DTRA-TR-10-67

12. DISTRIBUTION/AVAILABILITY STATEMENT
Approved for public release; distribution is unlimited.

13. SUPPLEMENTARY NOTES

14. ABSTRACT
This research conducted from FY 2006 through FY 2009 addressed to main objectives: 1) determination of the combustion kinetics of fine aluminum particles under conditions relevant to enhanced blast devices, and 2) examination of the effects of the passage of the detonation wave on the reactivity of aluminum particles in aluminized explosives. These to research thrust were conducted in parallel.

15. SUBJECT TERMS
Explosives Kinetics
Aluminium Combustion

16. SECURITY CLASSIFICATION OF:			17. LIMITATION OF ABSTRACT	18. NUMBER OF PAGES	19a. NAME OF RESPONSIBLE PERSON
a. REPORT	b. ABSTRACT	c. THIS PAGE			Michael Robinson
Unclassified	Unclassified	Unclassified	SAR	170	19b. TELEPHONE NUMBER *(Include area code)* (703) 767-3076

FINAL REPORT
DTRA Award HDTRA1-07-1-0011

Fundamental Particle Combustion Kinetics Measurement in the Shock Tube in Support of Enhanced Blast Weapons Development

Principal Investigators:
Nick Glumac and Herman Krier
University of Illinois, Urbana Champaign

Program Manager:
Dr. Suhithi Peiris, DTRA
April 1, 2010

Table of Contents

I. Introduction and Summary of Research

This research conducted from FY 2006 through FY 2009 addressed two main objectives: 1) determination of the combustion kinetics of fine aluminum particles under conditions relevant to enhanced blast devices, and 2) examination of the effects of the passage of the detonation wave on the reactivity of aluminum particles in aluminized explosives. These two research thrusts were conducted in parallel.

The particle kinetics work was motivated by the observation that, as particle sizes approach the 10 micron level, the classical description of the combustion of aluminum particles – i.e. the diffusion limited model – no longer was applicable. Current correlations and theory were unable to predict combustion behavior of fine Al particles, especially within oxidizers such as CO_2 and H_2O, which are key elements of the detonation products in which Al particles are thought to combust. In addition, there has been significant concern over the relative roles of "aerobic" and "anaerobic" combustion of Al, with the former meaning combustion in air and the latter in detonation products. A common theory of enhanced blast proposes that anaerobic effects are either negligible or responsible only for pre-ignition, while aerobic combustion is required for full ignition and subsequent combustion. This work sought to quantify the relative oxidation rates of 1-10 micron Al in O_2, CO_2, and H_2O under elevated temperature ambient conditions similar to those in a fireball. The heterogeneous shock tube is uniquely suited to these measurements, and several hundred tests were performed, and correlations of burning time with particle size, ambient temperature, ambient pressure, and oxidizer content were developed. These correlations provide significant improvement in predicting the Al combustion rate for small particle sizes.

Further work in the area of understanding aluminum combustion dealt with the study of ultrafine Al particles or nano-aluminum, with particle diameters in the 85 nm range. Two competing theories – the solid-state diffusion mechanism and the melt dispersion mechanism – have been proposed to explain the puzzling combustion dynamics of nanoscale Al combustion. A key difference between these mechanisms is the role of the gas-phase species in combustion. To address this difference, we developed the techniques to measure the gas phase Al and AlO concentration around burning nano-Al particles at various temperatures, and we compared these results to Al burning in the diffusion-limit. We observed that the melt dispersion mechanism cannot account for the observed results, since no Al is observed when the particles are subjected to rapid heat-up without combustion, and the Al vapor concentration during combustion is two orders of magnitude lower than conventional gas-diffusion-limited combustion. On the other hand, the results are strongly supportive of a primarily surface-diffusion-limited combustion model.

In the area of detonation effects on particle reactivity, we looked at three basic configurations of Al loading in a high explosive (HE). The Al was either mixed uniformly within the HE, packed directly onto the surface of the HE, or held two charge diameters away from the HE. In each case, we observed the fireball cloud with time-resolved AlO spectroscopy to attempt to discern where and when the combustion of Al particles was occurring. We did observe significant differences in the time-dependent AlO signal for each loading case, with the first two cases – where the detonation wave was directly in contact with the particles – showing only a prompt

AlO signal lasting roughly 10 – 20 us. In the case in which the particles were entrained by the detonation product gases, but did not experience a strong shock, there was a prompt AlO signal, but also a long tail, representing an afterburn that lasted several hundred microseconds. These results suggested that the detonation may activate the metal particles significantly, resulting in much earlier heat release than conventional models predict. However, there were significant concerns about the use of spatially integrated AlO emission spectroscopy as a fireball diagnostic.

Follow-on research on shock effects addressed the particle size distribution of the Al particles before and after passage of the detonation wave. A rapid quench chamber was constructed, and aluminized charges were exploded in the diverging section of a low pressure supersonic helium jet. Particle reactivity was determined to be negligible, and particles were collected and sized. These measurements suggest that the particle size distribution is not significantly altered by the passage of the detonation wave. This experimental work provides direct support for a common assumption (e.g. in the SHAMRC simulations) that the size distribution of Al particles is the same in the dispersed cloud as in the unreacted explosive.

A detailed series of tests of aluminized charges was performed in our newly developed instrumented chamber in which simultaneous high speed shadowgraph imaging, transient spectroscopy, pyrometry, and spatially resolved pressure measurements could be obtained. Al particle size and loading were varied in explosive charges, as was the ambient environment (air vs. N_2 vs. CO_2 vs pure O_2). Residue was collected and analyzed for degree of oxidation. These studies demonstrated clearly that 1) nearly complete particle oxidation in detonation products is possible, 2) particle size and loading strongly affects whether a late time Al afterburn is observed, and 3) the spatially and temporally integrated AlO emission intensity is not directly proportional to total Al oxidation. However, the concerns about interpretation of the AlO signals, on which much of the analysis was based, continued to be significant.

These concerns led to several research projects aimed at improving the ability of researchers to use fireball emission spectroscopy to monitor conditions within a fireball. The initial study involved characterization of optical depth of aluminized fireballs using laser techniques. Existing analyses of pyrometry and AlO spectroscopy data from fireballs often assumed implicitly the optically thin assumption and/or a uniform fireball. Our work quantified the optical depth of such fireballs and definitively demonstrated that these were optically thick, which made all previous analyses subject to reinterpretation.

A second study then addressed the specific issue of pyrometry measurements of aluminized fireballs. Previous works had used a variety of assumptions on emissivity variation with wavelength and had typically not addressed the optical depth issue. Using the shock tube we quantified the variation of emissivity of alumina particles with wavelength at high temperatures and found the results to be highly temperature sensitive. Combining this analysis with an optical depth analysis we generated a set of guidelines that provides protocols for analysis of pyrometric data from aluminized fireballs under various conditions, improving the accuracy and reliability of such measurements significantly.

Finally, in light of the observation of optically thick aluminized fireballs, we developed two techniques to allow us to make spatially and temporally resolved measurements of Al

combustion in these nearly opaque environments. The first technique involved fiber probes placed within the fireball at strategic locations, then using the HSFC as a spectroscopic detector to obtain simultaneous temporal, spatial, and spectral resolution of aluminum combustion emission signatures within the fireball. The second technique explored laser based absorption, which is much more quantifiable than emission, and used a custom broadband laser technique to penetrate the fireball and provide spatially and temporally resolved absorption spectra from which the concentration of molecular and atomic intermediates could be inferred. Both of these techniques proved very useful for small scale blast testing, and further development of these tests is contining, and laboratory collaborations with ARL and NAVAIR are in progress.

In this report, each research topic will be presented as a separate section with its own figures and references. General conclusions will be discussed at the end of the report.

Personnel Supported

Two PIs, Nick Glumac and Herman Krier, supervised this research. Three graduate students, Patrick Lynch, Kim Chesterfield, and Jennifer Mott Peuker, conducted the primary research. Several undergraduates were supported throughout the three year effort to assist the graduate students.

Interactions with Other Groups

Interactions with DTRA personnel, as well as those at DoD labs were critical for this work. Extensive discussions with the program manager, Dr. Peiris, helped to keep the project focused. Frequent interactions with Dr. Bill Wilson, Dr. Fan Zhang, Dr. Kibong Kim and Dr. Ed Dreizin were essential developing the experiments reported here. Our interactions with NSWC-IH, especially Dr. Joel Carney's group, changed the direction of the research as new, unexpected results were reported. Regular discussions with NAVAIR personnel Drs. Curtis Johnson and Kelvin Higa led to new diagnostic tools being developed and tested on advanced candidate thermobaric materials. In addition, we had infrequent interactions with other DTRA awardees, notably the groups at Minnesota and Dayton, as well as Mike Zachariah's group at Maryland.

Publications and Presentations

This work led to a series of presentations and journal publications, and these are listed below:

Presentations

"Combustion of 5-μm Aluminum Particles in High Temperature, High Pressure, Water Vapor Environments" P. Lynch, N. Glumac, and H. Krier, 43rd AIAA/ASME/SAE/ASEE Joint Propulsion Conference & Exhibit 8-11 July 2007, Cincinnati, OH

"Combustion Times of Aluminum in the Transition Regime" P. Lynch, H. Krier, and N. Glumac, Central States Section of the Combustion Institute Spring Technical Meeting, 4 April 2008, Tuscaloosa, AL

"Making Burn Time Measurements in Heterogeneous Shock Tubes" P. Lynch, H. Krier, and N. Glumac, Central States Section of the Combustion Institute Spring Technical Meeting, 4 April 2008, Tuscaloosa, AL

"Combustion of Aluminum Particles in the Transition Regime Between the Diffusion and Kinetic Limits " P. Lynch, N. Glumac, and H. Krier, 44th AIAA/ASME/SAE/ASEE Joint Propulsion Conference & Exhibit 21-24 July 2008, Hartford, CT

"A Correlation for Burn Time of Aluminum Particles in the Transition Regime" P. Lynch, H. Krier, and N. Glumac, 32nd International Symposium on Combustion, 4-8 August 2008, Montreal, CAN

"The Presence of Gas Phase Species in Micro- and Nano-Aluminum Combustion" P. Lynch, G. Fiore, H. Krier, and N. Glumac, AIAA Aerospace Sciences Meeting, 5-8 January 2009, Orlando, FL

"The Emissivity of Micro- and Nano-Particles in Non-Reacting Environments" P. Lynch, H. Krier, and N. Glumac, AIAA Aerospace Sciences Meeting, 5-8 January 2009, Orlando, FL

"Optical Measurements Inside the Fireballs of Aluminized Explosives," 6th National Combustion Meeting, May 2009, Ann Arbor, MI.

"Heterogeneous Shock Tube Measurements of Nano-Aluminum Combustion: A Comparison of Predictions of Various Models," PT Lynch, H Krier, N Glumac, 6th National Combustion Meeting, May 2009, Ann Arbor, MI.

"Optical Spectroscopy of Aluminized Fireballs," N. Glumac, APS Condensed Matter 2009, Nashville, TN.

Publications

Emissivity of Particle Clouds of Aluminum Oxide: Application to Pyrometry of Explosive Fireballs, Patrick Lynch , Herman Krier and Nick Glumac, submitted to Journal of Thermophysics and Heat Transfer, April 2009.

Absorption Spectroscopy Measurements in Optically Dense Explosive Fireballs using a Modeless Broadband Dye Laser, Nick Glumac, Applied Spectroscopy (in press).

Lynch P, Krier H, Glumac N, "A correlation for burn time of aluminum particles in the transition regime," Proceedings of the Combustion Institute, 32, 1889 (2009)

"Gas-phase reaction in nano-aluminum combustion," PT Lynch, G. Fiore, H. Krier, and N. Glumac, submitted to Combustion, Science and Technology (in revision).

Peuker, JMP, Lynch P., Krier, H., and Glumac, N., "Optical Depth Measurements of Fireballs from Aluminized High Explosives,"Optics and Lasers in Engineering, 47, 1009 (2009).

Bazyn, T., Lynch, P., Krier, H., and Glumac, N.,"Combustion measurements of fuel rich aluminum and molybdenum oxide nano composite mixtures," Propellants, Explosives, and Pyrotechnics, (accepted).

II. Kinetics of Micron-scale Aluminum Combustion

Abstract

A study of the combustion times for aluminum particles in the size range of 3-11 μm with oxygen, carbon dioxide, and water vapor oxidizers at high temperatures (>2400 K) and high pressures (4-25 atm) and oxidizer composition (15-70% in inert diluent) in a heterogeneous shock tube has generated a correlation valid in the transition regime. The deviation from diffusion limited behavior and burn times that could otherwise be accurately predicted by the widely accepted Beckstead correlation is seen, for example, in particles below 20 μm, and is evidenced by the lowering of the diameter dependence on the burn time, a dependence on pressure, and a reversal of the relative oxidizer strengths of carbon dioxide and water vapor. The strong dependence on temperature of burn time that is seen in nano-aluminum is not observed in these micron-sized particles. The burning rates of aluminum in these oxidizers can be added to predict an overall mixture burnout time adequately. This correlation should extend the ability of modelers to predict combustion rates of particles in solid rocket motor environments down to particle diameters of a few microns.

Introduction

Aluminum is a very energetic material that burns with a variety of oxidizers, notably in solid rocket motors (SRMs). There has been a recent trend towards smaller particle sizes to improve energy release rate and reduce the required in-rocket residence time in SRMs. Particles above 30 μm have been well studied and have been most often observed to burn in a diffusion limited regime. In this regime, aluminum vaporizes and then burns in the gas phase, generating the product aluminum oxide (Al_2O_3). Diffusion limited droplet theory [1] predicts the time it takes for a particle to complete combustion is dependent on the initial diameter squared, hence the d2 law. Additionally, the combustion time is independent of ambient pressure (for fixed ambient oxidizer mole fraction) and relatively independent of ambient temperature as well.

Several deviations from the strict diffusion limited structure have been observed, even for large particles. Early experimental results by Friedman and Macek [2] showed that the diameter dependence had an exponent of 1.2 – 1.5, significantly smaller than 2. For particles below 20 μm, Parr [3] observed an exponent much smaller than 1. Over the years, various reasons have been given to raise or lower this exponent, including convective effects, the formation and accumulation of the condensed phase product aluminum oxide, the transition towards a kinetically limited structure at small diameters, and the agglomeration and fragmentation of particles. Beckstead [4] presents a widely accepted correlation for aluminum in various oxidizers, temperatures, pressures, and sizes, which works very well for particles larger than 20 μm. This correlation predicts a weak temperature and pressure dependence, uses n=1.8 for the diameter dependence and predicts the burning rate of Al in H2O being about half that of Al in O2 and that of Al in CO2 being about one fifth of the rate in O2.

The combustion of very small metal particles has also been studied [5], especially in recent years, and these are expected not to follow the classical diffusion limit. Both quasi-steady as well as transport limited assumptions may not be valid. In the quasi-steady kinetic limit, the limiting factor becomes the kinetics of the reaction rather than the transport, and the burn time is proportional to d (not d2) and to 1/P [6]. Additionally in this kinetic regime, the ambient

temperature affects not only the ignition but the burning rate of aluminum to a far greater extent than is seen in larger particles [5]. It is commonly assumed that at small particle sizes and low pressures (enhanced diffusive transport), the diffusion limited approximation will fail. In general, transition towards the kinetic limit will be experimentally observed as a weakening of the n exponent in the dn law, an enhanced pressure dependence on the burning rate, and possibly an enhanced temperature dependence as well. For small Al particles, however, the quasi-steady approximation will likely fail before the kinetic limit is reached. Though many studies have addressed transient particle combustion, there is no clear consensus on how burn time is expected to differ when the quasi-steady assumption for Al combustion is no longer valid.

This paper presents a systematic study of Al particles burning in the transition regime, where the Beckstead correlation begins to fail. For particles in this regime (we cover the range of 3-11 μm diameter and 4-25 atm), we present data from which an alternative correlation is derived, allowing for the more accurate prediction of combustion times of Al in H_2O, O_2, and CO_2 in this intermediate size range.

Experimental Approach

The heterogeneous shock tube facility at the University of Illinois generates a high temperature, high pressure environment ideal for igniting small clouds of particles. The driven section (the test section) is 8 m long and 8.9 cm internal diameter. Other relevant dimensions and descriptions of this facility can be found in previous publications [7-9]. Through the pressure ratio of the driver and driven sections, a strength selectable shock can produce a combustion environment for approximately 2 ms in this shock tube. Various compositions of test gases can be used, notably the oxidizers of aluminum: O_2, CO_2, and H_2O in mixtures with Ar or N_2.

For each test, the tube is evacuated, flushed, and filled with the desired test gas, typically between 20 and 70% oxidizer with the balance argon. The driven section of the shock tube is heated to approximately 335 K in order to keep the small partial pressures of water in the vapor phase and prevent it from condensing into droplets. Temperatures exceeding 3000 K and pressures up to 30 atm are achievable.

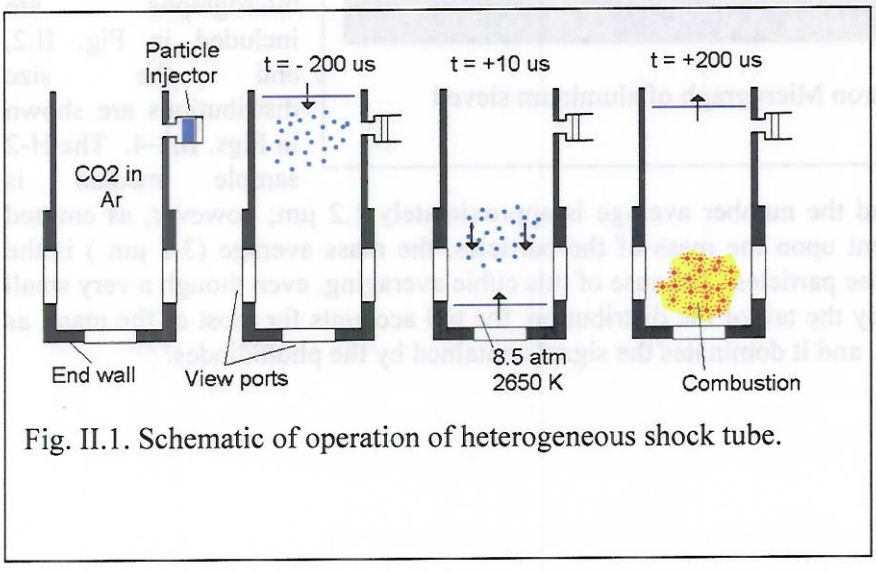

Fig. II.1. Schematic of operation of heterogeneous shock tube.

Figure II.1 shows a schematic of the operation of the shock tube. Approximately 2 mg of aluminum particles are injected into the tube from the side at a port 1.44 m upstream from the end wall of the tube. Through the rupture of a double diaphragm section, the shock is quickly fired while the cloud of particles is suspended in the test

gas. The cloud of particles drifts towards the end wall as the gas is accelerated behind the incident shock. When the shock reflects against the end wall, it meets and stops the particles in the test section where they react in the high temperature and high pressure zone. Optical access to the burning particles is acquired through fiber optics placed along the test section in the places predicted by a particle trajectory model. This model has been used by us previously [8] to predict the position of assumedly spherical particles. The fibers are filtered for 486 nm light and passed to a photodiode. The aluminum monoxide (AlO) $\Delta v = 0$ B-X transition is centered at 486 nm, and the presence of this aluminum combustion intermediate is used to characterize a burn time.

In order to characterize the diameter dependence of particles, two different size distributions of aluminum were studied. The first was size distribution "H-2" purchased from Valimet Inc; these particles are nearly spherical with a distribution centered nominally at 2 μm. The second size was a sample sieved from a -325 mesh 99.999% Al powder purchased from Alfa Aesar. The sample was sieved through a 10 μm sieve, but did not pass trough a 5 μm sieve. Scanning electron micrographs of these particles showed they were less spherical than the other sample and with a mass averaged diameter of approximately 11 μm. The 11 μm particle micrographs are included in Fig. II.2, and the size distributions are shown in Figs. II.3-4. The H-2 sample median is approximately 0.9 μm and the number average is approximately 1.2 μm; however, as emitted light intensity is dependent upon the mass of the particles, the mass average (3.1 μm) is the appropriate averaging of the particles. Because of this cubic averaging, even though a very small number of particles occupy the tail of the distribution, the tail accounts for most of the mass, as well as the energy release, and it dominates the signals obtained by the photodiodes.

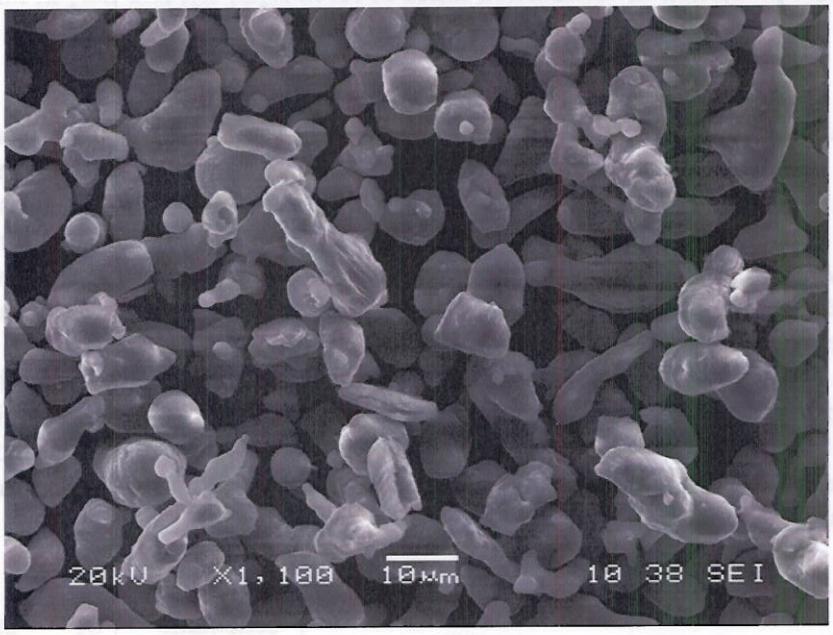

Fig. II.2. Scanning Electron Micrograph of aluminum sieved through 10 μm sieve.

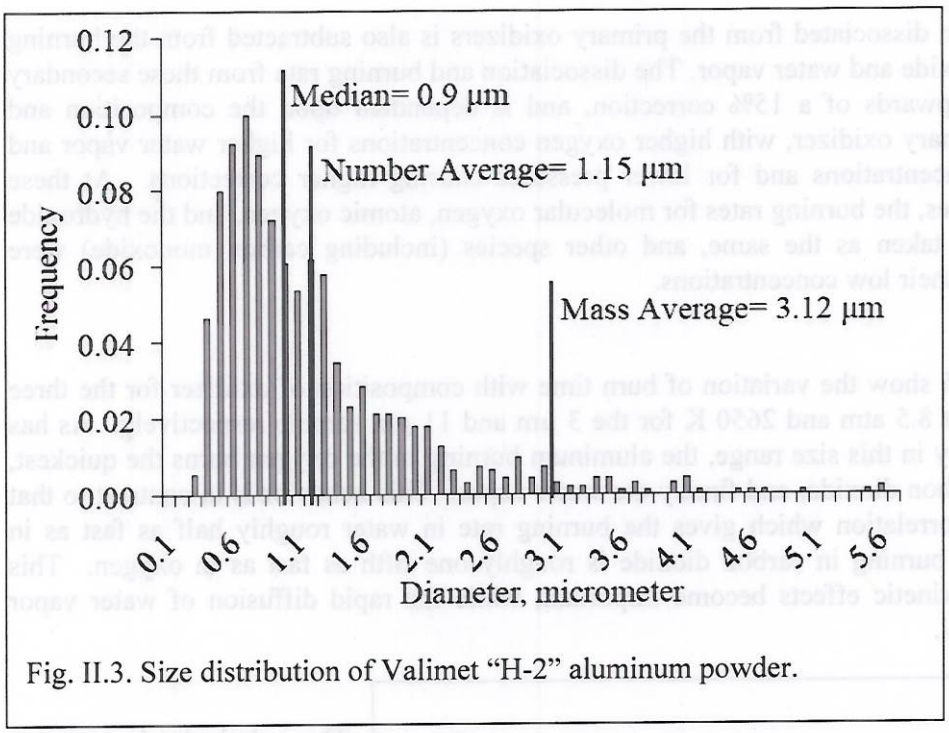

Fig. II.3. Size distribution of Valimet "H-2" aluminum powder.

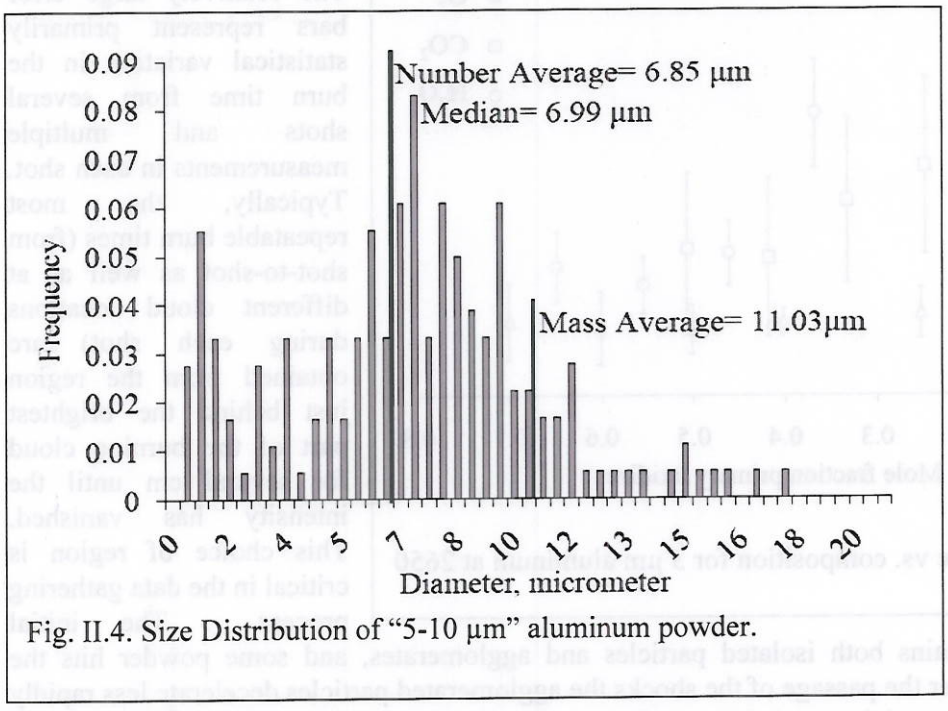

Fig. II.4. Size Distribution of "5-10 µm" aluminum powder.

Burn times for particles were based on the 10-90% area method of the AlO emission, as used in previous studies. The burn times have a small correction (less than 10%) to account for the motion of particles across the field of view of the fiber optics while they are being stopped by the reflected shock [8]. In order to isolate the kinetics of each individual oxidizer, the contribution to the burnin

g rate of the oxygen dissociated from the primary oxidizers is also subtracted from the burning rates for carbon dioxide and water vapor. The dissociation and burning rate from these secondary oxidizers can be upwards of a 15% correction, and is dependent upon the composition and pressure of the primary oxidizer, with higher oxygen concentrations for higher water vapor and carbon dioxide concentrations and for lower pressures causing higher corrections. At these elevated temperatures, the burning rates for molecular oxygen, atomic oxygen, and the hydroxide radical (OH) were taken as the same, and other species (including carbon monoxide) were ignored because of their low concentrations.

Results

Figures II.5 and II.6 show the variation of burn time with composition of oxidizer for the three primary oxidizers at 8.5 atm and 2650 K for the 3 μm and 11 μm sample respectively. As has been seen previously in this size range, the aluminum burning in the oxygen burns the quickest, followed by the carbon dioxide, and finally the water vapor. This behavior is in contrast to that of the Beckstead correlation which gives the burning rate in water roughly half as fast as in oxygen, while that burning in carbon dioxide is roughly one fifth as fast as in oxygen. This reversal comes as kinetic effects become important, while the rapid diffusion of water vapor becomes less critical.

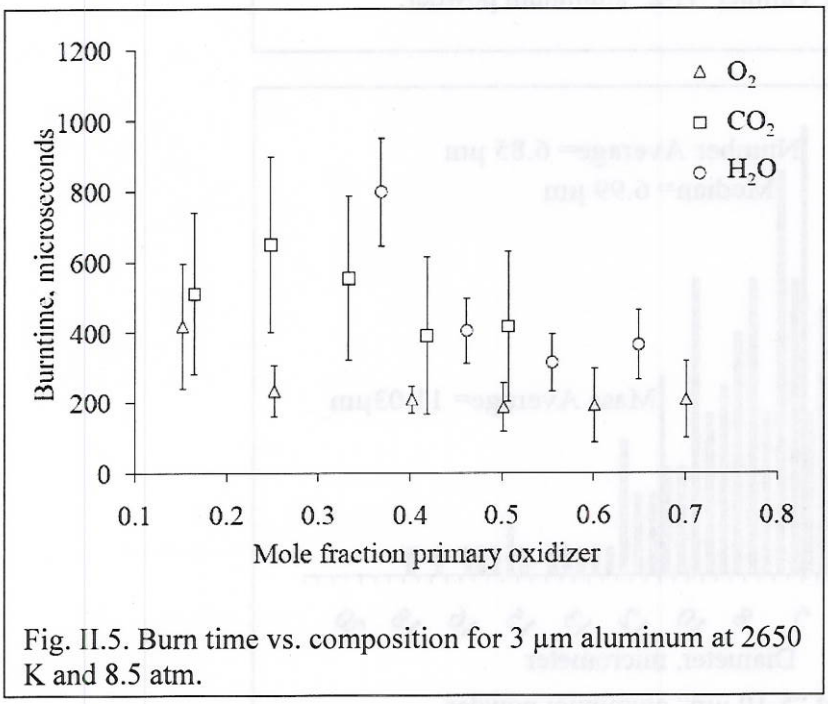

Fig. II.5. Burn time vs. composition for 3 μm aluminum at 2650 K and 8.5 atm.

The relatively large error bars represent primarily statistical variation in the burn time from several shots and multiple measurements in each shot. Typically, the most repeatable burn times (from shot-to-shot as well as at different cloud locations during each shot) are obtained from the region just behind the brightest part of the burning cloud for several cm until the intensity has vanished. This choice of region is critical in the data gathering process. The initial injected cloud contains both isolated particles and agglomerates, and some powder hits the chamber walls. After the passage of the shocks the agglomerated particles decelerate less rapidly than the individual particles, and these end up at the front (downstream end) of the burning cloud. Emission from these particles must be rejected. Likewise, particles from the walls are entrained into the flow after the passage of the shock, and these have a different thermal history than the particles that are always outside the boundary layer. Emission from these particles, which will end up at the upstream end of the burning cloud, must also be rejected. By

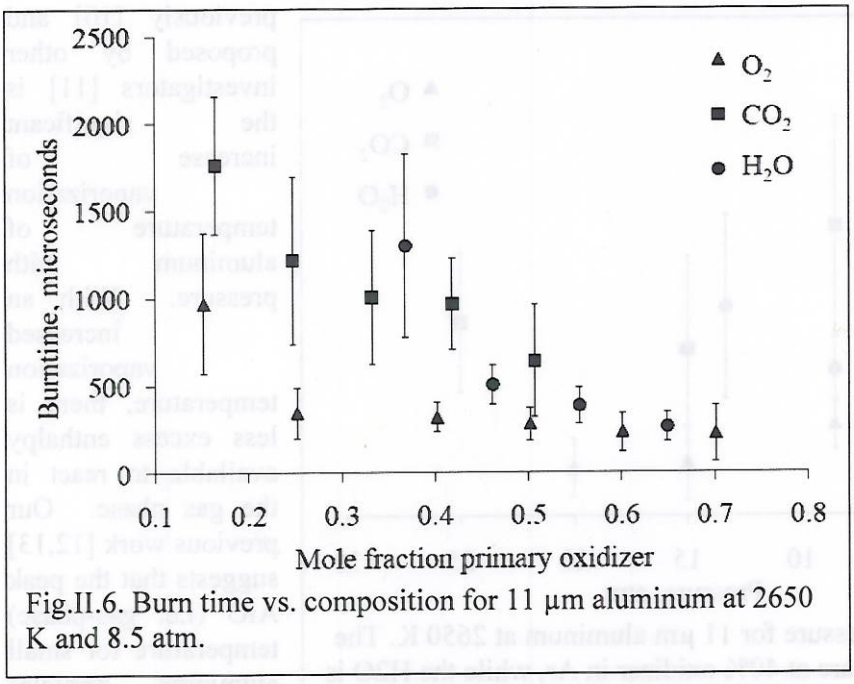

Fig.II.6. Burn time vs. composition for 11 μm aluminum at 2650 K and 8.5 atm.

appropriately selecting the region of the burning cloud that consists of single particles accelerated in the freestream, the spurious effects of agglomeration and wall impacts are avoided.

While water vapor may have the largest diffusion coefficient, it is not the first oxidizer to exhibit a transition away from diffusion limited behavior as can be seen by analyzing the pressure dependencies on the burn time as shown in Figs. II.7 and II.8 for the 3 and 11 μm samples respectively. Oxygen, for example, has a pressure dependence that approaches $\tau_b \sim P^{-1}$ for both the larger and smaller particles. On the other hand, the pressure dependence of carbon dioxide is rather indeterminate. Previous work for 10 μm particles suggests $\tau_b \sim P^{0.3}$ [8], but the uncertainty in the exponent does not preclude a 0 or even slightly negative exponent. With water vapor as an oxidizer, the burn time increases with pressure.

The increase of burn time with pressure that is seen with carbon dioxide and water vapor oxidizers likely happens for two reasons. The first is that radical recombination, which increases with pressure may deplete the radical pool and slow the reaction. This effect is more pronounced in the transitional regime than in the diffusion limited regime because the kinetics are becoming important. The other reason discussed

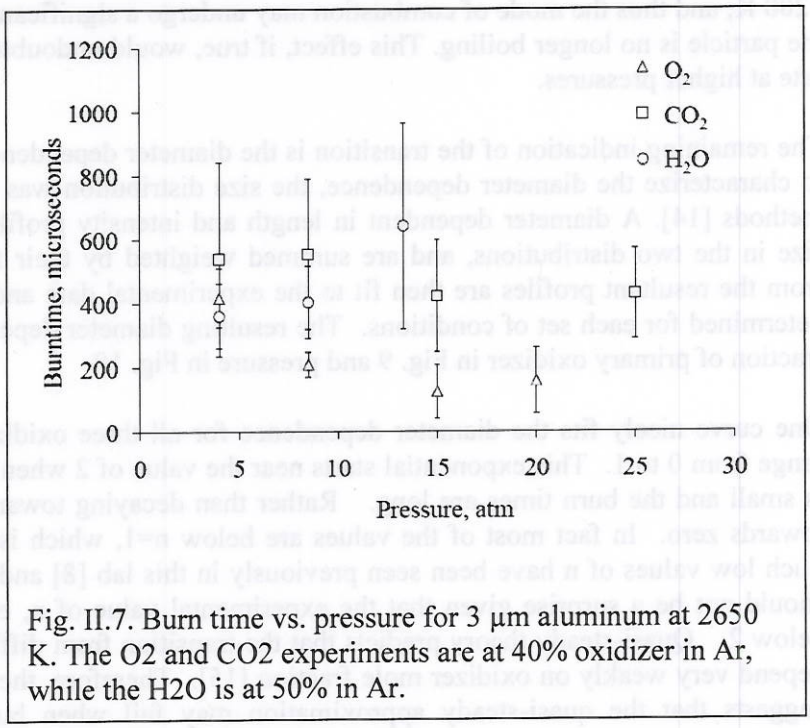

Fig. II.7. Burn time vs. pressure for 3 μm aluminum at 2650 K. The O2 and CO2 experiments are at 40% oxidizer in Ar, while the H2O is at 50% in Ar.

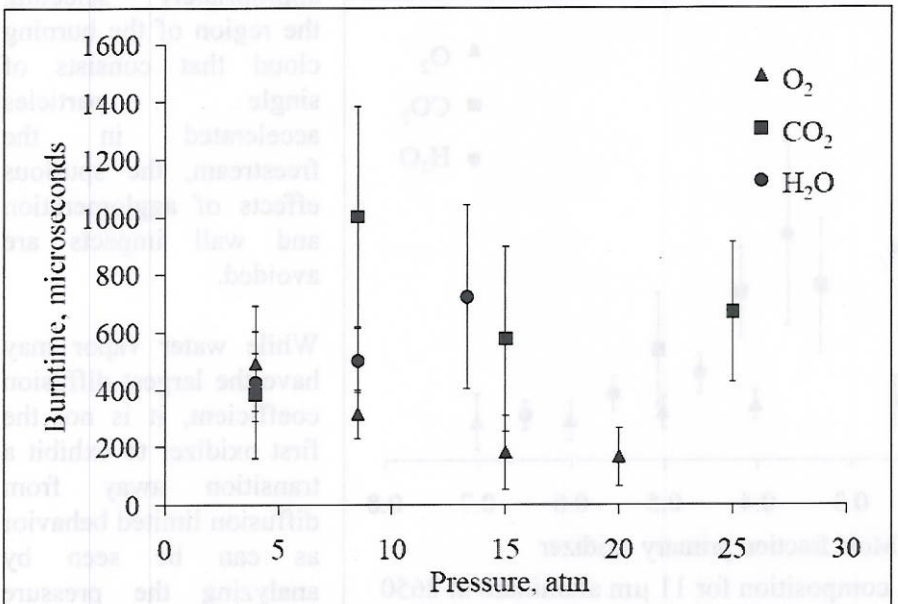

Fig. II.8. Burn time vs. pressure for 11 μm aluminum at 2650 K. The O2 and CO2 experiments are at 40% oxidizer in Ar, while the H2O is at 50% in Ar.

previously [10] and proposed by other investigators [11] is the significant increase of vaporization temperature of aluminum with pressure. With an increased vaporization temperature, there is less excess enthalpy available to react in the gas phase. Our previous work [12,13] suggests that the peak AlO (i.e. gas-phase) temperature for small aluminum particles during combustion is about 3200 K (even though the adiabatic flame temperature is significantly higher). This temperature is fairly independent of composition, pressure, and temperature. In the vicinity of 10-15 atm for example in water vapor, the vaporization temperature of the particle surpasses 3200 K, and thus the mode of combustion may undergo a significant change where the surface of the particle is no longer boiling. This effect, if true, would undoubtedly decrease the combustion rate at higher pressures.

The remaining indication of the transition is the diameter dependence on the burn time. In order to characterize the diameter dependence, the size distribution was accounted for using Bazyn's methods [14]. A diameter dependent in length and intensity profile is created for each particle size in the two distributions, and are summed weighted by their frequencies. The burn times from the resultant profiles are then fit to the experimental data and a diameter dependence n is determined for each set of conditions. The resulting diameter dependencies are plotted vs. mole fraction of primary oxidizer in Fig. 9 and pressure in Fig. 10.

One curve nicely fits the diameter dependence for all three oxidizers across the mole fraction range from 0 to 1. This exponential starts near the value of 2 when the mole fraction of oxidizer is small and the burn times are long. Rather than decaying towards 1, the dependence decays towards zero. In fact most of the values are below n=1, which is the theoretical kinetic limit. Such low values of n have been seen previously in this lab [8] and by other researchers [3] and should not be a surprise given that the experimental value of n, even in the diffusion limit, is below 2. Quasi-steady theory predicts that the transition from diffusion to kinetic limits should depend very weakly on oxidizer mole fraction [15]. Therefore, the observed strong dependence suggests that the quasi-steady approximation may fail when burn times are fast for small particles used here.

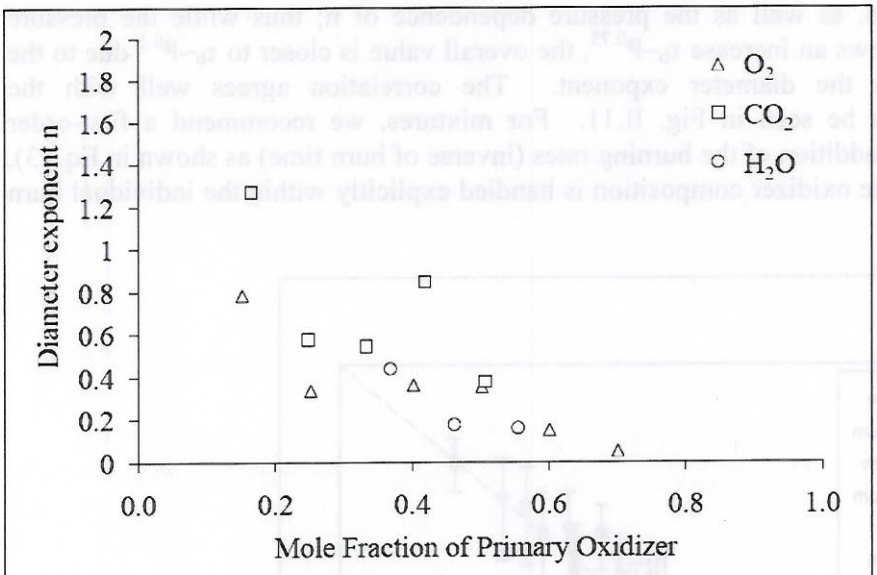

Fig. II.9. Diameter exponent n vs. composition of primary oxidizer at 8.5 atm and 2650 K.

Additionally, there is a weak but noticeable pressure dependence seen in the diameter exponent in the three oxidizers as can be seen in Fig. II.10, it ranges from $n \sim P^{-0.2}$ to $n \sim P^{-0.4}$ and thus the value of -0.3 was chosen for all three oxidizers. This dependence is counterintuitive as pressure would serve to reduce the diffusion and should inhibit the transport and raise rather than lower the diameter exponent. However, in the transition region, several competing phenomena appear to be active, and thus it is unclear how useful intuition based solely on idealized limiting behaviors is.

Based on these results we propose the correlation in Eqs. (1-3) along with the coefficients found in Table 1, where τ_b is the burn time in microseconds, P is the pressure P_0 is 8.5atm, X_{OX} is the mole fraction of primary oxidizer, and d is the diameter in microns. The starting point was the relation for the diameter exponent n, which contained the previously discussed pressure and composition dependence. From there, the overall pressure dependence, oxidizer composition dependence and leading coefficient were obtained by least squares fit of all the data

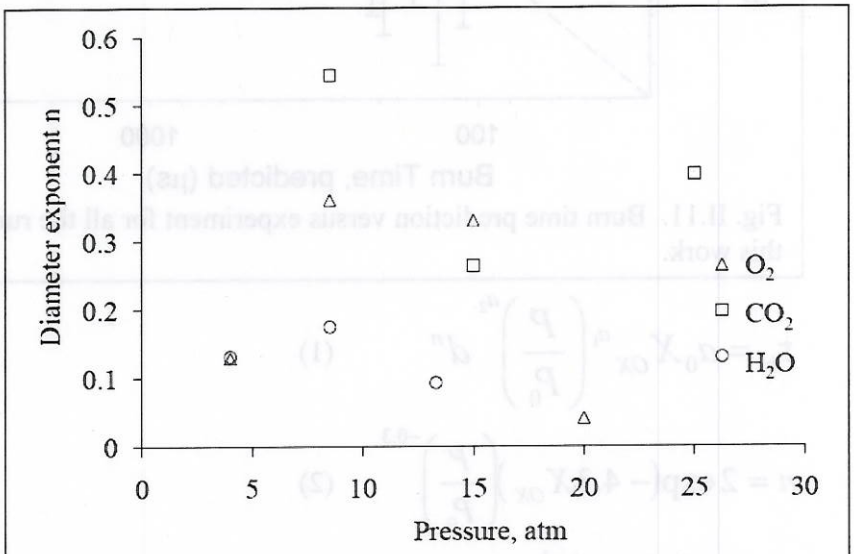

Fig. II.10. Diameter exponent vs. pressure at 2650 K. The O_2 and CO_2 experiments are at 40% oxidizer in Ar, while the H_2O is at 50% in Ar.

using an assumed power law. It is important to note that pressure contributes to the correlation both in the pressure term, as well as the pressure dependence of n; thus while the pressure coefficient a_2 for H_2O shows an increase $\tau_b \sim P^{0.75}$, the overall value is closer to $\tau_b \sim P^{0.5}$ due to the pressure dependence on the diameter exponent. The correlation agrees well with the experimental data as can be seen in Fig. II.11. For mixtures, we recommend a first-order approximate approach of addition of the burning rates (inverse of burn time) as shown in Eq. (3), where the weighting of the oxidizer composition is handled explicitly within the individual burn time Eqs. (1) and (2).

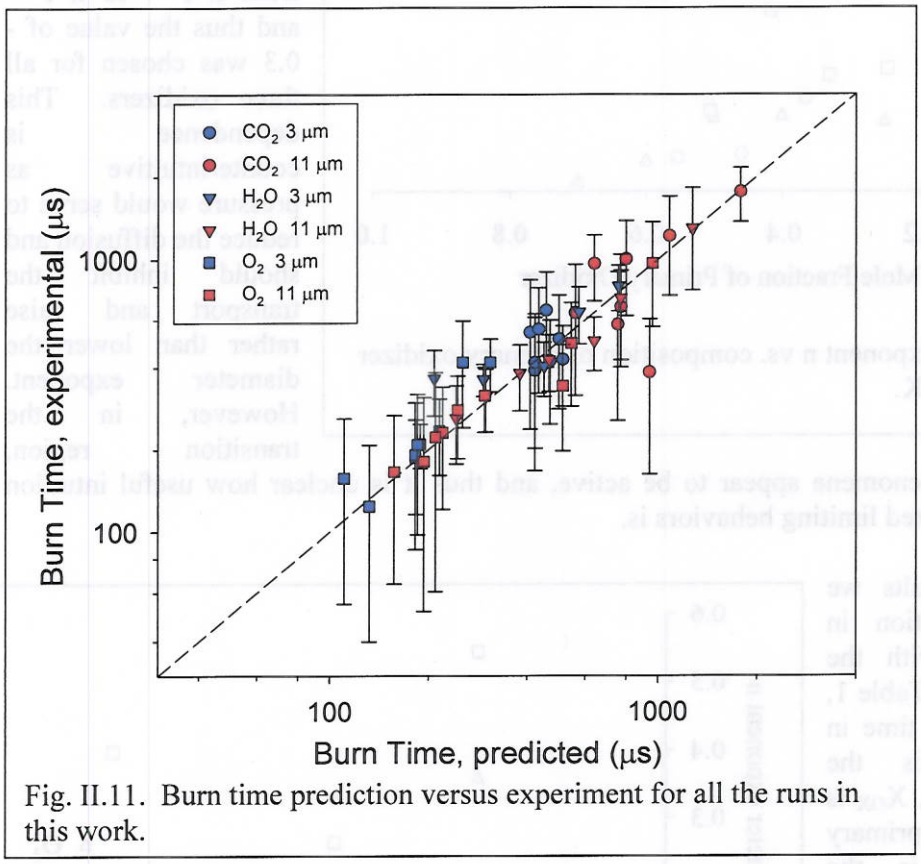

Fig. II.11. Burn time prediction versus experiment for all the runs in this work.

$$\tau_b = a_0 X_{OX}^{\,a_1} \left(\frac{P}{P_0}\right)^{a_2} d^n \qquad (1)$$

$$n = 2\exp(-4.3X_{OX})\left(\frac{P}{P_0}\right)^{-0.3} \qquad (2)$$

$$\tau_{b,mix} = \left(\sum_{i=1}^{n} \frac{1}{\tau_{b,i}}\right)^{-1} \qquad (3)$$

Table 1: Coefficients for use in equations 1-3

Oxidizer	a0, μs	a1	a2
O_2	200	0.5	-0.5
CO_2	500	0.6	0.3
H_2O	86	-1.7	0.75

Equation (3) was tested for mixtures, and one such test, a composition of 20% O_2, 30% CO_2, and 50% Ar was tested for several shots at 2650 K and 8.5 atm, using the 11 μm aluminum. The results are shown in Table 2. A composition of 50% CO_2 at these conditions has a burn time around 580 μs, while a 50% O_2 composition at the same condition has a burn time less than half that of CO_2. When shocked, the dissociation causes the composition to shift to about 21% O_2, 28% CO_2, 49% Ar, and about 2% relatively slow reacting CO which is ignored. Based on the burn time (and burning rate) of these oxidizers, even though the composition contains more CO_2, one would expect the overall rate to be closer to that of oxygen. From Eq. (3), the predicted burn time of the mixture was around 390 μs, and the experimental burn time was around 384 μs. This is perhaps fortuitous agreement, but the trends agree with intuition and lend validity to the concept of simply adding the burning rates in this first order scheme. Agreement within 20% was reached with the 3 μm powder at this condition as well.

Table 2: Mixture results for Equation 3

Mixture	21%O_2/28%CO_2 (in inerts)
τ_b, 50% CO_2	580
τ_b, 50% O_2	250
τ_b, 28% CO_2	980
τ_b, 21% O_2	640
τ_b, mix, Eq. (3)	390
τ_b, exp	384.4

There are at least three effects that are neglected in our analysis. The first effect is the temperature dependence of the burning rate. Although the increase in temperature has been shown to increase the burning rate for nano-Al, which burns below the ignition temperature of micro-Al [5], this effect is not yet seen in micro-Al. With aluminum particles on the 5 μm scale in water vapor for instance, the temperature dependence was nearly non-existent as long as the sample was fully ignited, which matches nicely with the Beckstead correlation, even though the pressure dependence has been shown to be quite different [13].

A second neglected effect would be the diameter's effect on the diameter exponent. There is certainly dependence here, but it is impossible to track over our narrow size range, especially considering the size distributions of particles used in our samples. For now, we must assume that the exponent is constant for all particles in the sample. If there were a way to ensure an even more tightly-controlled, size-selectable distribution, for example all particles within one micron of a center peak, then a diameter dependence on the diameter exponent could be tracked, but it is a daunting challenge.

The final neglected effect is that of convection on the burning rate. In the shock tube, the particles are not stationary during combustion, and typically decelerate during combustion. Relative velocities depend on the conditions, but trajectory modeling suggests that at ignition (T ~2300 K), the particles have Reynolds numbers in the range of 3-40, with velocities relative to the gas in the range of 20-300 m/s. During combustion, particles continue to decelerate, and by the end of combustion, velocities in the range of cm/s or lower are expected. The effect of convection on the burning rate is unknown, but remains of significant concern. By using conditions behind the reflected shock that are close to the ignition temperature, the convective effect can be minimized since ignition is delayed, giving the particles a chance to slow down. Under these conditions, (e.g. $T_{ambient}$ = 2400 K), similar burn times are observed, suggesting that the convective effects may be minimal, but no detailed study has yet been undertaken.

Conclusions

Based on a large dataset of heterogeneous shock tube tests, a correlation for aluminum particles in the 3-11 μm size range for oxidizers H_2O, CO_2, and O_2 for pressures in the 4-25 atm range at ambient temperatures of 2400-3000 K has been generated. Significant differences in the sensitivity of the burn rate with respect to particle diameter, pressure, and oxidizer content are observed, as compared to the Beckstead correlation which holds well for larger particles. This correlation should extend the ability of modelers to predict combustion rates of particles in SRM environments down to particle diameters of a few microns.

References

[1] I. Glassman, Combustion, 3rd ed., Academic Press, San Diego, CA, 1996, Chap. 6.

[2] R. Friedman, A. Macek, Combust. Flame 6 (1962) 9-19.

[3] T. Parr, C. Johnson, D. Hanson-Parr, K. Higa, K. Wilson, 39th JANNAF Combustion Subcommittee Meeting, Colorado Springs, CO, 2003.

[4] M.W. Beckstead, Combust., Explosion, and Shock Waves 41(5) (2005) 533-546.

[5] T. Bazyn, H. Krier, N. Glumac, Combust. Flame 145 (4) (2006) 703-713.

[6] R.A. Yetter, F.L. Dryer, in H.D. Ross (Ed.), Microgravity Combustion: Fire in Free Fall, Academic Press, San Diego, 2001, Chap. 6.

[7] J. Servaites, H. Krier, J.C. Melcher, R.L. Burton, Combust. Flame125 (1-2) (2001) 1040-1054.

[8] T. Bazyn, H. Krier, N. Glumac, J. Prop. Power 21 (4) (2005) 577-582.

[9] T. Bazyn, H. Krier, N. Glumac, Proc. Combust. Inst. 31(2) (2007) 2021-2028.

[10] P. Lynch, N. Glumac, H. Krier, 43rd AIAA/ASME/SAE/ASEE Joint Propulsion Conference, Cincinnati, OH, 2007.

[11] V. Sarou-Kanian, J.C. Rifflet, F. Millot, I Gökalp, Combust. Flame 149 (4) (2007) 329-339.

[12] T. Bazyn, N. Glumac, H. Krier, T. Ward, M. Schoenitz, E. Dreizin, Combust. Sci. Tech. 179 (3) (2007) 457-476.

[13] N. Glumac, H. Krier, T. Bazyn, and R. Eyer, Combust. Sci. Tech. 177 (3) (2005) 485-511.

[14] T. Bazyn, Spectroscopic Measurements of the Combustion of Aluminum and Aluminum-Based Energetic Material Particles Using a Heterogeneous Shock Tube, PhD Dissertation, University of Illinois, Urbana, IL, 2006.

[15] C. L. Yeh and K. K. Kuo, Prog. Energy Combust. Sci., 22 (1996) 511-541.

III. Fundamental Studies of the Gas Phase Around Burning Nano-Aluminum

Abstract

The presence or absence of gas phase species during combustion of aluminum nano-particles (n-Al) is a crucial observable in evaluating competing theories such as a diffusive oxidation mechanism and the melt dispersion mechanism. Absorption spectroscopy is used to probe the ground state of Aluminum monoxide (AlO) and Al vapor in order to quantify the amount of Al and AlO present under conditions where these species were not observed in emission previously. Absorption measurements were made during combustion of nano-aluminum and micron-sized aluminum in a heterogeneous shock tube. AlO was detected in absorption at temperatures as low as 2000 K in n-Al combustion, slightly below the limit seen in micro-Al combustion. Al vapor was detected during n-Al combustion at temperatures as low as 1500 K, significantly lower than in micro-Al combustion, suggestive of a gas phase component. It was, however, much weaker than that seen in 10 um Al combustion. A comparison with n-Al in an inert environment did not show Al vapor at temperatures below 2300 K, suggesting a nearly pristine oxide coat that inhibits the production of Al vapor in appreciable quantities without reaction. However, at these temperatures, we would have been able to detect Al vapor from equilibrium partial pressures if Al is present at the surface of a particle. These results are contrary to predictions of the melt dispersion mechanism, which should result in the generation of aluminum vapor from high energy Al clusters produced from n-Al particles that spallate from mechanical stresses under rapid heating regardless of bath gas.

Introduction

Aluminum Monoxide (AlO) is an important gas phase combustion intermediate of aluminum with oxygen containing oxidizers, such as H_2O, CO_2, and O_2. Typically, it is seen in emission and absorption during combustion of aluminum particles at temperatures greater than 2300 K. The spectrum is used to measure a temperature of the gas phase, and along with particle temperature from pyrometry [1] can be used to assemble a flame structure [2] suggestive of a combustion mechanism. Atomic Al emission has also been observed during Al combustion, and it may also be used as an indicator for combustion because high enough concentrations for detection should only be present in a high temperature reaction zone.

Large Al particles (>20 um) burn in the vapor phase with a classical diffusion flame [3]. Peak combustion temperatures approach the alumina volatilization temperature, and the particles are also at elevated temperatures. The ignition and combustion times of these particles are well characterized [4-10].

Previous work, however, [11] showed very weak AlO emission during n-Al combustion, and no detectable AlO emission under most conditions. In particular, AlO was not observed for n-Al burning in CO2 under any conditions, and only for the highest pressures (~30 atm) was it observed when burning in mixtures of O_2 and Ar. In the cases in which AlO was observed, the pyrometry measurements indicated a condensed phase temperature of above 3000 K, consistent with vapor phase Al combustion, while cases where no AlO was observed were characterized by a temperature rise of a few 10s to a few 100s of degrees above the ambient 1200 - 1800 K. Lack of AlO emission during low temperature combustion may be due to a change in combustion mechanism from vapor phase combustion to a surface mode of combustion, or it may simply be

due to the fact that at lower temperatures there is much less excited AlO and so less emission. One goal of this study is to differentiate between these possibilities.

A surface mode of oxidation has been proposed for n-Al [12,13], and in the limit of small particle size, classical particle combustion theory predicts [3] that transport to the surface will be sufficiently rapid so that all relevant oxidation reactions will occur at or near the surface. In nano-particles, heat loss is rapid due to high surface to volume ratio, and thus heat transfer considerations alone may preclude the heatup of a particle enough to sustain a vapor phase structure. However, there is reaction at 1200 K and lower, with the theoretical limit at the melting point of aluminum around 933 K. Thus, detection (or lack thereof) of vapor phase species during low temperature combustion of n-Al can assist in validating the predictions of competing theories of the fundamental mechanisms for the ignition and combustion of metal particles and the heat release time of these particles. One such theory is based on diffusive-oxidation, and the other is a melt dispersion mechanism (MDM).

For example, one diffusive-oxidation mechanism, the shrinking core mechanism [12,14-17], predicts that the oxidizer diffuses into the particle through the oxide shell surrounding each aluminum particle and reacts heterogeneously at the surface of the aluminum core. Heat generated by oxidation at the particle surface or inside the oxide layer is lost primarily by rapid conduction to the ambient gas. As the particle size increases, heat losses are reduced, and the particle temperature increases, eventually transport limitations become important as the particle transitions into a diffusion limited flame structure. At some point, presumably, the aluminum vapor pressure becomes sufficient such that Al diffuses outward producing a gas phase fuel. At this point, transport limitations become important and a flame front develops a distance away from the particle. This structure is what is commonly observed in large particle (e.g. 50+ um diameter) Al combustion.

In the melt dispersion mechanism (MDM) [18-20], mechanical stress in the nano-particle oxide coat during rapid heating (106 – 108 K/s), is suggested to cause the particle to spallate into nano-clusters (1-5 nm in diameter) of aluminum atoms which react with oxidizer in a kinetically limited fashion [21].

The theories offer competing predictions, some of which can be directly tested. MDM predicts that the product particle size should be smaller than the initial particle size. On the other hand, the shrinking core model predicts that the product particle size should be larger than the initial particle size. In both mechanisms, the reaction rate should depend upon the initial oxide layer thickness, but with opposite trends. Furthermore, the shrinking core mechanism does not predict high enough reaction rates to raise the particle temperature to sustain gas phase species components. The MDM predicts gas phase species components like Al vapor because of the presence of the high energy nano-clusters because Al clusters (1-5 nm) will by definition have an enhanced Al vapor pressure [21,22].

The highly controlled environment of the shock tube allows the predictions related to gas-phase species related to combustion to be quantitatively assessed. We proposed that the appearance of enhanced Al in the gas-phase would be evidence against a purely (surface) diffusive oxidation model, though it would be difficult to separate the predictions of a classic vapor phase model and

the MDM on this basis alone. In addition, since the spallation proposed in the MDM is caused by mechanical stress from high heating rate instead of reaction, the bath gas should not be a factor for the presence of high temperature aluminum clusters. Therefore, Al vapor should be seen even in the absence of reaction from Al nano clusters spallated during a melt dispersion reaction.

Experimental Methods

The heterogeneous shock tube at the University of Illinois was developed and optimized during the past several years for the study of aluminum combustion. Previous work has focused on the particle size range of 1-20 microns [23,24], and we have worked with 80 nm aluminum particles [11]. The shock tube allows us to produce high temperature, high pressure, controlled environment combustion conditions and vary the particle diameter injected into the tube. Descriptions and dimensions of the shock tube can be found in previous publications [23-28]. Through the pressure ratio of the driver and driven sections, a strength selectable shock can produce a controlled combustion environment for approximately 2 ms in this shock tube. Various compositions of test gases can be used. Temperatures exceeding 4000 K and pressures up to 30 atm are achievable. The intent for this work was to run in lower temperatures and pressures in testing conditions used with n-Al, which ignites well below 2000 K [11].

Ordinarily, measurements in these low temperature conditions would be made in the incident shock region, but particles in the incident shock are moving, and it would be difficult to focus light through a transient burning cloud, especially when moving. Therefore, measurements were made in the reflected shock region.

Figure III.1 shows the schematic of the shock tube. Due to the high signal levels and precise focusing of optics needed, the aluminum particles were loaded on a knife edge to better control their location during the experiment. When the shock was fired, through the rupture of a double diaphragm, these particles initially loaded on the knife edge became entrained in the gas behind the incident shock in the test section. The reflected shock stopped the particles and heated them to a controllable temperature. High speed imaging was used to verify the location of the particles during the event, which was dependent upon conditions. For reflected shock temperatures above 2300 K, the particles were located ahead of the knife blade, while for temperatures below 2300 K, the particles were located within the 2.5 cm between the endwall and the knife blade.

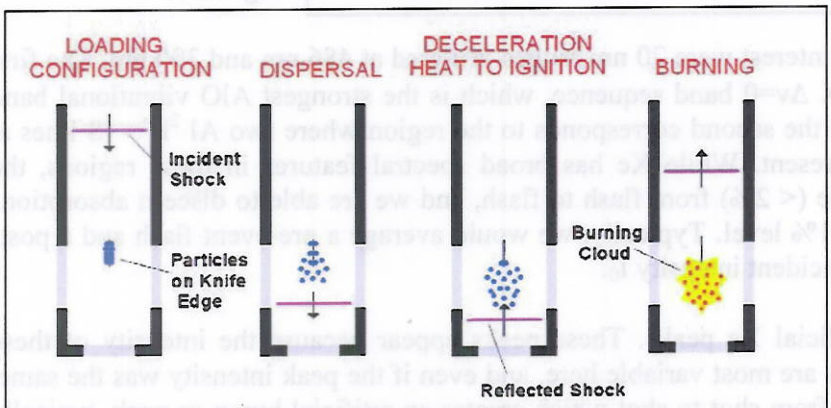

Figure III.1. Schematic of operation of heterogeneous shock tube with knife blade loading.

Conditions in which the particles were tested were 40% O_2/60% Ar, approximately 7 atm reflected shock pressure, and reflected shock temperatures starting as high as 2400 K, but working down in increments of about 100 K until the species of interest were not seen in absorption. This procedure was repeated for the active aluminum as well as non-reacting alumina samples. In addition, aluminum was tested in an inert environment, 100% Ar, also at 7 atm reflected shock pressure and at temperatures up to 3000 K.

Figure III.2 shows the diagnostics used for the absorption measurements. Light from a retroreflected, focused Oriel Xe flash lamp is passed through the cloud of reacting particles. A lens system collects the light from the Xe flash lamp through the test section, spatially filters it to limit the contribution of any broad emission from the particles, as well as any particles that may hit the endwall. This light is passed to a JY SPEX 270M spectrometer with a 2400 g/mm grating before being collected by a Hamamatsu back-thinned CCD array. Photodiodes are also used to ensure the timing of the flash overlaps precisely with the period in which the particles are hot and emitting as shown in Fig. III.3.

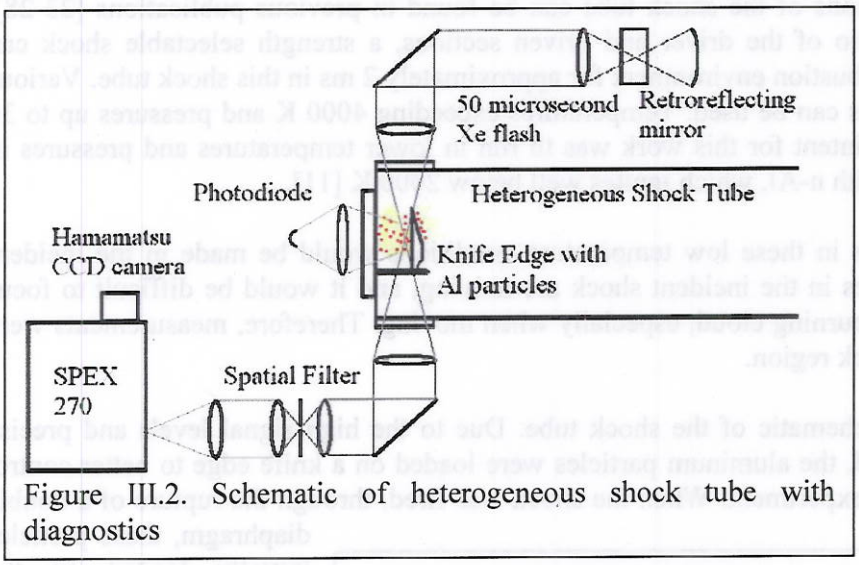

Figure III.2. Schematic of heterogeneous shock tube with diagnostics

The two spectral regions of interest were 20 nm ranges centered at 486 nm and 390 nm. The first corresponds to the AlO B-X $\Delta v=0$ band sequence, which is the strongest AlO vibrational band sequence in the visible, and the second corresponds to the region where two Al $^2P^o$ - ^2S lines at 394.4 and 396.2 nm are present. While Xe has broad spectral features in these regions, the intensity is highly repeatable (< 2%) from flash to flash, and we are able to discern absorptions down to approximately the 1% level. Typically, we would average a pre-event flash and a post-event flash to generate the incident intensity I_0.

Occasionally there are artificial Xe peaks. These peaks appear because the intensity of these peaks in the I_0 and I_1 signals are most variable here, and even if the peak intensity was the same, the line can appear broader from shot to shot which creates an artificial bump or peak, typically less than 2% absorption. While many of these artifacts are mostly removed by normalization with the incident intensity, they persist in some tests.

In some of the higher temperature conditions, (e.g. above 2300 K) there was a noticeable emission signal and spectrum during the test time. In order to account for this, several emission spectra were taken without the presence of the flash, at the same condition. An average emission

signal, weighted by the spectrally integrated photodiode intensity (which was observed to be the most consistent intensity measurement) was subtracted from the I_1 signal. In all cases, the emission was a small correction to the absorption measurement.

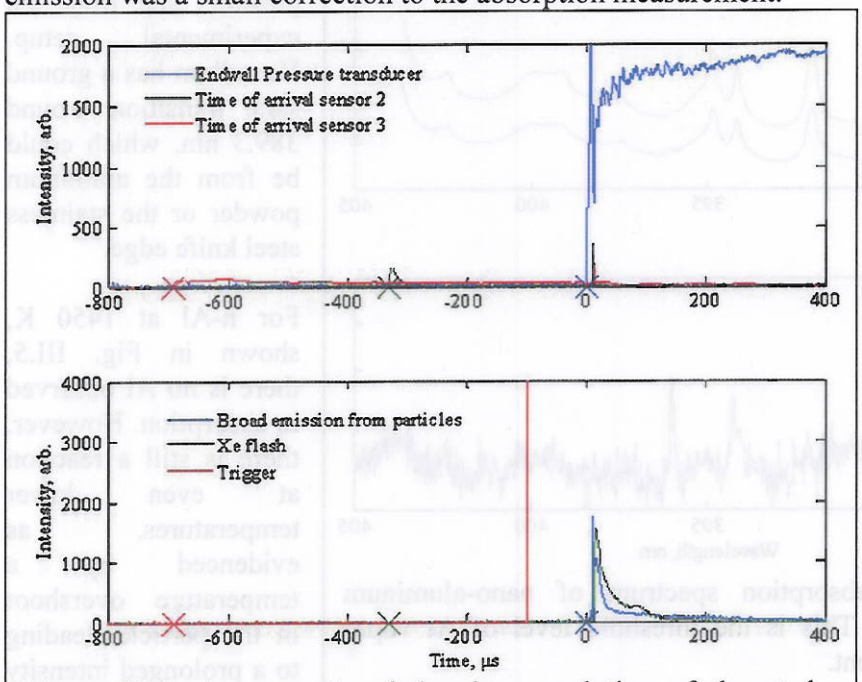

Figure III.3. An example of the time resolution of the study. Times are from endwall reflection. The Xe lamp (with a FWHM of 50 us) flashes during the combustion of the nano-aluminum, at this temperature also on the order of 50 us.

Two different size distributions of aluminum were studied. The first was size distribution "H-2" purchased from Valimet Inc. These particles are nearly spherical with a distribution centered nominally at 2 um. The number average is approximately 1.2 um and the mass average is 3.1 um. The second distribution was an 80 nm aluminum sample from Nanotechnologies. The average particle size of this material is 80 nm and the specific surface area is 28 m^2/g. Additionally, two distributions of alumina were used to compare the presence of AlO and Al that is a result of combustion with any Al or AlO that is generated thermodynamically by dissociation of Al_2O_3. A 3 um alumina size distribution was very similar to the H-2 size distribution albeit less spherical, and a nano-alumina distribution with a particle size of 75 nm was very close to the 80 nm aluminum.

Results and Discussion

Regardless of any molecular or atomic absorption of the flash signal, in all cases where the flash was correctly focused and timed to match the combustion of the aluminum particles, there was a noticeable extinction of light, continuous across the wavelength range. This broadband extinction signified the presence of particles in the test section at the prescribed time. This effect was typically small, less than 10% extinction, and so the cloud was assumed optically thin. In processing the data, a weakly linear function was fit to the total extinction signal $(I_1-I_0)/I_0$ and divided from the signal. Absorption signals are thus presented as absorption beyond the continuum extinction due to particulate scattering and any broadband absorption.

Figure III.4 shows an example of the near UV absorption spectrum of nano-aluminum combustion in 40% O_2 in Ar inert at 1517 K, which represents the lower limit of detection of Al vapor. The prominent features are Al lines at 394.4 and 396.2 nm. There are also trace elements

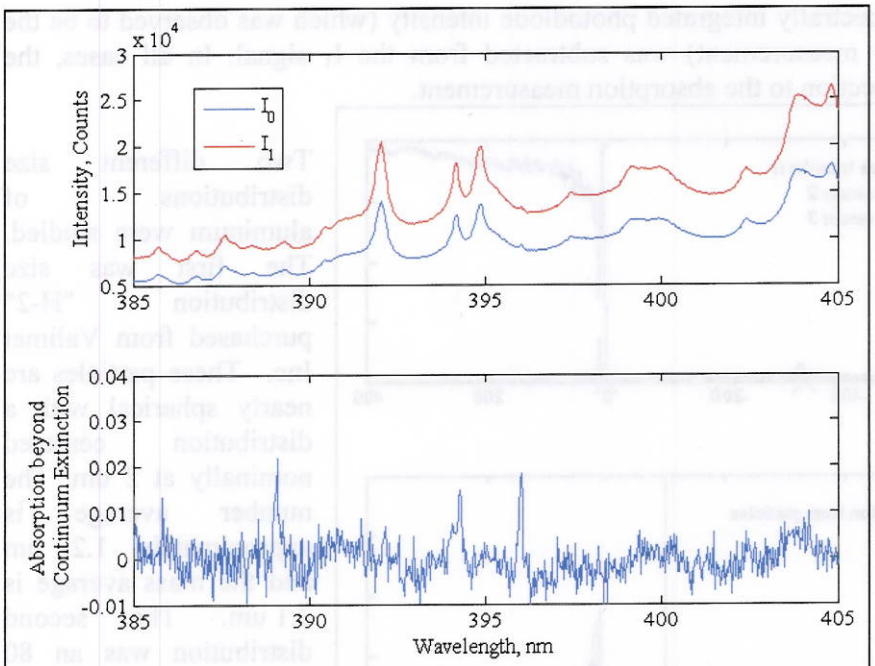

Figure 4. Near UV absorption spectrum of nano-aluminum combustion at 1517 K. This is the threshold level of Al vapor detection in our experiment.

from contaminants both in the aluminum powders and from the experimental setup. Vanadium has a ground state transition around 389.3 nm, which could be from the aluminum powder or the stainless steel knife edge.

For n-Al at 1450 K, shown in Fig. III.5, there is no Al observed in absorption. However, there is still a reaction at even lower temperatures, as evidenced by a temperature overshoot in the particle, leading to a prolonged intensity peak that fades within the shock tube test time. These intensity traces are indicative of a combustion event rather than simply a particle heat up with thermal decay. Similar photodiode traces were observed down to 1200 K.

Overall, absorption intensities were smaller for nano-aluminum than they were for micro-aluminum. While the mass loaded on the razor blade in the tube was roughly the same, about 100 ug, there is no guarantee that the mass of particles entrained was the same. An additional consideration in measuring nano-aluminum absorption which was less of an issue for micro-aluminum was timing. At 2300 K, the FWHM

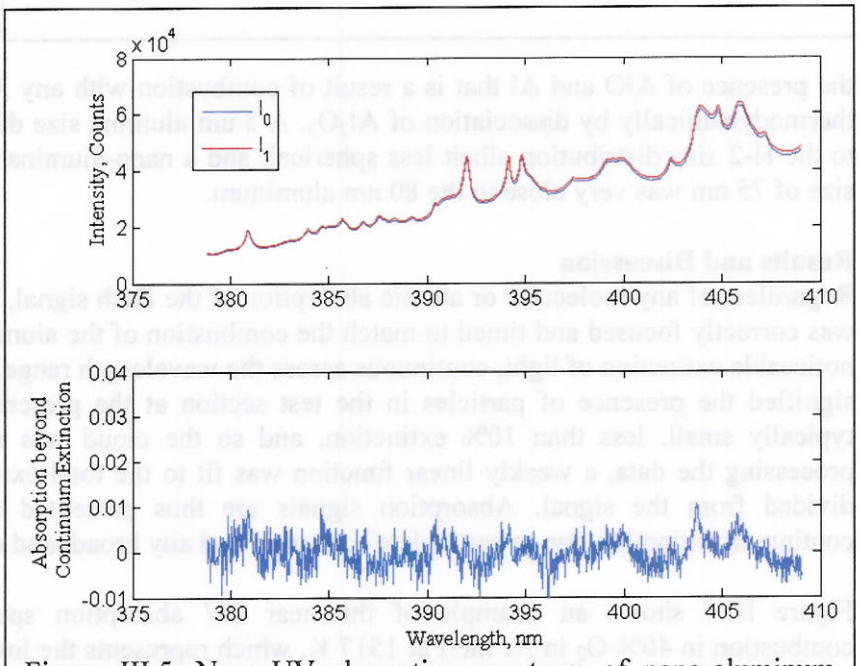

Figure III.5. Near UV absorption spectrum of nano-aluminum combustion at 1450 K. Al vapor is not detected.

burn time of the distribution is only 50 us, as can be seen in Fig. II.2, and 50 us is comparable to the flash time. However, as the temperature decreased to 1400 K, the burn time was approximately 500 us, but the intensity is greatly reduced. These results are in line with our previous work [11]. We varied the trigger delay on the flash lamp in order to capture both the absorption during the peak event, as well as that ahead of the peak and after the peak. In the off-peak cases, we observed less molecular and atomic absorption.

When 2 um aluminum particles were burned, the lowest temperature for which Al vapor was observed was 1700 K. Below this temperature, Al was not observed, nor did the intensity traces seen in the photodiodes decay during the test time, so it is unclear if the particles burned during the test time.

We also observed the AlO absorption spectrum of these powders. Figure III.6 shows the absorption spectrum of the 2 um powder at 2083 K, which was the lowest temperature at which we observed significant amounts of AlO absorption in micro-aluminum combustion. In this case, the $\Delta v' = 0$ peak generates nearly 10% peak absorption for a 1 Å spectral FWHM. At lower temperatures, such as 1900 K shown in Fig. III.7, AlO does not appear above the level corresponding to 1% absorption. At this temperature, we know there is still some reaction because the Al signal remains high (7% absorption) and the photodiode intensity traces show a peak in intensity that fades within the test time. Therefore, we conclude that the particles are still burning at 1900 K, though AlO is below the detection limit.

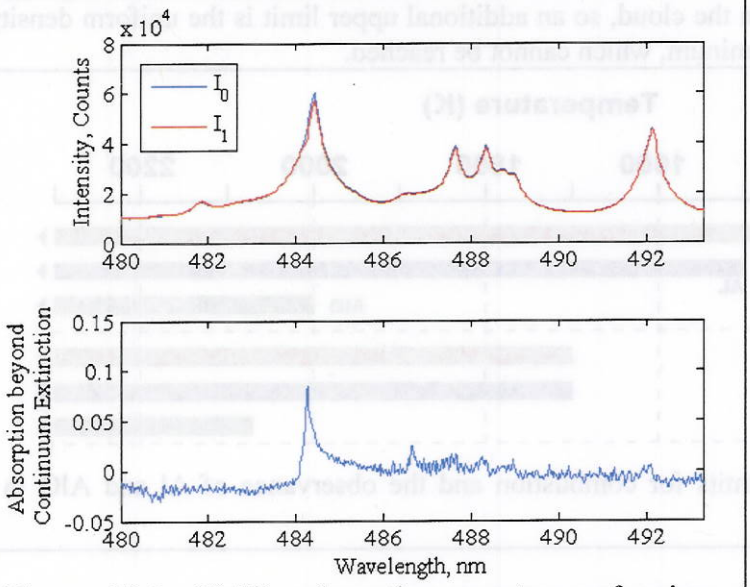

Figure III.6. Visible absorption spectrum of micro-aluminum combustion at 2083 K. AlO is detected.

As anticipated, the smaller particle size supported gas phase combustion with AlO at a lower temperature than the 2 um distribution. However, this threshold only dropped to 1996 K from 2083 K. This, as well as previous results in with emission spectroscopy [11, 23], suggest that AlO is not present in the gas-phase for the bulk of the nano-aluminum combustion experiments. The lack of gaseous AlO is consistent with most proposed mechanisms for nano-aluminum, which suggest that reaction will occur almost exclusively heterogeneously at relatively low temperatures. Increasing the pressure, however, should extend the limit of AlO presence for example, in high-pressure O_2 environments (~32 atm) it is present presumably because the particle structure begins to assume the transitional flame structure when reactions get faster, combustion temperatures increase, heat does not escape the particle as fast, and significant aluminum vaporization occurs.

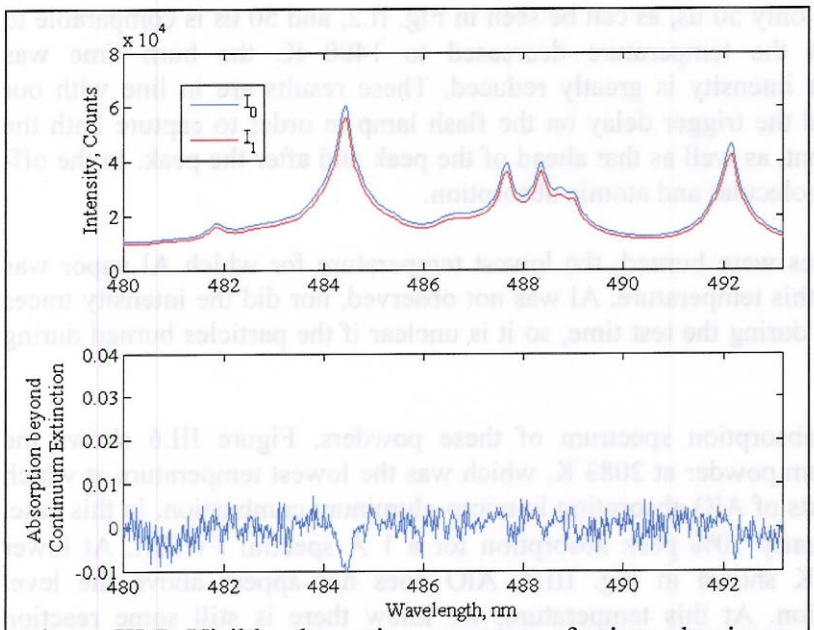

Figure III.7. Visible absorption spectrum of micro-aluminum combustion at 1900 K. AlO is not detected.

The qualitative results for the detection of gas phase species and combustions with ambient temperature for the two different reacting powders are shown in Fig III.8. We quantified the concentration of the Al vapor (using the 396.15 nm transition) and compared it to the concentration that could be present from the Al vapor pressure at the ambient temperature. This comparison represents an upper limit on the amount of Al that could be observed if the particle temperature were at the ambient temperature. In practice, however, this number might exceed the amount of aluminum in the cloud, so an additional upper limit is the uniform density from complete vaporization of aluminum, which cannot be reached.

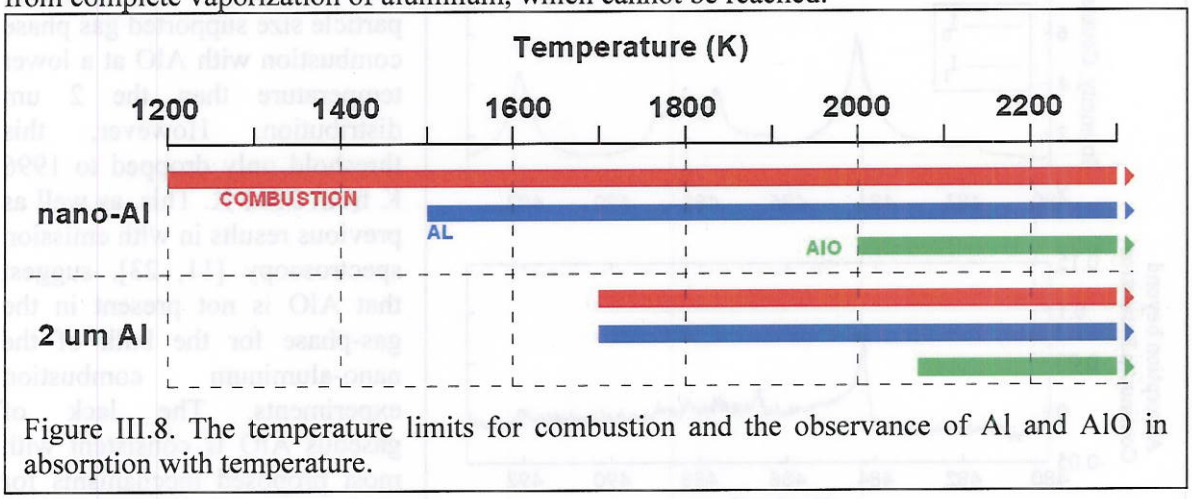

Figure III.8. The temperature limits for combustion and the observance of Al and AlO in absorption with temperature.

The detection limit of 1% absorption for the 396.15 nm line of aluminum vapor corresponds to an Al number density of approximately $1x10^{12}$ cm^{-3} for a 2.5 cm path length This path length assumes that the Al atoms are uniformly distributed throughout the collection volume, which would be the lowest limit of concentration near the reacting particle. More likely, the Al vapor is concentrated near the surface of the burning particle.

Calculations assuming a uniformly distributed cloud suggest as many as 3 x 10^8 particles in the collection volume, but this number is likely lower due to particles not detaching from the knife edge, or impacting upon the endwall. The interparticle distance may be as low as 100 particle

diameters (but should not be expected to increase by orders of magnitude) while the volume accessible by diffusion of Al vapor during the time of the flash encompasses as many as 500 particle diameters. Because the interparticle distance is small compared to the diffusion length, the uniform concentration assumption appears acceptable as long as the number density is smaller than that from vapor pressure. The density cannot be uniform at the vapor pressure for single particle combustion, and this would be an indication that the vapor is concentrated near the particle and not uniform.

Figure III.9 plots the number density of Al measured at the particle temperature as well as the limits of the aluminum vapor pressure and the maximum density from the total amount of aluminum in the cloud. This plot also includes data from 10 um Al particles tested at higher temperatures. Particles of that size in those conditions sustain a more vigorous diffusion limited or at least transitional structure. The error associated with the measured number density is attributed to the uncertainty in path length and volume of the cloud and the uncertainty in the absorbed equivalent width, which is greatly magnified in the micro-aluminum Al density because of the shallow curve of growth. The error associated with the maximum density is attributed to the uncertainty both in the mass of Al in the cloud and the cloud volume

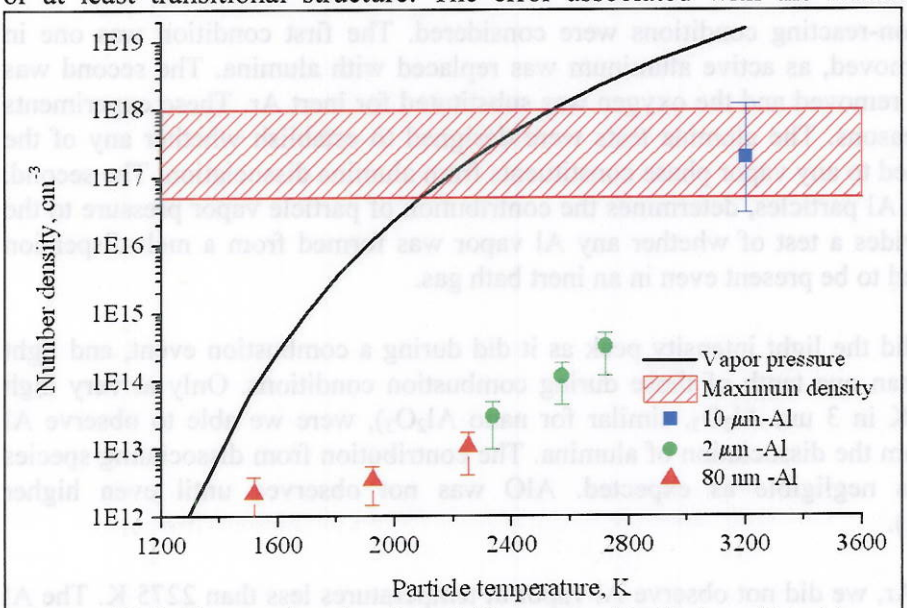

Figure III.9. The number density of Al compared to that predicted by the vapor pressure or the maximum density for complete vaporization of added Al for various temperatures and particle

The nano particle temperatures in these plotted conditions were not significantly higher than the ambient temperature. Particle temperatures were measured for similar conditions in our previous paper [11]. The temperatures of reacting 2 um powders and 10 um powders at the higher ambient temperatures were measured using emission spectroscopy. In conditions of the same temperature, pressure, and oxidizer conditions, particles were injected. Measurements were made using two spectrometers: a 50 mm f/5 spectrograph with 2 Å resolution over a 100 nm range and a 180 mm spectrograph with a 200 nm range. The former setup is used to isolate the AlO B-X $\Delta v = +1$ transition for temperature fitting where it presented strongly in emission, and the latter was used to measure the broadband continuum and fit that to a grey body temperature. These measurements were calibrated before each test with a 3200 K color temperature tungsten calibration source. The particles were assumed grey.

For the condition the 10 um powder was tested, both the condensed phase temperature and the gas phase temperature were around 3200 K. This is in line with previous results with these particles [23,29]. For the 3 um powders, the AlO signature was weak, but the condensed phase temperatures were about 300 K higher than the ambient gas temperature. This increased the Al number density predicted by vapor pressure about 1 order of magnitude.

The Al number density is about 10% of that predicted by the vapor pressure for 10 um reacting particles. For micro-and nano-aluminum combustion burning at lower temperatures, the expected number density from vapor pressure is 100 to 10^5 that seen. This suggests that while there are gas phase components in nano-aluminum combustion (at least as low as 1500 K) a gas phase mechanism is not as dominant as it is in larger particles.

Finally, two sets of non-reacting conditions were considered. The first condition was one in which the fuel was removed, as active aluminum was replaced with alumina. The second was when the oxidizer was removed and the oxygen was substituted for inert Ar. These experiments were useful for two reasons. The alumina tests were designed to establish whether any of the signal could be attributed to any vapor phase constituents from alumina dissociation. The second, inert environment with Al particles, determines the contribution of particle vapor pressure to the signal, as well as provides a test of whether any Al vapor was formed from a melt-dispersion type spallation predicted to be present even in an inert bath gas.

In no inert condition did the light intensity peak as it did during a combustion event, and light intensities were less than one tenth of those during combustion conditions. Only at very high temperatures, (>2350 K in 3 um Al_2O_3, similar for nano Al_2O_3), were we able to observe Al vapor in absorption from the dissociation of alumina. The contribution from dissociating species at low temperature is negligible as expected. AlO was not observed until even higher temperatures (~2700 K).

For nano Al in 100% Ar, we did not observe Al vapor at temperatures less than 2275 K. The Al number density detection limit of 1×10^{12} cm^{-3} suggests that we should be able to observe equilibrium partial pressure of aluminum at temperatures as low as 1200 K. However, in non reacting n-Al, Al vapor was not observed until the temperature approached the melting point of alumina. This result suggests that negligible amounts of Al vapor are allowed to escape through an the oxide coating during combustion time scales. There may be diffusion through pores or cracks on a longer time scale, but the high temperatures of combustion are needed to sustain an appreciable vapor phase. Furthermore, these observations suggest that Al vapor is not present from high energy Al clusters, which should be created by a melt-dispersion mechanism spallation. We would be able to detect Al vapor vaporized from unoxidized Al from equilibrium partial pressure if its temperature was as low as 1200 K. We do not observe this phenomenon.

One of the primary distinctions between the two nano-aluminum combustion mechanisms is the fraction of Al that oxidizes through a vapor route. The surface diffusion model assumes diffusion through the particle, where Al and oxidizer react heterogeneously. The diffusion in the particle limits the reaction, and oxidizer transport to the surface is fast enough to keep a constant concentration at the surface. Because of these assumptions, the amount or Al vapor produced as

well as that which oxidizes through the vapor route should be very small. In the MDM, on the other hand, the presence of high-energy nanoclusters should mean a significant fraction should oxidize through a vapor route.

Measurements of Al vapor density alone do not allow us to directly quantify the oxidation that passes through a vapor route. Assuming a two step irreversible mechanism Al(s) → Al(g) and Al(g) → products, the relative rates would determine the interpretation, and we do not know the rates for either process well. We must make inferences based on density comparison to a more vigorous vapor phase combustion, which we have with the 10 um Al at higher temperatures.
We do in fact observe some fraction of Al vapor that is unexplained by a pure surface model. The ratio of Al measured to the Al predicted from vapor pressure at the particle temperature is significantly less for nano-aluminum than it is for the 10um Al. The mechanism will have to account for a transition with some vapor phase component at a lower temperature than previously seen.

While the appearance of a small vapor phase component is somewhat consistent with MDM, there are two problems. While it is unclear how much vapor should be expected, the amount observed is small relative to any metric, the amount that could be put out from Al's partial pressure, or the Al that we see from a more vigorous vapor phase combustion condition, like that seen with the 10 um particles. More importantly no Al vapor is observed when the bath gas is Ar. There should be more Al vapor in that case because there is no gas phase oxidation sink for Al but the same heating rate as the supposed source of Al nanoclusters. The MDM should account for this.

Conclusions

An experimental study of the absorption of gas phase species during micro- and nano-aluminum combustion was conducted and yielded the following conclusions:

AlO was detected in absorption during micro-aluminum combustion at temperatures as low as 2083 K, and during nano-aluminum combustion at temperatures as low as 2000 K

.

Al vapor was detected in absorption during 2 um aluminum combustion at temperatures as low as 1700 K; it could be detected in nano-Al combustion at temperatures as low as 1500 K. The ratio of the number density observed to that predicted by Al vapor pressure considerations is much lower than that of 10 m Al, which sustains a vigorous gas phase component in combustion.

The lack of detection of Al vapor during non-reacting conditions in nano-aluminum at temperatures below the melting point of aluminum oxide suggests a pristine oxide layer prevents the escape of aluminum and the absence of Al clusters generated by the melt dispersion mechanism, even in inert bath gases.

References

[1] N. Glumac et al., Combustion Science and Technology 177 (3) (2005) 485.
[2] S. Goroshin et al., Proceedings of the Combustion Institute 31 (2) (2007) 2011.
[3] I. Glassman, Combustion, 3rd Edition, Academic Press, San Diego, CA, (1996).

[4] M. Beckstead, Combustion, Explosion, and Shock Waves 41 (2005) 533.
[5] J. Melcher, H. Krier, and R. L. Burton, Journal of Propulsion and Power 18 (2002).
[6] R. Friedman and A. Macek, Combustion and Flame 6 (1962) 9.
[7] S Olsen and M. Beckstead, Journal of Propulsion and Power 12 (1996).
[8] K. Brooks and M. Beckstead, Journal of Propulsion and Power 11 (1995).
[9] E. Dreizin, Combustion and Flame 105 (1996) 541.
[10] P. Bucher, et al., Combustion and Flame 117 (1999) 351.
[11] T. Bazyn et al., Combustion and Flame 145 (2006) 703.
[12] O. Levenspiel, Chemical Reaction Engineering 3rd Ed., Wiley: New York (1999).
[13] M. Trunov, M. Schoenitz, E. Dreizin, Propellants, Explosives, Pyrotechnics 30 (2005) 36.
[14] K. Park et al., Journal of Physical Chemisty B 109 (2005) 7290.
[15] K. Aita, et al. 44th AIAA Aerospace Sciences Meeting and Exhibit Paper 2006-1156 (2006).
[16] A. Rai et al., Combust. Theory Modeling, 10 (2006) 843.
[17] S. Yagi and D. Kunii, Chemical Engineering Science 16 (1961) 364.
[18] V. Levitas et al., J. App. Phys, 101 (2007).
[19] V. Levitas, M. Pantoya, B. Dikici, App. Phys. Ltrs. 92 (2008).
[20] K. Watson et al., Combustion and Flame, 155 (2008) 619.
[21] T. Campbell, et al., Physical Review Letters 82 (1999) 4866.
[22] H. Farrell et al. Journal of Vacuum Science and Technology B, 25 (2007) 1441.
[23] T. Bazyn, H. Krier, N. Glumac, Proceedings of the Combustion Institute 31(2007) 2021.
[24] P. Lynch, H. Krier, and N. Glumac, Proceedings of the Combustion Institute 32 (2009) 1887.
[25] J. Servaites, Master's thesis, University of Illinois at Urbana-Champaign, Urbana, IL (2001).
[26] T. Bazyn, Ph.D. thesis, University of Illinois at Urbana-Champaign, Urbana, IL (2006).
[27] M. Spalding, MS. thesis, University of Illinois at Urbana-Champaign, Urbana, IL (2000).
[28] T. Roberts, R. Burton, and H. Krier, Combustion and Flame 92 (1993) 125.
[29] T. Bazyn, et al., Combustion Science and Technology 179 (2007) 457.

IV. Shock Effects on Particle Reactivity from AlO Emission Spectroscopy

Abstract

The effects of a detonation shock on the reactivity of aluminum particles were examined experimentally using small scale charges, varied Al loadings, and time-resolved AlO spectroscopy. There are indications that early time reaction of aluminum is seen in cases where the Al powder experiences the full detonation wave. However, significant concerns over the robustness of the AlO emission spectroscopy diagnostic are raised.

Motivation

Ignition of micron sized aluminum is dominated by the oxide layer ordinarily surrounding every aluminum particle. While oxide layer thicknesses are typically on the order of 3-4 nm for particles in the 1-10 μm range, the oxide layer is strong enough to prevent the aluminum from diffusing out to the surface of the particle or into a vapor which would react with oxidizers present. Large particles do not ignite at temperatures below 2300 K which is the melting temperature of the aluminum oxide layer. Because of surface tension, the molten alumina retracts to a cap which takes up a smaller surface area, and the aluminum diffuses out and burns in the gas phase. Below this temperature, there is cracking and healing of the oxide shell, but not significant gas phase reaction. Enhanced ignitibility of aluminum particles should occur after the aluminum passes through a strong detonation wave. The detonation wave may strip the particles of the oxide layer, or deform them in a way that exposes molten aluminum and enhances the ability of aluminum to further react with the products in the explosive fireball, releasing extra energy.

Experimental setup

Tests of the effects of the detonation wave on the combustion of different sized Al particles were conducted in the wake of 50 mg PBX charges. The explosive fireball expanded into ambient air.

We used three methods to introduce aluminum into the blast wave. The first method of introducing aluminum into the blast was to use standard RISI RP-2 detonators layered with a small amount of aluminum powder (1 mg) pressed on the end (a in Fig. IV.1). During the event, aluminum particles experience the detonation wave as well as a combination of post detonation gases and ambient air as they pass through a 2 mm diameter tunnel approximately 1 cm from the detonator. The detonator chamber was specifically designed to preclude

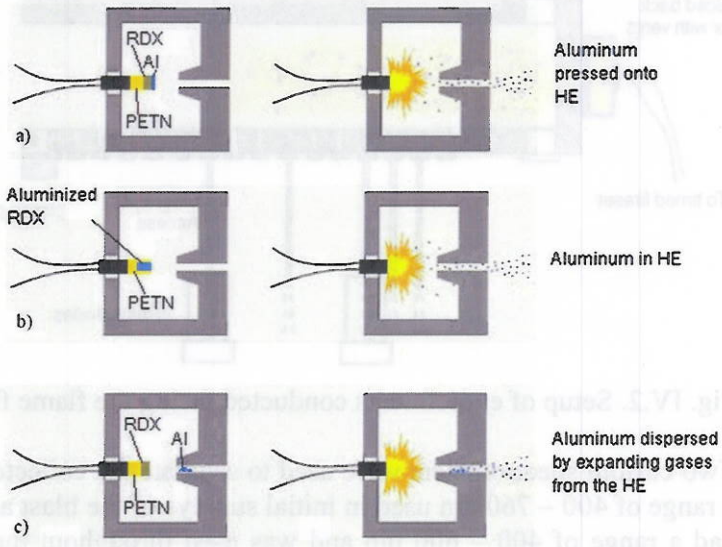

Fig. IV.1. Loading Strategies for Al.

the expanding casing from entering into the tunnel. In order to pack additional powder onto the end of the detonator, thin layers of epoxy or vacuum grease were applied to the end of the charge before powder was packed on. It is unlikely that the thin layers changed the oxidizer concentration that the Al powders experienced during the event, and while the light intensity was larger, the shape and duration was not substantially longer than without the layers.

The second method (b in Fig. IV.1) was to have the aluminum imbedded in the detonator. Teledyne/RISI created custom RP-2 detonators in which the RDX was replaced with a 20% Al / 80% RDX mixture. The initial particle size of the aluminum used in the charges was a 15-20 μm distribution. During the event, the aluminum experienced the detonation wave and post detonation gases as it is passed through the choke tunnel. The powders have less opportunity to interact with ambient oxidizers, but there is probably ample mixing. Finally, we introduced aluminum into the expanding gases of the high explosive passing through a 2 mm diameter tunnel. The particles initially attached to the tunnel walls are entrained in the mixture of high temperature gases and ambient air, but should not experience the full strength of the detonation wave (c in Fig. IV.1).

We examined the ignition delay, burn time and temperature of aluminum particles in the blast wave using optical diagnostics. At first, tests were performed with diagnostics aimed upstream at the detonator and blast as shown in Fig. IV.2, although there was also fiber optic access at different axial locations along the tube for photodiodes. Optics were initially focused approximately 1 cm downstream of the exit of the choking tunnel, through which the explosive fireball would emanate. However, this was found to underestimate the burning time of the aluminum particles because the collection volume was biased to this region of initially intense blast and underrepresented the contribution from late burning particles which may burn several cm from focus of our optics. Instead we collimated our optics which reduced this effect.

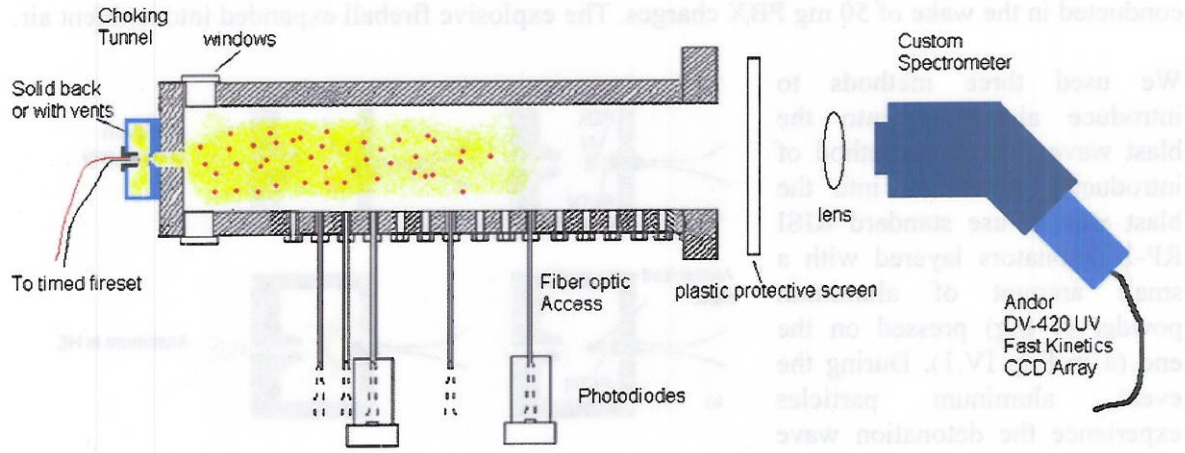

Fig. IV.2. Setup of experiments conducted facing the flame front.

Two custom spectrometers were used to separate the collected light by wavelength. The first had a range of 400 – 760 nm used in initial surveys of the blast across the visible spectra. The second had a range of 400 – 600 nm and was used throughout the rest of the study. The Andor DV-420UV-FK CCD array was used to record the spectra. The 1024 x 1 pixel Fast Kinetics array could take up to 127 spectra with exposure times as low as 1 μs. Wavelength calibrations were

performed with a Hg light source, and intensity calibrations were performed with a 3200 K color temperature tungsten lamp. Figure IV.3 shows example spectra of the emission of Al in the tube at three different times during combustion. Aluminum Monoxide (AlO), a combustion intermediate of aluminum in its reaction with CO_2, O_2, and H_2O was observed strongly in emission, indicating reaction.

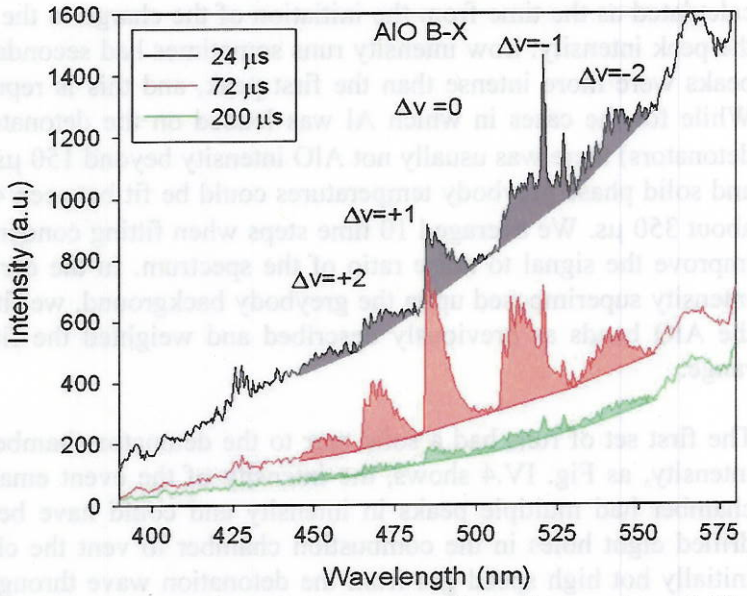

Fig. IV.3. Example emission spectra from the reaction of Al particles in the tube, highlighting the AlO B-X bands. The shaded area shows the AlO intensity which was integrated and indicative of burn time.

In all detonator spectra, and in particular in the first tests that were focused near the tunnel through which the fireball emanated, the first frames (1-4 μs) were extremely bright, and spectral features were very broad. After this initial brightness and the expansion of the cloud, spectral features could be resolved. Besides AlO, atomic and molecular interferences were present from Cr, Na, and FeO, however their contribution to the overall intensity is negligible, and only one Cr line was observed in the AlO spectrum.

Burning times were calculated from the presence of light intensity emitted from AlO. For each spectrum, we fit a linear background to each of the five vibrational band heads between 440 nm and 550 nm and integrated AlO signal beyond this background. An example AlO signal would be the shaded regions in Fig. IV.3. This was repeated for the different spectra taken during each experiment (through time). The burning time was then calculated as either the 10-90% limits on the cumulative intensity of AlO or by using a full-width at half-maximum of the intensity peak. The ignition delay was

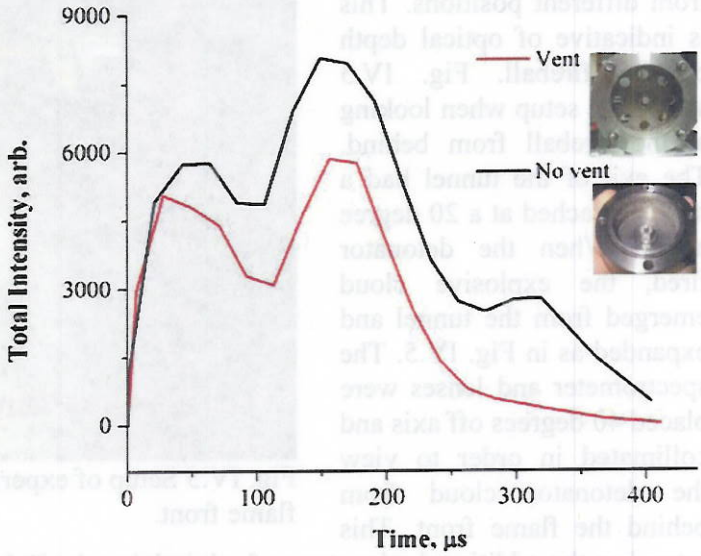

Fig. IV.4. The effect of including a vent in the combustion chamber for an aluminized detonator.

calculated as the time from the initiation of the charge to the time when the AlO signal reaches the peak intensity. Low intensity runs sometimes had secondary peaks, and rarely the secondary peaks were more intense than the first peak, and this is represented with long ignition delays. While for the cases in which Al was loaded on the detonator or in the detonator (aluminized detonators) there was usually not AlO intensity beyond 150 μs, it was present in some conditions and solid phase greybody temperatures could be fit between 450 and 650 nm wavelengths up to about 350 μs. We averaged 10 time steps when fitting condensed phase temperatures in order to improve the signal to noise ratio of the spectrum. In the early spectra when there was an AlO intensity superimposed upon the greybody background, we fit a background around the bases of the AlO bands as previously described and weighted the fit less strongly in the 450-550 nm range.

The first set of runs had a solid rear to the detonator chamber. In our initial results of the total intensity, as Fig. IV.4 shows, the intensity of the event emanating from the solid 'not vented' chamber had multiple peaks in intensity and could have been indicative of confinement. We drilled eight holes in the combustion chamber to vent the chamber and ideally allow only the initially hot high speed gas from the detonation wave through the choke tunnel and reduce the contribution of gases coming through the tunnel after an overpressure in the combustion chamber. Fig. IV.4 also shows the intensity of the event emanating from the 'vented' chamber, which showed two peaks around the same time as the first peaks, however a third peak at about 325 μs was suppressed. The same effect was seen for all loading configurations and in cases with only RP-2 detonators and no aluminum added to the system. As the AlO intensity rarely extended to 325 μs, the effect of confinement on the aluminum combustion was negligible.

During our tests, we noted differences in AlO intensities when we viewed the cloud from different positions. This is indicative of optical depth of the fireball. Fig. IV.5 shows the setup when looking at the fireball from behind. The exit of the tunnel had a mirror attached at a 20 degree angle. When the detonator fired, the explosive cloud emerged from the tunnel and expanded as in Fig. IV.5. The spectrometer and lenses were placed 40 degrees off axis and collimated in order to view the detonator cloud from behind the flame front. This setup has the additional advantage of minimizing the light from the detonator behind the tunnel and allowed us to collect only light that had passed through the tunnel and was in the explosive fireball. Because the flame front expanded as a jet as it exited the tunnel, the cloud was thinner

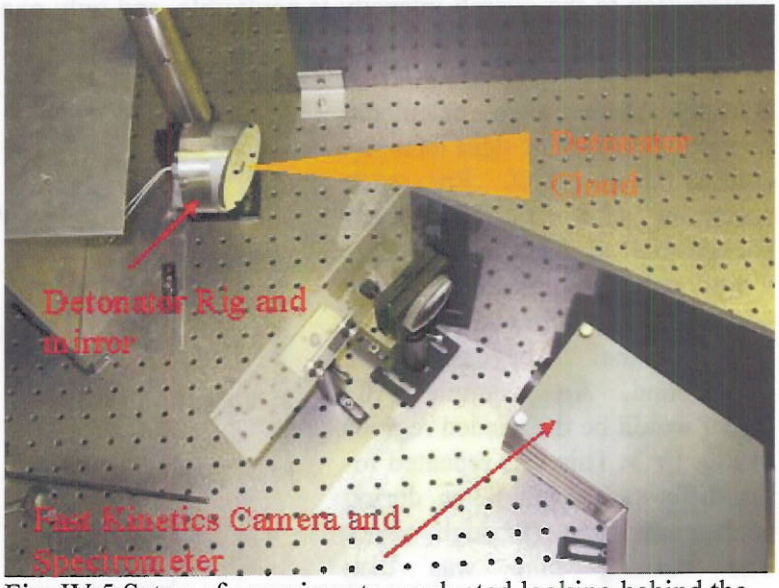

Fig. IV.5 Setup of experiments conducted looking behind the flame front.

and we were able to see deeper into the cloud. Finally, looking behind the flame front allowed us to see the fireball as it exited the tunnel, and the difference between the view from the front and from the rear, indicates if there are some entrainment effects of Al powder, initially on the wall passing through the tunnel late. If burn times of Al initially in the tube viewed from the front would have been significantly shorter than when viewed from the rear, the entrainment time scale may have been too long, however the opposite was observed.

Table IV.1. Matrix of Tests Performed

Viewing Configuration	Particle size (μm)	Loading Configuration	Ignition Delay (μs)	Burntime (μs) 10-90% Area	Burntime (μs) FWHM
Front	*10*	On Det 1	50	88	75
		On Det 2	16	30	29
		In Tube 1	16	148	35
		In Tube 2	12	23	21
	20	On Det 1	20	153	124
		On Det 2	28	207	253
		On Det 3	8	9	7
		On Det 4	10	26	23
		On Det epoxied 1	12	102	61
		On Det epoxied 2	150	300	300
		In Tube 1	40	75	64
		In Tube 2	25	71	71
		In Tube 3	155	185	197
		In Tube 4	126	188	196
		In Tube 5	0	175	170
		In Tube 6	0	194	7
		In Tube 7	0	281	12
		In Tube 8	34	183	57
		In Tube 9	2	147	6
		In Tube 10	2	169	5
		In Tube 11	2	165	7
		Aluminized 1	3	7	5
		Aluminized 2	3	12	6
		Aluminized 3	5	11	7
		Aluminized 4	1	4	3
		Aluminized 5	2	5	4
Rear	*20*	On Det 1	7	17	10
		On Det 2	7	103	8
		On Det 3	3	19	7
		On Det 4	5	17	11
		On Det 5	7	24	13
		On Det Epoxied	8	38	12
		In Tube 1	5	280	14
		In Tube 2	6	31	11
		In Tube 3	7	211	14
		Aluminized 1	8	34	11
		Aluminized 2	10	45	14
		Aluminized 3	8	28	10

Table IV.1 shows the test matrix of all the experiments performed with these initial setups. Ignition times and burn times are tabulated for each experiment.

One of the first parameters tested was the particle size. Comparisons were made with tests from the front. The only configurations that could be tested were with Al loaded in the tube and on the detonator because the initial batch of aluminized detonators only included 15-20 μm Al powder. Figure. IV.6 shows the AlO intensities from the 20 μm powder. Both the on detonator and in tube times were similar with burn times around 150 μs. There are some extended tails as can be seen in both configurations. One epoxy case, in which there were significant layers, had an extended burn time.

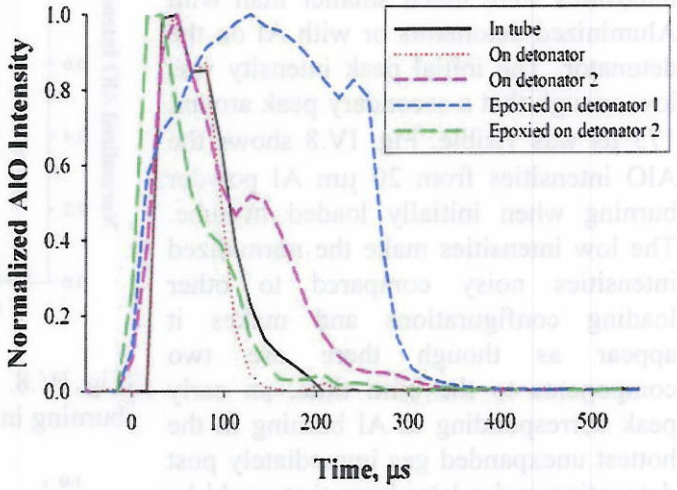

Fig. IV.6. AlO intensities of 15-20 μm Al powders in various configurations viewed head-on

Figure IV.7 shows the AlO intensities from a 5-10 μm Al powder placed either in the tube or on the end of the detonator. Burn times are shorter, averaging around 75 μs, but the tails appear more distinctively extended. The ignition delays are roughly the same. This suggests that the burn time is be approximately proportional to diameter, ($t_b \sim d^1$), consistent with a kinetically limited reaction rate.

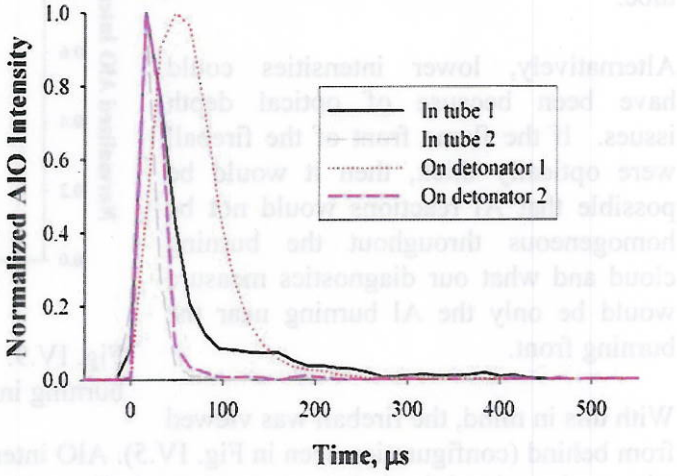

Fig. IV.7. AlO intensities of 5-10 μm Al powders in various configurations viewed head on.

When viewing the explosive fireball from the front (configuration seen in Fig. IV.2) with Al initially in the tube, the absolute intensities were much smaller than with Aluminized detonators or with Al on the detonator. The initial peak intensity was low enough that a secondary peak around 175 μs was visible. Fig. IV.8 shows the AlO intensities from 20 μm Al powder burning when initially loaded in tube. The low intensities make the normalized intensities noisy compared to other loading configurations and makes it appear as though there are two components to the burn time, an early peak corresponding to Al burning in the hottest unexpanded gas immediately post detonation and a later burn that could be affected by entrainment of the Al in the tube.

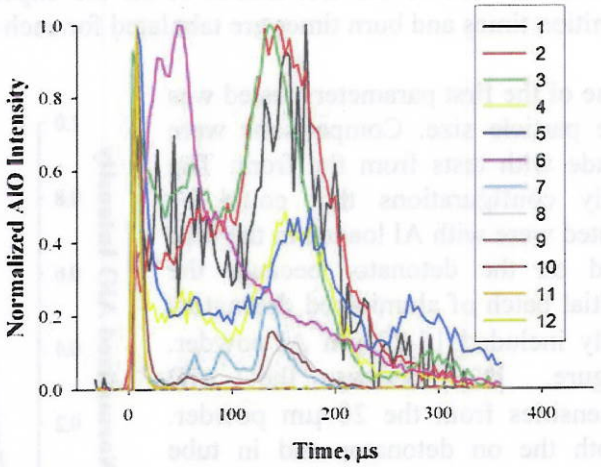

Fig. IV.8. AlO Intensities for 20 μm Al powder burning in tube, viewed head on.

Alternatively, lower intensities could have been because of optical depth issues. If the flame front of the fireball were optically thick, then it would be possible that Al reactions would not be homogeneous throughout the burning cloud and what our diagnostics measure would be only the Al burning near the burning front.

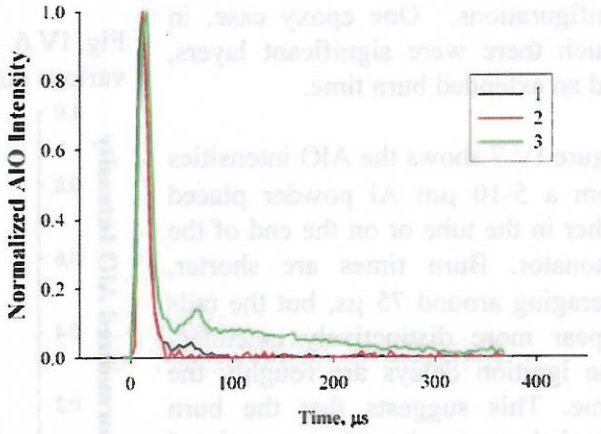

Fig. IV.9. AlO Intensities for 20 μm Al powder burning in tube viewed from the rear.

With this in mind, the fireball was viewed from behind (configuration seen in Fig. IV.5). AlO intensities from Al loaded on the detonator or when using aluminized detonators were similar when viewing from the front or back. Peak shapes were similar, and as can be seen in Table IV.1, the ignition delays and burn times were very similar but the aluminized detonator burntimes were slightly longer. AlO intensities when viewing from the rear of Al burning when initially loaded in the tube was much higher than when viewing from the front, and because of this, the signal to noise ratio is much larger as can be seen in Fig. IV.9.

Ignition delays appear smaller because the ignition delay is dependent upon the peak intensity, which is higher when viewed from the rear. Burn times, when calculated using the 10-90% cumulative intensity were similar though. Fig. IV.10 and IV.11 show the cumulative burn intensity when viewed from the front and rear respectively.

Aluminized detonators and Al on detonator conditions have about the same burning profile, the on detonator burn times are slightly faster, and the aluminized detonators burn slightly slower with Al burning to completion within about 50 μs. On the other hand, when Al is initially loaded in the tube, the Al requires much longer time to burn to completion. The extended burn time from Al in tube may still be attributed to the entrainment of the Al into the cloud when initially attached to the walls of the tube, however, since the cloud is rather optically, this effect should be seen more strongly when viewing the cloud from the rear as opposed to through the front. As we see late burning in both configurations, extended burn times should not be attributed to entrainment alone.

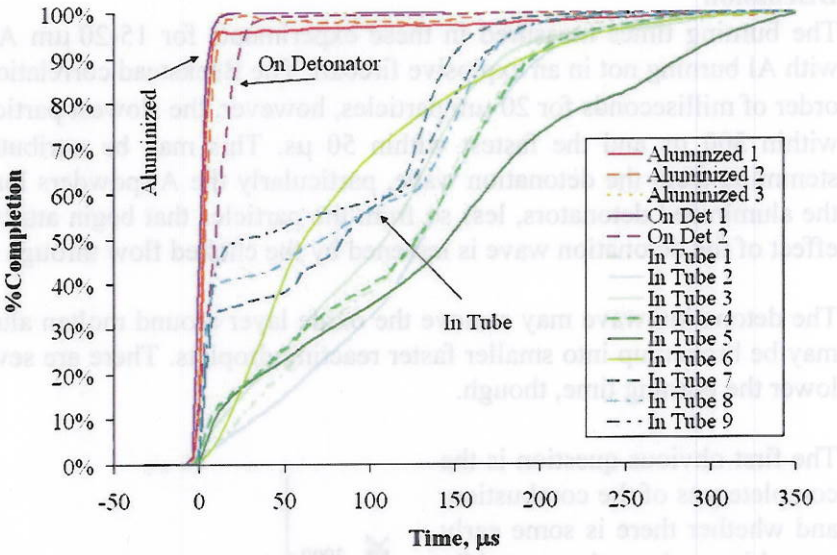

Fig. IV.10. Cumulative burn intensity from runs when viewed from the front.

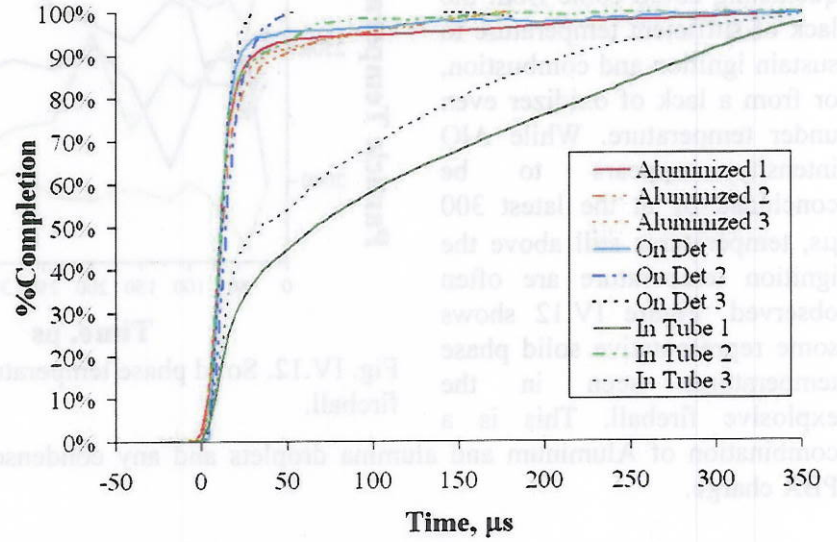

Fig. IV.11. Cumulative burn intensity from runs when viewed from the rear.

Discussion

The burning times measured in these experiments for 15-20 μm Al are quite small compared with Al burning not in an explosive fireball. The Beckstead correlation predicts burn times on the order of milliseconds for 20 μm particles, however, the slowest particles appear to have burnt out within 300 μs and the fastest within 50 μs. This may be attributable to enhanced reactivity stemming from the detonation wave, particularly the Al powders loaded on the detonators or in the aluminized detonators, less so from the particles that begin attached to the tube in which the effect of the detonation wave is lessened by the choked flow through the 2 mm tube.

The detonation wave may remove the oxide layer around molten aluminum, and the Al droplets may be broken up into smaller faster reacting droplets. There are several other factors that could lower the burning time, though.

The first obvious question is the completeness of the combustion, and whether there is some early quenching in the rapidly expanding fireball. Early quenching could come from the lack of sufficient temperature to sustain ignition and combustion, or from a lack of oxidizer even under temperature. While AlO intensity appears to be concluded by at the latest 300 μs, temperatures still above the ignition temperature are often observed. Figure IV.12 shows some representative solid phase temperatures seen in the explosive fireball. This is a combination of Aluminum and alumina droplets and any condensed phase products from the PBX charge.

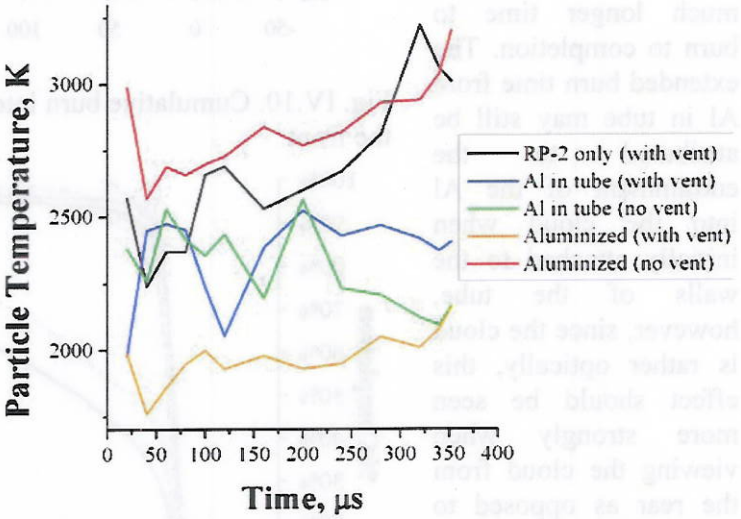

Fig. IV.12. Solid phase temperatures seen in the explosive fireball.

Temperatures vary from about 2000 K to 3000 K and do not show a sharp drop between 150 μs and 350 μs, which may have been expected if AlO signatures are quenched in this regime. There should be significant gas phase reaction with temperatures above 2300 K, but we have also seen reactions with temperatures for micron sized particles as low as 2000 K, so based on temperature, we should expect combustion to be complete if we do not see AlO. It is unlikely that particles would remain above the ignition temperature and not react. *Ex situ* analysis of the post detonator products in other tests showed nearly complete reaction to alumina.

The second factor influencing the completeness of combustion is if there is sufficient oxidizer. It is unclear how much mixing there is between the ambient air and the products of the detonation, so the most conservative estimate should include only the products of the detonation blast.

Chemical equilibrium calculations were performed for 20% aluminum PBX charges, without an additional oxidizing environment using the Gordon-McBride code. The assigned pressure, enthalpy problem was used. The pressure was set to 1 bar. PETN, RDX were entered as reactants along with the aluminum. The number of moles of reactants was used based on the amount of PETN/RDX/Al in the RP-80 and environment gas inside the chamber, but scales down for RP-2 size charges. The results of the equilibrium calculations are shown in Table IV.2.

Table IV.2. Results from Gordon-McBride equilibrium calculations of aluminized PBX charges.

20% Al RP-80			
Product	Mass Fraction	Product	Mass Fraction
AlO	0.79%	N_2	24.87%
AlOH	2.01%	O	2.04%
CO	32.48%	OH	3.25%
CO_2	5.21%	O2	1.30%
H_2O	6.28%	$AL_2O_3(L)$	18.96%
NO	0.97%		

Aluminized RP-80's have some unreacted Al in the vapor phase, but significant amounts of liquid Al_2O_3. Products with significant amounts also include CO, which reacts slowly with Al. Even without an environment, the majority of the Al, by mass, is oxidized to Al_2O_3. Based on the GM calculations, it appears there is enough oxidizer to support full oxidation, especially if there is some mixing with oxygen from the environment

The third factor that may contribute to a deceptively fast burn time is optical depth. Optical depth clearly is an issue since we see different signals when looking upstream at the detonator or downstream from the rear of the detonator. We see a slight increase in burn time of aluminized detonators when looking from behind when Aluminized detonators should have Al distributed most evenly through the explosive fireball. Additionally, we see higher intensity from particles when initially starting in the tube when viewed from behind, through an optically thinner section of the fireball. This indicates that the fireball is optically thick and we only see the reaction of particles near the edge of the explosive fireball. Al particles could still be burning for an extended period of time inside the fireball, likely because the PBX detonation products are slower oxidizers than oxygen for example. The outer edge may burn out in the air or be quenched because of the mixing with the cold air and not show burn times as long as seen in the shock tube or in solid rocket motors.

Finally, it is possible that there is a significant heterogeneous component to the reaction, perhaps from broken up smaller particles, and less AlO. The initially seen AlO peaks may be dissociation from initially hot Al_2O_3.

V. Shock Effects on Particle Size Distribution

Abstract

A rapid quench reaction chamber was designed to detonate small scale aluminized charges in an environment where particle reactivity was strongly suppressed. Particle size distribution was analyzed before and after detonation to examine any differences. The effectiveness of the particle quench was shown experimentally using emission spectroscopy and *ex situ* residue analysis. Significant fragmentation and agglomeration of the particles was not observed, supporting the idea of using the same size distribution in reacting flow calculations after the passage of the detonation. In addition, preliminary experiments on AlO emission spectroscopy in aluminized charges were conducted, including some 2-D time resolved imaging AlO emission measurements using the High Speed Framing Camera and selected interference filters.

Introduction

In modeling enhanced blast effects of aluminized charges, the size distribution of the particles is known before detonation. However, there is speculation that passage of the detonation leads to significant particle deformation and perhaps fragmentation or agglomeration. Since the particle size distribution figures strongly into the predicted thermobaric effects, it is critical to get this portion of the calculation right. In this work, we examine the effect of the detonation wave on the particle size distribution by constructing a special facility to rapidly quench the particle chemistry in small charges, then analyzing the residue in detail.

Experimental

The experimental setup used to quench the combustion reactions following the detonation of an aluminized HE detonator is shown in Figure V.1. An aluminized detonator was secured in the center of the throat section of a convergent-divergent nozzle, then fired into the expanding region. A high speed flow was created in the nozzle by connecting a vacuum pump to the downstream flange and a helium gas cylinder to the upstream flange. An inert working fluid was used to limit the presence of oxidizers in the environment which, in addition to the high speed flow, prevented the aluminum combustion.

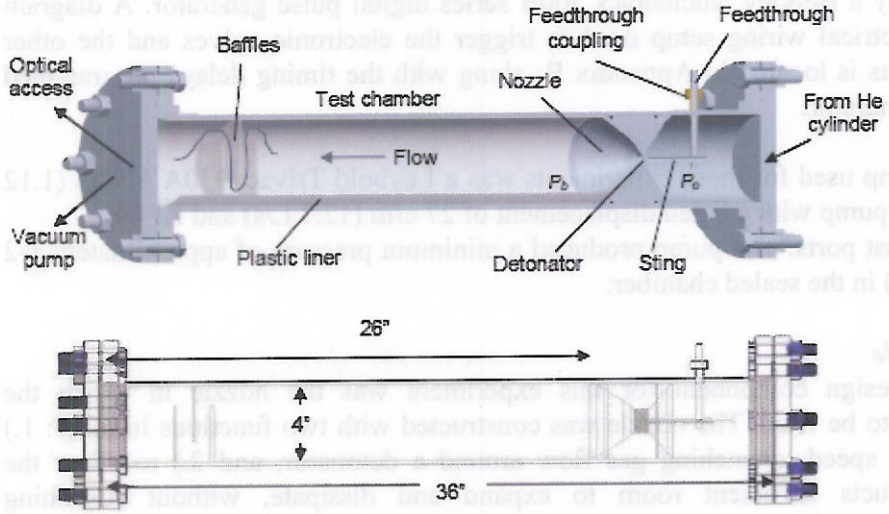

Figure V.1 Flow chamber for detonation quenching.

The test chamber for this investigation consisted of a 4 in (10.16 cm) inner diameter by 36 in (91.44 cm) long stainless steel tube with threaded flanges on both ends. The tube, threaded flanges and end blank flanges, along with many of the other commercially available components, were purchased from McMaster-Carr. A table of the major components and their part numbers is provided in Appendix A. The tube was modified to include two NPT ports for pressure gauges and a hole for a feed-through tube, which holds the detonator. Two tapped holes were also added to the tube for set screws to secure the nozzle in place. End flanges were bolted to the chamber and sealed with O-rings. Flow was created in the chamber by connecting a vacuum pump to the downstream flange and a gas cylinder to the upstream flange, by an NPT port and compression fittings, respectively. A nozzle separated the high and low pressure sides and induced a high speed, expanding flow into which the detonators were fired. By regulating the pressure from the gas cylinder, the conditions in the divergent section of the nozzle could be controlled. On the gas inlet side, a 12 V nominally-open solenoid valve allowed the pressure regulated helium to flow during test setup. This valve was electronically timed to shut off when the detonator fired. The vacuum-side flange had a 1-1/4" NPT port and a 17/32 in unthreaded hole into which a custom fiber optic probe was inserted. A custom 2-3/4 in CF flange to 1-1/4 in NPT adapter connected the threaded port on the end flange to a Varian L8500-304 1.5 in pneumatic gate valve. The vacuum port was made sufficiently large to accommodate the desired flow rates. Compressed air at approximately 110 psi (760 kPa) was connected to a 24 V nominally-closed solenoid valve, which released the air and closed the gate valve when triggered. The gate valve requires approximately 60 ms to close completely and was therefore triggered slightly before the detonator was fired. This delay was determined by focusing light through the valve and recording the change in brightness as it closes with photodiodes and a digital oscilloscope. The combination of the inlet and vacuum valves closing as the detonator fires allows the flow to quench the detonation products but then traps the gases and debris in the chamber before they can be vacuumed away. Timing for detonation triggering and valve closing

was controlled by a Berkley Nucleonics 500B series digital pulse generator. A diagram showing the electrical wiring setup used to trigger the electronic valves and the other timed components is located in Appendix B, along with the timing delays programmed into the pulse generator.

The vacuum pump used for these experiments was a Leybold Trivac D30A 1.5 hp (1.12 kW) rotary vane pump with a listed displacement of 27 cfm (12.7 L/s) and KF40 intake and exhaust ports. The pump produced a minimum pressure of approximately 1-2 torr (133-266 Pa) in the sealed chamber.

Supersonic Nozzle

An important design component for this experiment was the nozzle in which the detonators were to be fired. The nozzle was constructed with two functions in mind: 1.) to create a high speed, quenching gas flow around a detonator, and 2.) to allow the detonation products sufficient room to expand and dissipate, without sustaining significant damage. The nozzle assembly is made of two parts: the nozzle base and a replaceable throat piece, shown in Figure V.2. The base of the nozzle was machined from an aluminum cylinder then anodized for protection from the detonation blast. The throat section was made from a stainless steel UNC 1-1/4 in threaded rod and was geometrically designed to bear the majority of the initial radial blast from the detonator.

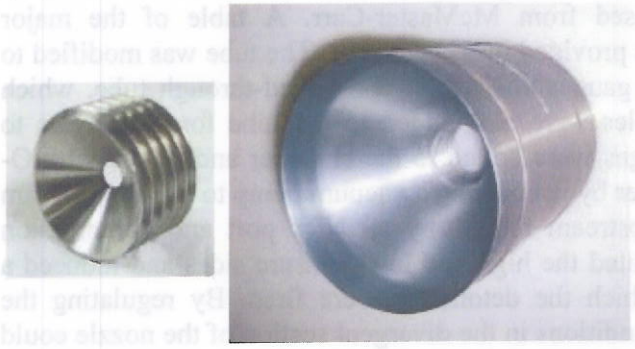

Figure V.2 Stainless steel throat insert and Al nozzle base (not to scale).

The throat of the nozzle, where the minimum flow area occurs, was a critical parameter in the nozzle design. If the throat were too large, the mass flow rate required to achieve supersonic velocities would be too high to maintain. If it were too small, alignment issues and increased blast damage would make achieving consistent results difficult. For each test, a detonator was inserted into the throat of the nozzle such that the explosive portion was exposed to the expanding helium flow on the divergent side. By this setup, the throat area used for calculations was the annular area between the detonator and the throat piece. Practical limitations, including achievable vacuum pressures, led to the final nozzle design. All calculations regarding fluid flow through the nozzle were derived from Oosthuizen and Carscallen Compressible Fluid Flow [26] and from Compressible Fluid Flow coursework at the University of Illinois. Isentropic flow and ideal normal shock equations were programmed into Engineering Equation Solver (EES) for ease in

repeating iterative calculations. As a precise theoretical model was not necessary to determine a nozzle that would perform adequately, and since flow characteristics could be controlled to a certain extent by varying the pressures on either side of the throat after the nozzle had been made, viscous effects were assumed negligible.

The throat piece was designed to expand with a 55° slope which transitions smoothly into the 30° slope of the nozzle base. The throat was designed with a steep slope to allow for rapid expansion of the detonation gasses and minimum containment of the blast. The body had a decreased slope to maintain a high 19 flow velocity for a longer duration. The nozzle base had two O-ring slots machined into the outer diameter to help prevent leakages around the edges along with a slot for set screws (not shown) to lock it in place.

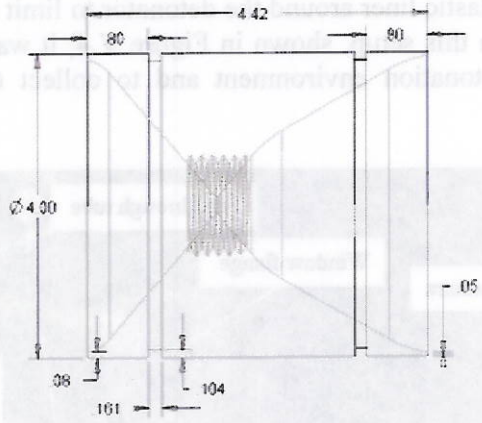

Figure V.3 Exterior dimensions for nozzle base (units in inches).

Early tests were performed on the nozzle using a stand-in detonator model held at the throat to confirm flow characteristics. This stand-in was made from a small stainless steel tube which was filled with epoxy. Because of the tube sized used, the model had a slightly larger diameter (by approximately 0.02 mm) than the actual detonators. Initial pressure ratios across the nozzle indicated leakages. To prevent this, vinyl tape was additionally used to seal the gap around the edge of the nozzle base for each test. These points are similar to the calculations and follow the expected trends. The red diamonds indicate the pressure conditions for the actual detonators fired in the quenching experiments. As expected, the actual test pressures correspond to a slightly larger throat area than the trial pressures with the stand-in. When considering the numerous variables that contribute to the theoretical performance deviating from actual, including machine tolerances, slight variations in detonator diameter, pressure gauge inaccuracies, actual pump performance and neglected viscous considerations, the nozzle performs reasonably as predicted. Further calculations were performed to determine the theoretical pressure and temperature conditions downstream of the detonator, denoted „quenching" conditions, and also to determine the location of a normal shock in the nozzle. For the test conditions, a normal shock is predicted to have occurred early in the divergent section at around 6 mm before the tip of the detonator. Immediately after the tip of the detonator, quenching pressure, temperature and velocity were approximately 7 – 9 kPa (1 – 1.3

psia), 280 K and 430 m/s respectively. It is important to note, however, that determining the precise quenching conditions would require a more sophisticated model which considers the unsteady nature of the turbulent flow around the detonator and also includes the detonation event.

Slight modifications were made to the original design of the flow chamber to facilitate an additional series of tests on the detonators. The vacuum pump and detonator support system remained the same, though a gas inlet port was added to the vacuum-side flange. The end flange which previously acted as the helium inlet was replaced with a window flange and was attached to the downstream side of the chamber. The nozzles and baffles were not used for these experiments and the plastic liner was extended to cover the entire 3 ft (91.44 cm) length of the chamber. A steel ring approximately 4 in (10.16 cm) wide was inserted inside the plastic liner around the detonator to limit damage to the liner from the explosive blast. With this setup, shown in Figure V.4, it was possible to control the gases present in the detonation environment and to collect the detonator debris for analysis.

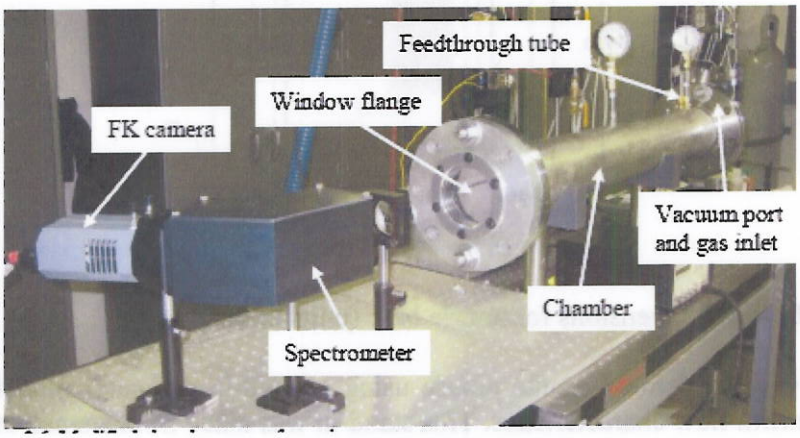

Figure V.4 Modified chamber setup for quiescent tests.

Detonator and Firing System

The exploding bridgewire (EBW) detonators used in these experiments were produced by RISI, a subsidiary of Teledyne Reynolds Company. The standard RP-2 EBW detonator (P/N 167-4379) was chosen for its precise timing and has the dimensions and composition shown in Figure V.5 [28].

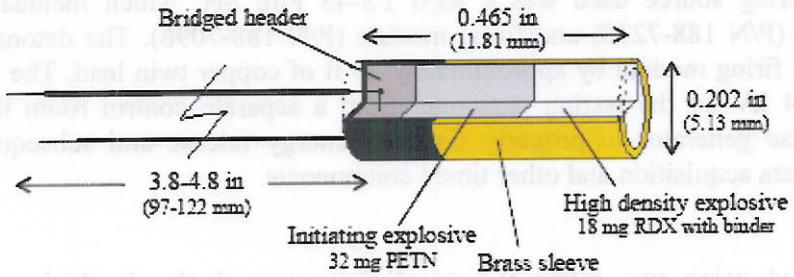

Figure V.5 Schematic of RISI RP-2 EBW detonator.

In the RP-2, 32 mg of the secondary explosive PETN is used for the low density section of the detonator while 18 mg of RDX combined with a binder is used for the high density section. The explosive charge is cased in brass while the bridged header is covered by plastic. The tip of the detonator is uncovered, but ships with a plastic cap. The RP-2 has a function time of 1.65 μs [28]. The apparatus used to secure the detonator during experiments is shown in Figure V.6. The feedthrough tube, which contains connecting wires sealed with epoxy to connect the triggering current source to the detonator, is inserted through the chamber wall and the vertical feedthrough coupling is temporarily tightened. The position of the feedthrough tube needs to be adjusted after the detonator is loaded. The detonator is inserted into a separate stainless steel tube, wires first. The detonator tube, dubbed the "sting" for differentiation, is sized such that the detonator can be inserted with little force but is held securely. The loaded sting is then inserted perpendicular to the feedthrough tube. Both tubes are adjusted to align the detonator with the throat of the nozzle, or with the center of the test chamber as applicable, then a set screw is used to secure the sting to the feedthrough tube and the coupling is fully tightened. The alligator clips on the ends of the feedthrough wires are then attached to the detonator leads.

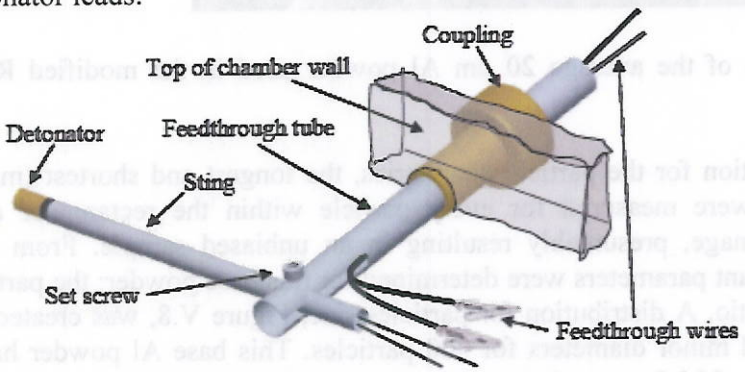

Figure V.6 Detonator holder assembly.

A brass feedthrough coupling, similar to the stainless steel coupling was purchased from the Kurt J. Lesker Company. The coupling base was silver soldered to the top of the test chamber. The threaded top could be loosened to allow for the feedthrough tube to be inserted and adjusted, then tightened to form a vacuum quality seal.

The detonator triggering source used was a RISI FS-43 Fire Set, which includes a separate control unit (P/N 188-7238) and firing module (P/N 188-7096). The detonator was connected to the firing module by approximately 50 ft of copper twin lead. The fire set was charged to 4 kV by the testing personnel from a separate control room then triggered by the pulse generator to properly time the energy release and subsequent detonation with the data acquisition and other timed components.

Aluminum Powder

Tests were performed using two different sets of detonators, both of which were manufactured on custom order by RISI. The first set of RP-2 detonators was modified to include approximately 20% by mass 20 μm average diameter aluminum powder mixed with the high density RDX explosive section. The second set contained approximately 20% of 15-20 μm aluminum powder. The base aluminum powder used for these experiments was nominally 20 μm Al (by mass average) of 99.9% purity from Sigma-Aldrich. An SEM image of a sample of this powder is shown in Figure V.7, along with a detailed close up of a particle to show surface characteristics.

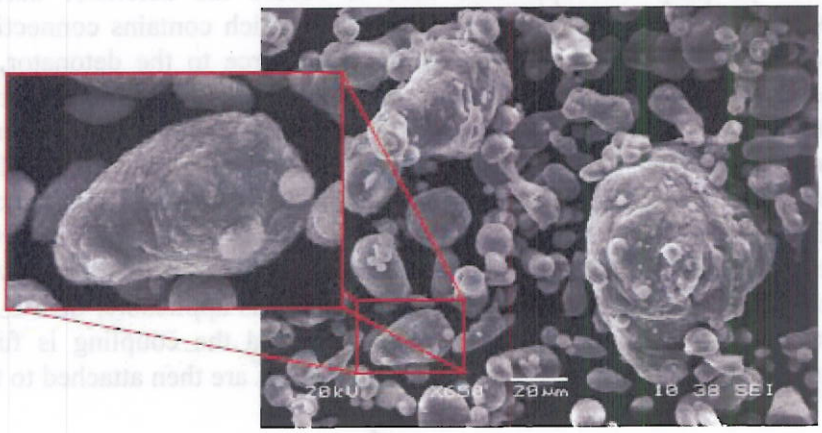

Figure V.7 SEM image of the average 20 μm Al powder used in the modified RP-2 detonators.

To determine a distribution for the particle geometries, the longest and shortest (major and minor) diameters were measured for every particle within the rectangular area recorded in an SEM image, presumably resulting in an unbiased sample. From this information, two important parameters were determined for this base powder: the particle size and the diameter ratio. A distribution for particles size, Figure V.8, was created by averaging the major and minor diameters for 400 particles. This base Al powder has a mass averaged diameter of 25.0 μm and a number averaged diameter of 10.0 μm. Figure V.9 is a distribution for the ratio of minor diameter to major diameter. For this base powder, the mean diameter ratio is approximately 0.77.

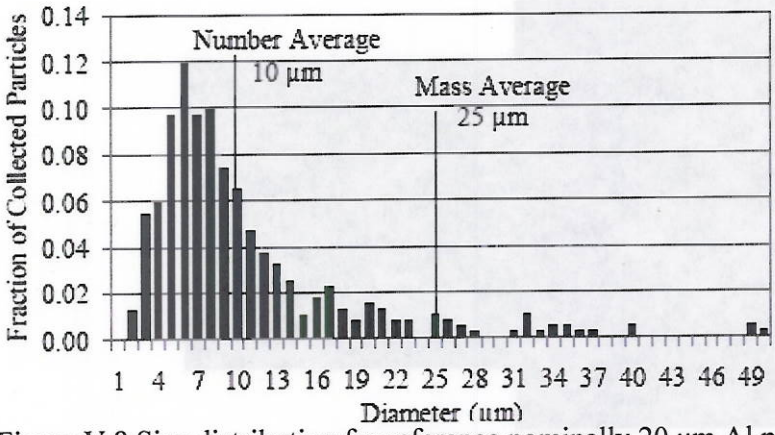

Figure V.8 Size distribution for reference nominally 20 µm Al powder.

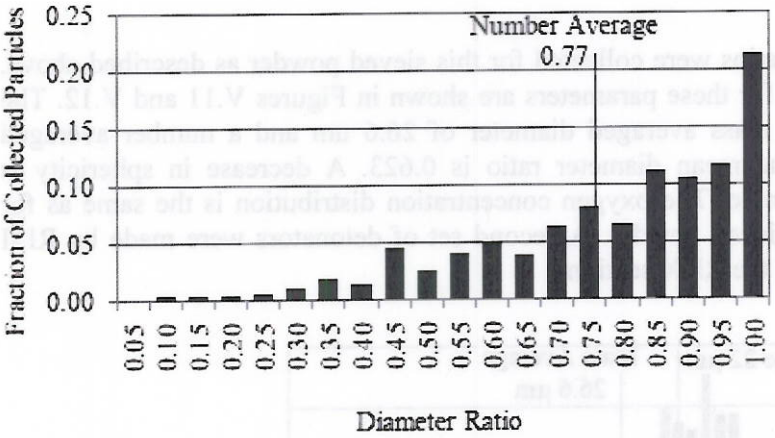

Figure V.9 Diameter ratio distribution for reference nominally 20 µm Al powder.

In addition to the geometry of the powder, a 50 sample distribution was created for the amount of oxygen present in each aluminum particle, indicating the amount of oxide coating. These data will be presented in Section 2.7.

To achieve a tighter size distribution, the base aluminum powder was sieved using a Gilson Gilsonic Automatic Sieving Machine, to produce a sample with powder in the 15 to 20 um range. The sample passed through a mesh with 20 um openings and was collected above a mesh with 15 um openings. The increased uniformity in particle size is apparent in Figure V.10.

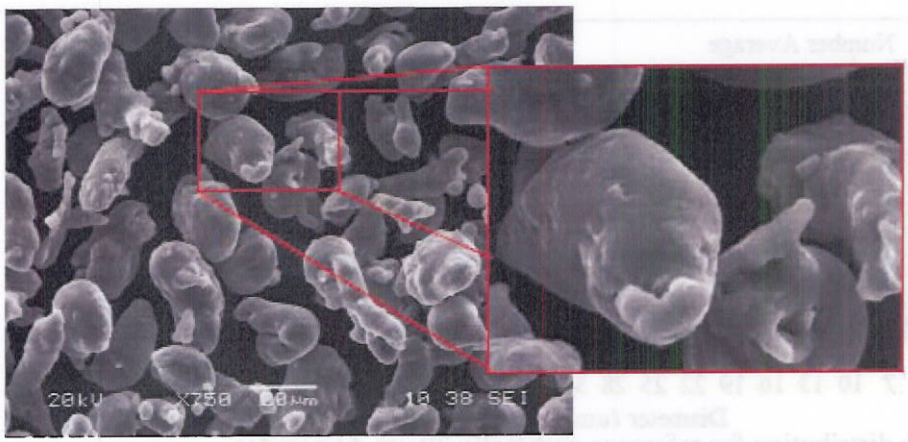

Figure V.10 SEM image of the 15-20 μm Al powder used in the modified RP-2 detonators.

Diameters and diameter ratios were collected for this sieved powder as described above. 400 particle distributions for these parameters are shown in Figures V.11 and V.12. The 15-20 um powder has a mass averaged diameter of 26.6 um and a number averaged diameter of 22.0 um. The mean diameter ratio is 0.623. A decrease in sphericity is noticed in this sieved sample. The oxygen concentration distribution is the same as for the nominally 20 um unsieved powder. A second set of detonators were made by RISI with this powder added to the RDX section.

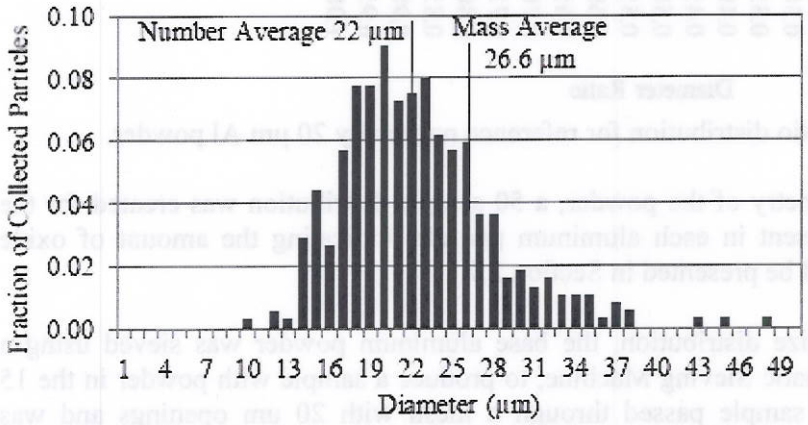

Figure V.11 Size distribution for reference 15-20 μm Al powder.

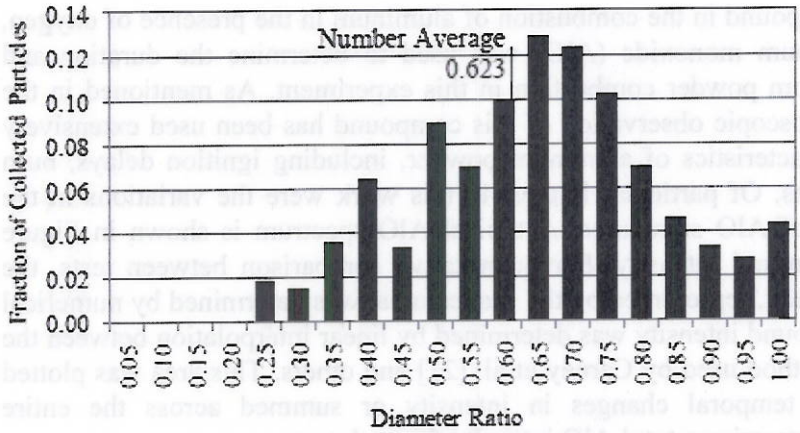

Figure V.12 Diameter ratio distribution for reference 15-20 μm Al powder.

Optics

Emissions from the detonation events were transmitted through a spectrometer to a Fast Kinetics (FK) CCD detector to produce time-resolved spectra. The CCD detector used was an Andor model DV420-FK, shown in Figure V.13, and the events were recorded in Fast Kinetics mode with 4 μs resolution. The custom spectrometer was a 50 millimeter focal length f/1.4 spectrometer with an 1800 gr/mm equivalent volume phase holographic (VPH) grating with peak efficiency greater than 50% and a 2:1 inlet to exit focal length ratio.


Figure V.13 Andor FK CCD detector mounted to custom spectrometer.

For the quenching tests, the flange area downstream of the detonator was limited by the vacuum port. For this setup, a lens was mounted to the vacuum flange to focus the light emission into a fiber optic cable, then to the spectrometer and FK camera. This lens was a 25 mm diameter achromat and was positioned to focus collimated light onto the fiber tip. In this configuration, the collection efficiency for light emanating from anywhere inside the cylinder of diameter of 25 mm was approximately equal. For the quiescent tests, the spectrometer was aligned along the axis of the chamber viewing the detonation head on through the window flange.

As an intermediate compound in the combustion of aluminum in the presence of oxygen, the presence of aluminum monoxide (AlO) was used to determine the duration and intensity of the aluminum powder combustion in this experiment. As mentioned in the introduction, the spectroscopic observation of this compound has been used extensively to determine burn characteristics of aluminum powder, including ignition delays, burn time and burn intensities. Of particular interest in this work were the variations in the duration and intensity of AlO signatures. A typical AlO spectrum is shown in Figure V.14, above the background intensity. For quantitative comparison between tests, the area under the $\Delta v = 0$ peak, represented by the shaded area, was determined by numerical integration. The background intensity was determined by linear interpolation between the valleys, as shown, a method used by Carney et al. [21] and others. This area was plotted against time to view temporal changes in intensity or summed across the entire observance of AlO to determine a total AlO intensity for each test.

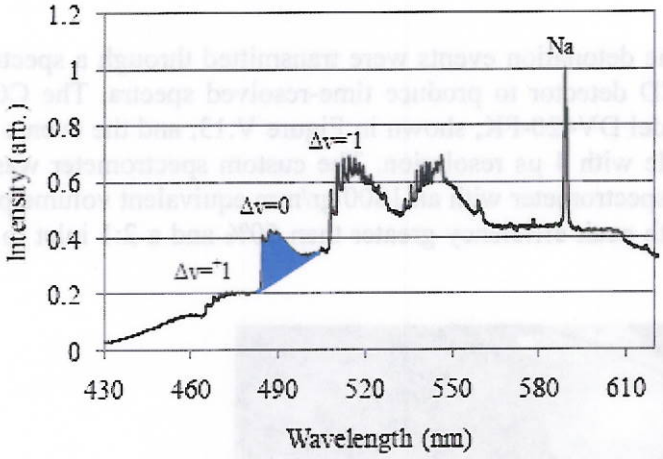

Figure V.14 Characteristic AlO signal.

A new facility at the University of Illinois is the pair of Cooke Corporation High Speed Framing Cameras (HSFC) which are capable of recording up to 8 frames each at 1280x1024 pixel resolution. Each HSFC has four intensified CCDs which can record up to 500 mega frames per second in single frame mode or 2 mega frames per second in double frame mode [29]. Each of the CCD cameras can be set to an independent delay and exposure time. The two HSFCs are arranged as shown in Figure V.15.

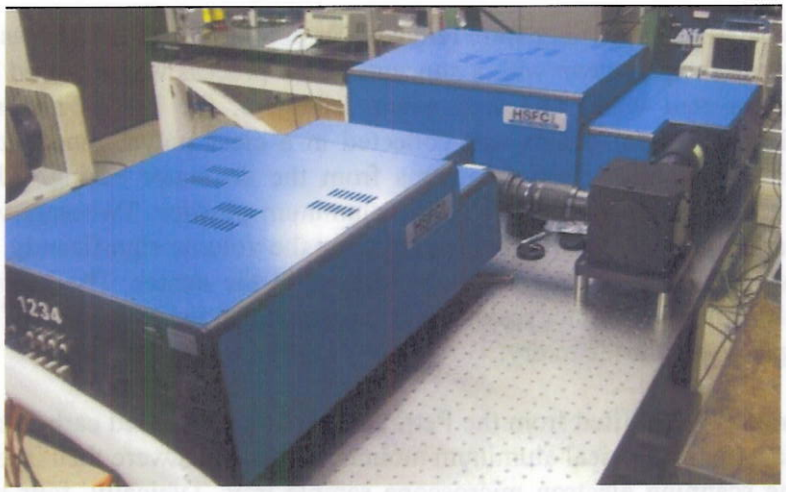

Figure V.15 Cooke Corp. high speed framing cameras.

This setup will be used to image the detonation of an aluminized detonator. One HSFC will be filtered to observe AlO emissions around 488 nm and the other will be filtered to observe the background only. Images will be recorded of the early time detonation characteristics with a pair of images taken at each of 8 selected time delays following detonation. These images will then be overlayed to highlight regions of increased intensity in the 488 nm band, indicating the location of AlO emissions.

Particle Collection and Analysis

To facilitate collection and removal of the detonation debris from the flow chamber, a 1/32 in (0.8 mm) thick polypropylene sheet from U.S. Plastic Corp. was used to line the tube wall downstream of the nozzle. Polypropylene was determined to outperform both LDPE and HDPE in these conditions due to its superior scratch and chip resistance, allowing for the same liner to be used for multiple tests before surface damage began to hinder particle removal. The sheet was cut to the appropriate dimensions, leaving a notch for the downstream pressure gauge, then rolled into a tube and slid into place for each test.

For the quenching experiments, baffles for the low pressure section of the tube were made from 4 in (10.16 cm) diameter by 1/8 in (3.18 mm) thick clear acrylic discs, also from U.S. Plastic. The hand-made baffles dislodge particles from the flow and also protect the optics and the vacuum system downstream of the detonator. Particle impacts from the detonation caused chipping on the exposed surfaces, though the acrylic contaminants were easily separated from the debris sample after the test. The damaged baffles were replaced as necessary, typically for every other test. Collection efficiencies for this type of baffled momentum separator are examined in [30], which was referenced in the design of these baffles. The collection efficiencies were not investigated in this experiment, however, and need not have been high, so long as the collection system as a whole captured the majority of the detonation debris. The baffle assembly was slid into the vacuum side of the flow chamber following the liner. The grey ABS legs held the baffles in place and prevented them from sliding toward the vacuum port. Following

each test, the baffles and the liner were removed, as applicable. The liner was misted with distilled water and wiped clean with a squeegee. This process was repeated 2 or 3 times until the accumulated water appeared clean. Likewise, the baffles and nozzle were squeegeed clean. The wet debris was collected in a clear polystyrene Petri dish. The debris contained primarily brass fragments from the detonator casing. Also typically present was a lighter ash in addition to the aluminum powder. Tweezers were used to remove the larger particles from the dish, reducing the volume significantly. By swirling the remaining sample, the material was coalesced in the center. The heavier particles settled quickly, while the lighter residue, primarily ash, tended to drifted off center. This reduced sample was set aside to dry.

The dried samples were lifted from the Petri dish with double-sided carbon tape attached to 9.5 mm diameter cylindrical aluminum mounts. The mounts were then inserted into the holder for the scanning electron microscope sample tray. Typically, four mounts were used to view the residue from each detonator, allowing the entire sample to be viewed in the scanning electron microscope in one sitting. The mounted samples were saved for reviewing as necessary. The debris samples were viewed using the JEOL 6060LV scanning electron microscope at the Center for Microanalysis of Materials at the University of Illinois. The 6060LV is a high performance, general purpose SEM with resolution of up to 4 nm and magnification of up to 300,000x. SEM images were primarily viewed with an accelerating voltage of 20-28 kV and a spot size of 40-50. The JEOL 6060LV is equipped with backscattered and secondary electron detectors as well as an Oxford Instruments Energy Dispersive X-ray Spectrometry (EDS) system. The EDS system included Oxford"s Link ISIS analytical software [31] which was very useful in isolating aluminum particles within the debris samples. The EDS spectrum in Figure V.16 shows the primary constituents of the detonator debris.

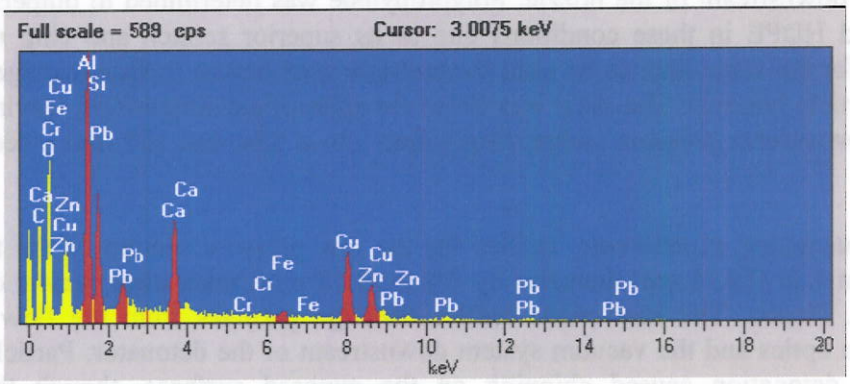

Figure V.16 EDS spectrum of detonator debris.

Peaks from aluminum, copper and zinc are prominent, as expected from the aluminum powder and the brass detonator casing. The carbon is picked up from the carbon mounting tape, in addition to post-combustion residues. The oxygen (O) signal will be used to quantify the amount of oxide present on specific aluminum particles. Peaks for chromium and iron are also present, likely from the stainless steel sting that held the detonator. Calcium and silicon impurities are also evident in addition to other elements in smaller amounts. Aluminum particles were found in the debris by using the SpeedMap

EDS analysis program. The SpeedMap produced an elemental map for the viewed area, as shown in Figure V.17, highlighting specified elements. In this way, aluminum particles were found in the debris. To ensure that the same area was not viewed twice, a weaving pattern was used to view one small section of the sample at a time. The sample was typically viewed at a magnification of 500x to locate aluminum particles then the located particles were magnified further for a clear view. By this method one distinct 200 μm rectangle was viewed at a time. The aluminum particles were imaged and dimensions were recorded to determine size distributions.

Figure V.17. SpeedMap EDS program used to locate Al.

It is important to note that this method of particle location may lead to samples that are biased toward larger particles or particles that are less oxidized and therefore stand out more clearly as aluminum. By zooming in on an aluminum particle so that only the particle surface was visible in the viewing area of the SEM and EDS detectors, the relative concentrations of aluminum and oxygen could be determined by the LINK ISIS SEMQUANT EDS program [31]. The SEMQUANT software allows for quantification of the relative percentages of elements present. Once a particle was located, a spectrum was recorded to determine if there were significant contaminants present in the view. Contaminants blocking the surface of the particle would result in inaccurate readings for the aluminum particle analysis, especially if the contaminants contained oxygen. If significant peaks were apparent for elements other than Al and O in the spectra, either a different area of the particle was viewed or, if a clear view was not available, the particle composition was not included in statistics. Very few particles were neglected for this reason. Figures V.18 and V.19 show the EDS spectra and SEMQUANT results for reference samples of aluminum oxide (Al_2O_3) and Al, respectively. The element percentages have been normalized to include only Al and O in the readings. The peak centered at 0 keV is the "noise peak" from the noise produced by the detector electronics. It is always present in EDS systems, though vendors typically suppress it.

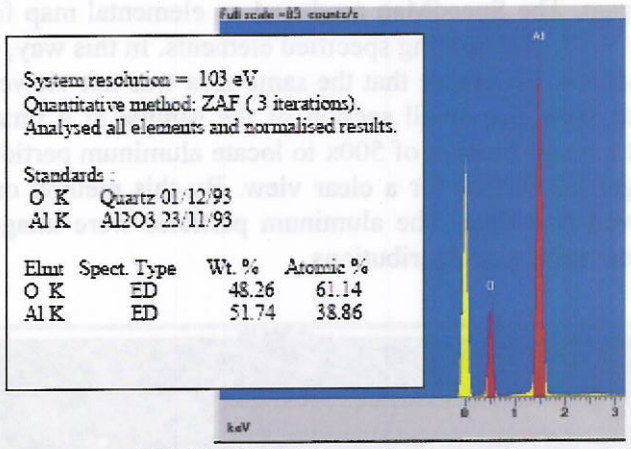

Figure V.18 EDS spectrum and SEMQUANT results for a reference Al2O3 sample.

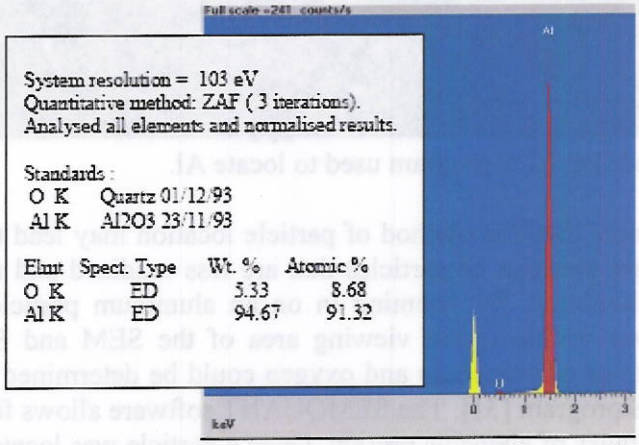

Figure V.19 EDS spectrum and SEMQUANT results for a reference Al sample.

Immediately apparent is the contrast between the relative intensities of the Al and O peaks. In the oxide sample, the O peak is significantly higher, indicating a larger percentage of oxygen. It was assumed that the percent of oxygen was approximately uniform across the surface of the particle during analyses. For pure Al_2O_3, the mass fraction of oxygen is 47.1% stoichiometrically. The EDS software determined that the sample was 48.26% oxygen. Comparatively, O only represented 5% by mass in the aluminum sample. Because the EDS system does not penetrate completely through the sample, it is expected for the oxide layer to be weighted more heavily when calculating the mass fraction of oxygen on the surface of aluminum particles. For this reason, the reported oxygen percentages are higher than actually present in the particle, although there remains a distinct contrast between oxide and un-oxidized aluminum. Tested particles will be collected and compared to reference particles to determine the amount of oxidation. The SEMQUANT software was used to determine 50 sample distributions for the amount of oxygen present in the reference aluminum powder and in the reference Al_2O_3, shown in Figure V.20.

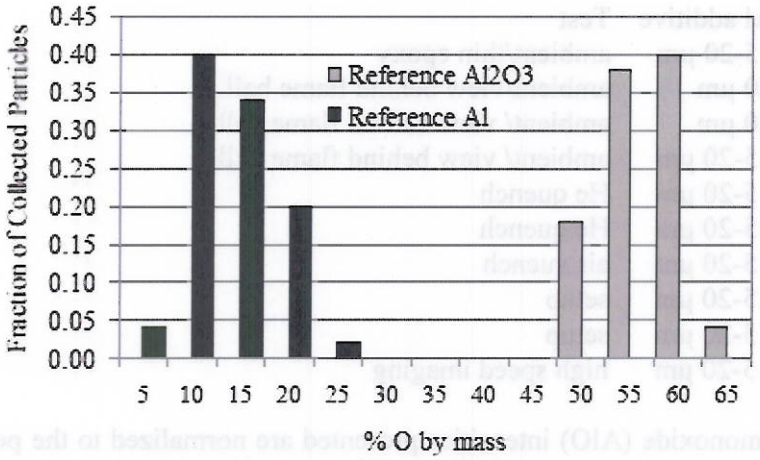

Figure V.20 Oxygen concentration for reference Al and Al_2O_3.

The reference aluminum powder contained less than 25% oxygen while the alumina reference had between 45% and 65% oxygen. Particles collected from the detonator debris which were determined to have 25% oxygen or less were deemed unreacted while particles with more than 25% oxygen were assumed to be at least partially combusted. The percent oxygen determined by SEMQUANT varied up to 10% across the particle surface and up to 15% if viewing near the particle edge. Typical variances, however, were around 3% across the surface. Changing the magnification or focus did not significantly change the quantified mass percentages.

Results and Discussion

In total, twenty-one detonators were fired during the quiescent, quenching and imaging tests. Five detonators were quenched, eight were examined in a variety of stationary environments, four were imaged specially and the remainders were used during calibration and setup. A list of these detonators is presented in Table V.1 in chronological order. In the presentation of data in this section, detonators will be described by number and environmental conditions.

Table V.1 List of detonators fired.

Detonator #	Al additive	Test
1	none	setup
2	20 μm	setup
3	20 μm	He quench
4	20 μm	ambient
5	20 μm	He quench
6	15-20 μm	N_2
7	15-20 μm	ambient
8	15-20 μm	ambient/thick epoxy
9	15-20 μm	CO_2
10	15-20 μm	ambient/thin epoxy
11	15-20 μm	N_2

Detonator #	Al additive	Test
12	15-20 μm	ambient/thin epoxy
13	20 μm	ambient/view behind flame ball
14	20 μm	ambient/ view behind flame ball
15	15-20 μm	ambient/ view behind flame ball
16	15-20 μm	He quench
17	15-20 μm	He quench
18	15-20 μm	air quench
19	15-20 μm	setup
20	15-20 μm	setup
21	15-20 μm	high speed imaging

All aluminum monoxide (AlO) intensities presented are normalized to the peak intensity from an aluminized detonator fired in air (Detonator 7). AlO intensities recorded for different optical configurations were scaled based on the relative brightness of exploding aluminum wires, which were imaged before each set of tests and provided a fairly constant intensity reference. For example, a comparison of the AlO intensities for aluminum wires fired in air showed that the signals were 1.26 times brighter through the direct view (described above for the quiescent tests) than through the optical fiber used in the quenching tests. The spectra from the quenching tests were scaled by this factor, then normalized to the reference AlO signal from an ambient detonator.

Four aluminized detonators were fired in the flow chamber with helium as the quenching fluid. An additional test was performed with air as the quenching fluid to observe the effects of the expanding high speed flow alone. Time-resolved spectra were recorded for the latest of these tests and AlO intensities plotted with respect to time in Figure V.21. AlO intensity from the detonator fired in air is also plotted for reference. Because the spectra were so low during the helium quenched tests, these time-resolved AlO intensities are shown additionally in Figure V.22, on magnified scales. For these plots, time zero indicates the first appearance of spectral emissions from the detonation.

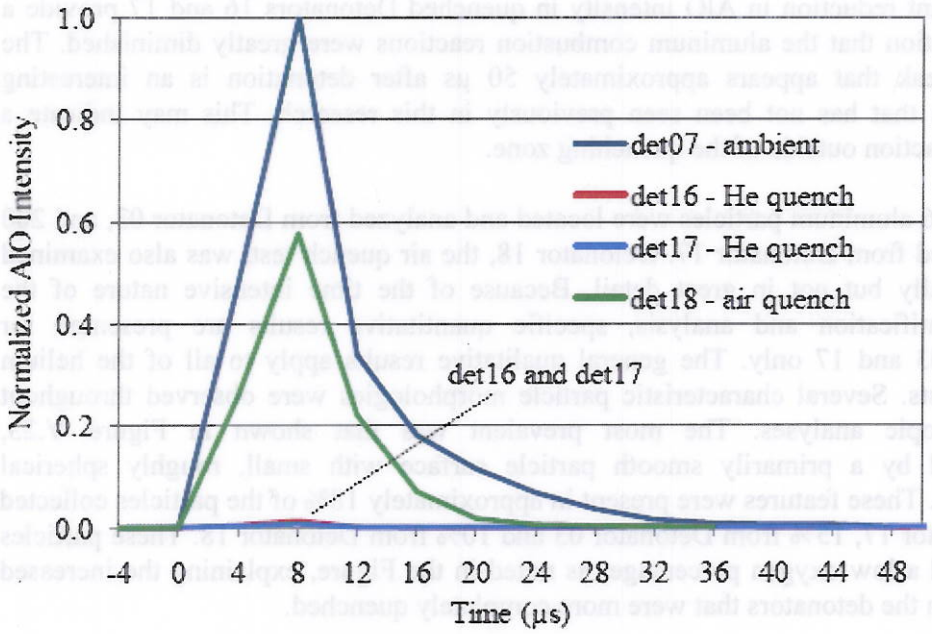

Figure V.21 AlO intensities for quenching tests.

In ambient conditions AlO appears rapidly following detonation and peaks after approximately 8 μs. The signal decreases rapidly but lingers as it fades, vanishing completely within approximately 45 μs. The same trends are observed from the air quenched detonation, though peak intensity and total signal duration are nearly halved, compared to the quiescent air test. The helium quenched AlO signals are around one percent of the peak intensity from the ambient detonator and are therefore plotted on a magnified scale, shown below.

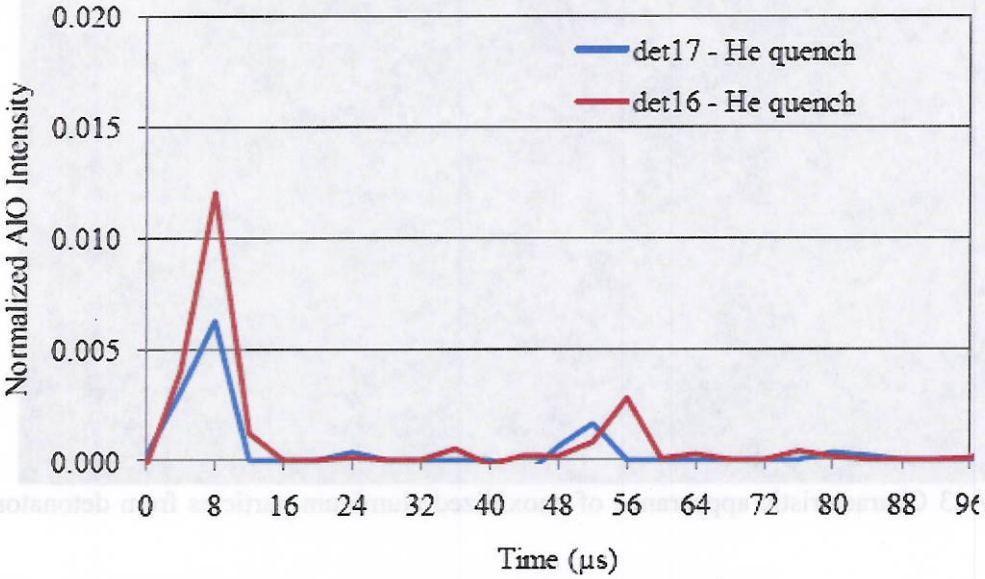

Figure V.22 Magnified AlO intensities for helium quenched tests.

The significant reduction in AlO intensity in quenched Detonators 16 and 17 provide a strong indication that the aluminum combustion reactions were greatly diminished. The secondary peak that appears approximately 50 μs after detonation is an interesting characteristic that has not been seen previously in this research. This may indicate a secondary reaction outside of the quenching zone.

A total of 116 aluminum particles were located and analyzed from Detonator 03, and 200 were analyzed from Detonator 17. Detonator 18, the air quench test, was also examined microscopically but not in great detail. Because of the time intensive nature of the particle identification and analysis, specific quantitative results are presented for Detonators 03 and 17 only. The general qualitative results apply to all of the helium quenched tests. Several characteristic particle morphologies were observed throughout the microscopic analyses. The most prevalent was that shown in Figure V.23, characterized by a primarily smooth particle surface with small, roughly spherical irregularities. These features were present in approximately 18% of the particles collected from Detonator 17, 15% from Detonator 03 and 10% from Detonator 18. These particles typically had a low oxygen percentage, as noted in the Figure, explaining the increased occurrence in the detonators that were more completely quenched.

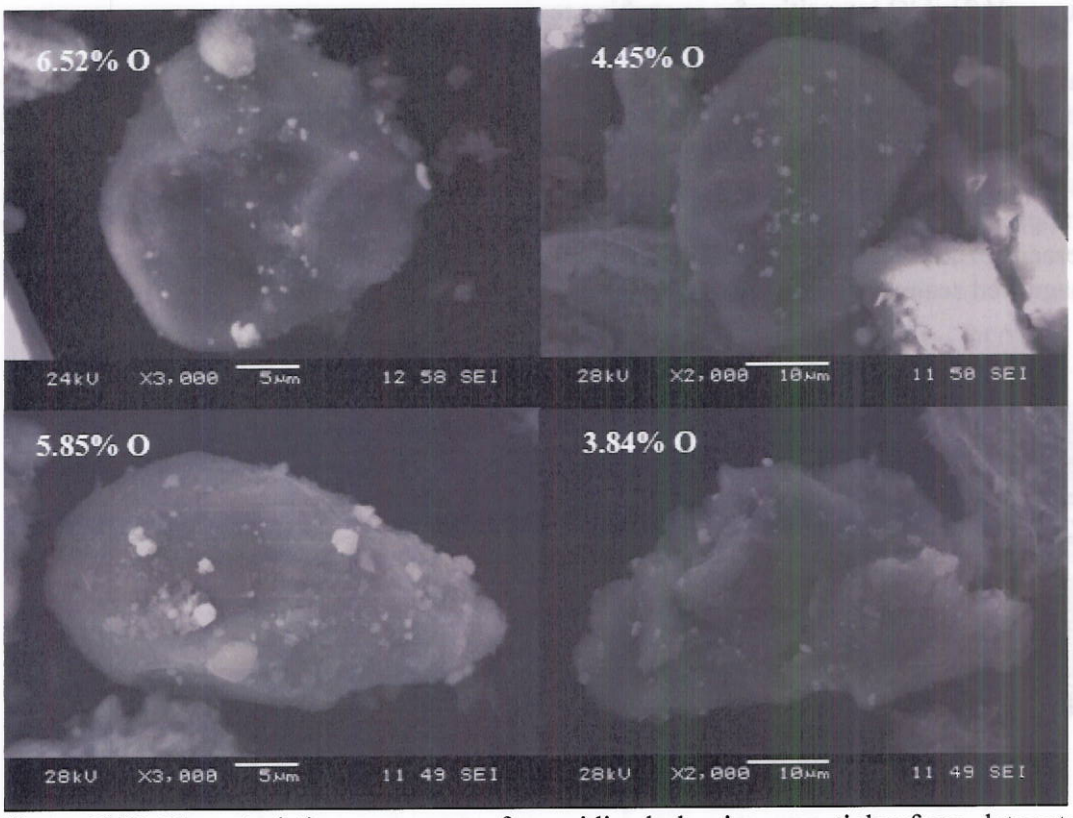

Figure V.23 Characteristic appearance of unoxidized aluminum particles from detonator debris.

Another common morphology corresponded to particles that were partially oxidized. These particles had a rougher surface with many more irregularities including jagged edges and a variety of distinct surface formations. Examples of these particles are displayed in Figure V.24 with oxygen percentages labeled.

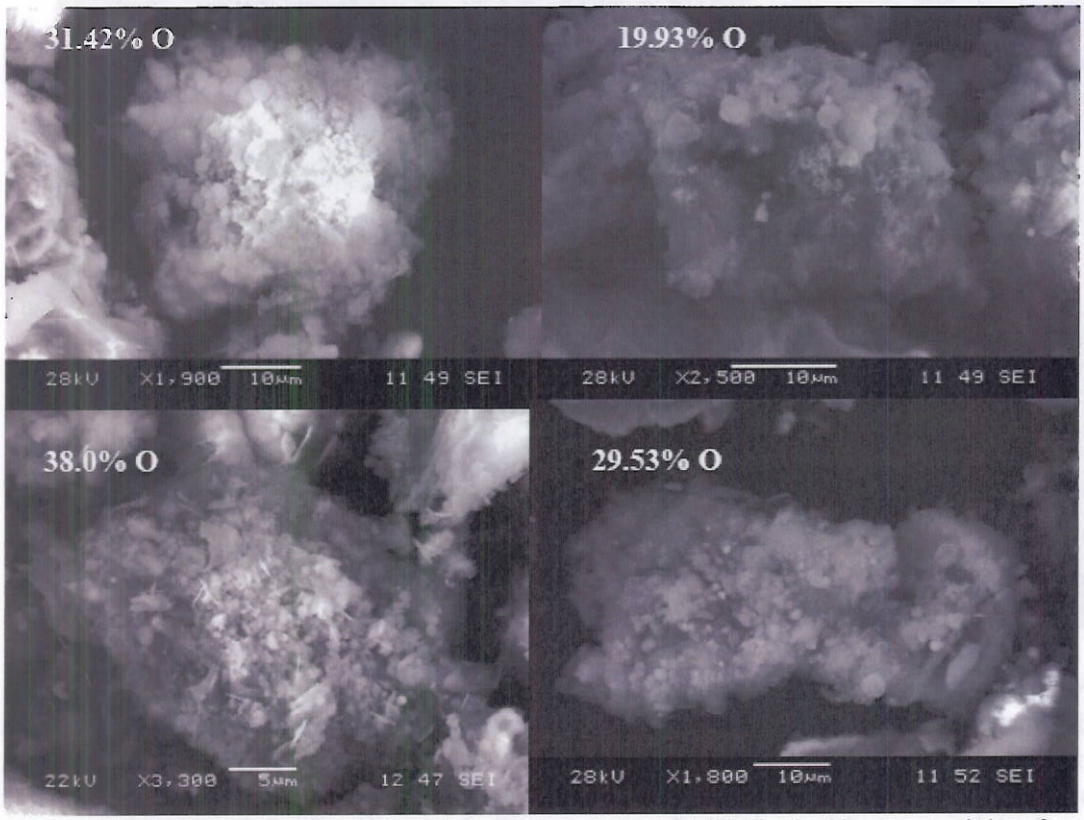

Figure V.24 Characteristic appearance of partially oxidized aluminum particles from detonator debris.

Fully oxidized particles had other distinct features. The surface irregularities present in the partially oxidized particles were also observed, but to an advanced degree. The oxidized particles shown in Figure V.25 were collected from Detonator 04 which was fired in air. Few particles with this degree of oxidation were observed in any of the quenched detonator debris.

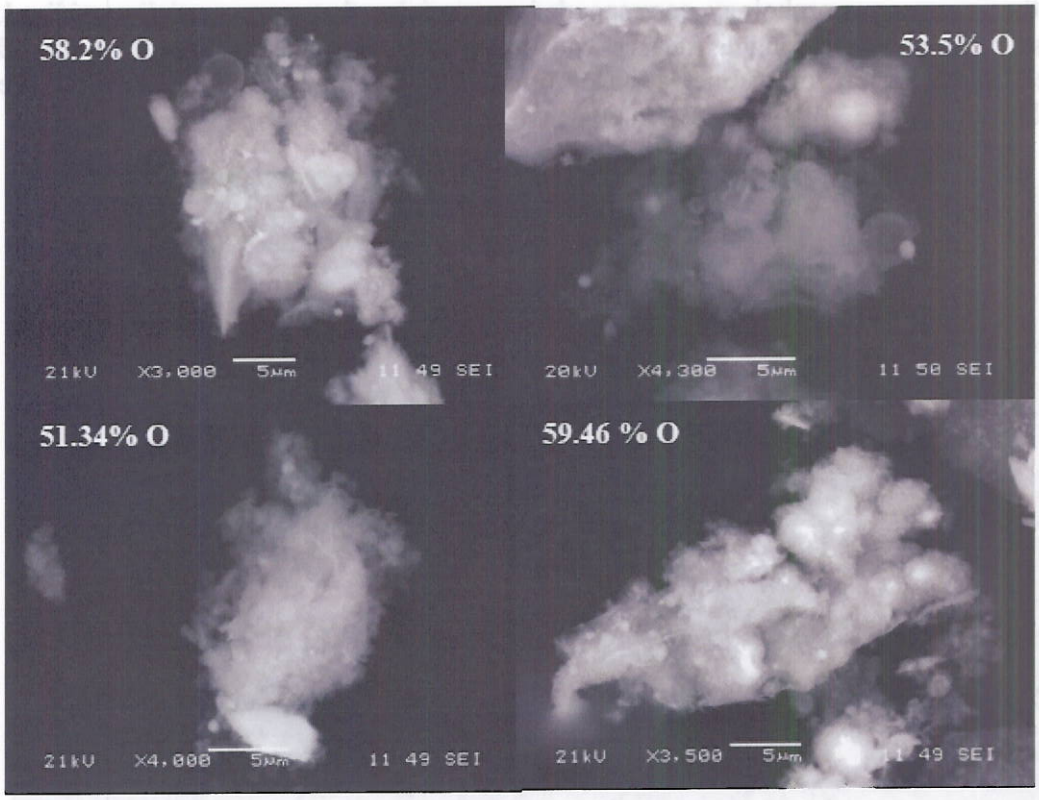

Figure V.25 Characteristic appearance of fully oxidized aluminum particles from detonator debris. Other repeated features were noticed in the quenched aluminum particles. In approximately 3-4% of the particles collected from Detonators 03 and 17, surface features that appeared to be cracks or fractures were present. An example of these cracks is shown in Figure V.26. Because it is likely that the aluminum particles were at least partially melted in the detonation, it is difficult to determine if these features are a direct result of the detonation blast or of other stresses within the particles.

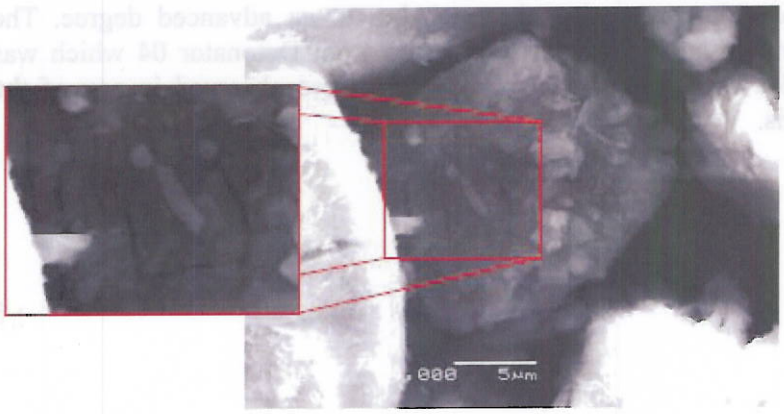

Figure V.26 Cracks apparent on 3-4% of quenched aluminum particles.

An array of particle features fell between these characteristic appearances. Not all particles with these morphologies corresponded to the expected amount of oxidation, but it was apparent that greater surface roughness typically corresponded to increased oxidation. Dimensions and oxygen content were recorded for the aluminum particles collected from the helium quenched Detonator 03 and Detonator 17. Histograms for the percentage of oxygen present in these particles are shown in Figure V.27. In addition to the low AlO intensities observed spectroscopically from the detonations, this plot provides strong evidence that the quenching was effective and that the majority of the aluminum particles did not significantly react. For Detonator 03, 24% of the particles contained more than 25% oxygen and were considered reacted. Only 18% of the particles recovered from Detonator 17 were significantly reacted.

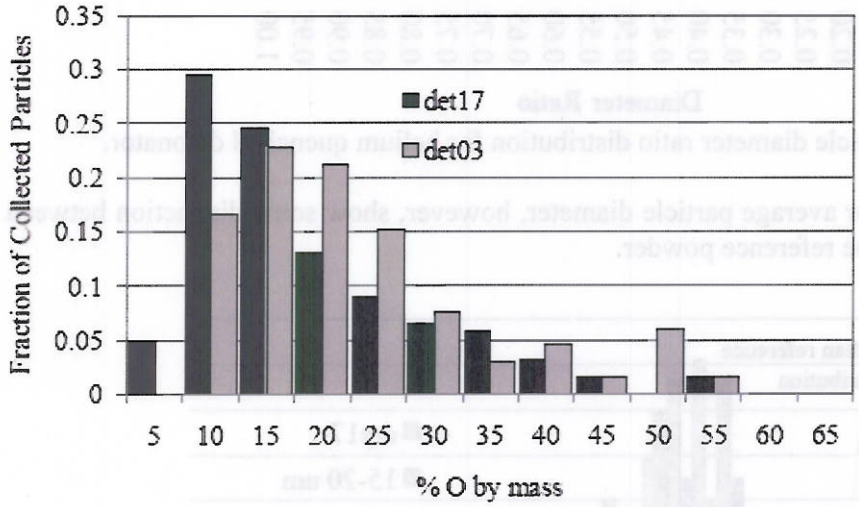

Figure V.27 Oxygen concentration in Al particles collected from quenched detonations.

Detonator 17 appears to have been quenched more thoroughly than Detonators 03. It is important to note that these two tests correspond to the highest and lowest quenching mass flow rates (respectively) of the tested detonators, plotted in Figure V.24. The larger flow rate appears to provide a more effective quenching environment, which indicates a direction to proceed in for future flow chamber optimization. The 200 particles analyzed from the helium quenched Detonator 17 had the diameter ratio distribution presented in Figure V.28, along with the distribution for the reference 15-20 μm powder. Detonator 17 had an average diameter ratio of 0.654 while the reference powder had an average ratio of 0.623. These are very similar and the plot does not indicate a significant difference between the two.

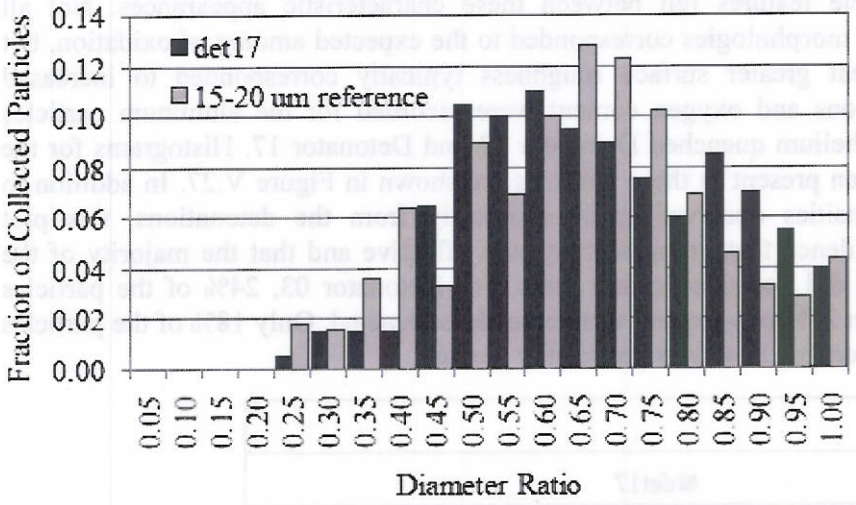

Figure V.28 Al particle diameter ratio distribution for helium quenched detonator.

The distributions for average particle diameter, however, show some distinction between Detonator 17 and the reference powder.

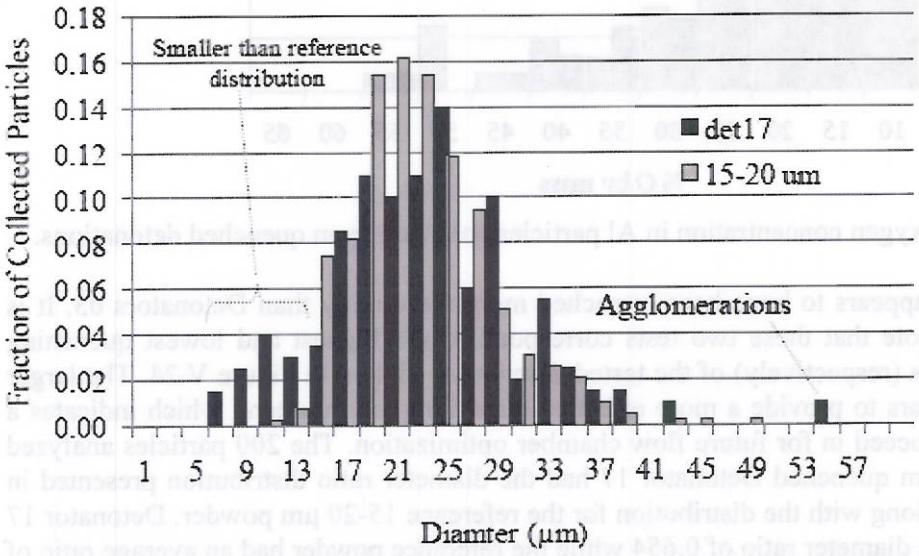

Figure V.29 Aluminum particle diameter distribution for helium quenched detonator.

Of the 200 particles recovered from Detonator 17, 11% (22 particles) had an average diameter less than 13 μm, compared to 1% in the reference powder. These particles had a low percentage of oxidation indicating that they were not significantly reacted. A histogram for the percent of oxygen in these small particles from Detonator 17 is presented in Figure V.30.

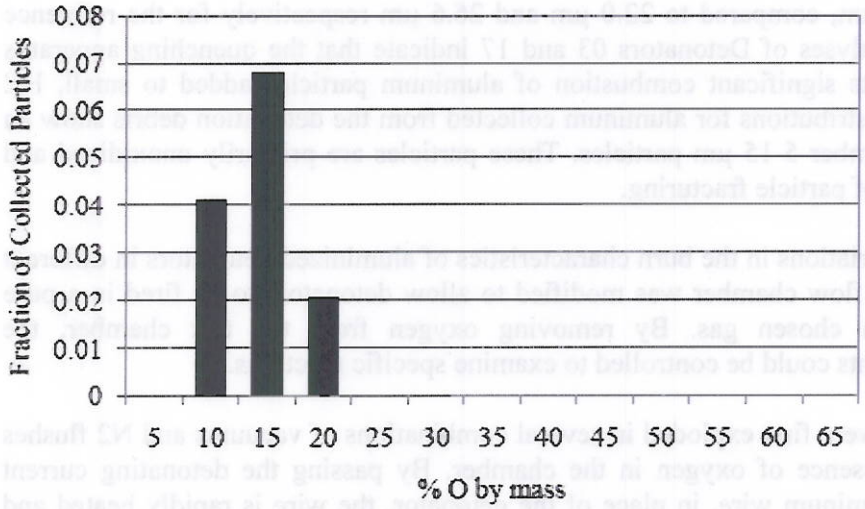

Figure V.30 Oxygen concentration in small Al particles collected from quenched detonator.

The diameter ratios for the small particles have a somewhat different distribution than the reference powder, as shown in Figure V.11. However, the average ratio of 0.67 is very near to the overall average of 0.654 for Detonator 17.

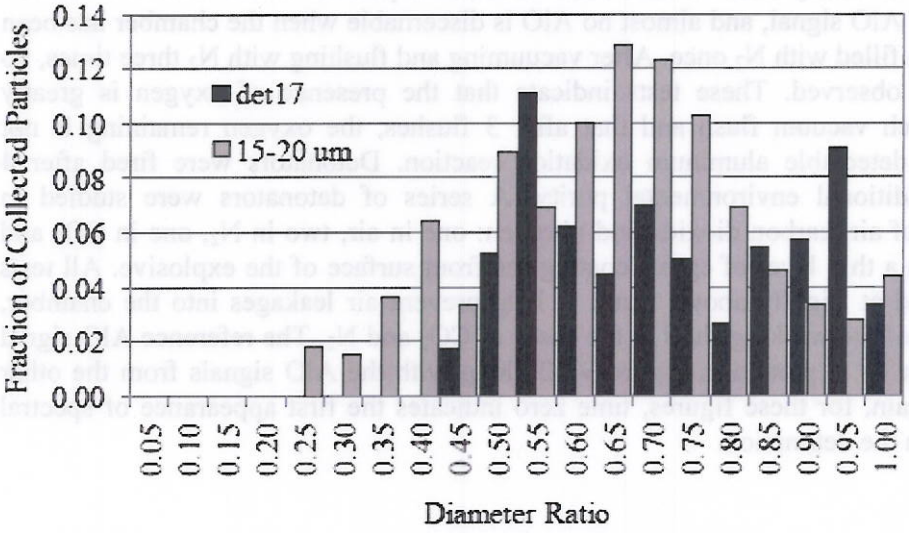

Figure V.31 Diameter ratio distribution for small Al particles recovered from quenched detonator.

Additionally, two of the 200 particles collected from Detonator 17 were significantly larger than the reference distribution, approximately 53 μm in average diameter. Images of these particles show what appear to be several particles sintered together. Though the frequency of these agglomerations is very low, the large particle size causes a significant increase in the mass averaged diameter for the collected particles. The particles collected from Detonator 17 have a number averaged diameter of 22.3 μm and a mass averaged

diameter of 30.6 μm, compared to 22.0 μm and 26.6 μm respectively for the reference powder. These analyses of Detonators 03 and 17 indicate that the quenching apparatus effectively prevents significant combustion of aluminum particles added to small, HE detonators. Size distributions for aluminum collected from the detonation debris show an increase in the number 5-15 μm particles. These particles are primarily unoxidized and may be the result of particle fracturing.

To examine the variations in the burn characteristics of aluminized detonators in different environments, the flow chamber was modified to allow detonators to be fired in a pure environment of a chosen gas. By removing oxygen from the test chamber, the combustion reactants could be controlled to examine specific reactions.

Aluminum wires were first exploded in several combinations of vacuums and N2 flushes to test for the presence of oxygen in the chamber. By passing the detonating current through a thin aluminum wire, in place of the detonator, the wire is rapidly heated and combusts. This technique was used frequently during setup and calibration of the experiments since the vaporized wire produces an AlO signal of similar intensity to detonators fired in air. When AlO is present in the spectroscopic emissions from a wire, oxygen must be present in the surrounding environment, since there are no secondary sources.

An AlO signal is clearly seen in wires fired in air, as expected. Wires fired in a vacuum display a weak AlO signal, and almost no AlO is discernable when the chamber has been vacuumed then filled with N_2 once. After vacuuming and flushing with N_2 three times, no AlO signal is observed. These tests indicate that the presence of oxygen is greatly reduced by each vacuum flush and that after 3 flushes, the oxygen remaining is not enough for a detectable aluminum oxidation reaction. Detonators were fired after 4 flushes for additional environmental purity. A series of detonators were studied in environments of air, carbon dioxide and nitrogen: one in air, two in N_2, one in CO_2 and two in air with a thin layer of epoxy coating the front surface of the explosive. All tests were performed at slightly above 1 atm to help prevent air leakages into the chamber, with 4 flushes of the working fluid in the cases of CO_2 and N_2. The reference AlO signal from Detonator 07 is plotted in Figure V.32 along with the AlO signals from the other detonators. Again, for these figures, time zero indicates the first appearance of spectral emissions from the detonation.

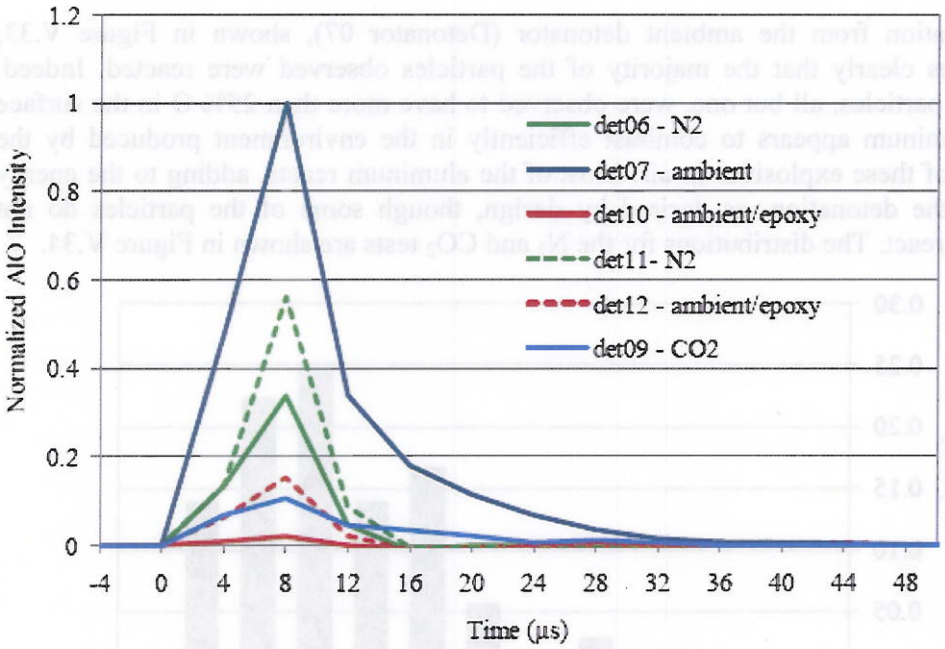

Figure V.32. AlO intensities for quiescent detonator tests, normalized to detonator fired in air.

Two tests were conducted with aluminized detonators in nitrogen. AlO is clearly observed, though at about half of the intensity and for half the duration as the air tests. The same trends are observed in the N_2 tests as in the air test, namely a sharp increase in signal for the first 8 µs. A more rapid decrease in intensity is observed in the nitrogen tests, however. The AlO signal observed in the air quench test, presented above, is similar in maximum intensity to these N_2 tests. Aluminum is expected to oxidize at least as well in CO_2 as in N_2 assuming that the same post-detonation products from the explosive are involved. Though the AlO emissions appear less intense in CO_2, additional factors must be taken into account for comparison with the nitrogen and air tests. When considering that CO_2 has a higher specific heat than N2 and that emission is strongly dependent on temperature, it is likely that similar reactions took place in the aluminum particles, but that they occurred at a lower temperature than in the N_2 environment. Additionally, CO_2 shows a longer emission of AlO, indicating that the Al reactions occur for nearly as long as in ambient. Unexpected results were observed from a pair of detonators fired in air with a thin epoxy layer across front, exposed face. These tests were performed to examine the hypothesis that an epoxy layer, though mechanically weak compared to the brass casing surrounding the sides of the detonator, may interrupt the dispersion and observation of the aluminum particles. A significant decrease in AlO intensity is observed in these epoxied detonators, surprising since the aluminum should react strongly in an oxygen rich environment, as demonstrated by the ambient detonator.

The debris from each detonator was collected following the tests and examined under the scanning electron microscope. 100 aluminum particles were located and analyzed as described above to produce histograms for the percent of oxygen present.

The distribution from the ambient detonator (Detonator 07), shown in Figure V.33, demonstrates clearly that the majority of the particles observed were reacted. Indeed, 99% of the particles, all but one, were observed to have more than 25% O in the surface layers. Aluminum appears to combust efficiently in the environment produced by the detonation of these explosives in air. Most of the aluminum reacts, adding to the energy release of the detonation, as desired by design, though some of the particles do not completely react. The distributions for the N_2 and CO_2 tests are shown in Figure V.34.

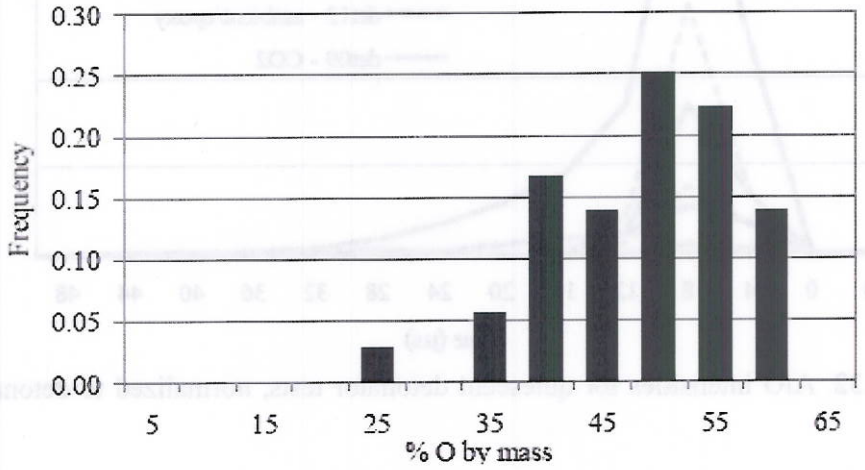

Figure V.33. Oxygen concentration in Al from detonator fired in air.

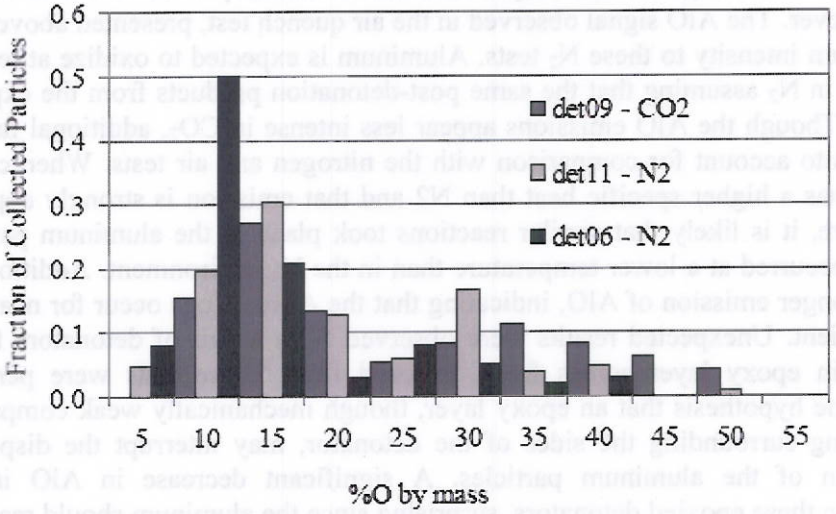

Figure V.34. Oxygen concentration in Al from detonators fired in N_2.

Approximately 10% of the particles showed significant oxidation in the first N_2 tests, compared to 26% in the second. The second N_2 test also showed higher intensity AlO emissions, implying a correlation between intensity and amount of particles reacted in N_2. Approximately 39% of the particles observed from the CO_2 test were reacted, more than

in either N_2 test. This confirms that the aluminum particles did in fact burn more completely in the CO_2 environment, but that the observed AlO intensity underrepresented the reactions. Two peaks are noted in all three of these tests with a valley near the 25% oxygen cutoff. This may indicate that some particles are exposed to combustion conditions while others do not react at all. Since the detonation products from the explosives are the main source of oxygen in these systems, it is probable that the product gasses do not mix completely with the aluminum powder during the interval when the local temperature is conducive to combustion. The particle distributions for the two detonators fired in air with a thin epoxy layer are shown in Figure V.35. These plots confirm that the epoxy layer does prevent a significant amount of oxidation and not just obscure the observation of the reactions. The second detonator resembles closely the N_2 tests with two peaks separated at 25% oxygen. The first detonator, on the other hand, shows relatively constant frequency with a dip at 35%. Both detonators show a marked decrease in reacted particles in comparison with the un-epoxied ambient detonator.

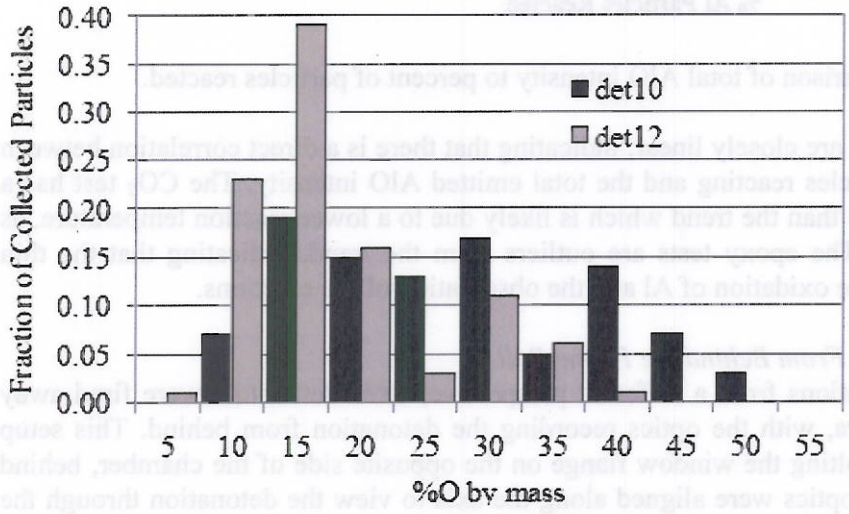

Figure V.35. Oxygen concentration in Al from detonators fired in air with an epoxy layer.

A value for the total AlO intensity for each detonator was determined by integrating under the time-dependent AlO intensity plots. A comparison of the total AlO intensities to percent of particles reacted for the six detonators tested is presented in Figure V.36.

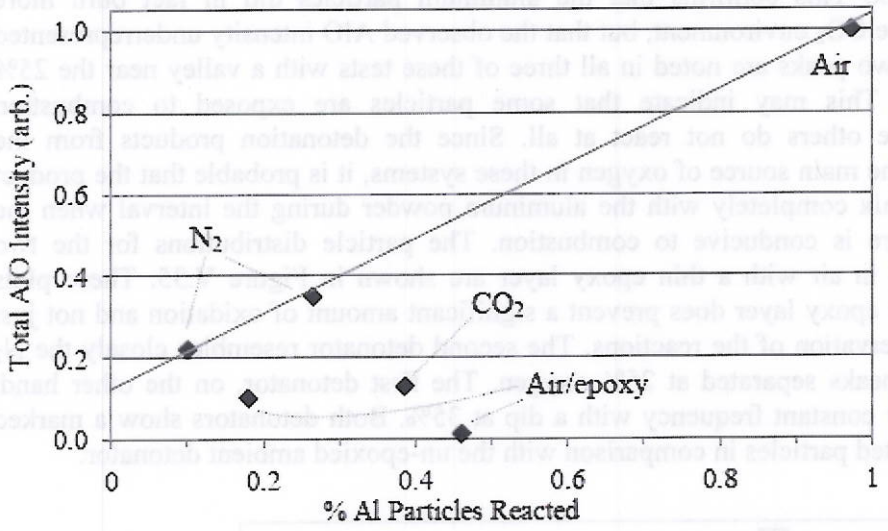

Figure V.36. Comparison of total AlO intensity to percent of particles reacted.

The N_2 and air tests are closely linear, indicating that there is a direct correlation between the amount of particles reacting and the total emitted AlO intensity. The CO_2 test has a lower total intensity than the trend which is likely due to a lower reaction temperature, as mentioned above. The epoxy tests are outliers from the trend, indicating that the thin layer affects both the oxidation of Al and the observation of the reactions.

Observation of AlO From Behind the Flame Ball

To view the detonations from a different perspective, three detonators were fired away from the FK camera, with the optics recording the detonation from behind. This setup was achieved by bolting the window flange on the opposite side of the chamber, behind the detonator. The optics were aligned along the axis to view the detonation through the window, similar to the other quiescent tests. Detonator 14 produced only very weak AlO signals for reasons that are unclear. The results from the other two tests, Detonators 13 and 15, are presented in Figure V.37 normalized to the reference detonator fired in ambient (not shown).

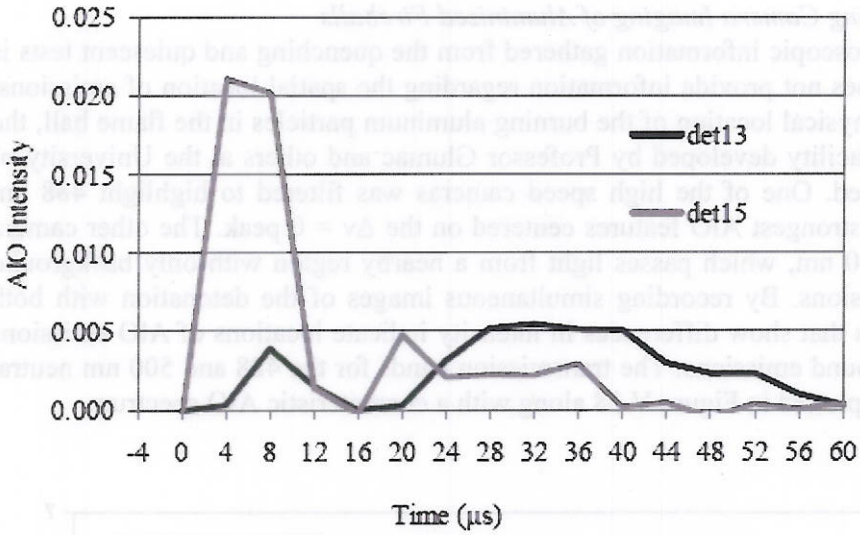

Figure V.37 AlO intensity from behind the detonation flame ball.

The intensities of these AlO signals are greatly reduced, compared to the ambient detonation. This is partly due to the method of observation. The detonators were held by the sting and feedthrough tube setup described earlier. Therefore, the central axis of the detonation cloud for approximately a 5 mm diameter was obscured from the spectrometer's view by the back of the detonator, reducing the intensity. These plots also represent a different aspect of the detonation than had previously be viewed, and therefore the normalization to the other detonators should be considered qualitative and not an absolute reference. A second peak in AlO intensity is observed in both cases, indicating a second stage of aluminum combustion. This secondary combustion phase was observed by Miller and Pangilinan [20], who concluded that the later signal is from aluminum particles reacting with the ambient environment following the initial detonation. This second peak was not observed in the spectra from the head-on camera orientation. As noted earlier, a second peak in AlO intensity was also observed in the helium quenching experiments. The secondary peaks in these quiescent tests occur on a much earlier time scale than in the quenching tests and for significantly longer, indicating the mechanism of reaction is different.

High Speed Framing Camera Imaging of Aluminized Fireballs

Though the spectroscopic information gathered from the quenching and quiescent tests is enlightening, it does not provide information regarding the spatial location of emissions. To examine the physical location of the burning aluminum particles in the flame ball, the new dual-HSFC facility developed by Professor Glumac and others at the University of Illinois was utilized. One of the high speed cameras was filtered to highlight 488 nm light, passing the strongest AlO features centered on the $\Delta v = 0$ peak. The other camera was filtered to 500 nm, which passes light from a nearby region with only background (continuum) emissions. By recording simultaneous images of the detonation with both cameras, locations that show differences in intensity indicate locations of AlO emissions above the background emissions. The transmission bands for the 488 and 500 nm neutral density filters are plotted in Figure V.38 along with a characteristic AlO spectrum.

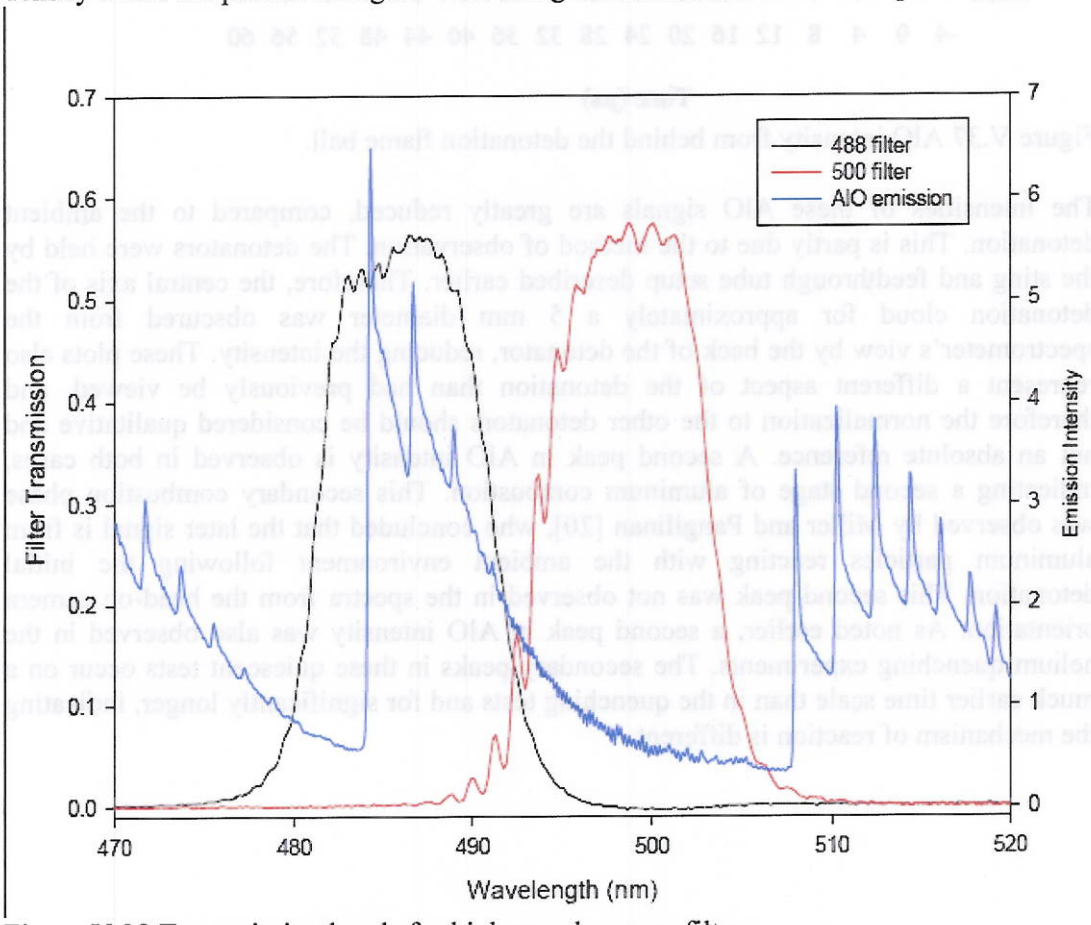

Figure V.38 Transmission bands for high speed camera filters.

Two detonators were fired during setup to optimize the magnification and exposure for each of the 8 frames that were to be recorded of the detonation. The final detonator (Detonator 21) was recorded at f/11. The camera settings are given in Table V.2 and the delay and exposure settings for each frame are given in Table V.3.

Table V.2 Camera settings for high speed imaging.

Camera Settings	
Camera Mode	Double Shutter
Gain setting	normal
Picture Size horz./vert.	1280/1024
ROI horz./vert.	0-1279/0-1023
Binning horz./vert.	x1/x1
External trigger	rising edge
MCP - Decay	0 ms
MCP - Gain	90.0%
Loops	1

Table 3.3 Delay and exposure settings for high speed imaging.

Camera	Frame	Delay (ns)	Exposure (ns)
1	1	5000	500
2	1	10000	500
3	1	20000	1000
4	1	30000	2000
1	2	35000	5000
2	2	40000	10000
3	2	40000	10000
4	2	40000	10000

The delay settings are with respect to the trigger for the first frame of each camera and with respect to the first frame, for the second frame. These settings resulted in images recorded at 5, 10, 20, 30, 40, 50, 60 and 70 μs following trigger. Before the detonator was fired, a reference image was recorded to aid in aligning the images and background images were recorded for each camera

.

Because two separate sets of cameras were used, differences in magnification and alignment existed between the image pairs. In order to accurately compare the two images at each time frame, they first had to be aligned. This was accomplished using the Image-Pro Plus V6.2 image processing software that accompanied the cameras. An additional macro was provided by Cooke Corporation to record the permutations used to register a reference image from one set of cameras to a reference image from the other set. These transformations were then applied to all of the images from one of the cameras, following the test. Because this alignment software was very particular about determining a transformation map from the reference images, all images were pre-

processed in Matlab to roughly align and magnify the two sets of images. These modifications were consistent throughout each camera set, including the reference images. The processed images from the 488 nm filtered camera and the 500 nm filtered camera are presented in Figures 3.39 and 3.40, respectively. The false color is added for contrast.

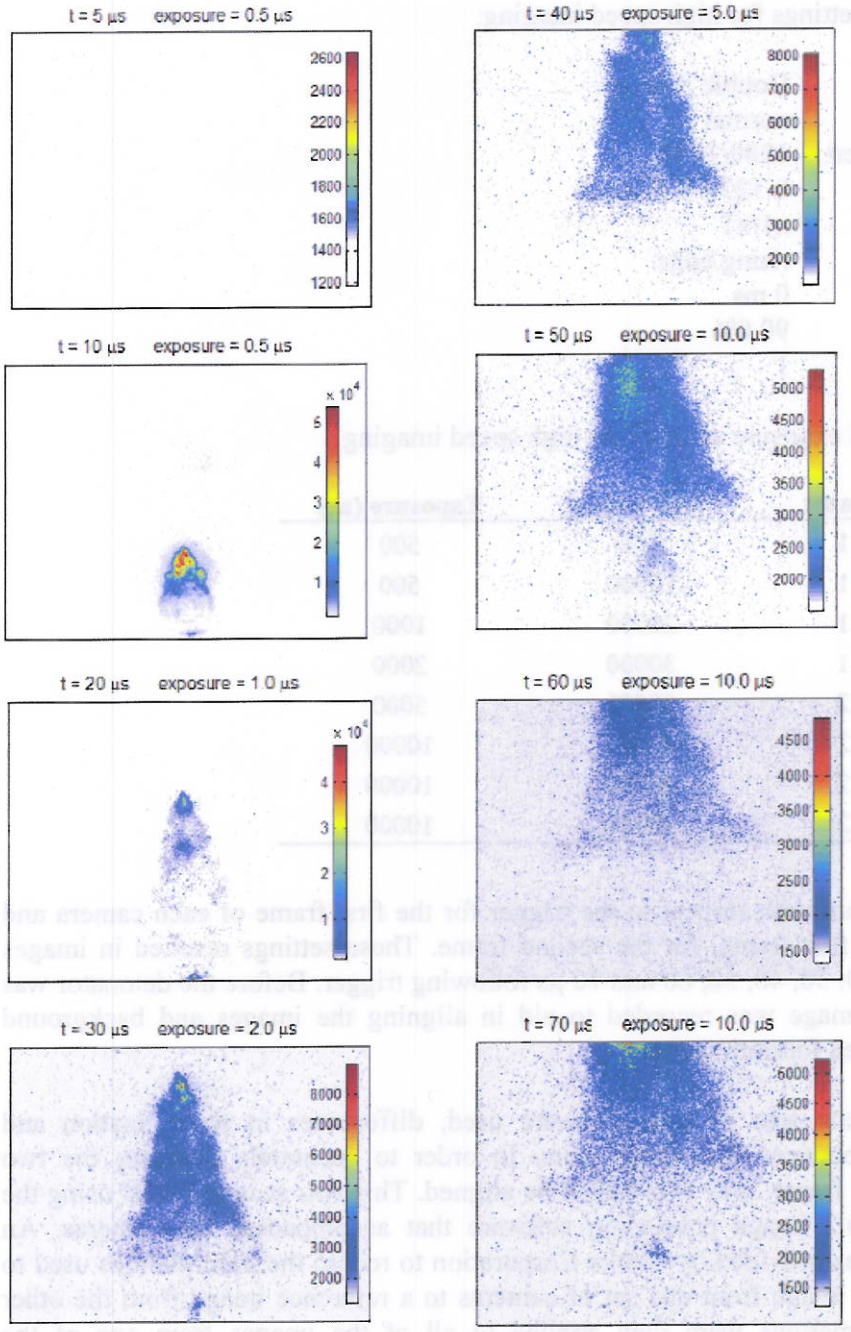

Figure V.39 High speed images of aluminized detonation viewed through 488 nm filter.

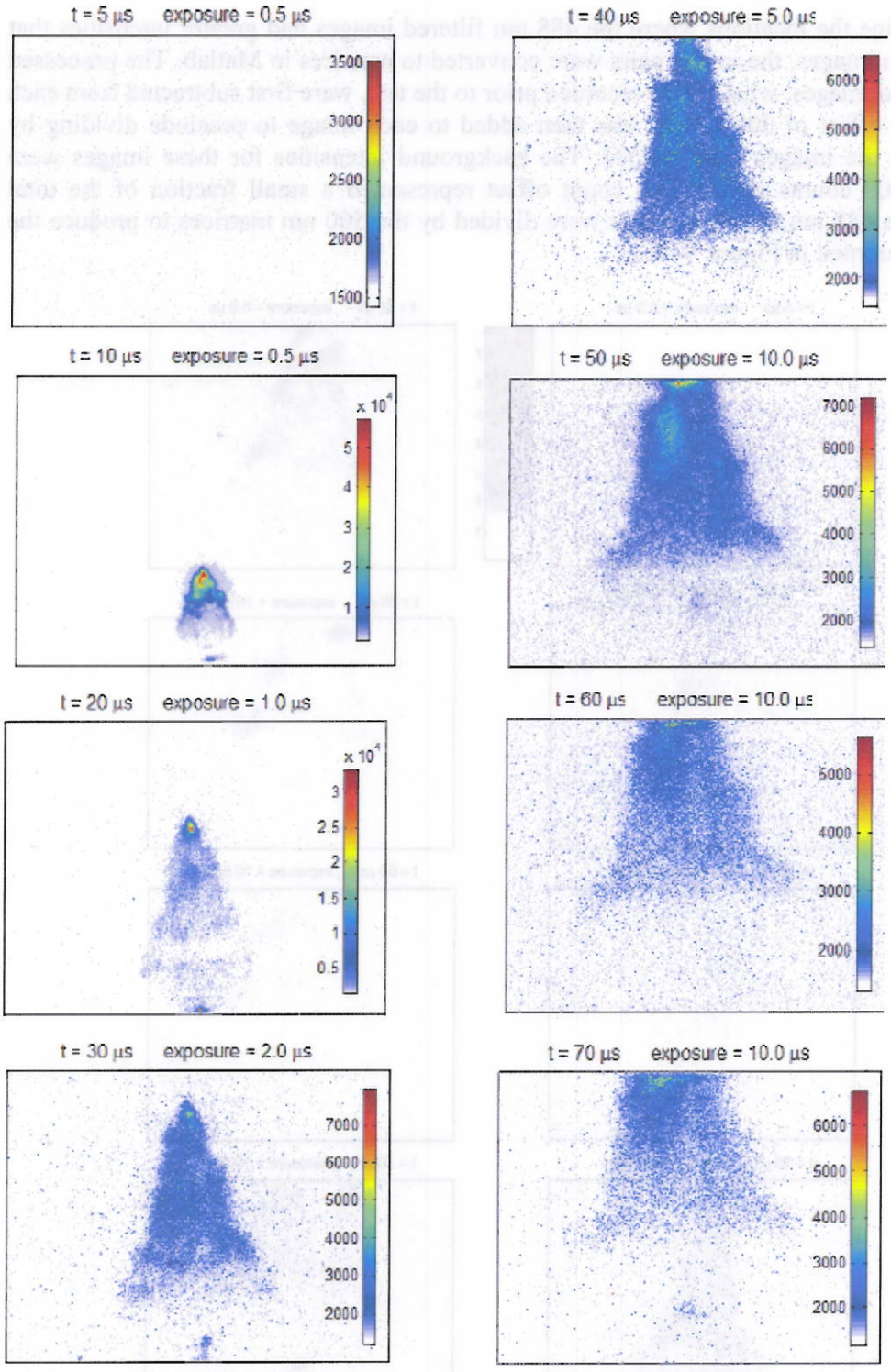

Figure V.40 High speed images of aluminized detonation viewed through 500 nm filter.

To determine the locations where the 488 nm filtered images had greater intensities that the 500 nm images, the image pairs were converted to matrices in Matlab. The processed background images, which were recorded prior to the test, were first subtracted from each frame. An offset of 300 counts was then added to each image to preclude dividing by zero when the images were ratioed. The background intensities for these images were around 3000 counts so this 300 count offset represented a small fraction of the total signal. The 488 nm image matrices were divided by the 500 nm matrices to produce the images presented in Figure V.41.

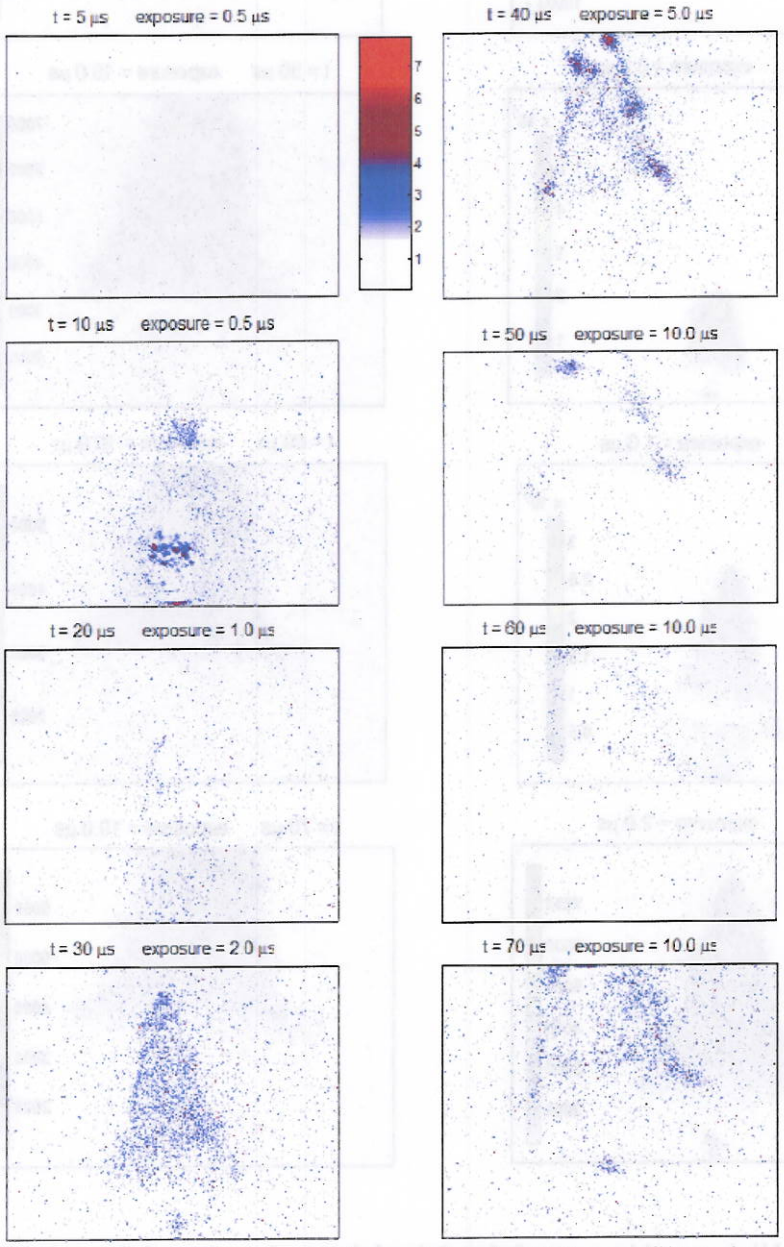

Figure V.41 Ratio of images from 488 nm filter to 500 nm filter: location of AlO emissions from aluminized detonator (constant scale).

The images show distinct areas that have an intensity ratio greater than 2, indicating regions where the 488 nm filtered image had an intensity that was at least twice as bright as the 500 nm filtered image. The AlO emissions appear to follow the flame ball volumetrically for the first 30 μs then concentrate near the leading edges of the cloud in later frames. The increased intensity around the edges at the later times may be due to the opacity of the flame ball obscuring the emissions near the center.

Conclusions

The detonation of aluminized explosives was examined spectroscopically in a variety of environments. Detonation debris was recovered and individual aluminum particles analyzed microscopically for oxygen concentration and average size. Together, this information has provided fundamental insight into the combustion of aluminum particles in the post detonation products from high explosives. To observe the effect of the initial detonation shock on the imbedded aluminum particles, aluminized 50 mg RDX-based detonators were fired in a high speed helium flow in a supersonic nozzle. Spectroscopic observation and recovered particle analysis confirmed the effectiveness of the quenching apparatus. For the two quenched detonator tests examined in detail, less than 25% of the recovered aluminum particles showed a significant increase in oxygen content, indicating that the majority of the particles remained uncombusted. A comparison of the minor to major diameter ratio showed that the average sphericity of the shocked particles remained unchanged from the reference unshocked aluminum powder. Additionally, 11% of the aluminum particles recovered from the detonator debris had an average diameter less than 13 μm, compared to only 1% of the reference powder. These small particles showed very little oxidation, and may be the result of fragmentation of the larger particles. Occasional agglomerations of aluminum particles were also noted, resulting in particle sizes larger than 50 μm in diameter. Together, these observations indicate that the initial detonation shock produced by a HE has a definite impact on imbedded aluminum particles. The detonation of aluminized explosives was studied in quiescent environments of either air, CO_2 or N_2 to observe the variations in aluminum combustion efficiency with different oxidizers. Spectroscopic analysis showed that the characteristic AlO signature had the highest peak intensity in air, followed by N_2 at approximately half the intensity of the ambient test, then finally CO_2. The strong AlO signal in a nitrogen (oxygen-free) environment demonstrates that the detonation products from an explosive play an important role in the combustion of imbedded aluminum particles.

Analysis of aluminum particles recovered from the detonation debris showed a correlation between the intensity of the spectroscopic AlO signal and the percentages of particles oxidized by the detonation. The aluminum particles recovered from the detonators fired in air were nearly completely combusted while histograms from the N_2 and CO_2 tests showed a distinct separation between partially combusted and uncombusted aluminum particles. An average of 20% of the particles were significantly reacted in the N_2 tests and approximately 40% were reacted in the CO_2 test. Spectroscopy and debris analysis from aluminized detonators fired in air with a thin epoxy later covering the tip yielded unexpected results. The AlO intensity was significantly decreased compared to the un-epoxied detonators fired in air and recovered particles

showed that many of aluminum particles were uncombusted. The epoxy layer appears to affect both the observation of the aluminum oxidation reactions and the reactions themselves. Observation from behind the flame ball produced by the aluminized detonators revealed two peaks in AlO intensity, instead of the single peak observed in the head-on view. This secondary peak is typically about a fourth of the intensity of the initial peak and occurs approximately 16 μs later. High speed images of the detonation of the aluminized detonators were recorded to identify the location of the burning aluminum particles in the flame ball. Simultaneous images were taken by two separate cameras: one filtered to 488 nm to emphasize AlO emissions, the other filtered to 500 nm to emphasize the background. By aligning and overlaying these images, AlO emissions were observed to travel volumetrically with the flame ball and congregate toward the leading edges after the first 50 μs, though the optically thick cloud may be obscuring the later time observation of AlO near the center.

References

[1] Davis, J.J., and P.J. Miller. "Effect of Metal Particle Size on Blast Performance of RDX-based Explosives." 2002: 950-953.

[2] Trzcinski, W.A., S. Cudziło, and L Szymanczyk. "Studies of Detonation Characteristics of Aluminum Enriched RDX Compositions." Propellants, Explosives, Pyrotechnics 32, no. 5 (2007): 392-400.

[3] Kuo, K., G. Risha, B. Evans, and E. Boyer. "Potential Usage of Energetic Nano- sized Powders for Combustion and Rocket Propulsion." Materials Research Society Symposium Proceedings. Materials Research Society, 2004. 3-14.

[4] Gilev, S.D., and V.F. Anisichkin. "Interaction of Aluminum with Detonation Products." Combustion, Explosion, and Shock Waves 42, no. 1 (2006): 107– 115.

[5] Victorov, S.B. "The Effect of Al2O3 Phase Transitions on Detonation Properties of Aluminized Explosives." 12th Int. Detonation Symp. San Diego, CA, 2002. 369–376.

[6] Yoshinaka, A., F. Zhang, and W. Wilson. "Effect of Shock Compression on Aluminum Particles in Condensed Media." 15th APS Topical Conference. Kohala Coast, HI, 2007.

[7] Servaites, J., H. Krier, J.C. Melcher, and R.L. Burton. "Ignition and Combustion of Aluminum Particles in Shocked H2O/O2/Ar and CO2/O2/Ar Mixtures." Combustion and Flame 125 (2001): 1040-1054.

[8] Carney, J.R., J.S. Miller, J.C. Gump, and G.I. Pangilinan. "Atmospheric Effects on the Combustion of Detonating Aluminized Explosives." American Institute of Physics. 2006. 948-951.

[9] Rossi, S., E.L. Dreizin, and C.K. Law. "Combustion of Aluminum Particles in Carbon Dioxide." Combust. Sci. and Tech. 164 (2001): 209-237.

[10] Bayzn, T., N. Glumac, and H. Krier. "Oxidizer and Pressure Effects on the Combustion of 10-μm Aluminum Particles." Journal of Propulsion and Power 21, no. 4 (2005): 577-582.

[11] Beckstead, M.W. "Correlating Aluminum Burning Times." Combustion, Explosion, and Shock Waves 41, no. 5 (2005): 533–546.

[12] Glassman, I. Combustion. 3. San Diego, CA: Academic Press, 1996.

[13] Bazyn, T. "Spectroscopic Measurements of the Combustion of Aluminum and Aluminum-based Energetic Material Particles Using a Heterogeneous Shock Tube." PhD Thesis, Urbana-Champaign, IL, 2006.
[14] Lynch, P., N. Glumac, and H. Krier. "Combustion of 5-micron Aluminum Particles in High Temperature, High Pressure, Water-Vapor Environments." 43rd Joint Propulsion Conference. Cincinnati, OH, 2007. 6264 -6270.
[15] Dreizin, E.L. "Experimental Study of Stages in Aluminum Particle Combustion in Air." Combustion and Flame 105 (1996): 541-556.
[16] Dreizin, E.L. "On the Mechanism of Asymmetric Aluminum Particle Combustion." Combustion and Flame 117 (1999): 841-850.
[17] Trunov, M. A., M. Schoenitz, X. Zhu, and E.L. Dreizin. "Effect of polymorphic phase transformations in Al2O3 film on oxidation kinetics of aluminum powders." Combustion and Flame 140 (2005): 310–318.
[18] Ripley, R.C., F. Zhang, and F.S. Lien. "Detonation Interaction With Metal Particles in Explosives." 13th Detonation Symposium. Norfold, VA, 2006.
[19] Orth, L., and H. Krier. "Shock Physics for Nonideal Detonations of Metallized Energetic Explosives." 27th Symposium (International) on Combustion. Combustion Institute, 1998. 2327-2333.
[20] Miller, J.S., and G.I. Pangilinan. "Measurements of Aluminum Combustion in Energetic Formulations." Shock Compression of Condensed Matter. Portland, OR: American Institute of Physics, 2003. 867-870.
[21] Carney, J.R., J.S. Miller, J.C. Gump, and G.I. Pangilinan. "Time-resolved Optical Measurements of the Post-detonation Combustion of Aluminized Explosives." Review of Scientific Experiments 77 (2006): 063103-1-6.
[22] Volk, F., and F. Schedlbauer. "Analysis of Post Detonation Products of Different Explosive Charges." Propellants, Explosives, Pyrotechnics 24 (1999): 182- 188.
[23] Carlson, D., S. Deiter, R. Doherty, and V. Ringbloom. "Determination of Product Gases from Free-field Underwater Detonation of PETN and PETN- Aluminum." 21st International ICT Conference. Karlsruhe, Germany: 111-1- 10, 1990.
[24] "Technical Discussion on Explosives." Teledyne RISI, Inc. 2008. www.teledynerisi. com/products/0products_8td_page01.asp (accessed January 2008).
[25] "Technical Discussion Exploding Bridgewire (EBW) Detonators." Teledyne RISI, Inc.2008.www.teledynerisi.com/products/0products_8td_page03.asp (accessed January 30, 2008).
[26] Oosthuizen, P.H, and W.E. Carscallen. Compressible Fluid Flow. McGraw-Hill, 1997.
[27] "Leybold Vane Pumps Trivac A Series." PTB Sales. 2007.http://www.ptbsales.com /vacuum/pumps/ (accessed February 2008).
[28] "RP-2 EBW Detonator." Teledyne RISI Inc. 2008. http://www.teledynerisi.com/ products/0products_1ebw_page21.asp (accessed January 2008).
[29] Cooke Corporation. Intensified Cameras. 2008. http://www.cookecorp.com/cooke/ php/products/technical_1-en__01030202.html (accessed April 2008).
[30] El-Shobokshy, I.S., and I.A. Ismail. "Capture of Air Borne Particles by V-Shaped and Plane Baffles." Journal of Engineering Sciences, 1980: 137-145.
[31] Oxford Instruments. Link ISIS Operator's Guide: Rev. 3.2. Operation Manual, Buckinghamshire, England: Oxford Instruments Limited, 1997.

[32] Kamps, R. "Agent for the Separation of Dissolved and/or Undissolved Materials of Different Buoyancy Densities or Densities by Means of Solutions of True Metatungstate". US Patent 4557718. 1985.

VI. Detailed Parametric Studies of Aluminized Explosives

Abstract

Detailed studies on three 200 mg aluminzed charge types were performed: 50% Al loading of 3 um particles, 20% loading of 3 um particles, and 20% loading of 40 um particles. Diagnostics included time-resolved spectroscopy, pyrometry, and blast pressure, along with ex situ residue analysis using EDS techiques. Ambient atmosphere was varied between air, O_2, CO_2, and N_2. Many results of Carney et al. at NSWC-IH were replicated, and new results were obtained. Strong evidence for prompt Al combustion was seen in all cases. Afterburn effects were observed with excess Al loading and for large particles, but only in environments with significant O_2 content. Significant (40%) enhanced pressure blast effects were observed for all charges with respect to the unaluminized baseline. Data analysis is still on-going.

Introduction

Initial results with the RP-2 aluminized charges provided some compelling evidence that the ambient atmosphere has a significant effect on the oxidation of particles in aluminized charges. However, these charges were very small, and the data obtained were limited. This study was undertaken with much larger charges (200 mg), different loadings and particle sizes, and added diagnostics. The goal here was to further elucidate when and where the aluminum in aluminized charges burns, and how these processes vary depending on loading, ambient environment, and particle size.

Experimental

Five distinct charges based on the RP80 detonator manufactured by Teledyne RISI were used in these experiments. The original or bare RP80 contains 123 mg of RDX ignited by 80 mg of PETN, and initiated by an exploding bridgewire. The bare RP80 was used as a baseline case. Aluminum powder was added by RISI to the RDX section for three of the charges. Two sets of charges have 3 μm aluminum powder added to make 20/80 and 50/50 Al/RDX combinations and are designated as "20A" and "50," respectively. A third combination is 40 μm aluminum powder in a 20/80 Al/RDX mixture, and is designated as "20C." The last charge was a bare RP80 with 3 μm aluminum powder attached to the end of the charge by silicon grease. The amount of Al powder on the bare RP80 varied between 7 and 15 mg for the tests. The charges used are summarized in the Table VI.1. Each charge, except the end-loaded, was fired in two experimental setups: the tube chamber and the air blast tank (ABT). The end-loaded charge was fired only in the tube chamber.

Table VI.1. Charges used in the study

Charge Designation	Aluminum Powder Size	Al/RDX combination
Bare	-	-
20A	3 μm	20/80
20C	40 μm	20/80
50	3 μm	50/50
End	3 μm	-

In the tube chamber, each aluminized charge was fired in four environments: air, N_2, O_2, and CO_2. Except for air, the chamber was flushed four times with each gas before filling the

chamber for firing to ensure a pure environment. The chamber was evacuated to -96 kPa gage for each flushing. The starting pressure was 0 gage pressure for the air tests and 4 kPa gage for all other tests to ensure no air leaking into the chamber, besides the chamber being leak tested before the tests began.

The tube chamber has a 4 inch internal diameter and is 3 feet long and is shown in Figure VI.1. An adjustable chuck was used to hold the charge at the plastic head. The mount for the chuck fit into the chamber such that the charge fired toward the window and was centered radially in the tube. A steel ring behind the mount ensured that it did not move axially in the chamber during the firing. Aluminum bridge wires were used to check alignment and settings before each test.

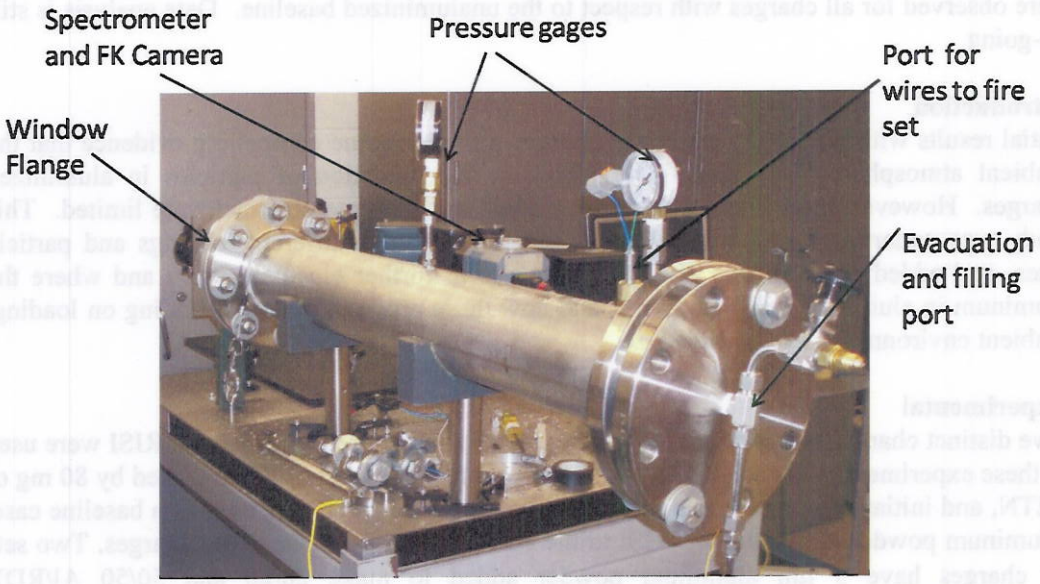

Figure VI.1. Tube chamber experiment set up

A window in the flange at the far end from the firing allowed for spectroscopy measurements with a custom built spectrometer and Fast Kinetics CCD detector. The CCD detector was an Andor model DV420-FK. The spectrometer is a 50 mm focal length f/1.4 spectrometer with 1800 groove/mm equivalent volumetric phase grating, 2:1 inlet to exit focal length ratio and a spectral resolution of 5 Å. Spectra were taken with 2 μs exposure every 2 μs during the first 200 μs of each firing. Intensity and wave length calibration spectrum were also taken for data analysis calibrations. The charge was checked during and after the flushing/filling with a mirror through the window to ensure the Al/RDX charge was in place before firing.

The tests completed in the tube chamber are listed in Table VI.2. Each test is distinguished by a title which details the test date, charge designation, and environment. These designations are used in many of the plot legends.

For the tests in the tube chamber, it was possible to collect the residue from the tests and save for analysis with an SEM and X-Ray to determine the percent oxidation of the aluminum particles. A plastic sheet was inserted into the tube, which covered the entire inside surface. After a test, the sheet was removed and cleaned with distilled water to collect the particle residue in Petri dishes. The collected residue was then allowed to dry. Large plastic and brass pieces from the charge casing were separated from the debris before attaching the fine

powder residue to aluminum cylinders via double sided carbon tape. All of the residue was collected from each test such that the location in the tube was indistinguishable, and therefore the particle tested could be assumed to come from every part of the tube.

Table VI.2. Summary of tests completed in the tube chamber and designation used within plots and the text

Test	Environment	Aluminized Loading	End Loading: Al Powder	Test Date	Designation
1.	Air	Bare	None/Set up	1/28/2009	0128 bare air
2.	Air	Bare	3 micron	2/9/2009	0209 end air
3.	Air	20% 40 μm	-	2/17/2009	0217 20C air
4.	Air	20% 40 μm	-	3/17/2009	0317 20C air
5.	Air	20% 40 μm	-	4/3/2009	0403 20C air
6.	Air	20% 3 μm	-	2/17/2009	0217 20A air
7.	Air	20% 3 μm	-	3/16/2009	0316 20A air
8.	Air	20% 3 μm	-	4/7/2009	0407 20A air
9.	Air	50% 3 μm	-	3/13/2009	0313 50 air
10.	Air	50% 3 μm	-	3/18/2009	0318 50 air
11.	N_2	Bare	3 micron	3/12/2009	0312 end N_2
12.	N_2	20% 40 μm	-	3/11/2009	0311 20C N_2
13.	N_2	20% 3 μm	-	3/11/2009	0311 20A N_2
14.	N_2	50% 3 μm	-	3/12/2009	0312 50 N_2
15.	CO_2	Bare	3 micron	3/4/2009	0304 end CO_2
16.	CO_2	20% 40 μm	-	3/6/2009	0306 20C CO_2
17.	CO_2	20% 3 μm	-	3/4/2009	0304 20A CO_2
18.	CO_2	50% 3 μm	-	3/4/2009	0304 50 CO_2
19.	O_2	Bare	3 micron	3/16/2009	0316 end O_2
20.	O_2	Bare	3 micron	3/18/2009	0318 end O_2
21.	O_2	20% 40 μm	-	3/13/2009	0313 20C O_2
22.	O_2	20% 40 μm	-	3/17/2009	0317 20C O_2
23.	O_2	20% 40 μm	-	4/8/2009	0408 20C O_2
24.	O_2	20% 40 μm	-	4/27/2009	0427 20C O_2
25.	O_2	20% 3 μm	-	3/13/2009	0313 20A O_2
26.	O_2	20% 3 μm	-	3/16/2009	0316 20A O_2
27.	O_2	50% 3 μm	-	3/13/2009	0313 50 O_2
28.	O_2	50% 3 μm	-	4/27/2009	0427 50 O_2

Particles from tests in each environment and aluminized charge were viewed using the JEOL 6060LV scanning electron microscope at the Center for Microanalysis of Materials at the University of Illinois. SEM images were primarily viewed with an accelerating voltage of 20 kV and a spot size of 40-60, usually around 50. The SEM used is equipped with an Oxford Instruments Energy Dispersive X-ray Spectrometry (EDS) system and Oxford Link ISIS software. In an area of residue, individual aluminum particles were identified with the SpeedMap function at a resolution of 500-2000x. The identified particles were then zoomed in on such that only the particle surface was visible in the SEM/EDS detectors. Using the SEMQUANT function available with the EDS software, the relative concentrations of aluminum and oxygen were determined. For each test sample, a minimum of twenty particles

was analyzed. The percent oxygen of the residue particles from the tests are compared to the measured amount of percent oxygen of a reference sample of Al_2O_3 particles. The percent oxygen of a reference sample of 3 μm Al particles was also determined. The results are presented as the fraction of complete oxidation based on the level of oxygen on the Al_2O_3 particles.

In the air blast tank (ABT), the charges were fired in air. A list of tests completed is presented in Table VI.3. The charges were securely mounted to fire vertically up, such that the entire charge was held in place in a steel block with the top of the charge flush with the top of the mount. Directly above the charge mount, a window flange allowed for 2-color pyrometry and spectroscopy measurements. The pyrometer uses narrow bandpass interference filters to isolate the 730 nm and 940 nm ± 2 nm wavelengths with approximately 10 nm FWHM bandpasses. The wavelengths were monitored with photodiodes and the output went to a picoscope. The time resolution of the pyrometer measurements is 0.4 μs. The same spectrometer and CCD detector was used for the ABT tests as the tube chamber tests. Spectra were taken with a 16 μs exposure every 16 μs. With this time resolution, the entire luminous event was able to be captured.

Table VI.3. Tests completed in the air blast tank

Test	Environment	Aluminized Loading	Test Date	Designation
1.	Air	Bare	4/27/2009	Bare Test 1
2.	Air	Bare	4/27/2009	Bare Test 2
3.	Air	20% 3 μm	6/29/2009	0629 20A
4.	Air	20% 40 μm	6/29/2009	0629 20C
5.	Air	50% 3 μm	6/26/2009	0626 50 or Test 1
6.	Air	50% 3 μm	6/30/2009	0630 50 or Test 2
7.	Air	50% 3 μm	7/16/2009	0716 50 or Test 3

Three pressure transducers recorded pressures as a function of time, two to record end-on pressure at 8.4 and 12.65 inches from the charge and one to measure side-on pressure at 8.4 inches away. The pressure transducers were oriented in a "lollipop" configuration, in which the transducer is mounted to a flat plate with a knife edge. Kissler 603B1 model transducers and 5000 series amplifiers were used. The output had a resolution of 10 psi/Volt and a range of 100 psi was used. The data was recorded using a picoscope using a time resolution of 0.2 μs.

Using a shadow-graph technique, the shock wave was imaged with a Phantom V5.2 CMOS high speed camera. The bare charge tests were shot with a 25,316 fps frame rate, 2 μs exposure and 96 x 256 pixel frame, while the aluminized charge tests were shot with a 35,714 fps frame rate, 2 μs exposure and 64 x 288 pixel frame. A Vivitar 352 camera flash, modified with a 0.150 inch pinhole, was used to illuminate the blast area and form a shadow of the shock wave on retro reflective material positioned behind the fireball. The ABT experimental schematic is shown in Figure VI.2, as viewed from the top, which shows the shock wave imaging set up and pressure transducer locations. Using Matlab, the images were processed to identify the shock wave and determine the shock wave velocity.

Each set up used a Teledyne RISI FS-43 firing system with a 4000 volt pulse with 1500 amp peak current to initiate the charges. The firing system and all diagnostics timing was

controlled by a Stanford Research System DG 535 pulse generator.

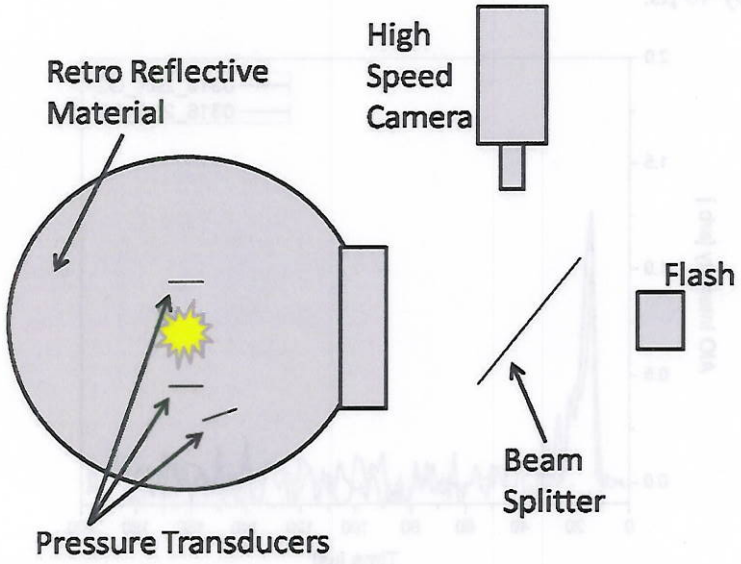

Figure VI.2. Air blast tank schematic, top view

Repeatability

The intermediate AlO was monitored via the spectrometer for each test. For the tube chamber tests, the intensity from the Δv = +1, 0, -1 AlO bands was integrated after subtracting the continuum background at each time step. All AlO intensity plots show the integrated AlO intensity as a function of time after detonation.

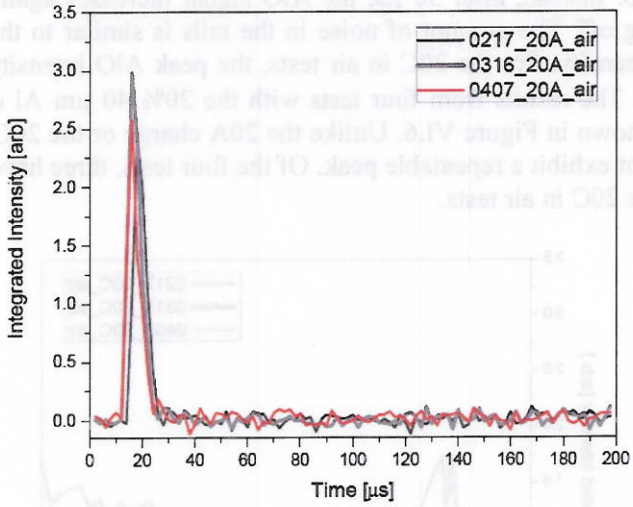

Figure VI.3. 20% 3 μm Al charge in air repeated tests in the tube chamber

The first four plots demonstrate the repeatability of the tube chamber AlO intensity measurements. Figure VI.3 and Figure VI.4 show tests with the 20 % 3 μm Al charges in air and O_2, respectively. These tests in air and in O_2 have a sharp peak in AlO signal within the first 25 us. The peak intensities vary between repeated tests but are within 20% of each other for each environment. For the tests in O_2, the time for the peak varies by one frame or 2 μs.

All 20% 3 μm charges in air and O_2 give the same result that the AlO signal is below detection limits by 40 μs.

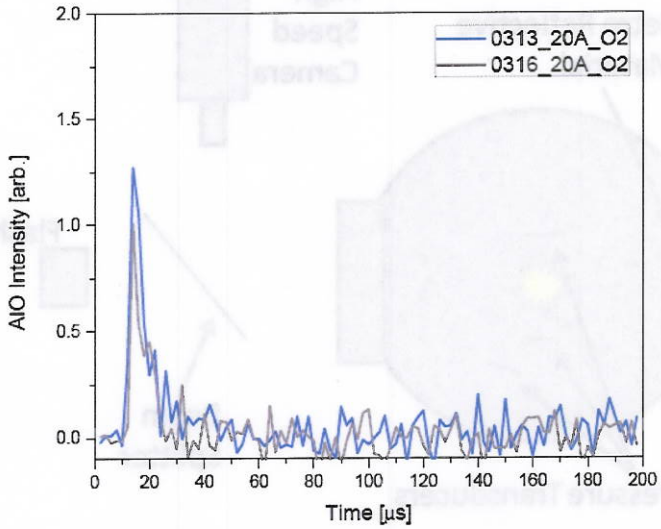

Figure VI.4. 20% 3 μm Al charge in O_2 repeated tests in the tube chamber

Repeated tests with the 20% 40 μm Al charges in air are shown in Figure VI.5. All tests have a sharp AlO intensity peak with in the first 25 μs, with an offset of one frame or 2 μs. For the 20C in air tests, the peak AlO intensity values are within 14% of each other. One test, 0317 20C air, drops off to zero intensity with the same trend as the 20% 3 μm Al charge tests. The AlO signal from the other tests drops off initially, indicating a sharp peak intensity, but does not drop off to zero. Instead, after 30 μs, the AlO signal increases again, more slowly this time before leveling off. The amount of noise in the tails is similar to the noise seen in the 0317 test at zero intensity. For the 20C in air tests, the peak AlO intensity values are within 14% of each other. The results from four tests with the 20% 40 μm Al charge in O_2 in the tube chamber are shown in Figure VI.6. Unlike the 20A charge or the 20C charges in air, the 20C test in O_2 do not exhibit a repeatable peak. Of the four tests, three have a long AlO signal similar to two of the 20C in air tests.

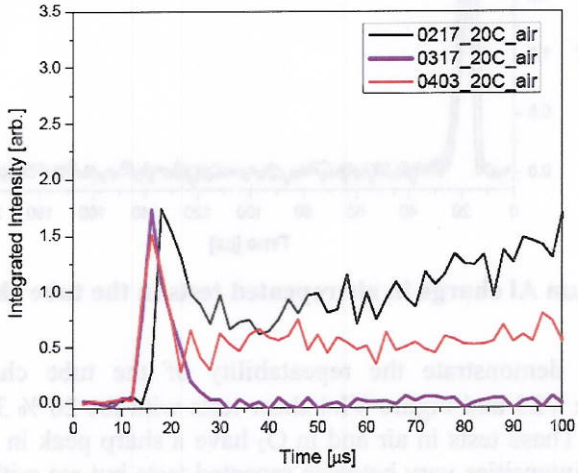

Figure VI.5. 20% 40 μm Al charge in air repeated tests in the tube chamber

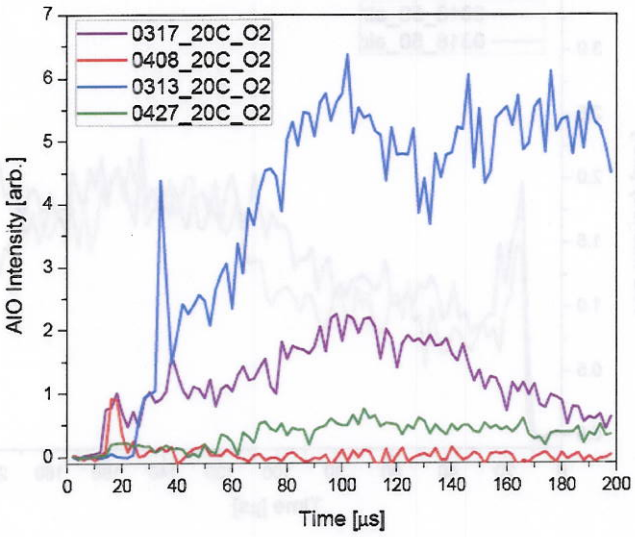

Figure VI.6. 20% 40 μm Al charge in O_2 repeated tests in the tube chamber

The average and standard deviations of the initial peak AlO intensity for the 20C and 20A tests in air are 1659 ±132 and 2660 ±295, respectively. The percent difference between the tests is 20% for the initial peak AlO intensity for all the tests in air for each charge.

Table VI.4. Average and standard deviation (STD dev) for initial peak AlO intensity signal for 20C and 20A tests in air

	Initial Peak AlO Intensity	
20C in air	average	1659
	std. dev.	132
20A in air	average	2660
	std. dev.	295

The 50% 3 μm tests in air and O_2 show repeatability, as shown in Figure VI.7 and Figure VI.8. In air, both tests have a sharp peak within the first 25 μs, and then have AlO intensity throughout the entire time recorded. The tail AlO intensity appears to increase with time and the noise is on the same order seen with previously shown test results. The initial peak AlO intensities are within 6% of each other. From the repeated tests with the 20% 40 μm and 50% 3 μm charges, there is repeatability of Al after-burning in air and O_2. Out of eleven tests, eight show evidence of after burn via the tail AlO signal as seen in Figures VI.5, 7, 6, and 8. It is also clear that the entire AlO signal was not collected in the tube chamber tests with a long AlO tail that does not return to zero within the date collection time frame.

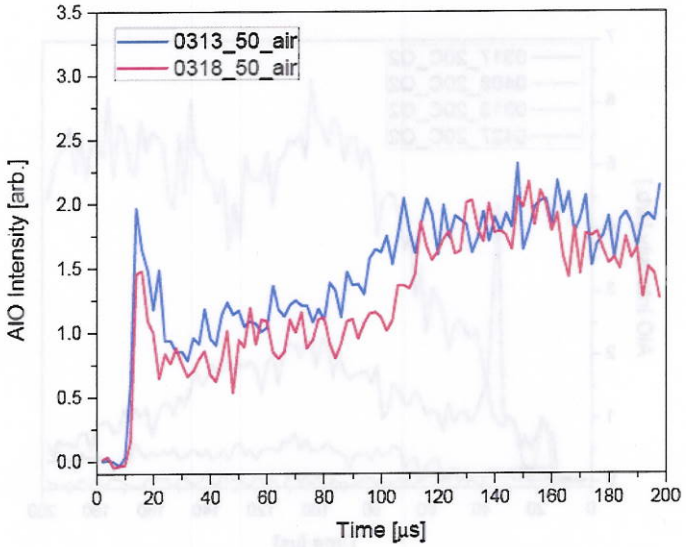

Figure VI.7. 50% 3 µm Al charge in air repeated tests

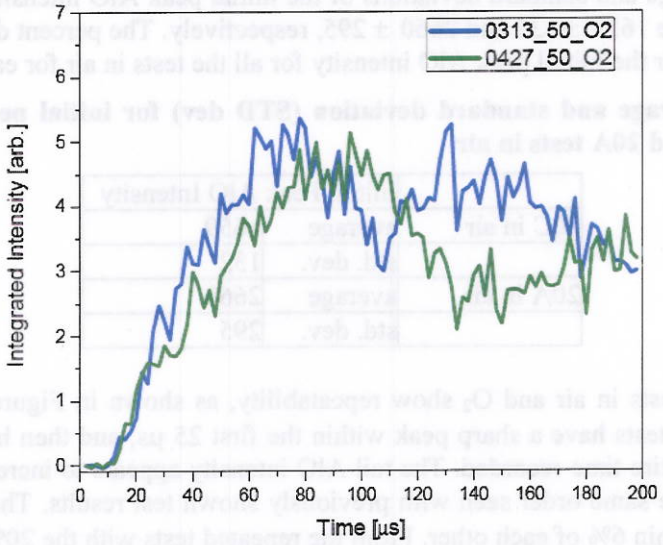

Figure VI.8. 50% 3 µm Al charge in O_2 repeated tests

In the air blast tank, three tests were completed with 50% 3 µm Al charges, and two with bare charges. The intensity from the Δv = +1, 0, -1, -2 AlO bands was integrated after subtracting the continuum background at each time step for the ABT tests. The AlO intensity from all 50% Al charges is shown in Figure VI.9. All tests had the same trend and have AlO signal through 400 µs, which was also seen in the tube chamber tests. The peak AlO intensities differ by 30% and the FWHM values differ by 23%, which are listed in Table VI.6.

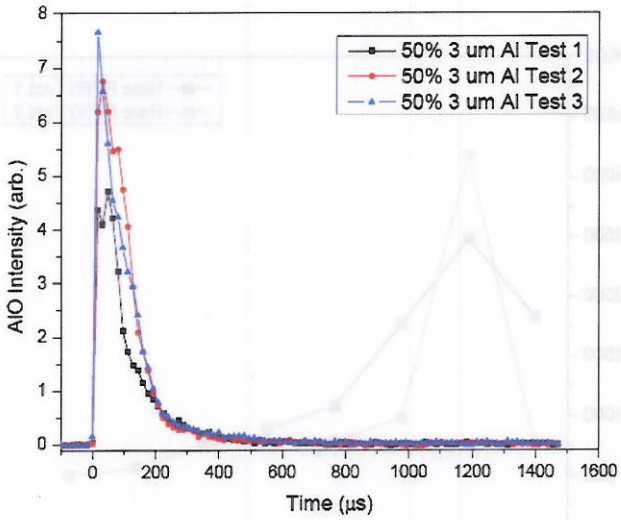

Figure VI.9. AlO Intensities from three tests with 50% 3 μm Al charge

The shock wave velocities are shown for the 50% Al and bare charges in Figures VI.10 and 11, respectively. The shock wave velocities are within 10% for both 50% Al charges after 100 μs, with higher variability early and the last data point, but still within 23%. The velocities from the bare charge vary more, between 10 and 60%. The shock velocities from the bare charge increase before decreasing with time. This first point may be due to difficulty in correctly identifying the location of the shock wave in the images from the high speed camera. In the first few frames, in which the fireball is the brightest and there is no clear shock wave visible, it is assumed that the shock wave location is the tip of the fireball; however this may not be the true shock wave location since the shock wave velocity is seen to increase before decreasing. Additionally, in the test with the 20% 40 μm Al charge, edges of what could be the shock wave can be seen in the first image, and it appears the true location of the shock wave is in the middle of the fire ball. This then, calls into question the validity of the first data point for the shock wave velocities.

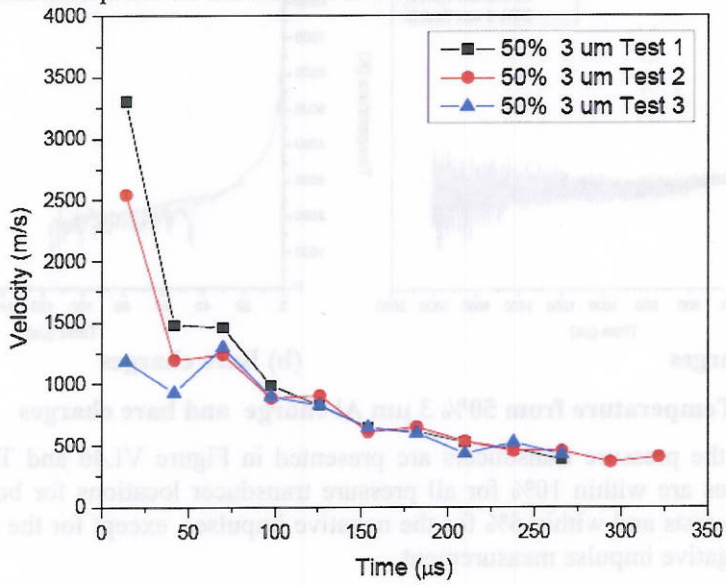

Figure VI.10. Shock Velocities from three tests with 50% 3 μm Al charge

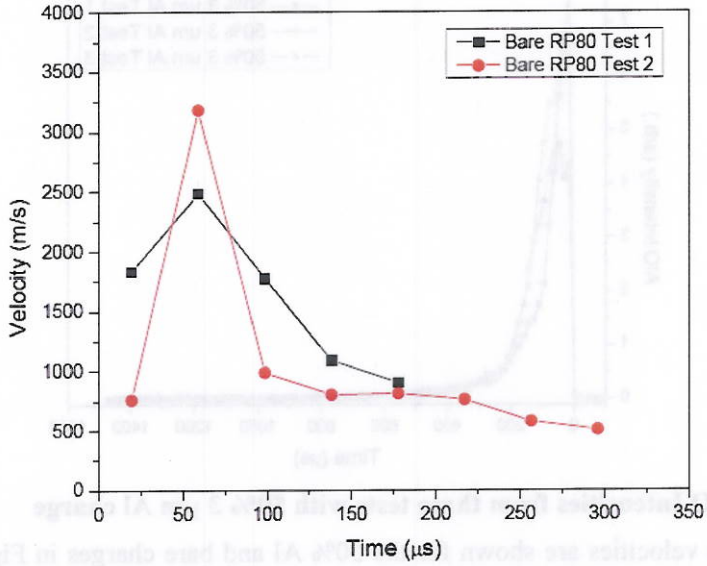

Figure VI.11. Shock Velocities from two tests with RP80 charges

The results from the pyrometer for the 50% Al charges and bare charges are presented in Figure VI.12. The temperatures are in good agreement between similar tests. The data from the pyrometer was valid for the times shown for the charges, i.e. the signal was not saturated or the noise too high for the temperature to be accurately determined. The temperatures are within 20% of each other for the same time for the 50% aluminum charges tests and within 60%, most within 30%, for the bare charges.

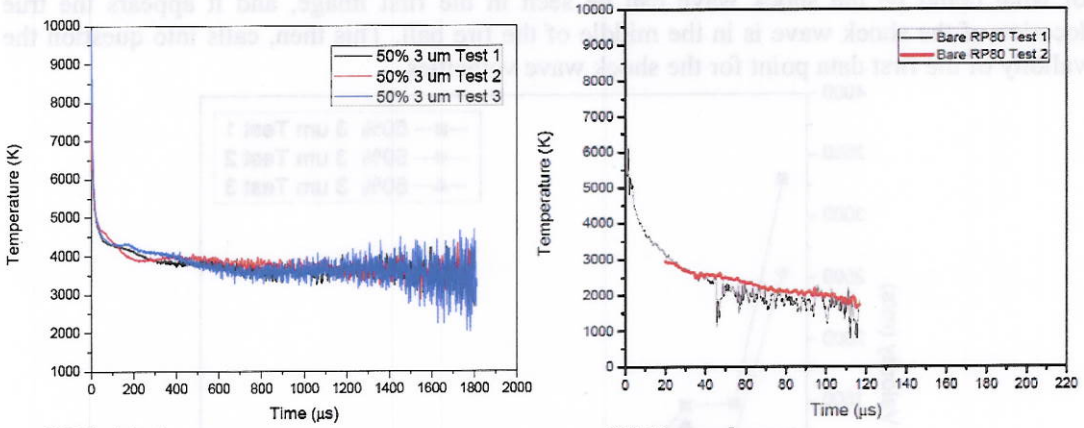

50% Al charges **(b) Bare charges**

Figure VI.12. Temperature from 50% 3 μm Al charge and bare charges

The data from the pressure transducers are presented in Figure VI.46 and Table VI.8. The positive impulses are within 10% for all pressure transducer locations for both the 50% Al and bare charge tests and within 6% for the negative impulses, except for the 50% Al charge tests side on negative impulse measurement.

AlO Emission

AlO emission intensity, normalized to the peak, from the two experiment set-ups are shown

in Figure VI.13. For the 20A charge, the AlO trends are the same within the constraints of the different time resolutions. Thus, the time resolution can influence the measurement of event time. For the 50% Al charges, both experiments show late (after 40 μs) AlO but with different trends. The tube chamber AlO signal increases with time after the peak AlO and the ABT tests decrease with time and show the end of the event, which is later than the time recorded with the tube chamber. For the 20C charge, both experiments have longer AlO signals than the 20A charges (omitting the one test that did not show it in the tube chamber). The late AlO is present longer for the tube chamber versus the ABT and looks like it should last longer than 200 μs, however; there is no AlO after approximately 112 μs with the ABT.

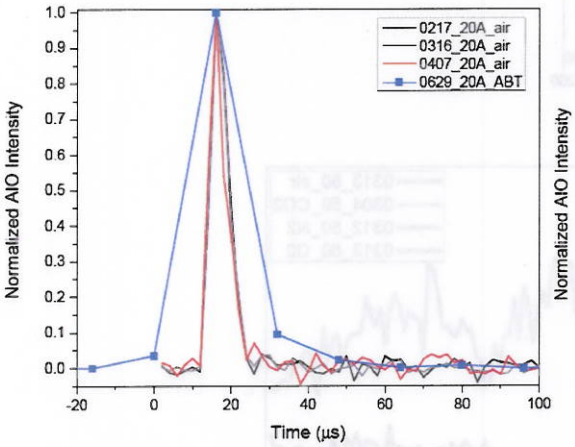

(a) 20% 3 μm

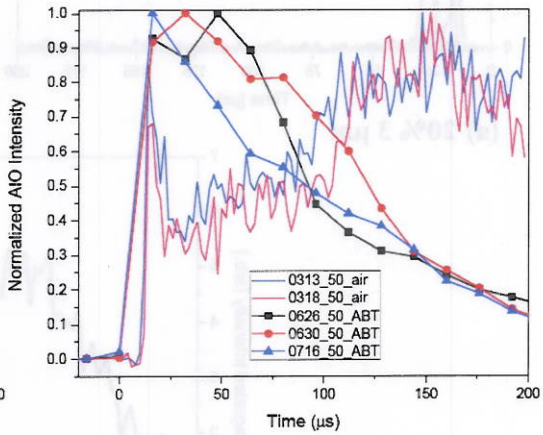

(b) 50% 3 um

(b)

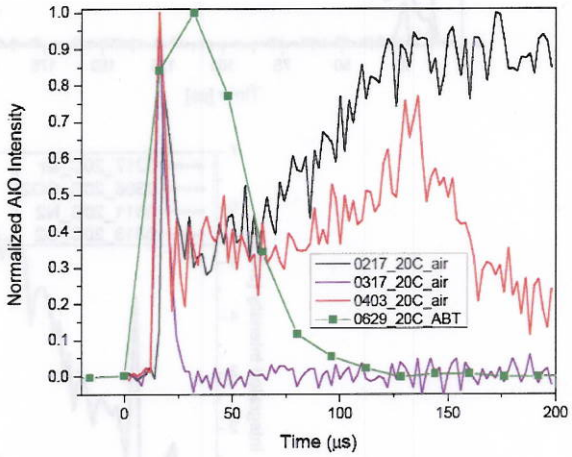

(c) 20% 40 μm

Figure VI.13. Normalized AlO intensities from both experiment setups for each aluminized charge

The integrated AlO intensity signals from the tube chamber experiments are shown in Figure VI.14 for each aluminized charge in the different environments.

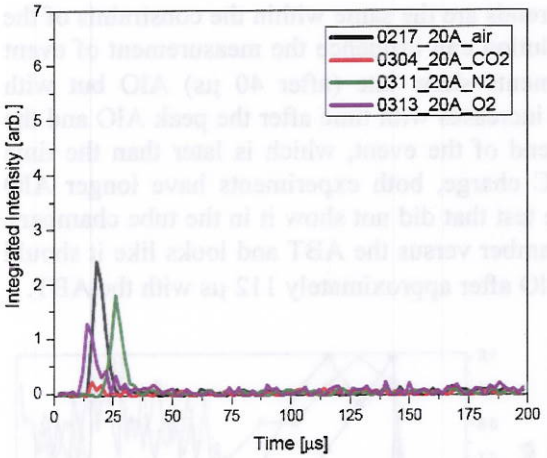

(a) 20% 3 µm

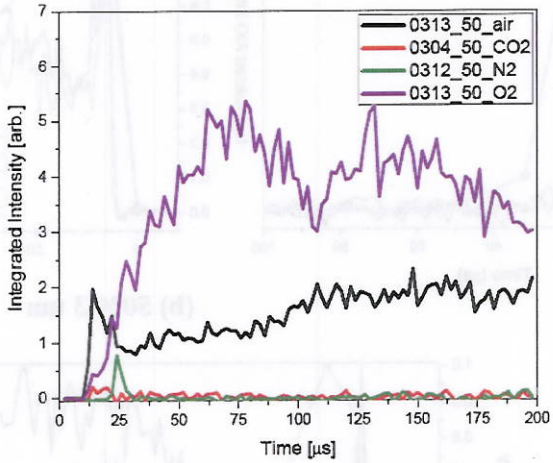

(b) 50% 3 µm

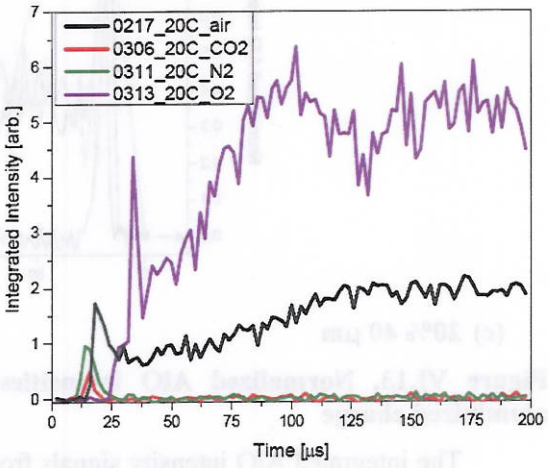

(c) 20% 40 µm

Figure VI.14. AlO intensities from the tube chamber tests for each aluminized charge in four environments

For the 20% 3 µm Al charge tests, Figure VI.14a, in N_2 the AlO intensity is delayed which may indicate combustion with the detonation product CO_2; however the CO_2 test shows no AlO signal. With the 20A charge tests there is no AlO signal longer than 35 µs after

detonation. With the 20% 40 μm Al charge tests, Figure VI. 14c, there is a delay in the AlO signal for the O_2 tests compared to other environments. The test in air is also delayed compared to the N_2 and CO_2 tests. The results from the 50% 3 μm Al charges are shown in Figure VI.14b. The test in CO_2 does not show any AlO intensity. There is a delay with the N_2 case similar to the 20% 3 μm Al case, however; air shows the first peak in AlO intensity, not O_2, although the intensity starts to increase for the O_2 case at the same time as the air test. The 50% 3 μm and 20% 40 μm Al charge tests in O_2 and air have AlO signals throughout the entire test time, which indicate after burn or post-detonation Al reactions.

All the tests in air show a sharp increase to a peak intensity within the first 25 μs. As shown earlier, the 20C and 50% Al charge tests have AlO signal throughout data collection. The peak AlO signals are smaller for the 50% 3 μm Al charge compared to the 20% 3 μm Al charge, which may be due to the reduced oxidizer from the RDX in the charge and thus in the detonation zone.

For the tests in CO_2, the 50% 3 μm and 20% 3 μm Al charge tests do not show much signal above the noise within the first 25 μs. The 20% 40 μm Al charge has an AlO peak signal similar in trend to that seen in the other environments, and occurs within the first 25 μs. The AlO signal in CO_2 is always lower than in N_2. All the tests in N_2 have sharp AlO peaks and return to zero within the first 25 to 40 μs. The first to peak in AlO signal is the 20% 40 μm Al charge, then the two charges with 20% Al at the same time. The 20% 3 μm Al charge has the highest intensity peak.

In Table VI.5, the initial peak and width of the AlO signal is presented for each of the aluminized charges in air for the tube chamber. The AlO peak decreases as the width increases for the 50% 3 μm Al, and 20% 40 μm Al charges compared to the 20% 3 μm Al charge. This peak AlO signal is from the aluminum burning in the detonation zone and is indicative of the amount of oxidizer in the charge and the burn time of the aluminum particles. The peak width data indicate that the small, 3 μm, Al burns faster than the larger, 40 μm, Al particles. The lower initial AlO peak for the 50% 3 μm Al charge indicates that there is less oxidizer in the charge with 50% versus 20% aluminum. The slower burn time for the 20% 40 μm Al charge also reduces the initial AlO peak.

Table VI.5. Initial peak and width of the AlO signal for the aluminized charges in air in the tube chamber

In Air		Initial Peak		FWHM (μs)	
Mod	Al Composition	Average	Percent Error	Average	Percent Error
A	20% 3 μm	2660	20%	5.25	7%
B	20% 40 μm	1659	6%	5.82	33%
C	50% 3 μm	1726	14%	9.23	1%

The AlO emission intensities for the three aluminized charge tests in the ABT are shown in Figure VI.15 and the peak and width of the AlO intensities are presented in Table VI.6. The 50% Al charge has the longest AlO signal time of approximately 416 μs, then the 20% 40 μm Al charge with 112 μs of AlO signal. The 20% 3 μm Al charge has the shortest AlO signal time of 48 μs. The 20% 3 μm Al charge never showed any tail AlO in any test, only a sharp

short AlO peak. Also, we can now see when the AlO emission event is over.

Similar analysis can follow here as with the tube chamber tests. With 50% aluminum, it takes longer to burn because of the number of particles thus a long AlO signal is expected. The large 40 μm Al particles also take longer to burn due to their size so a long AlO signal is seen. One difference between the ABT test results and the results from the tests in the tube chamber is that the peak AlO intensities are similar between the charges. The peaks are within 11.2% for the two 20% Al charges, with the courser Al charge peak being higher. In the tube chamber, the fine 20% aluminum charge had the highest peak intensity, while the 50% charge has the highest peak in the current tests, though still with fine Al particles. All peaks are within 21% of each other. It is speculated that the lower peaks in the tube chamber are due to reduced oxider in the 50% aluminum charge; however the peak for the 50% aluminum charge is higher with the ABT tests. Therefore, this shows that the AlO signal alone cannot indicate the amount of aluminum burning or whether there is complete aluminum combustion.

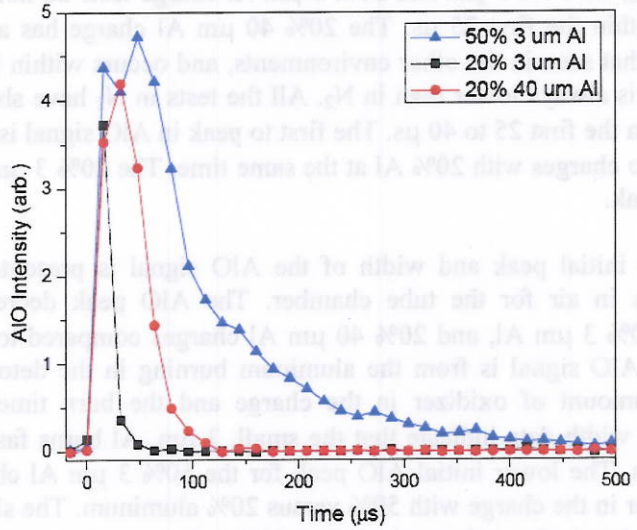

Figure VI.15. AlO intensities from all three aluminized charges in ABT tests.

Table VI.6. AlO Intensity for ABT tests

Test	Al Composition	Peak AlO Intensity	FWHM (μs)	AlO Time (μs)
0629 20A	20% 3 μm	371,892	15.76	48
0629 20C	20% 40 μm	418,866	44.19	112
0626 50	50% 3 μm	472,098	85.73	416
0630 50	50% 3 μm	674,834	111.9	416
0716 50	50% 3 μm	764,977	116.8	416

End Loaded AlO Emission Results

A difficultly with the end loaded bare charges is consistency with the amount of aluminum powder initially on the charge, and then keeping it on the charge in the process of setting up the test. Figure VI.16 shows two tests with end loading and fired in O_2. The legend denotes how much Al was added to the charge before mounting. Checking the charge with a mirror ensured that we knew the aluminum powder was still on the charge before firing but was not

a quantitative measure of how much powder remained in place throughout the mounting procedure. Despite the difference in initial aluminum powder loading between the tests, the tests have similar AlO intensity trends. Both tests show a slow increase in intensity to a peak and a slow decrease back to zero AlO signal. The test with less Al powder peaks earlier and has lower peak intensity which occurs at approximately 25 μs. The other test peaks later and the entire AlO signal last approximately 100 μs compared to 50 μs for the first test. Taking into consideration the difference in aluminum powder amounts, the tests appear repeatable.

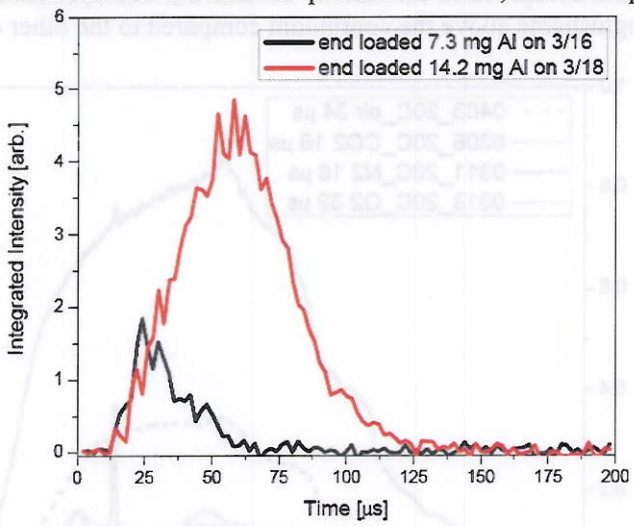

Figure VI.16. End loaded 3 μm Al charge in O_2 repeated tests

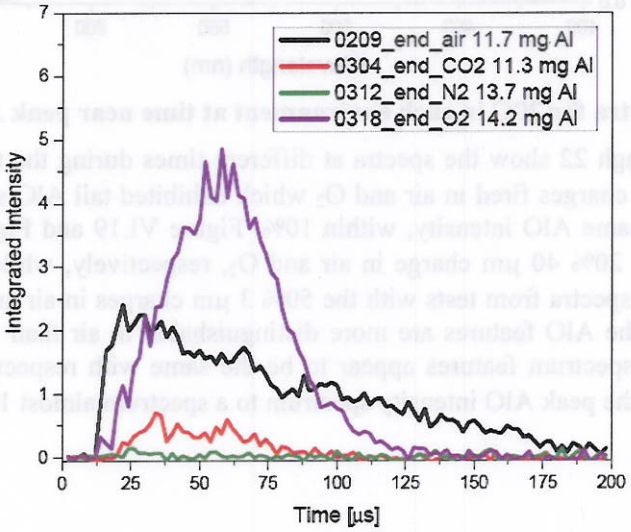

Figure VI.17. End loaded tests in different environments.

For the end loaded bare charges, shown in Figure VI.17, the amount of aluminum on the charges was 11.7 mg, 11.3 mg, 13.7 mg, and 14.2 mg for the tests in air, CO_2, N_2 and O_2, respectively. In air the AlO peaks quickest but then has a slow decline as time increases. Tests in CO_2 and O_2 show similar trends with a gradual increase and decrease in AlO signal and are both delayed. The end loaded test shows the most AlO signal of all the tests in CO_2 and is similar in shape to the O_2 test: a delayed peak and slow increase and decrease in intensity to/from the peak. The end loaded test matches the peak intensity with the 50% 3 μm and 20% 40 μm Al charges for the tests in O_2. The end loaded in air test has a gradual decline

in AlO signal with time, returning to approximately zero intensity at the end of the time recorded.

Shape of Spectra Features

Individual spectra from the 20% 40 μm tests in each environment are shown in Figure VI.18. The AlO emission bands are for the tests in N_2 and CO_2 are more distinguishable above the continuum background compared to the tests in air and O_2. The spectral features for the test in O_2 are least distinguishable above the continuum compared to the other environments.

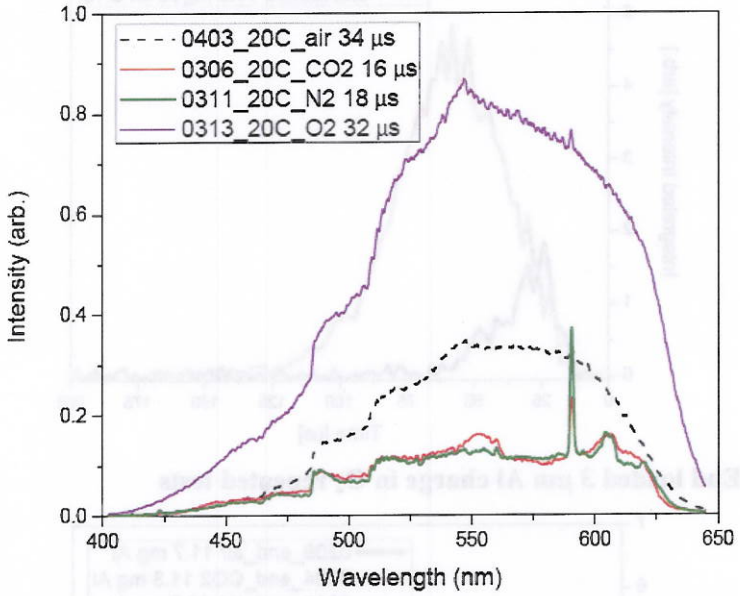

Figure VI.18. Spectra for 20C in each environment at time near peak AlO

Figures VI.19 through 22 show the spectra at different times during the test for the 20% 40 μm and 50% 3 μm charges fired in air and O_2 which exhibited tail AlO signals. The spectra shown are for the same AlO intensity, within 10%. Figure VI.19 and Figure VI.20 are both from tests with the 20% 40 μm charge in air and O_2, respectively, while Figure VI.21 and Figure VI.22 show spectra from tests with the 50% 3 μm charges in air and O_2, respectively. For both charges, the AlO features are more distinguishable in air than in O_2. At the same AlO intensity, the spectrum features appear to be the same with respect to the continuum, even at comparing the peak AlO intensity spectrum to a spectrum almost 100 μs later.

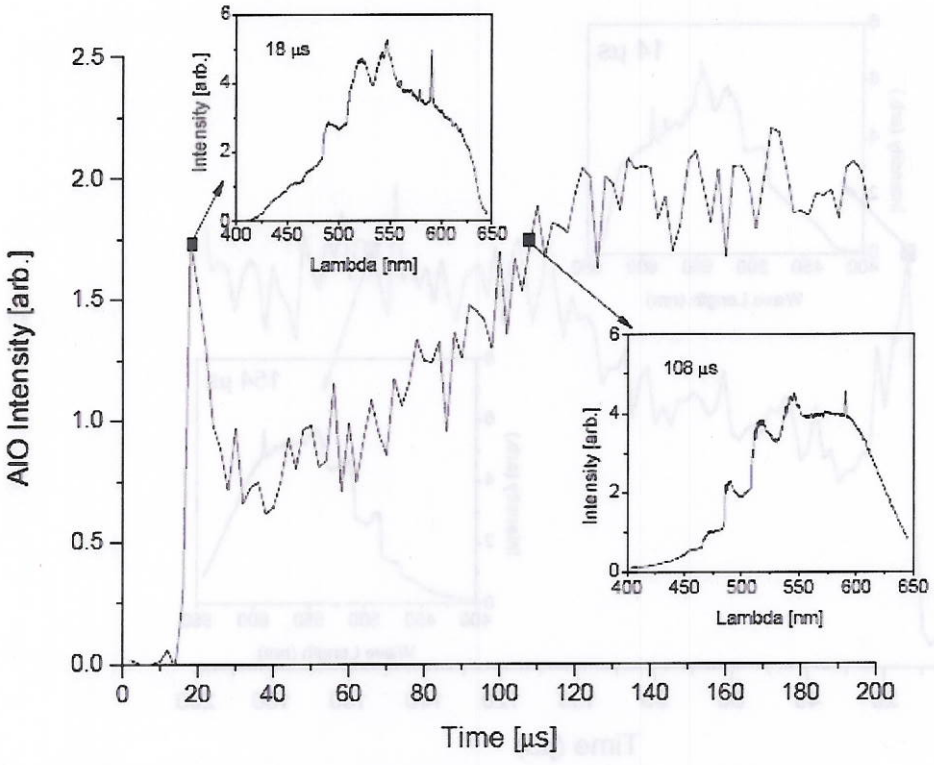

Figure VI.19. AlO intensity and spectra from a 20% 40 µm test in air

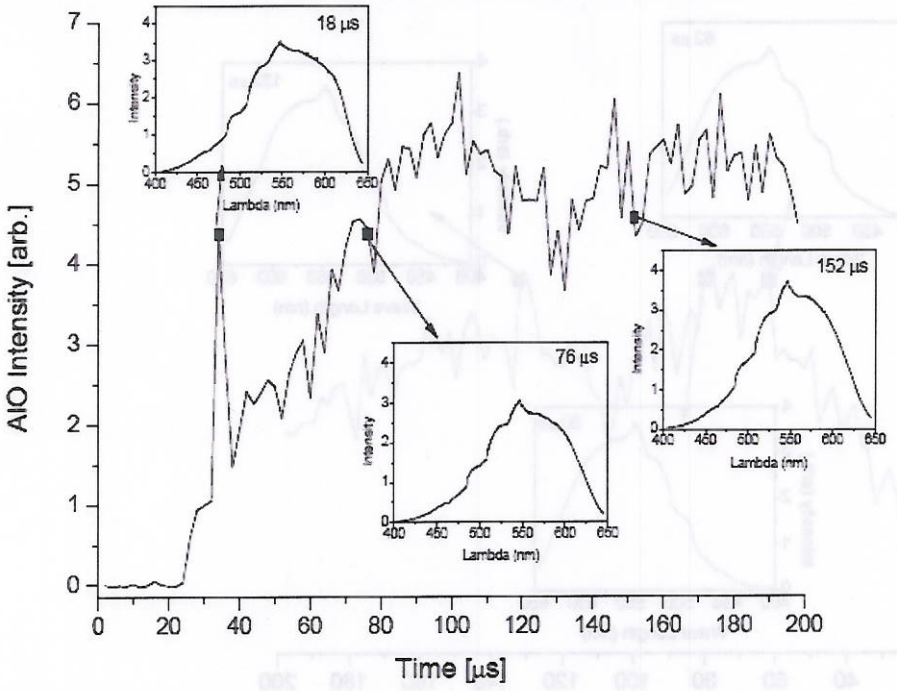

Figure VI.20. AlO intensity and spectra from a 20% 40 µm test in O_2

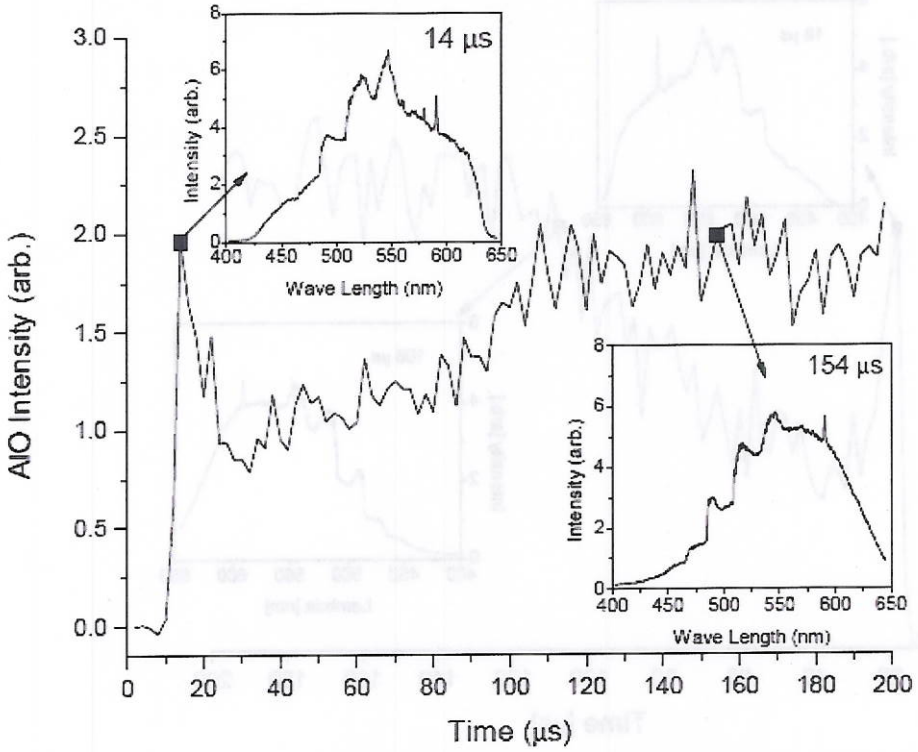

Figure VI.21. AlO intensity and spectra from a 50% 3 µm test in air

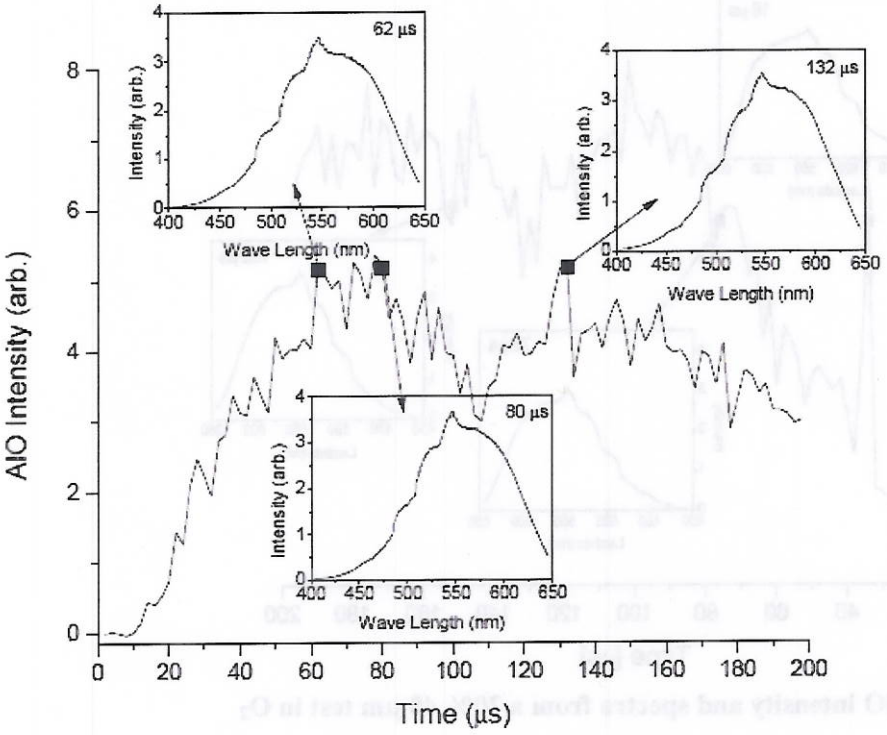

Figure VI.22. AlO intensity and spectra from a 50% 3 µm test in O_2

The AlO spectra features from tests in the ABT are shown in Figures VI.23 through 26. In the three of the Figures, the features for each charge are shown at different times. The

relationship of each spectra line is given with respect to the peak integrated AlO intensity. The spectra at the peak AlO intensity are shown in Figure VI. 26. At the peak, all charge tests spectra have in the AlO $\Delta v = +2, +1, 0, -1, -2$ bands. All charges show significant structural features in the $\Delta v = -1$ and -2 bands. The $\Delta v = 0$ band shows the more structure for the 50% and 20C charges than the 20A charge. For all the charges, the spectral features within the bands diminish at time increases and the integrated AlO intensity decreases. The features are significantly reduced by 10% of the peak AlO for both 20% Al charges, shown in Figure VI. 23 and 25. For the 50% charge the structure of the AlO features is diminished by 10% of the peak AlO for all bands expect the $\Delta v = -1$ band. The features of the $\Delta v = -1$ band are reduced with time but still visible throughout the AlO signal until about 5% of peak.

The AlO spectra with these tests have significantly more features than the tests in the tube chamber. This is probably a case of time resolution vs. spectra resolution.

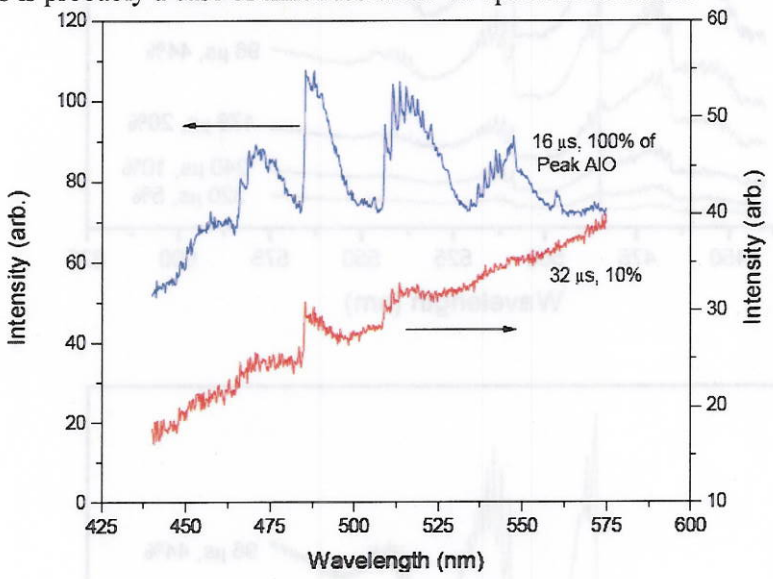

Figure VI.23. AlO features for 20% 3 µm Al charge

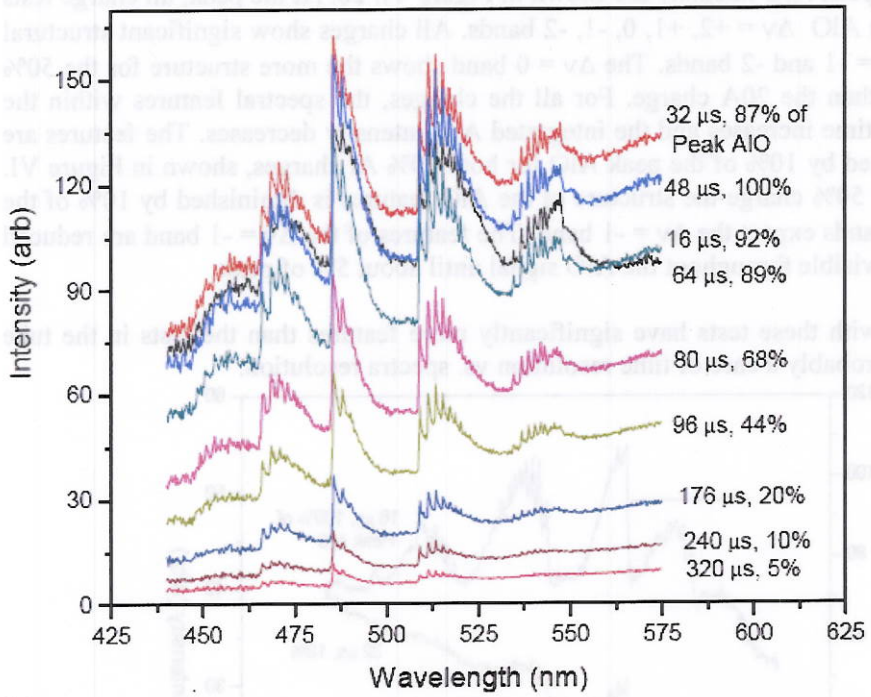

(a)

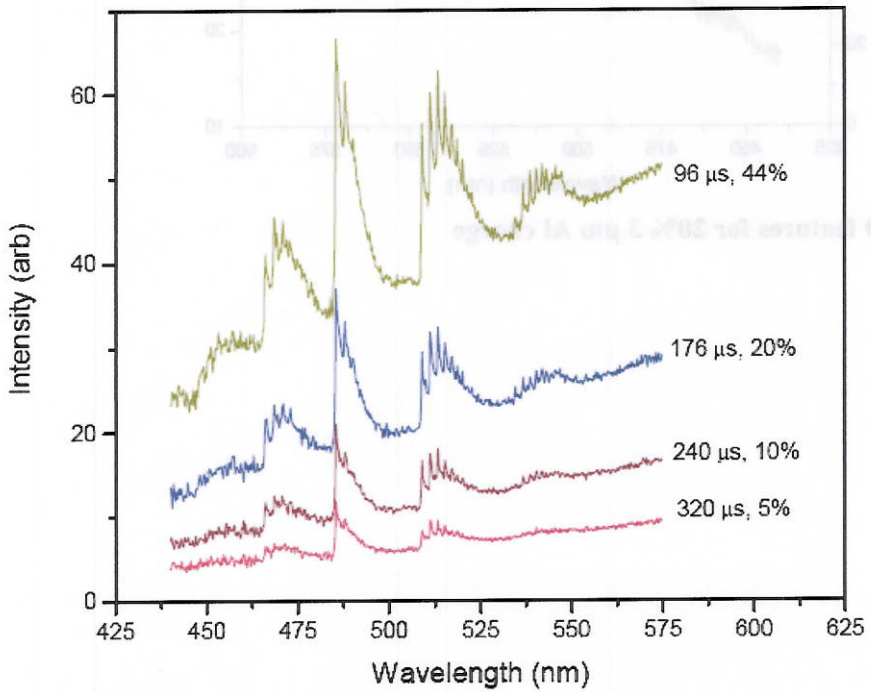

(b) Zoom in on later time AlO features

Figure VI.24. AlO features for 50% 3 µm Al charge

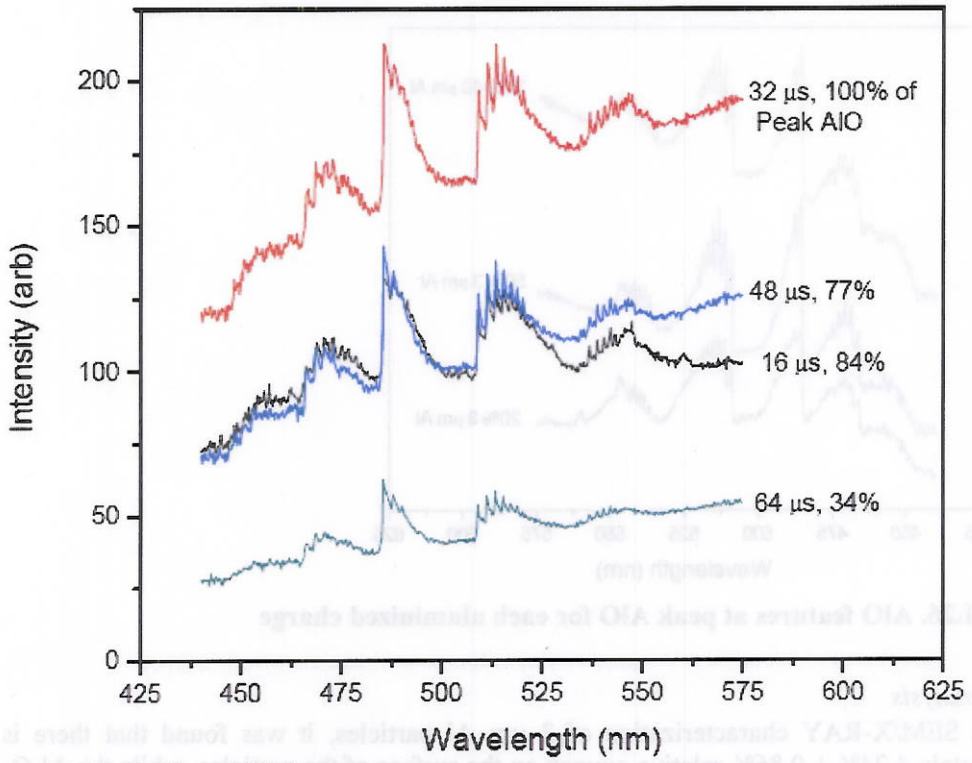

(a) Early time AlO features

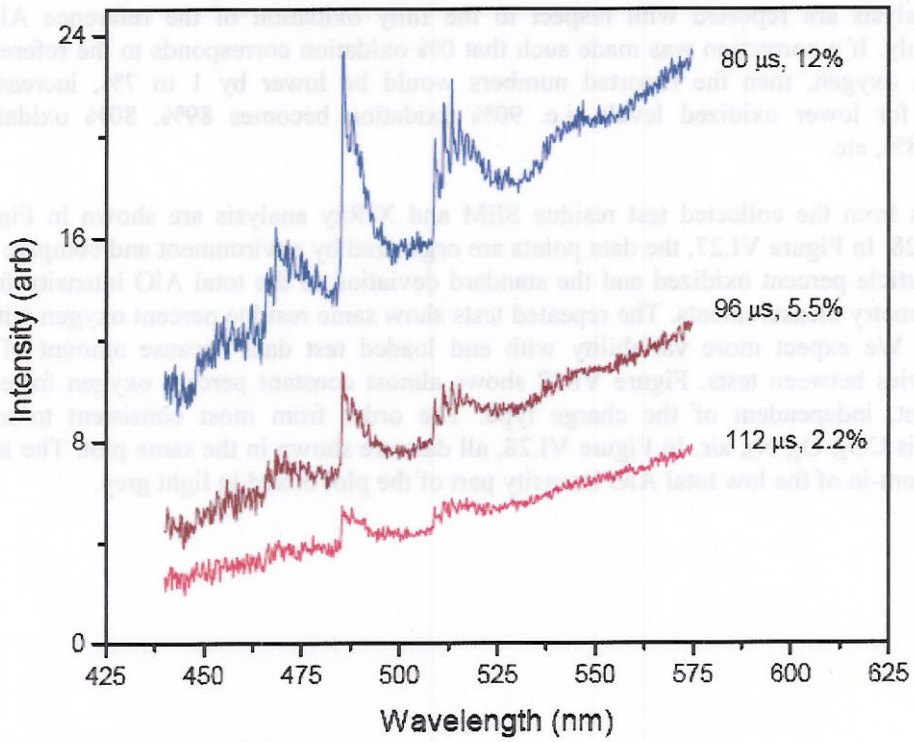

(b) Later time AlO features

Figure VI.25. AlO features for 20% 40 µm Al charge

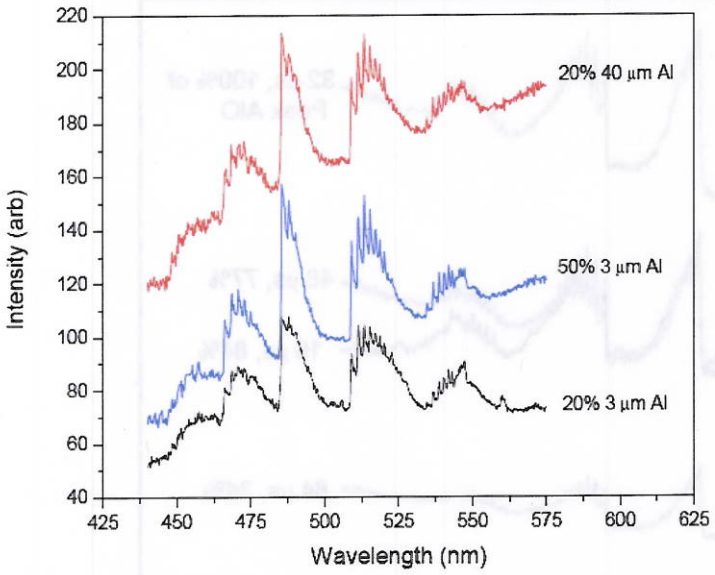

Figure VI.26. AlO features at peak AlO for each aluminized charge

Residue analysis

From the SEM/X-RAY characterization of 3 µm Al particles, it was found that there is approximately 4.24% ± 0.86% relative oxygen on the surface of the particles, while the Al_2O_3 particles had 61.37% ± 4.76% relative oxygen on the particle surface. The results from the residue analysis are reported with respect to the fully oxidation of the reference Al_2O_3 particles only. If a correction was made such that 0% oxidation corresponds to the reference Al particle oxygen, then the reported numbers would be lower by 1 to 7%, increasing correction for lower oxidized levels, i.e. 90% oxidation becomes 89%, 80% oxidation becomes 78%, etc.

The results from the collected test residue SEM and X-Ray analysis are shown in Figure VI.27 and 28. In Figure VI.27, the data points are organized by environment and compare the average particle percent oxidized and the standard deviation to the total AlO intensity from the spectrometry measurements. The repeated tests show same residue percent oxygen within error bars. We expect more variability with end loaded test data because amount of Al powder varies between tests. Figure VI.27 shows almost constant percent oxygen for each environment, independent of the charge type. The order from most consistent to most variability is CO_2, O_2, N_2, air. In Figure VI.28, all data are shown in the same plot. The inset plot is a zoom-in of the low total AlO intensity part of the plot boxed in light grey.

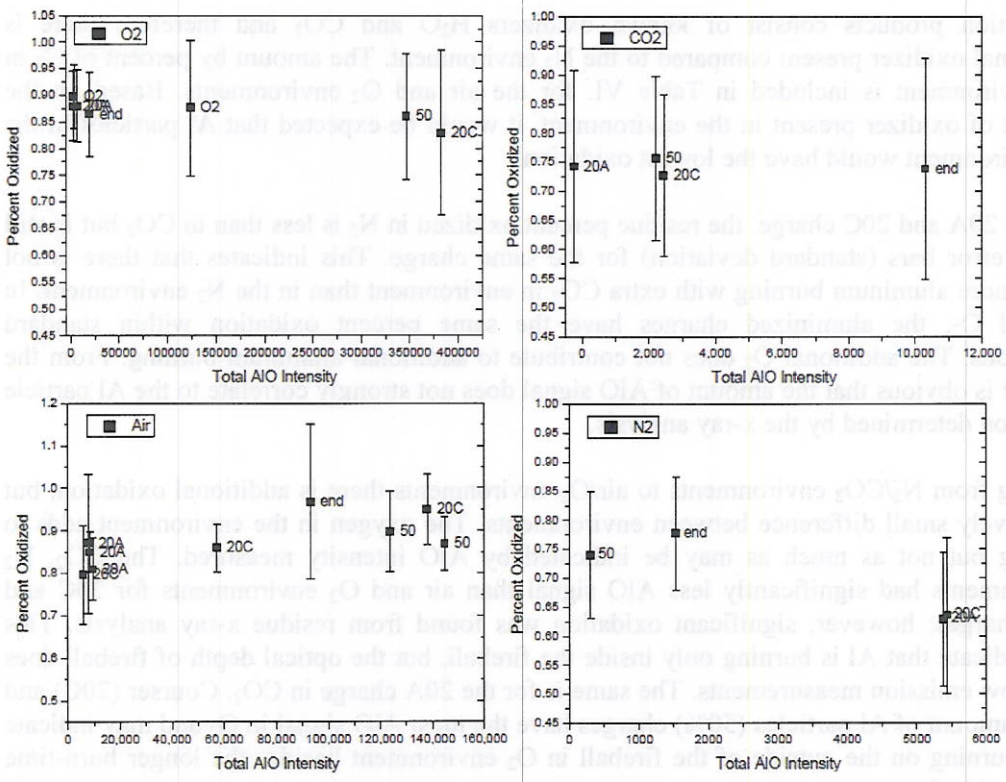

Figure VI.28. Comparison of percent oxidized to total AlO intensity by environment

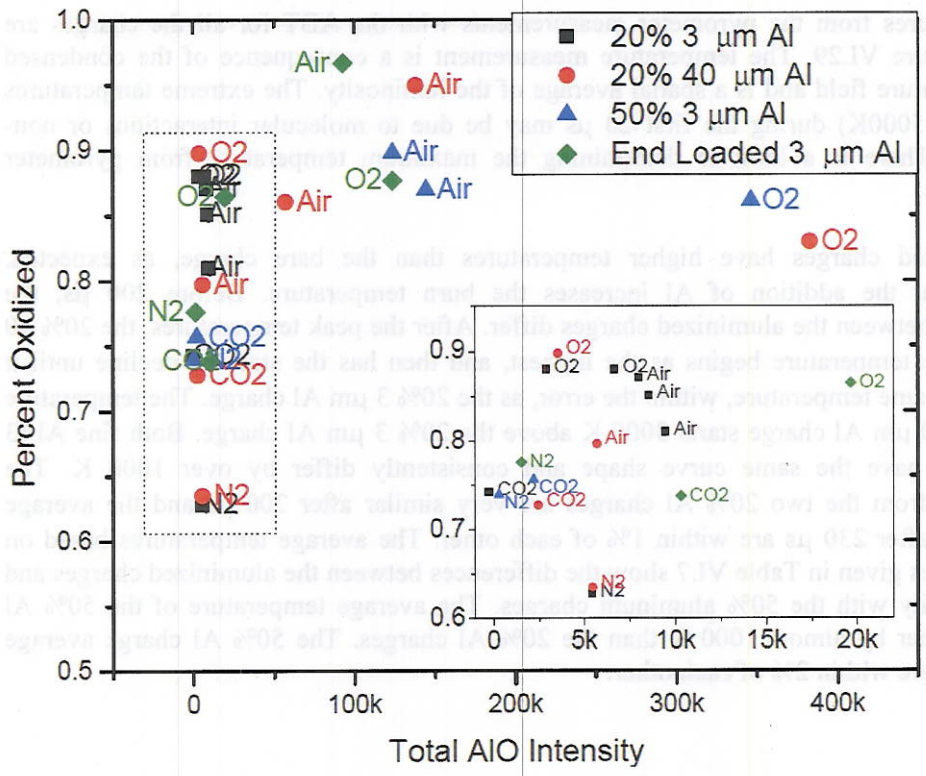

Figure VI.29. Residue percent oxidized for all tests. The inset plot zooms in on the low total AlO intensity data points boxed in light grey.

Detonation products consist of known oxidizers H_2O and CO_2 and therefore there is additional oxidizer present compared to the N_2 environment. The amount by percent of O_2 in the environment is included in Table VI. for the air and O_2 environments. Based on the amount of oxidizer present in the environment, it would be expected that Al particles in the N_2 environment would have the lowest oxidation.

For the 20A and 20C charge, the residue percent oxidized in N_2 is less than in CO_2 but is still within error bars (standard deviation) for the same charge. This indicates that there is not much more aluminum burning with extra CO_2 in environment than in the N_2 environment. In air and O_2, the aluminized charges have the same percent oxidation within standard deviations. The additional O_2 does not contribute to additional aluminum burning. From the plots, it is obvious that the amount of AlO signal does not strongly correlate to the Al particle oxidation determined by the x-ray analysis.

Moving from N_2/CO_2 environments to air/O_2 environments there is additional oxidation, but a relatively small difference between environments. The oxygen in the environment adds to burning but not as much as may be indicated by AlO intensity measured. The CO_2, N_2 environments had significantly less AlO signal than air and O_2 environments for 20C and 50% charges; however, significant oxidation was found from residue x-ray analysis. This may indicate that Al is burning only inside the fireball, but the optical depth of fireball does not allow emission measurements. The same is for the 20A charge in CO_2. Courser (20C) and larger amount of Al particles (50%) charges have the most AlO signal in O_2 and may indicate more burning on the outside of the fireball in O_2 environment besides the longer burn-time discussed before.

Temperature

The temperatures from the pyrometer measurements with the ABT for all the charges are shown in Figure VI.29. The temperature measurement is a consequence of the condensed phase temperature field and is a spatial average of the luminosity. The extreme temperatures (greater than 5000K) during the first 20 μs may be due to molecular interactions or non-equilibrium. There is a limit to determining the maximum temperature from pyrometer measurements.

The aluminized charges have higher temperatures than the bare charge, as expected, indicating that the addition of Al increases the burn temperature. Before 200 μs, the temperatures between the aluminized charges differ. After the peak temperatures, the 20% 40 μm Al charge temperature begins as the highest, and then has the steepest decline until it becomes the same temperature, within the error, as the 20% 3 μm Al charge. The temperature of the 20% 40 μm Al charge starts 3000 K above the 20% 3 μm Al charge. Both fine Al (3 μm) charges have the same curve shape and consistently differ by over 1000 K. The temperatures from the two 20% Al charges are very similar after 200 μs and the average temperatures after 230 μs are within 1% of each other. The average temperatures based on the time frames given in Table VI.7 show the differences between the aluminized charges and the repeatability with the 50% aluminum charges. The average temperature of the 50% Al charge is higher by almost 1000 K than the 20% Al charges. The 50% Al charge average temperatures are within 2% of each other.

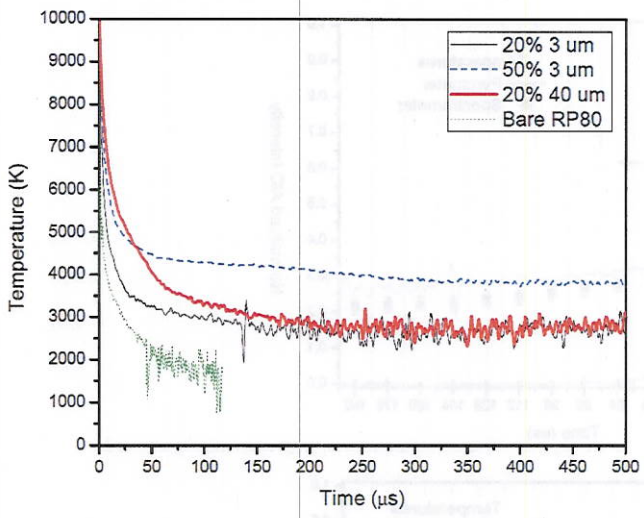

Figure VI.29. Comparison of temperatures from all charges

Table VI.7. Average Temperatures for ABT tests

Test	Al Composition	Average Temperature (K)	Error (K)	Time Range (µs)
0629 20A	20% 3 µm	2784	184	200-1800
0629 20C	20% 40 µm	2770	212	200-1800
0626 50	50% 3 µm	3613	193	400-1800
0630 50	50% 3 µm	3697	202	400-1800
0716 50	50% 3 µm	3608	285	400-1800

The temperatures determined from the pyrometer measurements and the spectrometer continuum measurements are shown in Figure VI.30 and compared to the normalized AlO intensity. For the spectrometer determined temperatures, temperatures could not be fit to the spectra at the peak AlO and just before the peak. The grid lines show the time resolution of the spectrometer data points. The temperatures determined from the spectrometer are always lower than the pyrometer temperatures at the same time but both techniques show the same trend. The peak temperature is approximately the same for all charges, around 4000 K, slightly lower for the 20A charge, based on the spectrometer measured temperatures. For the 20A charge, Figure VI.30a, the difference between the two techniques is less around the peak and approximately 500 K at the later times. For the 20C charge, Figure VI.31c, the difference between the two temperatures is approximately 800 K and less at earlier times around the peak AlO intensity. The biggest difference between the two temperature techniques is for the 50% Al charge, Figure VI.30b. After 100 µs, the difference is 1000 K.

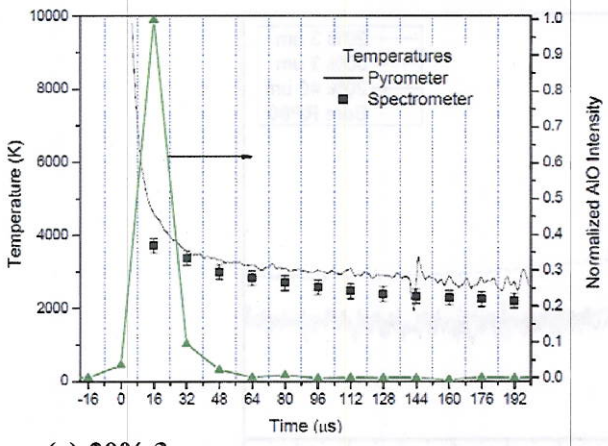

(a) 20% 3 μm

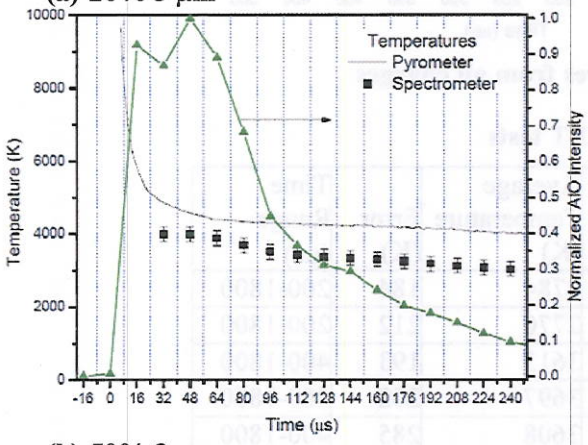

(b) 50% 3 μm

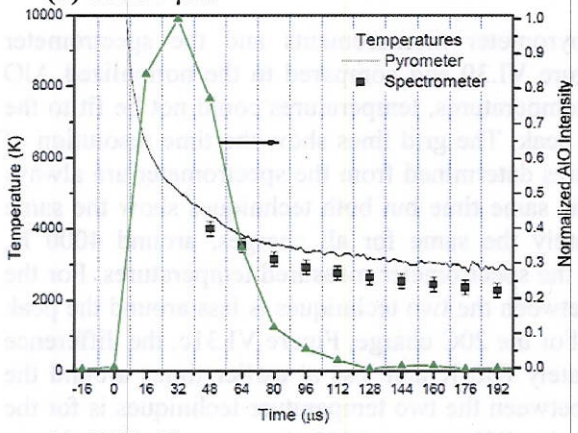

(c) 20% 40 μm

Figure VI.30. Condensed phase temperatures from two measurement techniques compared to normalized AlO emission for each aluminized charge

The condensed phase temperature fits from the chamber tests are presented in Figures VI.31 through 40. One trend with the temperatures is that the temperature is higher during the tests in which the tail AlO was seen than those without for the same charge. In Figure VI.31, the temperatures are compared in the different environments, by charge type. For the 20% 3 μm Al charge, Figure VI.31a, the temperatures are comparable between the different environments. The 50% 3 μm and 20% 40 μm Al charges have the same temperature trends.

The air and O_2 tests, which have the tail AlO, have higher temperatures, Figures VI.31b and 31c, and the higher temperatures are maintained longer. The CO_2 tests start at temperatures comparable to the air tests, but quickly decrease. The N_2 tests have lower temperatures, but the same decreasing trend as the CO_2 tests. The temperatures are lower for the CO_2 and N_2.

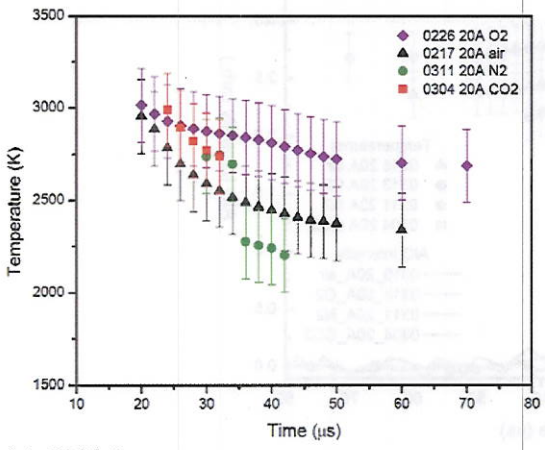

(a) 20% 3 μm

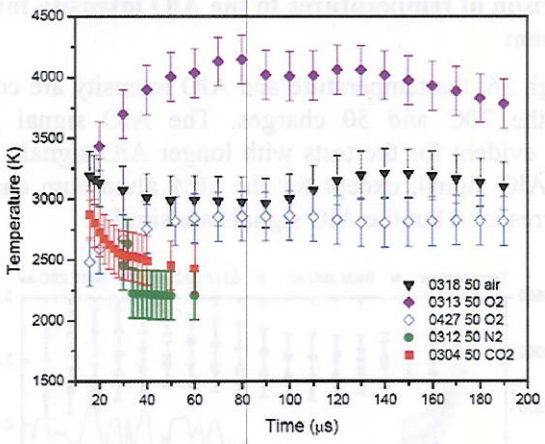

(b) 50% 3 μm

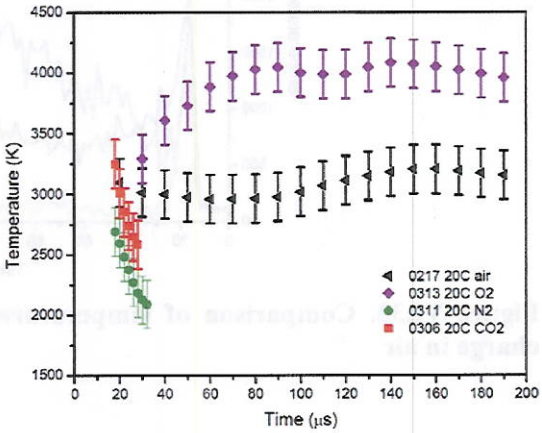

(c) 20% 40 μm

Figure VI.31. Condensed phase temperatures from tube chamber tests for each aluminized charge in each environment

The temperatures compared to the AlO intensity for the 20% 3 μm Al charge is shown in Figure VI.32. The CO_2 temperature is comparable to the O_2 and air temperatures, even without a significant AlO signal. The temperature in N_2 drops the quickest.

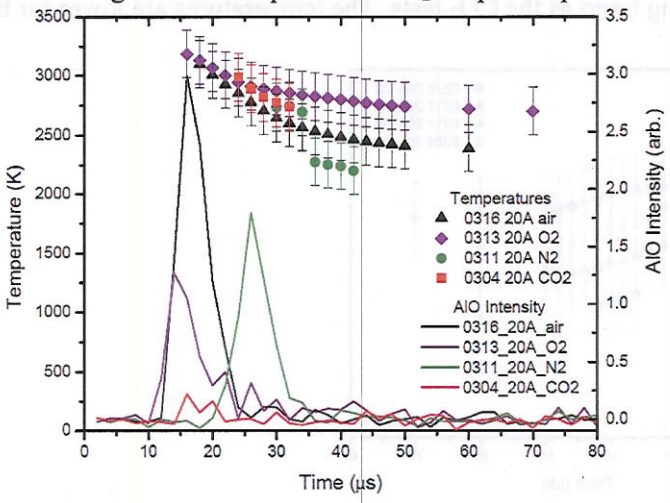

Figure VI.32. Comparison of temperatures to the AlO intensity for 20% 3 μm Al charge tests in each environment

In Figures VI.33 through 36, the temperature and AlO intensity are compared for the air and O_2 environments for the 20C and 50 charges. The AlO signal is proportional to the temperature, especially evident for the tests with longer AlO signal. The temperatures show the same trend as the AlO signal, except for the 50% aluminum charges in O_2, where the temperatures do not correspond but the AlO signals are similar.

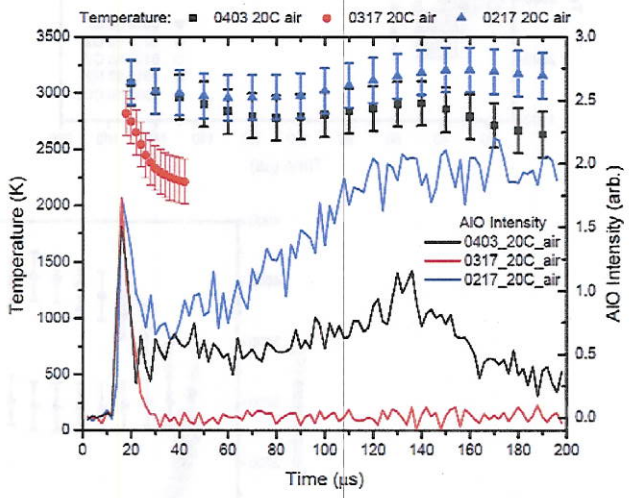

Figure VI.33. Comparison of temperatures to the AlO intensity for 20% 40 μm Al charge in air

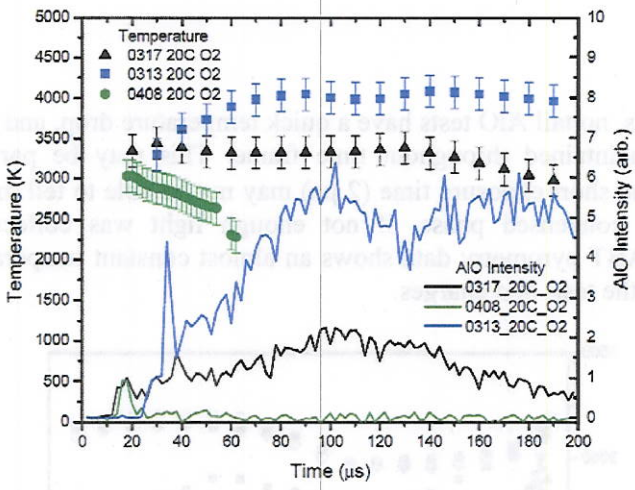

Figure VI.34. Comparison of temperatures to the AlO intensity for 20% 40 μm Al charge in O_2

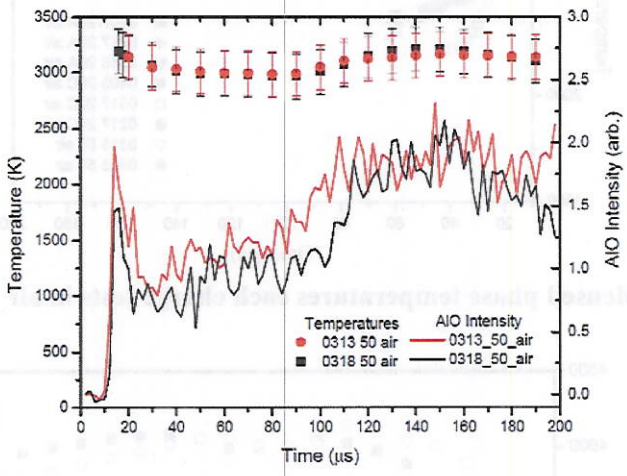

Figure VI.35. Comparison of temperatures to the AlO intensity for 50% 3 μm Al charge in air

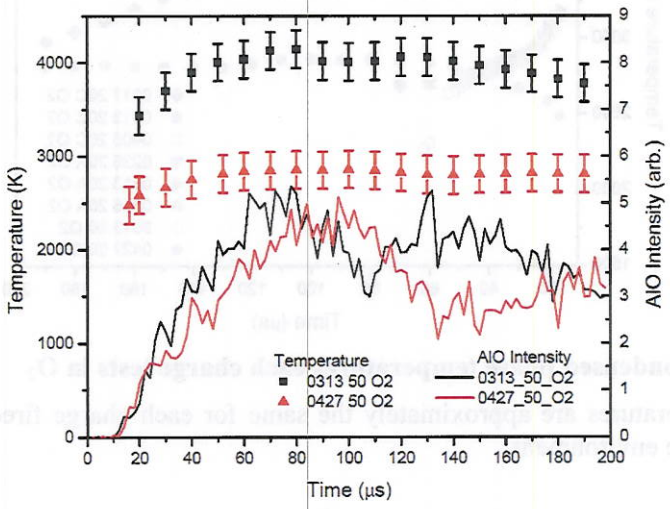

Figure VI.36. Comparison of temperatures to the AlO intensity for 50% 3 μm Al charge

in O_2

For the air and O_2 tests, no tail AlO tests have a quick temperature drop, and those with a tail, the temperature is maintained throughout time frame. This may be partial due to data collection settings. The short exposure time (2 μs) may not be able to tell the whole story of luminosity from the condensed phase, if not enough light was collected to enable a temperature fit. The ABT pyrometry data shows an almost constant temperature longer than the AlO signal for all the tests and charges.

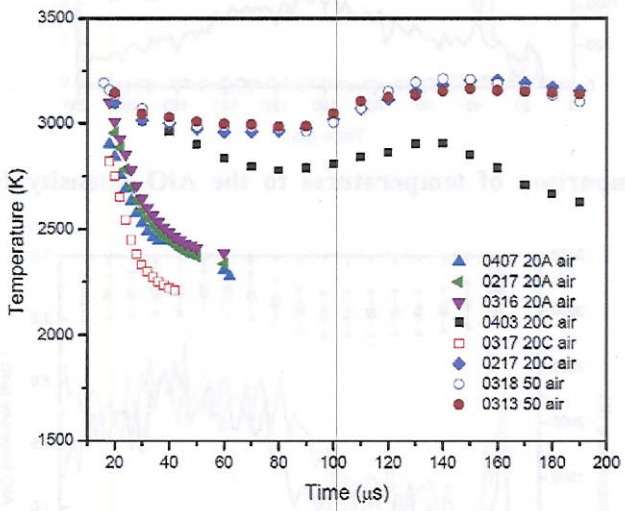

Figure VI.37. Condensed phase temperatures each charge tests in air

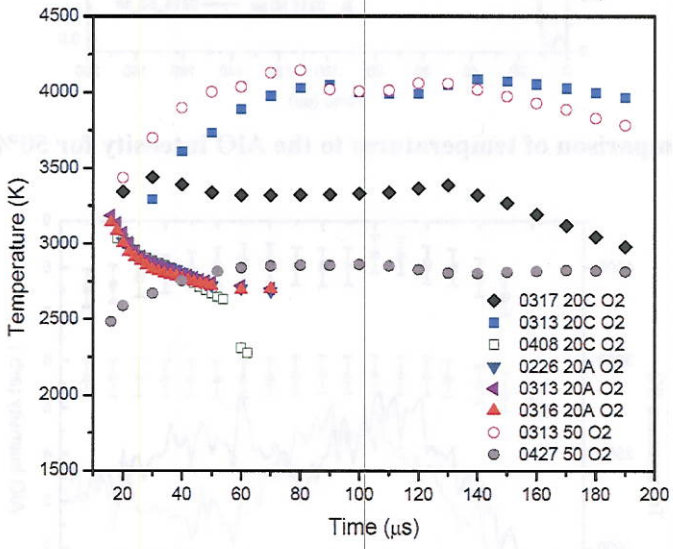

Figure VI. 38. Condensed phase temperatures each charge tests in O_2

The temperatures are approximately the same for each charge fired in CO_2 and N_2, with respect to the environment.

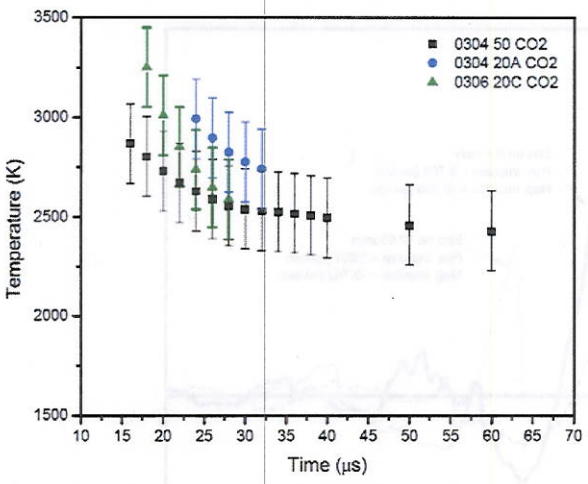

Figure VI.39. Condensed phase temperatures each charge tests in CO_2

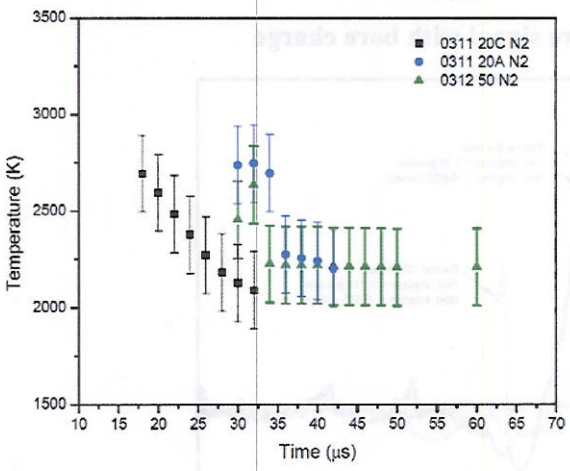

Figure VI.40. Condensed phase temperatures each charge tests in N_2

Pressure

The pressure traces as a function of time are shown in Figures VI.41 through 44. The pressure traces shown were smoothed using a FFT, but the impulses were calculated from the original data. The positive and negative impulses are listed in Table VI.8 and plotted in Figure VI.45.

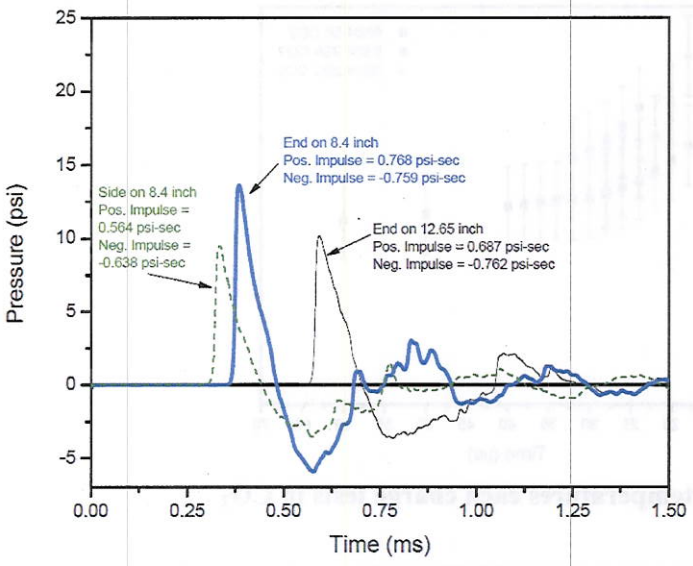

Figure VI.41. Pressure signal with bare charge

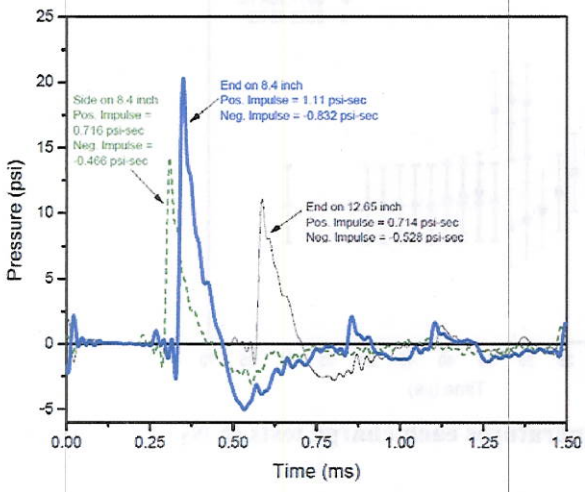

Figure VI.42. Pressure signal with 50% 3 μm Al charge

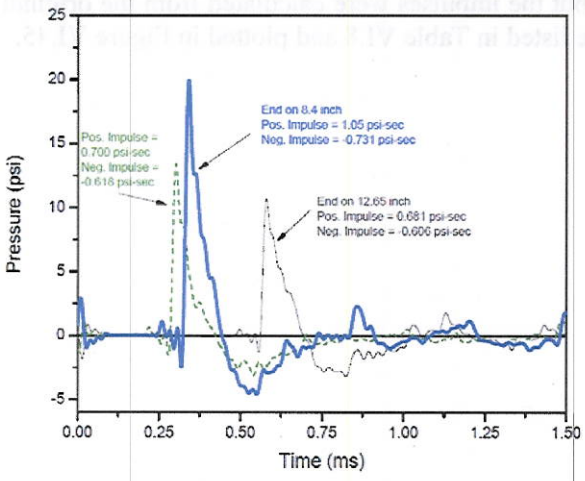

Figure VI.43. Pressure signal with 20% 40 μm Al charge

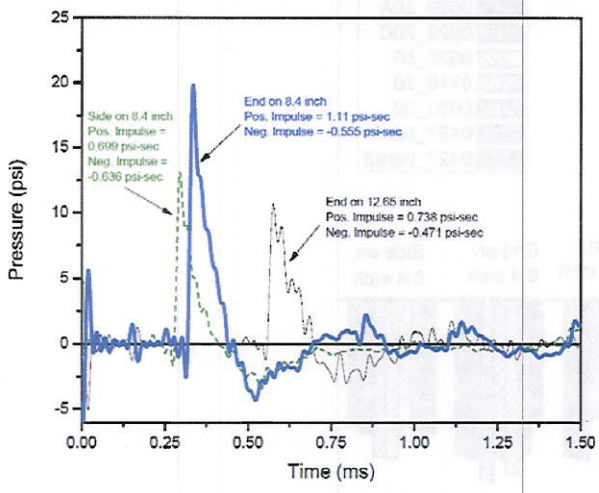

Figure VI.44. Pressure signal with 20% 3 μm Al charge

The aluminized charges are within 10% of each other for all the positive impulses, and therefore there is not much difference between the different Al/RDX combinations in terms of positive impulse strength. The aluminized charges have a higher positive impulse for the closer end-on pressure transducer than for the bare charge by 60% and similar positive impulses further away at the second end-on pressure transducer, within 15%. Therefore, closer to the charge, there is more difference between the impulses with the addition of aluminum to the charge. Similarly, the side-on positive impulses are higher by 40% for the aluminized charge than the bare charge. Additionally, the peak pressures are lower for the bare charge at the close pressure transducers and comparable further away.

There is more variability with the negative impulses between the charges. The bare charges had the highest negative impulse furthest away from the charges. The 50% Al charge has the highest negative impulse close end-on, while the 20% 3 μm Al charge had the least, and the bare charge is comparable to the 20% 40 μm Al charge. The side-on negative impulses were very similar to each other for all tests.

Table VI.8. Pressure impulses for all tests

Test	Al Composition	Positive Impulse (psi-s)			Negative Impulse (psi-s)		
		End on 12.65 inch	End on 8.4 inch	Side on 8.4 inch	End on 12.65 inch	End on 8.4 inch	Side on 8.4 inch
0629 20A	20% 3 μm	0.738	1.11	0.699	-0.471	-0.555	-0.636
0629 20C	20% 40 μm	0.681	1.05	0.700	-0.606	-0.731	-0.618
0626 50	50% 3 μm	0.714	1.11	0.716	-0.528	-0.832	-0.466
0630 50	50% 3 μm	0.783	1.23	0.788	-0.564	-0.869	-0.749
0716 50	50% 3 μm	0.753	1.08	0.742	-0.453	-0.756	-0.758
0427 bare1	-	0.687	0.768	0.564	-0.762	-0.759	-0.638
0427 bare2	-	0.661	0.733	0.518	-0.745	-0.740	-0.605

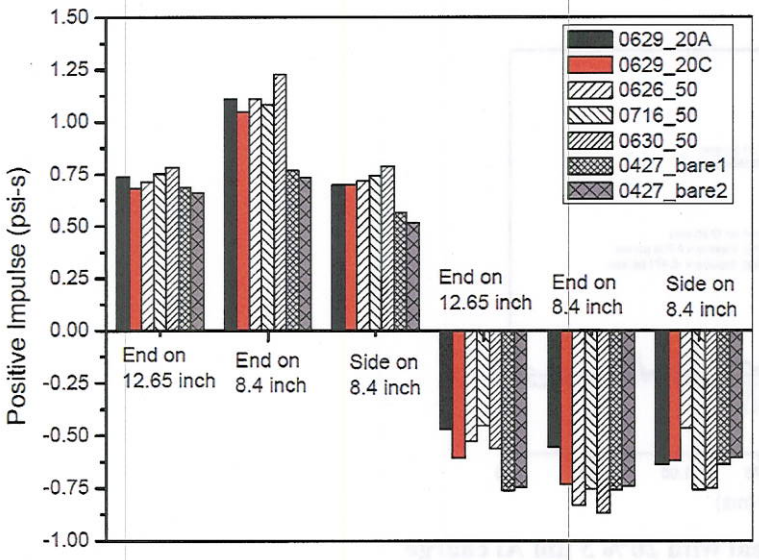

Figure VI.45. Comparison of pressure impulses from all charges

Shock Wave Velocity and Images

The images from the high speed camera of the shock wave and fireball are shown in Figures VI.46 through 49 for each of the fired charges. The time stamps in the Figures denote the time after detonation. There is a white spot visible in each image at the same location. This white spot is artificial and is a flash reflection and was ignored in all shock wave velocity determinations.

In most images, the shock wave is clearly visible. The top edge of the shock wave, shown in blue on the images, was used to determine the shock wave position and velocity. For the images in which the shock wave was not clearly distinguishable, the tip of the fireball was used as the shock wave location. This may not be an accurate assumption based on the first image for the 20% 40 μm Al charge, shown in Figure VI.48. At the edge of this image in the middle of the base of the fireball, there appears to be a shock wave which may indicate that the true location of the shock wave is not at the tip at that time. This first image point was ignored in the analysis of the 20% 40 μm Al charge test.

In the images for each aluminized charge the development of the fireball can be seen. During the time frame captured, there is no apparent clearing up of the fireball as was seen with the aluminized RP2 charge tests during the optical depth study. The times of the fireball images roughly correspond to the first 500 μs of the spectroscopy measurements. As shown and discussed later, the AlO intensity varies between the charges but is over by 500 μs for all the charges. Based on the high speed camera images and comparison to the RP2 images, it can be said that the fireball is optically thick and the AlO intensity comes mostly from the outer front of the fireball.

Based on the amount of saturation seen in the images and the number of frames the saturation occurs, the 50% 3 μm Al charge, Figure VI.49, is the brightest of the aluminized charges. All frames show some saturation; the 20% 40 μm Al charge, Figure VI.50, has seven frames of 'white out', making it the second brightest as the 20% 3 μm Al charge only has three frames with 'white out', Figure VI.47. The luminosity in the images and amount of saturatin occurring correlates to the AlO signal length from the spectrometer. The charges with longer

AlO signal, Figure VI.15, had more saturation in the high speed camera images.

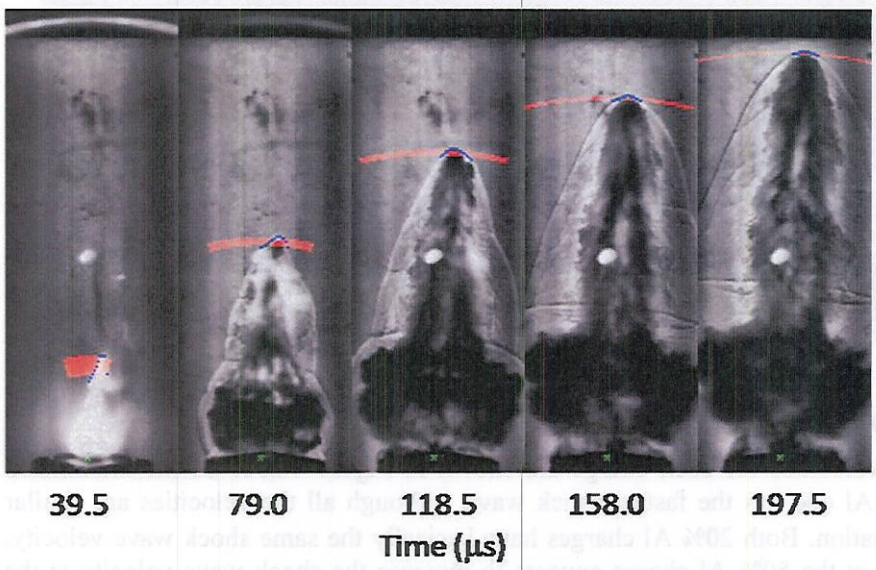

Figure VI.46. Shock wave images from bare charge

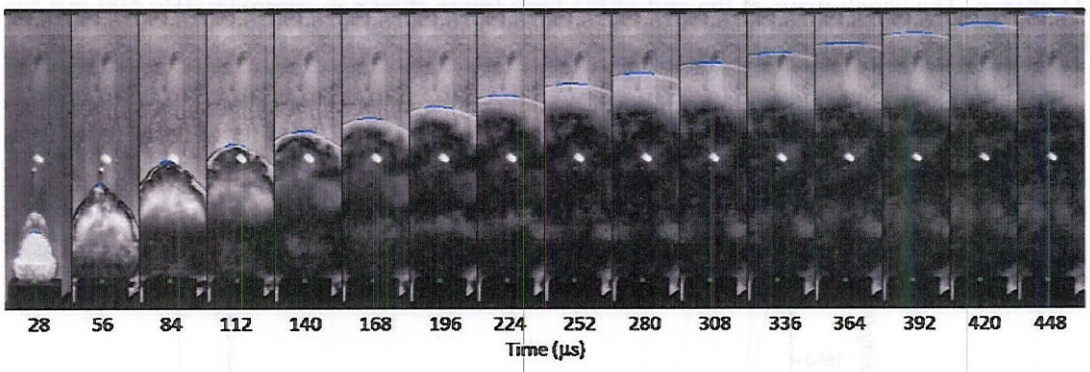

Figure VI.47. Shock wave images from bare 20% 3 µm Al charge

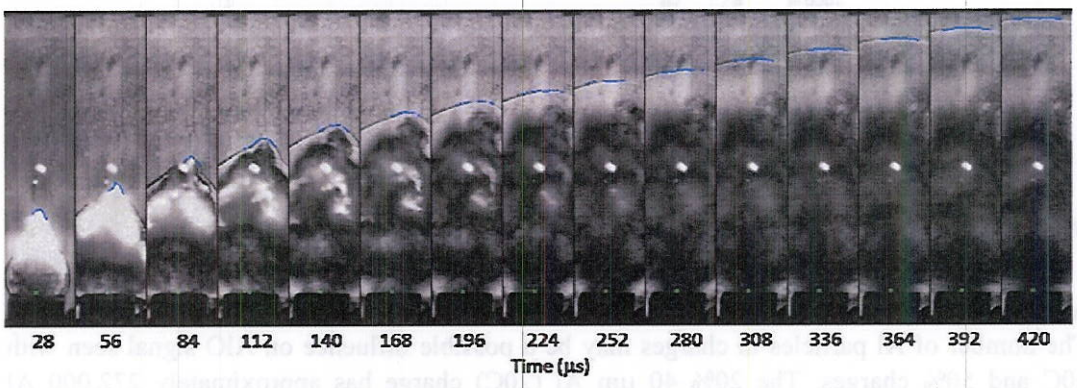

Figure VI.48. Shock wave images from bare 20% 40 µm Al charge

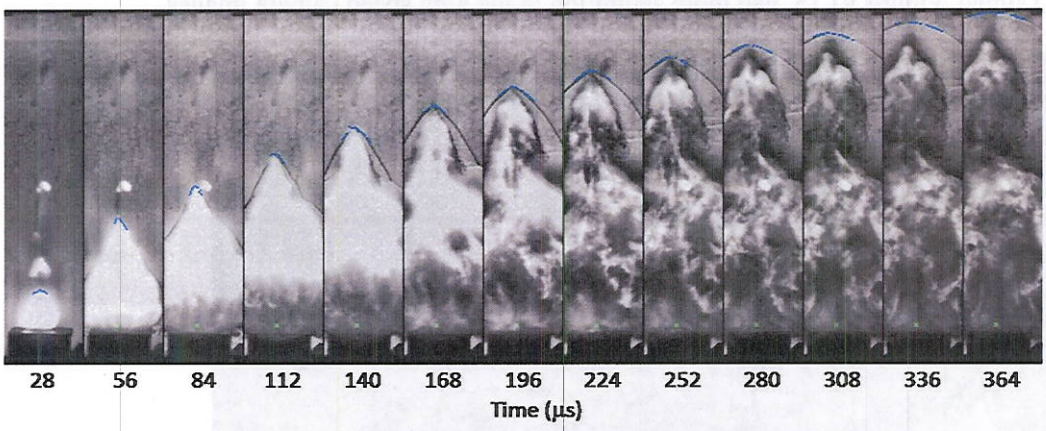

Figure VI.49. Shock wave images from bare 50% 3 μm Al charge

The shock wave velocities for each charge are shown in Figure VI.50. Of the aluminized charges, the 50% Al one has the fastest shock wave, although all the velocities are similar 200 μs after detonation. Both 20% Al charges have basically the same shock wave velocity. The additional Al in the 50% Al charge appears to increase the shock wave velocity at the beginning. The bare charge shock wave velocity is the fastest or most comparable to the 50% Al charge. The shock wave at the end of the time frame shown is approximately 500 m/s for the bare charge and approximately 420 m/s for the aluminized charges.

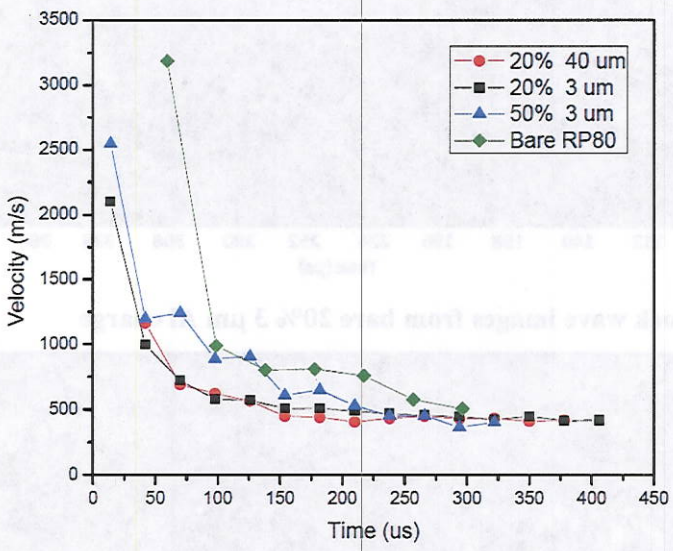

Figure VI.50. Comparison of the shock wave velocity from all charges

Analysis and Discussion

The number of Al particles in charges may be a possible influence on AlO signal seen with 20C and 50% charges. The 20% 40 μm Al (20C) charge has approximately 272,000 Al particles, the 20% 3 μm Al (20A) charge contains approximately 646 million Al particles and the 50% 3 μm Al charge has approximately 1.61 billion Al particles. For the 20% aluminum charges, there is over 2000 times more Al particles with the small particles compared to the large particles. This relatively low number of aluminum particles may not be uniformly dispersed in the fireball and may influence the AlO signal.

Inside the tube chamber there was 0.301 mole air in chamber at 1 atm (abs) for the air tests or 0.313 mole O_2 in chamber at 4 kPa (gage) for the O_2 tests. To have complete combustion 0.00160 mole air or O_2 is needed for the 20% Al charges and 0.00238 mole air or O_2 is needed for the 50% Al charges. Based on this calculation, there is enough O_2 in the air/O_2 environments by a factor of 100 to support complete combustion.

Chemical equilibrium calculations were done for 20% and 50% aluminum RP80 charges, in each environment and no explicit environment using Gordon-McBride (GM) software. The assigned pressure, enthalpy problem was used. The pressure was set to 1 bar for the air and no environment cases and 1.05 bar for O_2, N_2, CO_2 environments to account for 4 kPa pressure in chamber tube during experiments. PETN, RDX were entered as reactants along with the amount of aluminum for the two cases. The number of moles of reactants was used based on the amount of PETN/RDX/Al in the RP80 and environment gas inside the chamber. The results of the equilibrium calculations are shown in Table VI.10.

Table VI.9. Results from Gordon-McBride equilibrium calculations of the aluminized RP80's

20% Al RP80				50% Al RP80			
Product	Mass Fraction	Product	Mass Fraction	Product	Mass Fraction	Product	Mass Fraction
AlO	0.79%	N_2	24.87%	Al	4.66%	CO_2	1.20%
AlOH	2.01%	O	2.04%	AlO	6.31%	H_2O	1.34%
CO	32.48%	OH	3.25%	AlOH	7.90%	N_2	18.21%
CO_2	5.21%	O_2	1.30%	Al_2O	9.67%	O	1.67%
H_2O	6.28%	Al_2O_3(L)	18.96%	Al_2O_2	2.24%	OH	1.46%
NO	0.97%			CO	28.15%	Al_2O_3(L)	14.83%

Both aluminized RP80's have unreacted Al in the vapor phase, more for 50% aluminum charge, in the results as well as a significant amount of liquid Al_2O_3. Products with significant amounts also include CO, and N_2. Even without an environment, the majority of the Al, by mass, is oxidized to Al_2O_3 or partially oxidized to Al_2O and Al_2O_3 in the vapor phase.

Based on the GM calculations, it appears there is enough oxidizer to support the amount of oxidation found from the Al particles detonated in the N_2 environment, 65% to 75% oxidation, compared to the nearly complete combustion, 80% to 95% oxidation, in the air and O_2 environment. There is also the possibility of additional oxidizer in the detonation zone from the thin layer of alumina on the surface of the Al particles, which was proposed by Schloeffel (2009) as a reason to why AlO was seen during Al burning in Ar. From the SEM/X-RAY characterization of 3 μm Al particles, it was found that there is approximately 4.24% ± 0.86% relative oxygen on the surface of the particles. This additional oxide was not taken into account in any calculation, nor was any SEM/X-Ray characterization of 40 μm particles or the RDX/Al charges completed.

Other studies have investigated the location of the Al oxide reactions. Gilev (2006) investigated 60/40 RDX/Al and HMX/Al combinations and found from SEM analysis that the Al oxide reaction is on the surface and the inner part does not react. Additionally, smaller Al particles had an increased fraction of reacted Al. The rate of the Al sub-oxides condensing to Al_2O_3 is faster than the kinetic step of Al_2O_3 dissociation; therefore the liquid phase Al_2O_3 produced in the flame zone diffuses to the particle surface and deposits on the particle surface

(Beckstead, 2005). The SEM/X-Ray analysis only looks at the surface of the particles and therefore could be over estimating the actual oxidation of the particle. If the liquid Al_2O_3 is indeed deposited on the surface of the particle and the inner part of the particle does not react, especially possible with the larger 40 μm particles, then it could be expected to see a relatively high percent oxygen found in the residue based on x-ray analysis. This may partially explain why high oxygen percents were seen with the x-ray analysis of the Al particles.

The results from equilibrium calculations with environment showed that for both 20% and 50% Al charges in air and O_2, the products are only those that are expected for complete combustion, CO_2, H_2O, N_2, O_2, and Al_2O_3; thus implying complete combustion as previous calculations predicted, and other studies confirm for detonations in air (Trzcinski, 2008). In the N_2 and CO_2 environments, there are additional products for both amounts of aluminum in the charge: H_2, C and CO, which are the products of aluminum reacting with H_2O, CO and CO_2, respectively, to form Al_2O_3.Most notable in the products is that there is Al_2O_3, but no elemental Al. It appears that in equilibrium, all of the aluminum is reacted in the CO_2 environment and with the detonation products in the N_2 environment.

Table VI.10. Results from Gordon-McBride equilibrium calculations of the 20% Al RP80's, different environments

20% Al	Air		O_2		N_2		CO_2	
Temp(K)	574.97		557.43		475.23		496.26	
Products	Ar	0.00919	CO_2	0.00814	CH_4	0.00051	CH_4	0.00001
(mole	CO_2	0.00877	H_2O	0.00735	CO_2	0.00337	CO	0.00003
fraction)	H_2O	0.00763	N_2	0.00576	H_2	0.00027	CO_2	0.97348
	N_2	0.7725	O_2	0.97732	H_2O	0.00513	H_2	0.00005
	O_2	0.20041	Al_2O_3(a)	0.00143	N_2	0.98623	H_2O	0.00991
	Al_2O_3(a)	0.00149			$AL2O_3$(a)	0.00125	N_2	0.00782
					C(gr)	0.00324	Al_2O_3(a)	0.00194
							C(gr)	0.00676

Table VI.11. Results from Gordon-McBride equilibrium calculations of the 50% Al RP80's, different environments

50% Al	Air		O_2		N_2		CO_2	
Temp(K)	708.68		680.25		562.09		585.18	
Products	Ar	0.00924	CO_2	0.00661	CH_4	0.00071	CH_4	0.00001
(mole	CO_2	0.00718	H_2O	0.00581	CO	0.00001	CO	0.00081
fraction)	H_2O	0.00604	N_2	0.00422	CO_2	0.0007	CO_2	0.97111
	N_2	0.77489	O_2	0.97976	H_2	0.00152	H_2	0.00022
	O_2	0.19891	Al_2O_3(a)	0.00359	H_2O	0.00212	H_2O	0.00764
	Al_2O_3(a)	0.00373			NH_3	0.00001	N_2	0.00571
					N_2	0.98745	Al_2O_3(a)	0.00487
					Al_2O_3(a)	0.00313	C(gr)	0.00963
					C(gr)	0.00435		

Conclusions

This parametric study has yielded substantial information on the oxidation of aluminum in aluminized explosives. The data processing and analysis are still in process, and so it is not

possible to provide detailed conclusions at this point. However, some points can clearly be made:

1) Many of the larger scale results of Carney et al. have been replicated. AlO signals are indeed lower in CO_2 and N_2 environments, though we find AlO present, not completely absent as in the Indian Head tests. The amount of AlO emission is greatly reduced.

2) Evidence of afterburn from AlO spectroscopy is only seen under heavy loadings, large particle sizes, or end-loading. In the first two cases, it is also only seen in air and O_2 environments. The absence of AlO afterburn signal in the 20% loading cases in all ambients does suggest that rapid oxidation of the fine particles in the detonation products may be occurring on time scales much shorter than expected for particles that are not activated by the detonation wave (eg. in shock tube experiments).

3) EDS results suggest samples in all ambients have significant oxidation, but the issue of incomplete (i.e. surface) oxidation and its effect on the EDS signal are uncertain. It does appear likely that EDS overestimates oxidiation in partially oxidized particles based on the nature of the measurement.

4) The interpretation of AlO emission measurements remains uncertain since the optical depth of the cloud may be having significant effect. Since the fireballs are likely optically thick, the measurements are only probing the outside region of the fireball, which may not be representative of the entire fireball.

5) Blast pressure measurements do show the enhanced blast effect for aluminized charges at this small scale (200 mg), which is promising for future tests. For identically sized charges, aluminum addition generated blast enhancements at the 40% level with good repeatability. Far-field (~30 charge diameters) blast is significantly enhanced by all levels of Al addition. 50% addition provided improvement over 20% addition. Interestingly, 20% addition produced indistinguishable blast results for 40 um and 3 um particles, suggesting that rapid oxidation of even large particles is taking place in these charges. This effect is surprising and warrants further testing, especially since it is based upon a single test for each particle size.

6) Temperature measurements do show significant variation among cases, but it is unclear how to interpret these data since composition of products changes, and thus emissivity variation with wavelength will change. Such effects can lead to differences of 500 K or more, and thus the variations observed here fall within the uncertainty of the measurement. Discrepancies in the temperature obtained by using a contiuum fit to the spectrum (in the visible) versus the pyrometry (in the near infrared) suggest that this emissivity variation effect is significant, since these two measurements represent different spectral regions. If the variation of emissivity was truly grey, these measurements would be identical. Further work here is required to quantify these measurements.

7) Spatially and temporally integrated AlO emission intensity, taken from outside the fireball, does not necessarily correlate with total oxidation of the resultant particles. In many cases, the correlation is extremely poor.

References

M. Beckstead, Y. Liang and K. Pudduppakkam, Numerical Simulation of Single Aluminum Particle Combustion (Review), *Combustion, Explosion, and Shock Waves*, vol. 41, pp. 622-638, 11. 2005.

S. D. Gilev and V. F. Anisichkin, Interaction of aluminum with detonation products, *Combustion Explosion and Shock Waves*, vol. 42, pp. 107-115, 2006.

G. Schloeffel, A. Eichhorn, H. Albers, Ch. Mundt, F. Seiler, and F. Zhang, Experiments on the effect of a shock wave o nteh ignition behavior of aluminum particles in a shock tube, *Combustion and Flame,* 2009, [reviewed paper by NG/HK (received from HK)]

W. A. Trzcinski, S. Cudzilo, J. Paszula and J. Callaway, Study of the Effect of Additive Particle Size on Non-ideal Explosive Performance, *Propellants, Explosives, Pyrotechnics,* vol. 33, pp. 227-235, 2008.

VII. Optical Depth Measurements of Fireballs from Aluminized High Explosives

Abstract
Spatially and temporally resolved attenuation of 532 nm light by fireballs from aluminized high explosives is determined using photometric and imaging methods. For all measurements, the absorbance is found to peak during the early period of high reactivity of post-detonation gases. The characteristic attenuation length is less than 1 cm during the peak absorption period, and remains on the order of centimeters until a significant decrease in optical depth occurs about 160 μs after the detonation. These results suggest that, for gram-scale and larger aluminized charges, the optically thick assumption will most likely be valid for the period in which fireball luminosity is significant.

Introduction
Knowledge of the optical thickness of an explosive fireball is critical for interpretation of optical measurements such as pyrometry or emission spectroscopy. Of primary importance is the spatial region over which the measurement provides useful information. For optically thin fireballs, a path-averaged or volume averaged interpretation is valid. However, as opacity increases, measurements become more indicative of conditions at or near the surface of the expanding fireball. Furthermore, the effect on processing of pyrometry signals is also significant since some function for variation of emissivity with wavelength must be assumed in processing, and this function depends strongly on optical depth, with higher optical depths leading to greybody behavior, while thin clouds can have markedly non-grey distributions.

Though many works typically implicitly assume optically thin conditions, some past experiments indicate that a fireball from an explosive may indeed be optically thick at certain times during the lifetime of the fireball. Persson et. al. [1] indicated that the observations of light emitted from explosive disks made of 60%/40% RDX/TNT, may suggest that the reaction products are absorbent and the emission comes from a thin layer, 5 or 10 μm, near the front of the explosive disk. In another study of explosions of RDX, tritanol and H6 in air, the fireball was determined to be optically thick at infrared wavelengths (1800 to 6000 cm^{-1}) [2]. Carney and Wilkinson [3], observed Al and AlO features from streak spectroscopy that were significantly broadened by optical depth for explosions of PBXN-113, a fuel rich aluminized explosive, in air at atmospheric pressure. The authors also concluded that experiments in vacuum reduced the optical thickness of the fireball and allowed identification of detonation transients such as C_2. In a different study from the same group, Carney et. al.[4] concluded that fireball imaging under appropriate conditions may be used to determine the optical depth of an advancing fireball. Bouyer, Baudin and Le Gallic examined optical density of nitromethane detonation products, and found that the reaction products are optically thick in the spectral range of 600 to 850 nm and are optically thin within the range of 400 to 600 nm

[5]. Thus, while there is ample evidence that optical density is significant under some circumstances, there has been little work on precise quantification of optical depth of explosive fireballs for common energetic materials as a function of time, location, and wavelength.

In this work, we provide quantitative, spatially-resolved and temporally-resolved data on optical depth using several methods in fireballs from aluminized RDX-based high explosives (HEs) at 532 nm. Similar explosives are used in enhanced blast formulations to which optical diagnostics are commonly applied. The 532 nm wavelength is simple to generate in the lab, and it is also near (but not overlapping) the AlO features which are often studied in emission spectroscopy of aluminized explosives. Thus, we expect these results to be of use in evaluating optical strategies to monitor fireballs of aluminized HE.

Experimental

The charges used in these experiments were based on a modified RP-2 exploding bridgewire detonator from Teledyne RISI. An exploding bridgewire initiates a 32 mg PETN booster, which then ignites an 18 mg output pellet of 80% RDX/20%Al (by mass) produced by RISI. The charges were securely mounted to explode horizontally in the open air experiments. The blast produces a conical fireball that shows a brief (~30 μs) intense burst of light which includes strong molecular AlO emission, after which the intensity decays rapidly though luminosity is observed out to at least 200 μs. The fireball length and diameter are of the same order and grow from approximately 4 cm at 10 us after detonation to more than 10 cm at 100 us. The optical thickness of the fireball as a function of time and location is estimated by four different strategies described below.

Beam Splitter Tests

In these tests a 100 mW Nd:YAG CW laser beam was split into five separate beams using beam splitters. The five beams were aligned parallel to each other and perpendicular to the blast area in order to transverse the blast flame ball centerline as shown in Figure VII.1.

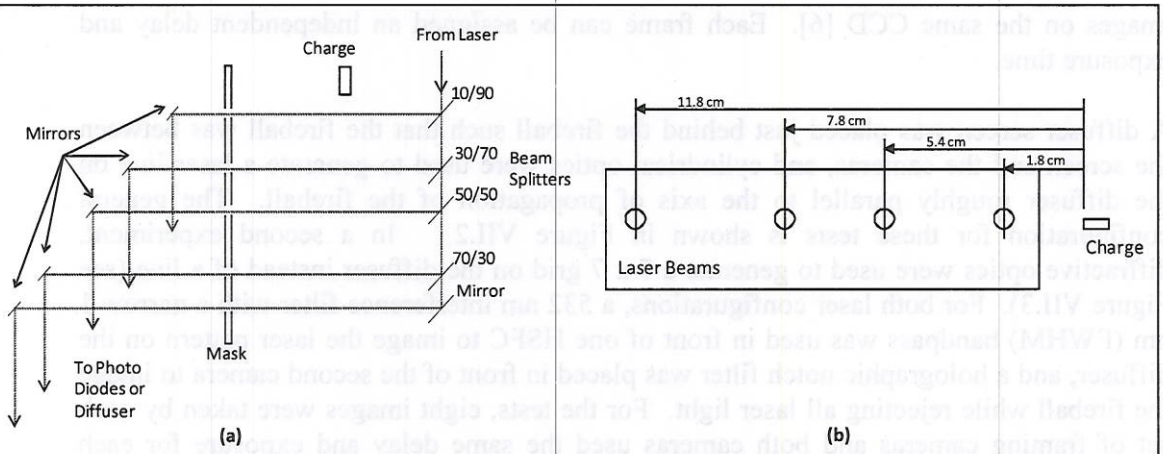

Figure VII.1 (a) Schematic of the set up of the photo diode measurements of the laser beams intensities and High Speed Camera images, (b) Side view of first four beams through the mask with the distance from the charge for each laser beam denoted

The laser beam intensity was measured using Thorlabs photo diodes with a time response of less than 14 ns. A mask with holes was positioned between the blast and the photo diode detectors to reduce the possibility of stray light from the blast being measured by the photo diode. The laser beams were set at 1.8, 5.4, 7.8, 11.8, and 13.9 cm from the front surface of charge to allow for spatial resolution of the flame ball optical thickness. The schematic in Figure VII.1 shows the location of the beams with respect to the charge location. The incident light intensity, I_o, was calculated by averaging the intensity signal approximately 50 μs before the charge was triggered at $t = 0$.

To address the possibility of beam steering and/or fireball luminosity affecting the results, a second test was performed with the photodiodes replaced by a diffuser screen onto which each beam impinged. The beams were visualized from behind the diffuser by a Phantom V7.0 CMOS high speed camera (HSC). The images were taken at 80,000 frames per second with a 7 μs exposure. A diagram of the setup for the HSC images is shown in Figure VII.1(b). The beam locations with the distances from the charge are denoted, and the box outline represents the edge of the images.

To compensate for any steering effects and background luminosity, the core of each laser beam was located in each image, and the background intensity around the core was averaged and subtracted from the core region. The initial intensity for the HSC images is the average beam intensity before the detonation for each beam. The ratio of transmitted to incident light, $I/I_{o,}$ is reported for all tests.

HSFC Tests

In order to simultaneously image the fireball and measure local optical depth, two Cooke Corporation High Speed Framing Cameras (HSFC's) were used in separate experiments. Each HSFC has four high resolution CCD image sensors (1280x1024 pixel resolution) that can record up to two images each with a minimum delay time of 500 ns between the

images on the same CCD [6]. Each frame can be assigned an independent delay and exposure time.

A diffuser screen was placed just behind the fireball such that the fireball was between the screen and the cameras, and cylindrical optics were used to generate a laser line on the diffuser roughly parallel to the axis of propagation of the fireball. The general configuration for these tests is shown in Figure VII.2. In a second experiment, diffractive optics were used to generate a 7 x 7 grid on the diffuser instead of a line (see Figure VII.3). For both laser configurations, a 532 nm interference filter with a narrow 1 nm (FWHM) bandpass was used in front of one HSFC to image the laser pattern on the diffuser, and a holographic notch filter was placed in front of the second camera to image the fireball while rejecting all laser light. For the tests, eight images were taken by each set of framing cameras and both cameras used the same delay and exposure for each image. The delay times after the charge was triggered are listed in Table VI.1 along with the exposure time for each image.

For both laser line and laser grid imaging, the reference intensities were determined using frames taken immediately prior to the test at identical settings. Background taken in the vicinity of the laser pattern was subtracted from each image separately. In this fashion, a local value of I/I_o could be determined and compared to the location in the fireball as shown by the second (notch-filtered) camera.

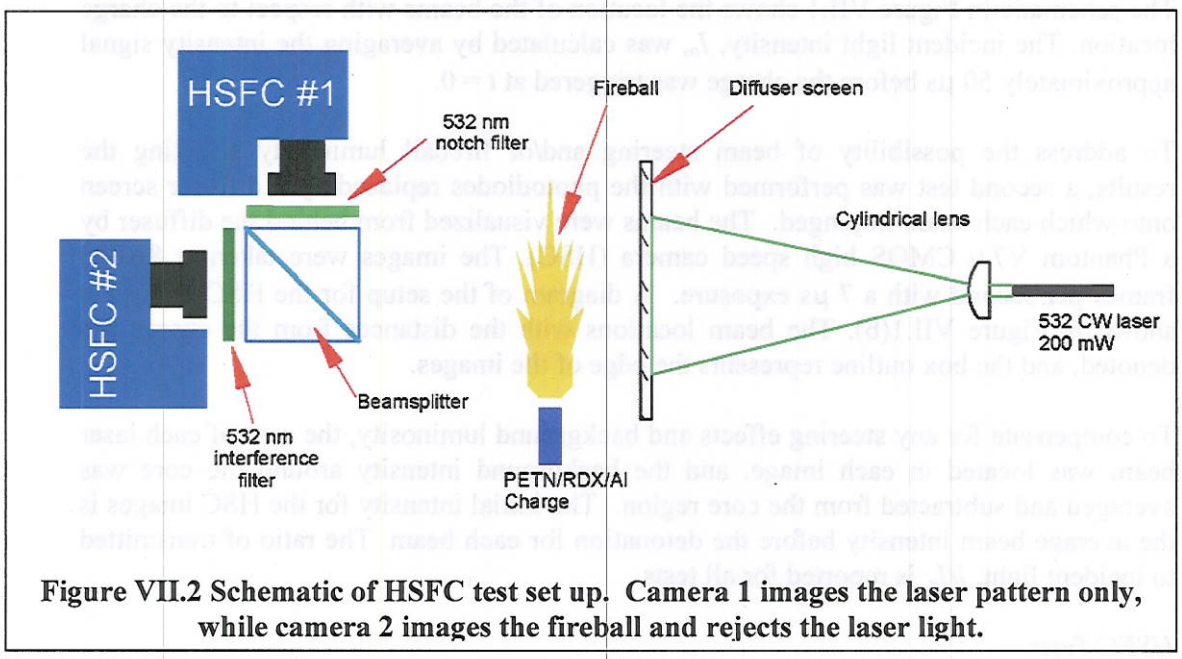

Figure VII.2 Schematic of HSFC test set up. Camera 1 images the laser pattern only, while camera 2 images the fireball and rejects the laser light.

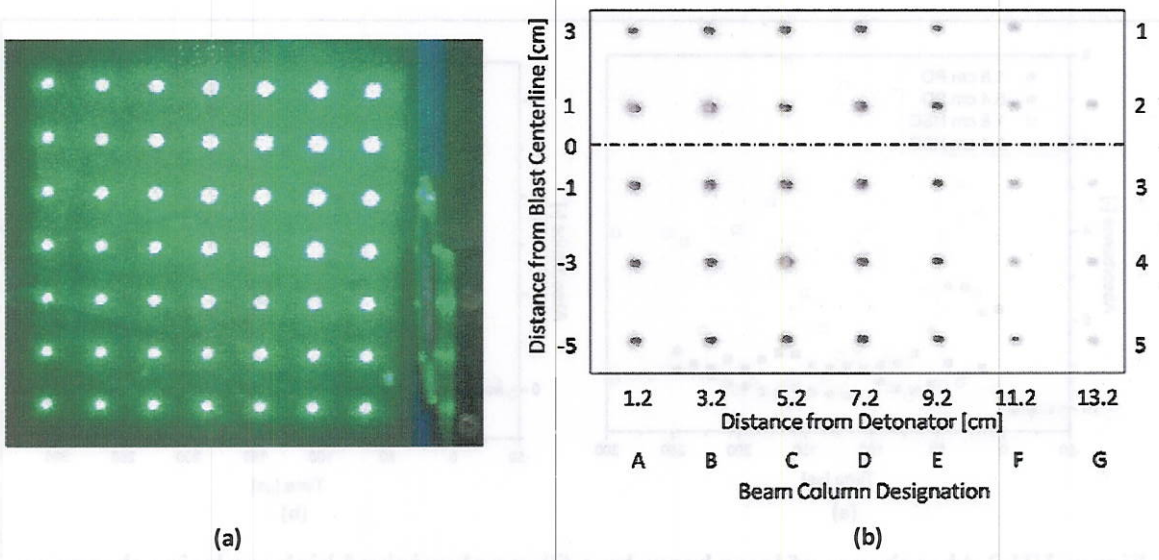

Figure VII.3 (a) 7x7 dot matrix, (b) Beam locations with respect to the charge location and individual beam designation

From the images of the fireball, a three dimensional estimate of the fireball geometry was made assuming axisymmetry. From this reconstruction, a local path length for each location at which the laser pattern is seen can be estimated. In this fashion, we can plot absorbance ($\ln I_o/I$) versus path length and thereby estimate the characteristic attenuation length of the fireball as a function of time and spatial location. For this analysis only beams or portions of the laser line inside the luminous fireball were analyzed.

Results and Discussion

Absorbance data for the multiple laser beams are shown in Figure VII.4 for four axial locations from 1.8 cm to 11.8 cm. At each axial location, absorbance rapidly rises from zero to ~3 (5% transmission) as the fireball reaches each laser beam. At all locations except the one closest to the charge, the absorbance peak lasts 30 - 40 μs before beginning an equally rapid decay. However, the decay is not to zero but rather somewhere in the 0.5 to 1 range (37-61% transmission) out to 200 μs. In general, there is good agreement between the two measurement methods, suggesting good test repeatability, as well as minimal effects of beam steering and fireball luminosity on the measurements. The one case in which there is a noticeable difference is in the HSC data at 1.8 cm, which shows a second late time attenuation peak not seen in the photodiode experiment. This late resurgence of attenuation is only observed very near the charge surface and is not observed in all shots. As such, we suspect is a result of shot to shot variation in the complex recirculating flow near the holder, perhaps drawing debris from the casing rupture into the first beam path.

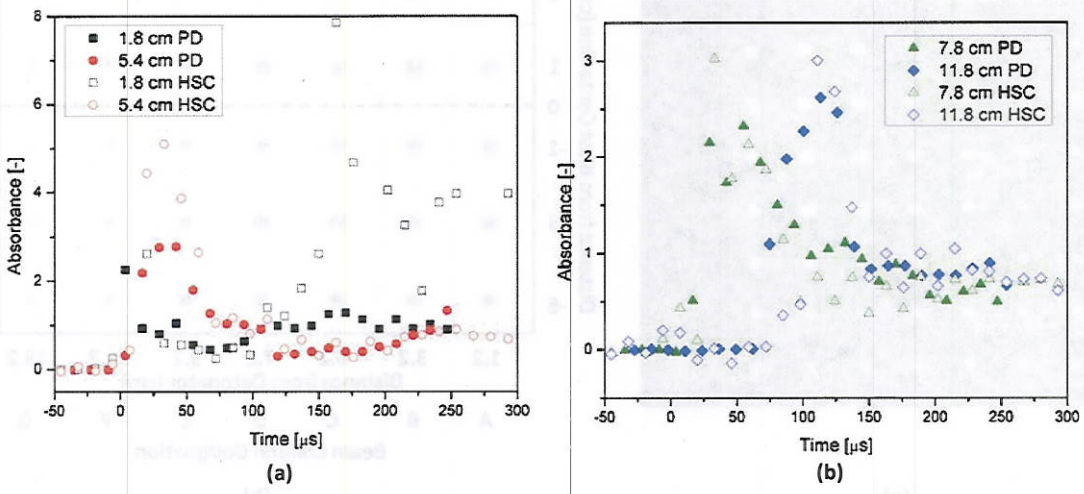

Figure VII.2 Absorbance of laser beam by a 50 mg aluminized high explosive charge as measured by the photo diodes (PD) and high speed camera (HSC) images for the beams located at (a) 1.8 cm and 5.4 cm (b) 7.8 cm and 11.8 cm from the charge

The beam data provide several useful insights into the attenuation of 532 nm light by aluminized fireballs. For fireballs with length scales on the order of a few centimeters, peak attenuation is 95% or greater. There is a period and location of maximum opacity which appears to correspond to the front of the fireball. For charges of this size, the duration of maximum opacity is less than 50 μs. However, these early times represent a critical period in the fireball as it is when key combustion intermediates Al, AlO, AlN, and CN have been observed[4, 7], indicating a rapidly reacting gas mixture. Thus, at the time in which emission spectroscopy measurements show the most prominent signals is when fireball opacity is maximum. After this initial burst of radical emission, the gas shows no molecular signatures, only a strong continuum indicating persistent high temperatures, suggesting that the reactivity has decreased, with the gas perhaps reaching at least partial equilibrium. For this mixture of weakly reacting fireball gases, there remains significant attenuation out to 200 μs, but it is an order of magnitude less than the peak opacity.

The laser beam set experiments provide high signal to noise attenuation data at fixed locations as a function of time. Unfortunately, one cannot definitively establish where the fireball is with respect to these locations. For those measurements, we use the HSFC image sets, with the trade-off of having a lower SNR due to a lower absolute signal level.

Figure VII.5 shows the results of the HSFC images using a single laser line imaged through the fireball. The two sets of images are superimposed and the laser line data are processed to show a colored strip at the location of the laser line with colors corresponding to transmission. Figure VII.6 shows the data from the images in Figure VII.5 processed to yield the quantitative transmission along the laser line. The image at

10 us shows attenuation ahead of the luminous fireball and inside it. Ahead of the fireball, the attenuation is small but significant, probably due in part to distortion of the imaging in the region behind the blast wave and ahead of the fireball. Such distortion would have a stronger effect on these imaging measurements as opposed to the beam measurements described above. Right at the edge of the luminous fireball, there is a significant increase in attenuation that persists through the entire luminous region, with a recovery of transmittance only at the very back end of the fireball. The images taken at 15 and 40 μs show similar behavior with strong attenuation within the bright parts of the fireball, especially where the path length is longest. Between 60 and 120 μs, the fireball continues to expand and dim - note that exposures are 40 times longer than the 10 and 15 μs shots in order to maintain sufficient signal. Despite the reduction in luminosity, the attenuation remains strong through at least 120 μs. At 160 μs, the beginnings of recovery of transmission are starting to appear, consistent with the photodiode/HSC measurements.

Figure VII.7 shows a plot of the 7 x 7 laser grid at 40 μs in a separate shot. This approach gives some additional two-dimensional information not possible with the laser line approach. Similar phenomena are seen here, with the strongest attenuation in the fireball core (longest path lengths), weaker attenuation at the edges, and non-negligible attenuation in front of and behind the luminous fireball.

To quantify the attenuation as a function of path length and time, we use the laser line data and estimate the path length at each point in the luminous fireball zone, plotting absorbance versus path length. These data are shown in Figure VII.8. Though there is understandably significant scatter, the monotonic increase in absorbance with path length is obvious. Each set of data (i.e. each delay time) can be fit to a line passing through the origin according, assuming:

$$\ln(I_o / I) = -\ln(I / I_o) = -\ln(e^{-\kappa L}) = \kappa L$$

where κ is a characteristic length scale for attenuation. The fits are shown as the dashed lines in Figure VII.8. The attenuation lengths and associated uncertainties are given in Table 1. The attenuation lengths vary from a fraction of a cm at 10 us and remain at the few cm scale until around 160 μs, when the fireball begins to clear. Though the uncertainty in these measurements remains significant, the critical result is the order of the attenuation length and its dependence on time. For similar mixtures at similar temperatures and pressures, it is thus reasonable to expect attenuation lengths to be of centimeter scale as well.Since the charges in this study are significantly smaller than those used in practical applications, scaling of the results is important. As charge mass is increased, energy release increases, but detonation pressure and temperature will not vary significantly, and so the composition of fireball gases will not be expected to vary as well. The fireball from a larger charge takes longer to expand to its final radius, and it stays hot longer due to a lower surface to volume ratio. Thus, the time dependence of attenuation observed in this study is not expected to be valid for larger charges, though it is possible that it could be scaled with appropriate modeling. However, since the composition, pressure, and temperature of the fireball are expected to be similar, the attenuation lengths during the luminous period of the fireball should be of the same order for i) similar explosives - 20% Al in RDX, and ii) similar wavelengths - 532 nm. For our 18 mg charges, the attenuation length is already of the order of the fireball dimensions.

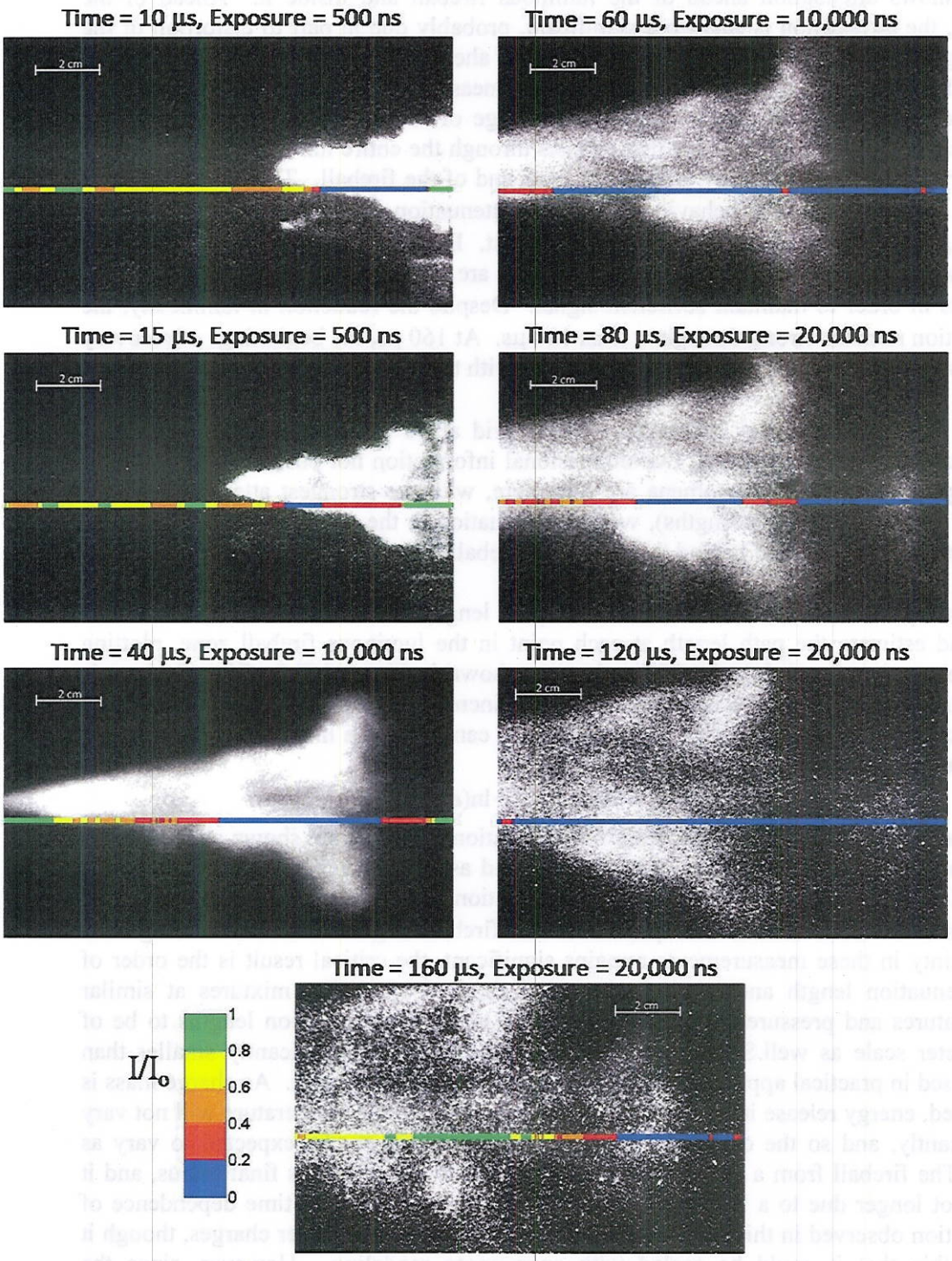

Figure VII.3 Transmission of laser line through fireball from a 50 mg aluminized charge at five different time intervals. The colored line represents the region in which the attenuation at 532 nm was measured,

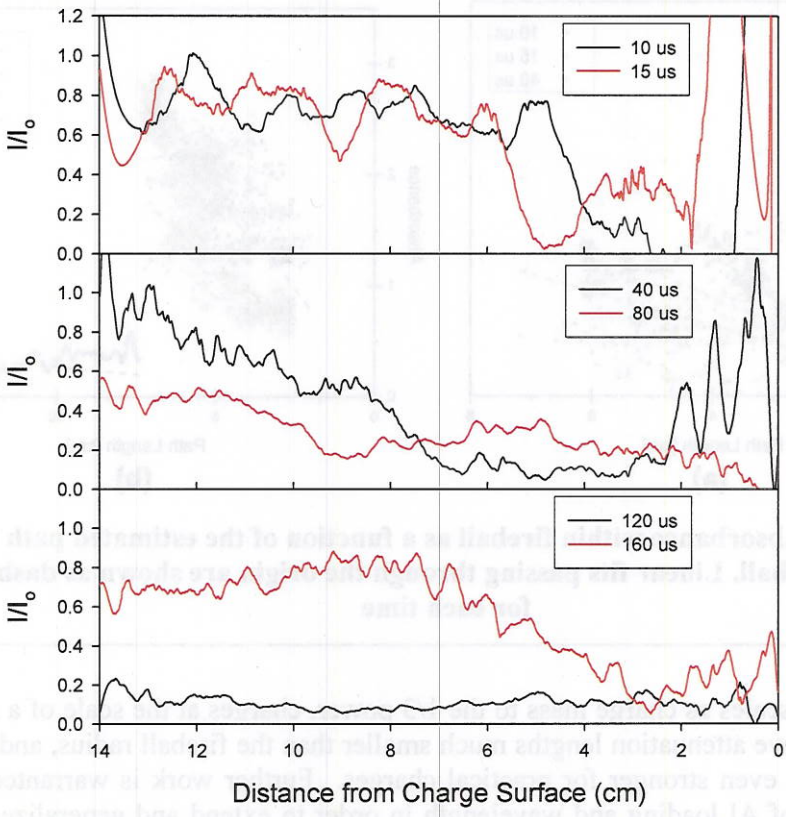

Figure VII.4 Transmission of the laser line for all delay times as a function of position from the initial charge surface. These data are taken from the images shown in Figure VII.5.

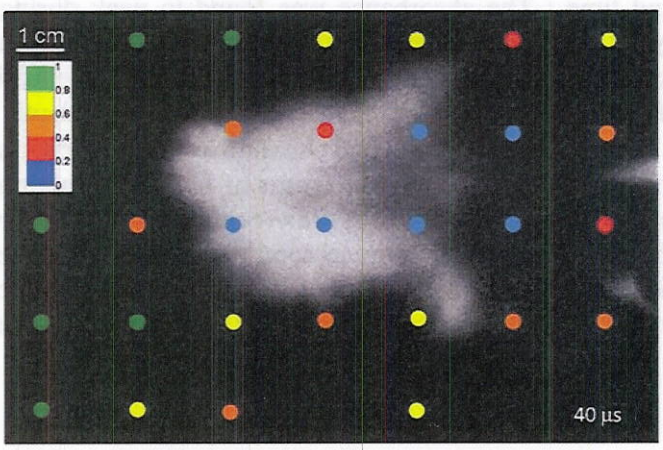

Figure VII.5 Transmission of dot matrix beams through the fireball at 40 µs in a separate experiment on the same charge.

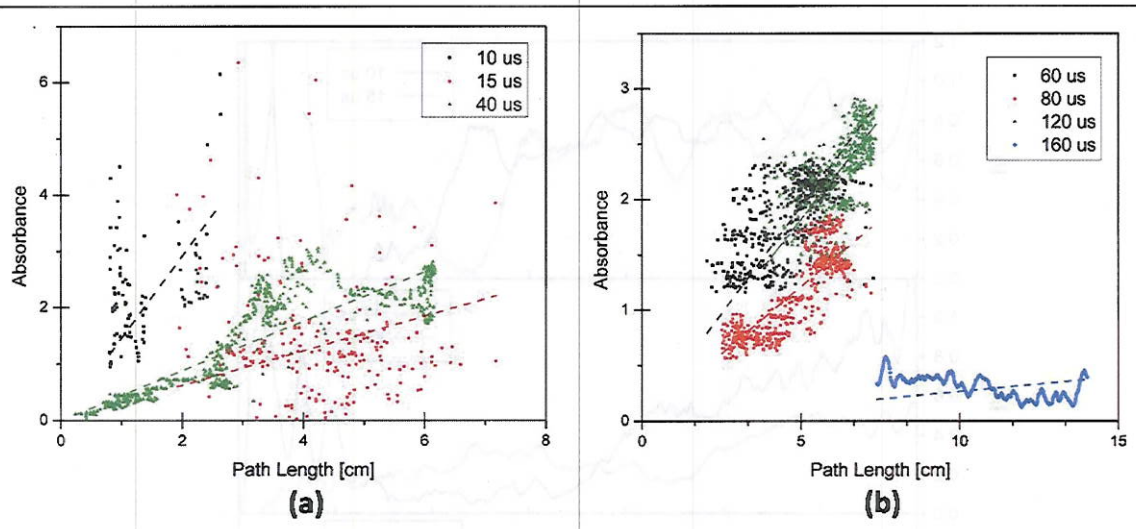

Figure VII.6 Absorbance within fireball as a function of the estimated path length through the fireball. Linear fits passing through the origin are shown as dashed lines for each time

Since fireball radius scales as charge mass to the 1/3 power, charges at the scale of a few grams will already have attenuation lengths much smaller than the fireball radius, and the optical depth will be even stronger for practical charges. Further work is warranted to examine the effects of Al loading and wavelength in order to extend and generalize the results presented here.

Conclusion

Attenuation of 532 nm light by fireball from an aluminized high explosive was measured as a function of space and time. The absorbance was found to peak during the early period of high reactivity of post-detonation gases, and the characteristic attenuation length was less than 1 cm. During the entire luminous event, the attenuation length remained at the centimeter scale, with significant decreases in optical depth beginning after 160 μs from the detonation, when fireball luminosity was fairly faint. The implications from this work are that optical measurements of fireballs of aluminized high explosives will penetrate and sample only the first few centimeters of the fireball, and thus measurements will be representative of surface conditions, not of volume averaged conditions. For aluminized charges at the gram scale and larger, the optically thick assumption, at least near 532 nm, appears appropriate for the period in which fireball luminosity is significant.

Table V1I.1 Delay and exposure times for images taken with the HSFC

Image	Delay [μs]	Exposure [ns]
1	5	500
2	10	500
3	15	500
4	40	10,000
5	60	10,000
6	80	20,000
7	120	20,000
8	160	20,000

Table VII.2 Attenuation length for each delay time and associated uncertainties

Time [μs]	Attenuation Length [cm]	2σ Uncertainty [cm]
10	0.7	0.2
15	3.3	2.9
40	2.3	0.2
60	2.6	0.2
80	4.1	0.2
120	2.7	0.3
160	37.5	13.3

References

[1] P. Persson, B. Andersson and S. Stahl, "A technique for detailed time-resovled radiation measurements in the reaction zone of condensed explosives," in *4th International Symposium on Detonation,* 1965,

[2] K. C. Gross, G. P. Perram and R. F. Tuttle, "Modeling infrared spectral intensity data from bomb detonations," in *Targets and Backgrounds XI: Characterization and Representation,* 2005, pp. 100-111.

[3] J. R. Carney and J. Wilkinson, "Atmospheric effects on time-resolved emission measurements of detonation and combustion products," in *13th International Detonation Symposium,* 2006,

[4] J. R. Carney, J. S. Miller, J. C. Gump and G. I. Pangilinan, "Time-resolved optical measurements of the post-detonation combustion of aluminized explosives," *Rev. Sci. Instrum.,* vol. 77, pp. N.PAG, 06. 2006.

[5] V. Bouyer, G. Baudin and C. Le Gallic. Temperature profile calculation from emission spectroscopy measurements in nitromethane submitted to plate impacts. Presented at 12th International Detonation Symposium.

[6]http://www.cookecorp.com/fileadmin/user_upload/db/products/datasheet/hsfc_pro_TCC_20080714_web.pdf, accessed November 5, 2008

[7] K. Chesterfield, "Effect of detonation on the combustion of 20 micron aluminum particles embedded in high explosives," 2008.

VIII. Emissivity of Aluminum Oxide at High Temperatures

Abstract

Pyrometry measurements of clouds of high temperature particles require an estimate of the spectral dependence of the particle emissivity. Common assumptions for this dependence range from $\varepsilon \sim \lambda^{-2}$ to $\varepsilon \sim$constant. Depending upon the assumption used, there is uncertainty in the temperature of 100s to 1000 K in high temperature clouds. Such errors are not apparent in goodness of fit of spectral data. A heterogeneous shock tube was used to measure the emissivity of aluminum oxide in an inert environment as a function of temperature (2000-3500 K), wavelength (550-950 nm), and particle diameter (50 nm-10 μm). In micron sized alumina particles, the spectral dependence upon temperature transitions from decreasing with wavelength to increasing with wavelength, with the dependence being roughly grey around 3000 K. Because of local minima in the ε vs. λ curve, a power law (λ^n) dependence is insufficient to describe the emissivity. However, if such a dependence is assumed, n transitions from -1.4 to 0.5 as temperature increases from 2500 K to 3500 K. Nano-sized alumina particles exhibit an even stronger spectral dependence, *n* is approximately -1.4 at 2678 K, but reaches as high as 2.1 at 3052 K. Considering optical depth issues there is merit in grey emissivity approximations for high temperature (~3000-3300 K) particles typical of aluminum particle combustion.

Introduction

High temperature particle thermometry is a common measurement, for example in evaluating the effects of an additive in a solid rocket motor engine or competing heterogeneous combustion mechanisms of burning metal clouds. Pyrometry is a non-intrusive optical measurement of condensed phase temperature that can also be used to provide an indication of gas temperatures when atomic or molecular emission methods fail. All condensed phase temperature measurements from spectral intensity require an assumption of the emissivity of particles or its spectral dependence. For example, in multi-color pyrometry, the continuum emission intensity at two or more wavelength regions (typically in the visible to near-IR) are fit to a temperature. However, an assumption needs to be made about the relative emissivity at the measured wavelengths of the particles. This effect is particularly important when the wavelengths of interest are separated by hundreds of nm, which is typically necessary to avoid local spectral biases and molecular interferences.

Common assumptions of the spectral dependence of alumina upon emissivity range from linear [1], to grey [2], to a λ^n dependence where *n* is commonly -1 or -2 [3, 4]. However, when fitting the intensities from different wavelengths to a temperature, as is done in Fig. VIII.1 for 10 μm aluminum powder burning in air, the emissivity spectral dependence choice can lead to 100's or even 1000's K differences in calculated temperature, which can lead to drastically different interpretation of combustion phenomena. For example, in Fig.1, the temperature is calculated by measuring the slope of the line formed by $\ln(I\lambda^5/\varepsilon\ (\lambda))$ vs. $(1/\lambda)$, and three such choices are presented for the emissivity. Even taken over a considerable wavelength range (~250 nm), these curves appear as lines, and no goodness of fit metric will allow the selection of the proper emissivity function. In Fig. VIII.1, the R^2 value differs only one part in 100,000, while the temperature measurement differs between 2792 K and 3794 K.

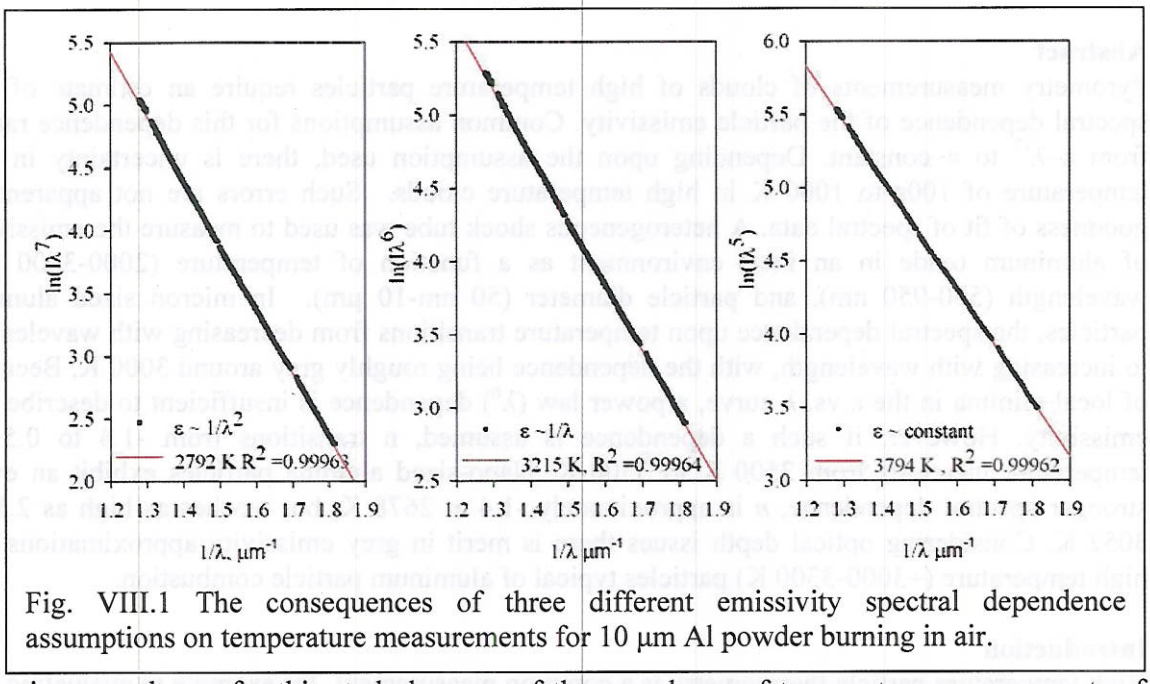

Fig. VIII.1 The consequences of three different emissivity spectral dependence assumptions on temperature measurements for 10 μm Al powder burning in air.

Alumina was chosen for this study because of the prevalence of temperature measurements of reacting aluminum particles [5] in applications such as solid rocket motors (SRM's). All aluminum is coated with an aluminum oxide coat, and condensed phase alumina, which accumulates on a burning particle's surface, is the product of aluminum's reaction with O_2, CO_2, and H_2O. Recent results with similar conditions for larger particles (100 – 400 μm) show the emission attributed to alumina on the particle surface dominates the particle intensity. Furthermore, the oxide smoke envelope around the flame zone accounts for another 5% of the intensity [6]. Because of this dominance of alumina emission during aluminum combustion, the properties of alumina are necessary to make temperature measurements. In previous measurements of alumina smoke in propellant flames, some variation in emissivity was observed that was likely due to trace metals as well as sources other than alumina [7]. To isolate the effect of alumina, we use high purity aluminum oxide particles and conduct our experiments in argon. The inert particles also allow control of particle temperature by varying ambient conditions since no reaction is occurring and thus the particle temperature quickly equilibrates to the ambient temperature.

While an abundance of research exists as to the emissivity of slabs and other surfaces, including of aluminum and alumina, and these are readily tabulated [8], the information on high temperature particle emissivity necessary for temperature measurements is incomplete.
Good calculations [9] and data [7, 10] are available at either limited wavelengths, or longer wavelengths, typically (2-20 μm). However, measurements in the visible to n-IR (<1 μm) are needed because the high temperatures give high signals in the visible regions, and these measurements are easier to make due to the availability of sensitive silicon or photomultiplier-based detectors in this spectral range. Additionally, data are available [11] for larger particles and lower temperatures, including where alumina is solid (< 2300 K). Larger particles, (1 mm for instance) behave much closer to slabs or films than particles. Smaller particles, (smaller than

class 10 μm) have full Mie scattering effects[4, 12, 13] that add complexity to their emissivity. A phase transition from solid to liquid results in an increase in overall emissivity, but the dependencies on temperature and wavelength are unclear.

Experimental Methods

The heterogeneous shock tube facility at the University of Illinois generates a high temperature, high pressure controlled environment ideal for making measurements in combustion conditions. The driven section (the test section) is 8 m long and 8.9 cm internal diameter. Other relevant dimensions and descriptions of this facility can be found in previous publications [1, 14, 15]. Through the pressure ratio of the driver and driven sections, a strength selectable shock can produce a controlled combustion environment for approximately 2 ms in this shock tube. Various compositions of test gases can be used. Temperatures exceeding 4000 K and pressures up to 30 atm are achievable.

Figure VIII.2 shows the experimental setup and diagnostics used in this experiment. Approximately 1 mg of particles are injected into the shock tube from a port 0.68 m from the endwall approximately 1 s before the rupture of the double diaphragm section. The particles are accelerated in the gas behind the incident shock wave toward the endwall. The reflected shock stops the particles in front of the diagnostics and heats them to a controllable temperature where they emit.

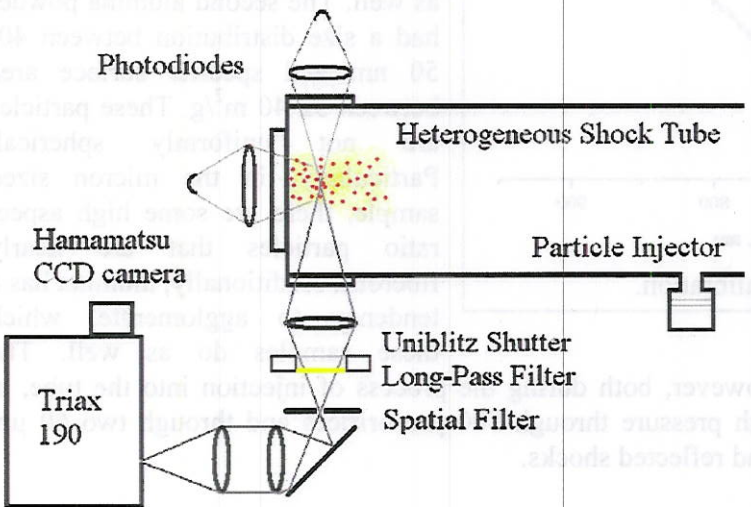

Fig. VIII.2 Schematic of Heterogeneous Shock Tube and Diagnostics

A f/8 lens system collects the light from the emitting particles and passes it through a Triax 190 spectrometer with a 300 g/mm grating before being collected by a Hamamatsu back-thinned CCD array. The optical train contains a 515 nm long pass filter to eliminate order overlap, a Uniblitz shutter to control the exposure time, and a spatial filter system to reject light away from the centerline of the shock tube. The shutter timer was changed under each temperature condition such that the intensity on each pixel of the CCD array was at least 10,000 counts (typically ~ 30,000) without saturating. The shutter was always closed by the end of the shock tube test time. If necessary, neutral density filters were used to attenuate the signal when time resolution could not.

The spectral region of interest was between 550 and 950 nm. This region avoids molecular interferences of AlO at wavelengths lower than 540 nm while extending into the near-IR. If molecular interferences are avoided, this region is suitable for making temperature measurements

using pyrometry. In order to preserve dynamic range across the entire region, a Roscolux "Apricot" R68963 color filter was used to attenuate the signal at the blue end of the spectrum.

Intensity calibrations were taken with every change in condition. Intensity calibrations were carefully matched to exact experimental conditions. The primary intensity source was a 1273 K NIST traceable black body generator. This source provided ample signal for wavelengths larger than 700 nm. However, the intensity of the blackbody source is insufficient below 700 nm. In order to extend the range of this calibration, an Oriel Tungsten lamp with nominal color temperature 3200 K was used. The lamp was calibrated to a blackbody temperature using the spectral region between 700-950 nm, and then this signal was used to generate an intensity calibration for wavelengths lower than 700 nm, where the signal level was ample as shown in Fig. VIII.3.

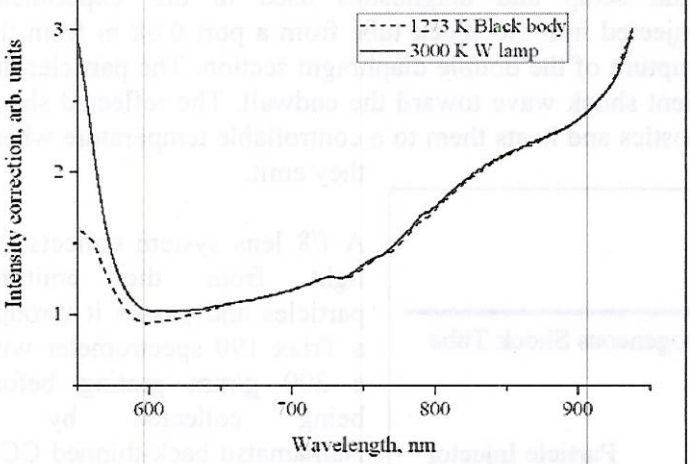

Fig. VIII.3 A typical intensity calibration.

Two different size distributions of alumina were studied. Both were purchased from Alfa Aesar and have purities greater than 99.5%. The first size distribution has particles in the 0.9-2.2 μm range, with some larger as well. The second alumina powder had a size distribution between 40-50 nm and specific surface area between 32-40 m^2/g. These particles are not uniformly spherical. Particularly, in the micron sized sample, there are some high aspect ratio particles that are nearly fiberous. Additionally, alumina has a tendency to agglomerate, which these samples do as well. The agglomerates should break up, however, both during the process of injection into the tube, in which they are accelerated at high pressure through 500 μm orifices and through two 60 μm meshes, but also by the incident and reflected shocks.

These particles were tested in 100 % Ar, approximately 10 atm reflected shock pressure, and reflected shock temperatures starting at 2400 K, and increasing up to 3500 K. This procedure was repeated for micro-alumina as well as nano-alumina samples, twice for each condition.

Processing

The emissivity of the particle at a given temperature was calculated using Eq. (1). The emissivity calculation shows the proportionality of emissivity along wavelengths at a given temperature. The proportionality constant cannot be calculated with this experiment because the absolute intensity (both of the experiment and the calibration) is not measured.

$$\varepsilon_\lambda(T) \sim \frac{I_{\lambda,exp}}{I_{\lambda,bb}(T_p)} \frac{I_{\lambda,bb}(T_{cal})}{I_{\lambda,cal}} \quad (1)$$

where $I_{\lambda,exp}$ is the experimental intensity, $I_{\lambda,bb}$ is the Planck blackbody intensity, $I_{\lambda,cal}$ is the experimentally measured intensity of the calibration source, T_{cal} is the calibration temperature in the spectral region, and T_p is the particle temperature.

The amount of powder injected into the shock tube is about 1 mg, and previous results have shown that only a fraction of this powder is distributed over at least 10 cm in the test section after the reflected shock (the rest, initially wall bound, remains outside of the test section during the reflected shock period). If particles are distributed uniformly throughout this volume, there are about 75 particle diameters of spacing between particles. For the micro-alumina, in the collection volume of the f/8 optics, there would be approximately 10,000 particles, while there may be as many as a billion nano-alumina particles. These numbers suggest the cloud of nano-alumina is optically thicker than the cloud of micro-alumina particles, perhaps significantly.

We have, however, tested the extinction through a similar density of particles (approximately 1 billion in the same collection volume). We measured less than 5% extinction of light through that cloud, which suggests the clouds of particles in these configurations are optically thin. The assumption of uniform distribution of particles in the cloud is somewhat naive, as many particles are concentrated near the cloud front and are lost to the endwall.

Low optical depth is important to ensure the intensity measurements are almost solely from emission of the particles, not from scattering or with a significant absorbed quantity, which would confound the wavelength dependence upon emissivity. As optical depth increases, intensity measurements tend to approach grey dependences as multiple scattering and absorption makes a region increasingly resemble an isothermal cavity [4].

With such a high spacing of the particles, the heat capacity of the environment is about 150 times that of the particles, meaning the particle heat up or emission effect on the gas is well within the temperature uncertainty from the reflected shock calculation which is 25 K. This effect is even smaller because the particles move throughout the gas as they are heated. For this reason, the ambient temperature was taken as the reflected shock temperature and was assumed to be unaffected by the low mass fraction of particles present.

The temperature of the particle, T_p, was set slightly less than that of the gas behind the reflected shock by a few degrees. A balance was calculated between the radiative loss of the particle (total emissivity was initially assumed at 0.3) and heat added to the particle from convection and conduction. The particle velocity and temperature history was calculated by our trajectory modeling program [1], and the conditions behind the incident and reflected shock were calculated using GASEQ [16] from the measured shock velocity. The maximum temperature difference between the particle and the ambient was only 30 K, and the difference was more dependent upon ambient conditions than it was on the assumed emissivity.

The particle heat-up time characteristic of the micro-alumina powder was 50 μs in raising the particle temperature from the incident shock ambient temperature to the reflected shock ambient

temperature. This time is at most 4% of the integration time on the CCD array, however, because the intensity is proportional to T^4, it accounts for less than 2% of the integrated intensity and within the shot noise. The heat-up time characteristic of the nano-powder was much smaller.

Results and Discussion

Figure VIII.4 shows the spectral dependence of emissivity of the intensity calibrated emission from 2 μm Al_2O_3 in 100 % Ar around 3000 K. The emissivity is normalized at value of 950 nm. Two conditions are shown. The first is 2985 K, and the second is 3033 K. The broadband signal at these temperatures, when normalized, overlap to a great extent showing very high repeatability. This repeatability was typical of the other conditions. Around 3000 K, the emissivity is roughly constant (i.e. grey) across wavelength, but does increase at the shorter wavelengths.

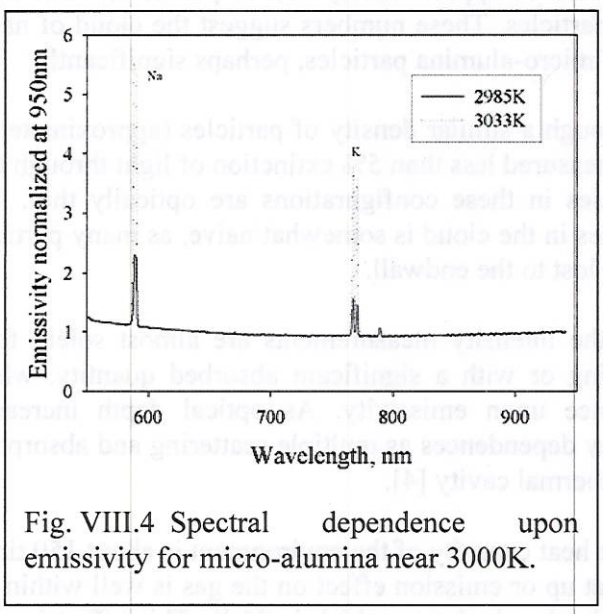

Fig. VIII.4 Spectral dependence upon emissivity for micro-alumina near 3000K.

Common molecular interferences of sodium and potassium are present in this and other conditions. These bands are ignored in the further analysis. There are however, large regions in the spectra without interferences that are appropriate for taking pyrometry measurements. Once the atomic and molecular interference bands are removed from the emissivity calculation, calculated by Eq. (1) the resulting emissivity is subjected to 20 pixel (7 nm) smoothing. This smoothing does not affect the shape of the emissivity across the spectra, but it does alleviate an experimental artifact of etaloning from the CCD array which was prevalent at wavelengths larger than 700 nm. The effect was minimal however, as the counts at each pixel differed by less than 2% the value generated by the 20 pixel smoothing.

Micro-alumina

Figure VIII.5 shows the emissivity of micro-alumina particles with respect to wavelength for temperatures between 2468 K and 3500 K. While the wavelength dependence on emissivity is measured, the absolute emissivity levels are estimated (at 700 nm) from an optically thin, full Mie scattering model [12, 13] that accounts for the temperature dependence upon the optical constants [7], as well as the size distribution [17], albeit with spherical particles. These absolute emissivity levels increase toward unity near 3500 K, which is an expected trend.

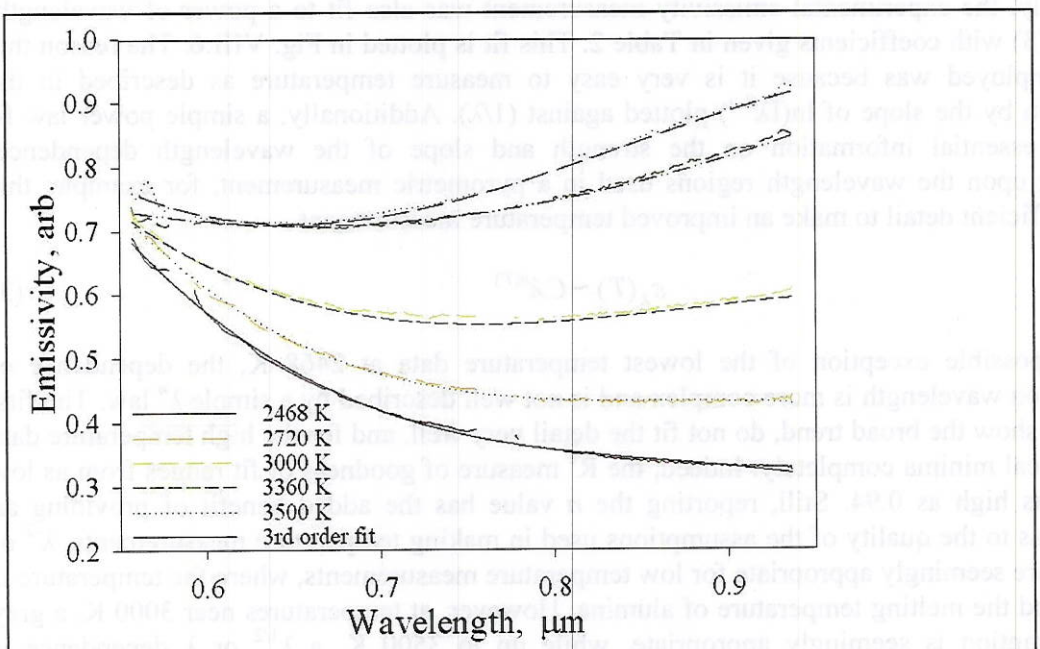

Fig. VIII.5 Temperature dependence upon emissivity for micro-alumina as well as a third order polynomial fit to the data.

The emissivity decreases with wavelength for temperatures below 2720 K, which is an expected and commonly assumed result. Near 3000 K, however, there is a slight decrease until about 770 nm, after which there is a slight increase. Overall however, the emissivity is quite level. At higher temperatures, there is again the decrease to a local minimum. However the local minimum occurs at lower wavelengths, around 650 nm for both 3360 K and 3500 K. At these temperatures, however, the increase of emissivity with wavelength at higher wavelengths is not negligible.

The emissivity of the micron alumina with temperature has been fit to both a third order function of wavelength and a simple power law. A third order equation, Eq. (2) was necessary to maintain the curvature of the emissivity throughout the wavelength region of interest for all temperatures. The emissivity is given by

$$\varepsilon_\lambda(T) \sim c_0 + c_1\lambda + c_2\lambda^2 + c_3\lambda^3 \qquad (2)$$

where λ is the wavelength in micrometers, and c_n are coefficients presented in Table 1. The third order fitting was sufficient to maintain a fit of $R^2 > 0.98$. This fit is plotted along with the experimental data in Fig. VIII.5.

We make a strong caution when using the third order fit for emissivity to not extrapolate the wavelength dependence very far outside of the region of 550 nm and 950 nm because the polynomial fit necessarily has local extrema outside the region of interest. Within the region of interest, however, local minima are experimentally observed.

Additionally, the experimental emissivity measurement was also fit to a power of wavelength, using Eq. (3) with coefficients given in Table 2. This fit is plotted in Fig. VIII.6. The reason this fit was employed was because it is very easy to measure temperature as described in the introduction by the slope of $\ln(I\lambda^{5-n})$ plotted against $(1/\lambda)$. Additionally, a simple power law fit gives the essential information on the strength and slope of the wavelength dependence. Depending upon the wavelength regions used in a pyrometric measurement, for example, this may be sufficient detail to make an improved temperature measurement.

$$\varepsilon_\lambda(T) \sim C\lambda^{n(T)} \tag{3}$$

With the possible exception of the lowest temperature data at 2468 K, the dependence of emissivity on wavelength is more complex and is not well described by a simple λ^n law. The fits, while they show the broad trend, do not fit the detail very well, and for the high temperature data miss the local minima completely. Indeed, the R^2 measure of goodness of fit ranges from as low as 0.4 to as high as 0.94. Still, reporting the n value has the added benefit of providing an indication as to the quality of the assumptions used in making temperature measurements. λ^{-2} or λ^{-1} values are seemingly appropriate for low temperature measurements, where the temperature is right beyond the melting temperature of alumina. However, at temperatures near 3000 K, a grey body assumption is seemingly appropriate, while up to 3500 K, a $\lambda^{1/2}$ or λ dependence is seemingly appropriate.

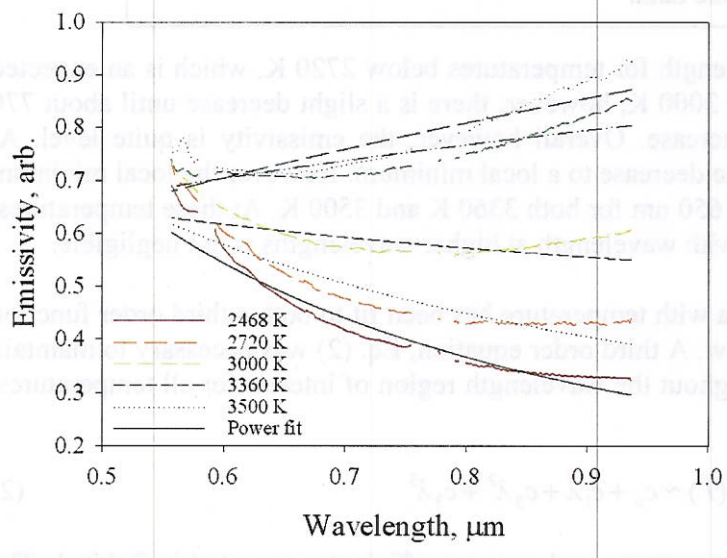

Fig. VIII.6 Temperature dependence upon emissivity for micro-alumina along with a power-law fit to the data.

Nano-alumina

The emissivity of nano-alumina was also tested to compare size effects. The micro-alumina powder is larger but on the order of the wavelength (~1 μm), but the nano-alumina powder (~50 nm) is less than one tenth the wavelength of light, therefore the scattering regime should be

different [13]. These results are shown in Fig. VIII.7. Both the third order fit for emissivity, Eq. (2), and the power law fit for emissivity, Eq. (3) were calculated, and the proper coefficients are displayed in Tables 3 and 4 respectively. However, only the power law fit is shown in Fig. VIII.7. The fit for the third order polynomial has a goodness of fit R^2 at 0.99 and again very closely resembles the experimental data.

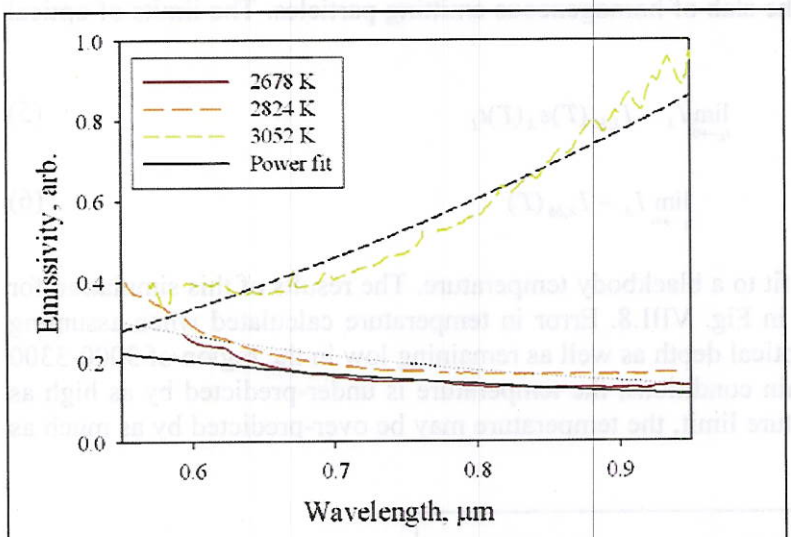

Fig. VIII.7 Temperature dependence upon emissivity for nano-alumina along with a power-law fit to the data.

At lower temperatures, the emissivity decreases with wavelength, while at higher temperatures it increases with wavelength. The dependences and transition, however, appears to be sharper than in micro-alumina. The power law dependence increases from n=-1.4 at 2678 K to n=2.1 at 3052 K. In comparison, micro-alumina at similar temperatures had n=-0.82 and n=-0.26 respectively.

Additionally, while the signals from the nano-alumina were much less intense than for the micro-alumina samples at the same temperature, the emissivity calculated using the absolute emissivity model resided at a higher overall level than for micro-alumina. This prediction comes from a region of the model, highest temperature and smallest particles, that contains the most amount of extrapolated data, and therefore, while the relative emissivity dependence is fairly precise, the absolute emissivity has significant uncertainty.

Finally, the optical depth of the nano-alumina clouds is greater than that of the micro-alumina clouds. While similar configurations we have measured suggest that the nano-alumina cloud that we have measured is still optically thin, increases in optical depth shift the emissivity distributions toward grey.

Application to Particle Temperature Measurements

Based on the experimental measurements of emissivity, we simulated the error associated with using the grey particle assumption. To do this, we assumed a 1-D homogeneous medium (a slab) of a certain optical depth and temperature. This medium emitted and interacted according to its

measured emissivity. The expected result was the transfer function Eq. (4). The spectral intensity beyond the interacting medium, that which is measured is:

$$I_\lambda \sim I_{\lambda,bb}(T)(1-\exp(-\varepsilon_\lambda(T)t_L)) \tag{4}$$

where t_L is the optical depth of the slab of homogeneous emitting particles. The limits of optical depth, Eqs. (5) and (6) reduce to:

$$\lim_{t_L\to 0} I_\lambda \sim I_{\lambda,bb}(T)\varepsilon_\lambda(T)t_L \tag{5}$$

$$\lim_{t_L\to \infty} I_\lambda \sim I_{\lambda,bb}(T) \tag{6}$$

This spectral intensity, I_λ is then fit to a blackbody temperature. The results of this simulation for micro-sized particles are shown in Fig. VIII.8. Error in temperature calculated when assuming grey emissivity decreases with optical depth as well as remaining low in the region of 3000-3300 K. Above 3300 K in optically thin conditions, the temperature is under-predicted by as high as 10%, while in the lower temperature limit, the temperature may be over-predicted by as much as 20% at 2500 K.

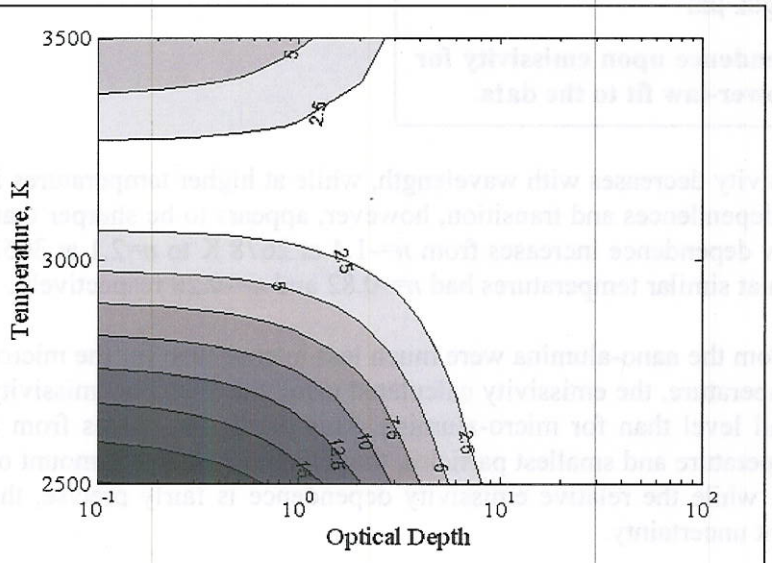

Fig. VIII.8 Percent error in measured temperature associated with using grey emissivity assumption with optical depth and particle temperature for micro-alumina.

This result is fortuitous for two reasons. 3000-3300 K is a typical peak combustion temperature of particles in this size range measured both with pyrometric measurements [5] and the temperature of a gas phase intermediate thought to be very close to the particle [18]. Other

results for larger particles (~100 μm) showed peak temperatures in this range as well [2, 19]. Furthermore, many applications of pyrometric particle temperature measurements, like aluminum combustion in a propellant or a fireball, are made in conditions that are often optically thick.

Some of the limitations of this analysis are optical depth, presence of other emitters besides alumina, and size distribution. Optical depth is a significant limitation in measurements, and careful consideration of optical depth must be taken in temperature measurement applications. If measurements are made in optically thick particle clouds of inhomogeneous temperature, like a propellant or a fireball, then the measured temperature will only be representative of the edge of the cloud and not of the core.

While the emissivity is very high in this high temperature region, a strong scattering component may change these results slightly. Additionally, while reacting aluminum particles are dominated by alumina emission, the presence of aluminum having a different emissivity spectral dependence will slightly alter the mean emissivity of a collection of particles. Finally, as has been described, the particle diameter has an effect on the emissivity dependence, therefore, the size distribution has to be somewhat known in making temperature measurements. However, as particle size increases, the grey assumption appears to give reasonable temperatures [2, 19] and effects that deviate from grey-particles appear negligible. Particularly, in the work by Dreizin [2], while using the grey particle assumption, the temperature steadied at the melting temperature of the aluminum oxide after the high temperature region, and in work with 10 μm particles in the shock tube [5], grey particles after the peak temperature decayed to the expected elevated ambient temperature within the test time.

Conclusions

An experimental study of the emissivity of micro- and nano-alumina particles was conducted in a shock tube for temperatures between 2500 K and 3500 K, in the wavelength region between 550 nm and 950 nm:

1. In micron sized alumina particles, the spectral dependence with increasing temperature transitions from decreasing with wavelength to increasing with wavelength, with the dependence being roughly grey around 3000 K.

2. While a power law (λ^n) dependence upon emissivity is insufficient to describe the emissivity in this region, roughly n transitions from -1.4 to 0.5 as temperature increases from 2500 K to 3500 K.

3. In nano-sized alumina particles, the spectral dependence is stronger than the micron sized particles and while n is approximately -1.4 at 2678 K, but reaches as high as 2.1 at 3052 K.

4. A grey particle emissivity assumption has merit for micron and larger size particles at combustion temperatures (3000 – 3300 K), especially considering optical depth effects in measurements.

References

[1] Bazyn, T., "Spectroscopic Measurements of the Combustion of Aluminum and Aluminum-Based Energetic Material Particles Using a Heterogeneous Shock Tube," Ph.D Dissertation, Dept. of Mechanical and Industrial Engineering, Univ. of Illinois at Urbana-Champaign, Urbana, IL, 2006.

[2] Dreizin, E. L., "Experimental Study of Stages of Aluminum Particle Combustion in Air." *Combustion and Flame,* Vol. 105, No. 4, pp. 541. doi:10.1016/0010-2180(95)00224-3

[3] Goroshin, S., Mamen, J., Higgins, A., Bazyn, T., Glumac, N., and Krier, H., "Emission Spectroscopy of Flame Fronts in Aluminum Suspensions," *Proceedings of the Combustion Institute*, Vol. 31, No. 2, 2007, pp. 2011-2019. doi: 10.1016/j.proci.2006.07.175

[4] Brewster, M. Q., *Thermal Radiative Transfer and Properties*, Wiley, New York, 1992.

[5] Glumac, N., Krier, H., Bazyn, T., and Eyer, R., "Temperature Measurements of Aluminum Particles Burning in Carbon Dioxide," *Combustion Science and Technology*, Vol. 177, No. 3, 2005, pp. 485-511. doi: 10.1080/00102200590909030

[6] Harrison, J. and Brewster, M. Q., "Infrared Emitted Intensity Measurements from Burning Aluminum Droplets in Solid Propellants," Combustion Science and Technology, Vol. 181, No. 1, 2009, pp. 18-35. doi: 10.1080/00102200802415029

[7] Parry, D. L., and Brewster, M. Q., "Optical Constants of Al_2O_3 Smoke in Propellant Flames," *Journal of Thermophysics*, Vol. 5, No. 2, 1991, pp.142-149.

[8] Mills, A. F., *Heat Transfer,* 2nd ed. Prentice Hall, New Jersey, 1998.

[9] Qiu T. Q., Longtin, J. P., and Tien, C. L., "Characteristics of Radiation Absorption in Metallic Particles," *Journal of Heat Transfer*, Vol. 117, No. 2, 1995, pp. 340-345.

[10] Konopka, W. L., Reed, R. A., and Calia, V. S., " Measurements of Infrared Optical Properties of Al_2O_3 Rocket Particles," *AIAA 18th Thermophysics Conference*, AIAA, Washington, DC, 1983.

[11] Sarou-Kanian V., Rifflet, J. C., and Millot, F., "IR Radiative Properties of Solid and Liquid Alumina: Effects of Temperature and Gaseous Environment," *International Journal of Thermophysics*, Vol. 26, No. 4, 2005, pp. 1263-1275. doi: 10.1007/s/0765-005-6725-5

[12] Bohren, C. F., and Huffman, D. R., *Absorption and Scattering of Light by Small Particles*, Wiley, New York, 1983.

[13] van de Hulst, H. C., *Light Scattering by Small Particles*, Dover, New York, 1981.

[14] Servaites, J., "Combustion of Aluminum Particles in Rocket Motor Oxidizers within a Shock Tube," Master's Thesis, Dept. of Mechanical and Industrial Engineering, Univ. of Illinois at Urbana-Champaign, Urbana, IL, 2001.

[15] Bazyn, T., Glumac, N., Krier, H., Ward, T., Schoenitz, M., and Dreizin, E., "Reflected Shock Ignition and Combustion of Aluminum and Nanocomposite Thermite Powders," *Combustion Science and Technology*, Vol. 179, No. 3, 2007, pp.457-476. doi: 10.1080/00102200600637261

[16] GASEQ: A Chemical Equilibrium Program for Windows, Software Package, Ver. 0.62, C. Morley., http://www.gaseq.co.uk, 2005.

[17] Bakhir, L. P., Levashenko, G. I., and Tamanovich, V. V., "Effect of Disperse Composition of Drops of Al_2O_3 in Flames on Their Coefficients of Absoprtion and Scattering," *Combustion Explosion and Shock Waves*, Vol. 12, No. 3, 1976, pp. 356-362.

[18] Bazyn, T., Krier, H., and Glumac, N., "Evidence for the Transition from the Diffusion-Limit in Aluminum Combustion," *Proceedings of the Combustion Institute*, Vol. 31, 2007, pp. 2021.
doi: 10.1016/j.proci.2006.07.161

[19] Goroshin, S., Frost, D., and Levine, J., "Optical Pyrometry of Fireballs of Metalized Explosives," Propellants, Explosives, Pyrotechnics, Vol. 31, No. 3, 2006, pp. 169-181.
doi: 10.1002/prep.200600024

List of Tables

Table 1 Emissivity wavelength dependence for micro-alumina with temperature.

Temperature, K	c_0	c_1	c_2	c_3	R^2
2468	6.63	-21.4	24.5	-94.5	0.99
2720	6.71	-21.8	25.3	-9.75	0.99
3000	5.12	-16.1	18.6	-7.06	0.99
3360	1.79	-3.6	3.47	-0.75	0.98
3500	5.12	-17.1	21.4	-8.47	0.99

Table 2 Emissivity wavelength dependence for micro-alumina with temperature.

Temperature, K	C	n	R^2
2468	0.27	-1.37	0.94
2720	0.37	-0.88	0.84
3000	0.54	-0.26	0.40
3360	0.82	0.30	0.74
3500	0.9	0.47	0.70

Table 3 Emissivity wavelength dependence for nano-alumina with temperature.

Temperature, K	c_0	c_1	c_2	c_3	R^2
2678	3.89	-12.8	14.5	-5.45	0.99
2824	6.01	-21.0	25.1	-9.97	0.99
3052	5.42	-19.1	22.4	-7.60	0.99

Table 4 Emissivity wavelength dependence for nano-alumina with temperature.

Temperature, K	C	n	R^2
2678	0.13	-1.41	0.80
2824	0.11	-1.19	0.79
3052	0.96	2.07	0.91

VII. Absorption Spectroscopy Measurements in Optically Dense Explosive Fireballs using a Modeless Broadband Dye Laser

Abstract

A modeless broadband dye laser is applied to probe inside optically dense fireballs generated by high explosives using single-shot, high resolution absorption spectroscopy. Despite attenuation of the main beam by 98%, high signal to noise ratio absorption spectra of Al, Ti, and AlO are readily obtained at resolutions of 0.007 nm, and luminosity from the fireball is strongly rejected. Detection limits for atomic species are less than 200 ppb. The method offers good time resolution of chemistry within the fireball, and scaling laws suggest that this technique should be valid in explosives tests at least up to the gram scale.

Introduction & Motivation

Detonations from high explosives generate luminous fireballs that can persist long after the passage of the initial blast wave. Of recent interest is the approach to enhancing blast effects through volumetric energy release. In this approach, the initial detonation disperses a second reactive component that reacts within the fireball, but over a slightly longer timescale. This secondary reaction generates substantial overpressure over a larger volume, leading to enhanced near-field and far-field blast effects. Reactions of reactive materials within the high temperature, high pressure, fireball region are poorly understood, and thus diagnostic probes of the chemical environment within such fireballs can potentially provide critical information to test kinetic models of reactivity. However, probing the fireball on the relevant timescales is a challenging task. Elevated temperatures and the need for high temporal resolution (e.g. less than 1 μs) preclude the use of many mechanical probe techniques. Optical techniques are more suitable, especially in emission, as the inherent fireball brightness is high. Such techniques have been applied with some success[1] to aluminized explosive mixtures, especially in monitoring the key combustion intermediate AlO. However, the optical depth of such fireballs is fairly high. A recent measurement of optical depth in aluminized fireballs found that nonresonant characteristic attenuation lengths in the visible region are of the order of a few centimeters during the period in which the secondary phase reacts[2]. Thus, for fireballs from gram scale experiments, which approach the scale of a few 10s of cm in diameter, attenuation of an incident light beam can exceed 99%. Under these conditions, any emission measurements will probe only the region near the outer edge of the fireball, and the conditions in this region, near the detonation products/air interface, can be substantially different than those within the fireball.

Clearly absorption techniques would be preferred in these cases since measurements are line-of-sight averaged, providing information from the inside of the fireball. In addition, absorption probes the electronic ground state, rather than the excited state, allowing access to a greater number of species than emission. Finally, absorption measurements are more readily quantified, though issues associated with path length estimation and homogeneity along the path length pose challenges for interpretation of the signal.

In fireballs, unfortunately, absorption measurements are exceedingly difficult due to the opacity and inherent brightness of the medium. For path lengths of a few cm, even the brightest broadband incoherent sources are attenuated so greatly that, when dispersed enough to achieve a high sensitivity measurement, they often produce insufficient signal at the detector to either exceed the inherent fireball emission signal and/or to generate sufficient counts from which a sensitive absorption signal can be extracted. This limitation is especially challenging when time-resolution at the microsecond scale is desired.

Broadband dye lasers (BDLs) offer the potential to address some of these effects. BDLs have been widely used as spectroscopic sources[3,4], mostly for fluorescence or coherent-Anti-Stokes Raman Spectroscopy (CARS)[5-9]. Pulses of less than 10 ns are generated with standard pump sources, and the spectral irradiance exceeds that of incoherent sources by several orders of magnitude. Spectral bandwidths of a few nm are not uncommon for commercially available dyes. By appropriate choice of dyes, different atoms and molecules can be targeted for absorption measurements. The temporal resolution of 10 ns is much faster than any relevant timescale within the fireball. Although single-shot measurements are easiest to implement, multiple shot measurements within a single event using pulse-burst approaches combined with a sufficiently high speed camera should be possible.

In this paper, we detail our experimental approach to making in-fireball measurements using a modeless broadband dye laser. Results from a sample high explosive system are also presented, and implications for extension of this technique to study larger charges and other systems are presented.

Experimental

Our experimental approach is shown in Figure IX.1. An Nd:YAG laser (Spectra Physics GCR-150-10) is frequency tripled, yielding 7 ns pulses of 355 nm light at 10 Hz with approximately 105 mJ per pulse. The beam is reflected off two windows so that the energy incident on the dye laser is 4 mJ/pulse. The dye laser consists of two quartz cylindrical lenses perpendicular to each other. The concave cylindrical lens spreads the beam in the horizontal direction, and the convex cylindrical lens focuses in the vertical direction. The pump laser line (approximately 25 mm wide at the focus) is focused onto a 40 mm long quartz cuvette that is rotated vertically at 20 degrees off axis to avoid internal etaloning effects. A full reflecting mirror forms the back end of the laser cavity, and the front end is either empty (modeless mode) or uses a 50% reflecting output coupler. Without the output coupler the dye conversion efficiency is approximately 5%, while it exceeds 25% with the output coupler in place.

For the spectral range of 394-397 nm, we use a mixture of Exalite 391 and Exalite 398 dyes (Exciton Inc.), both at 0.1 grams/liter concentration in 1,4 dioxane. For the 484 nm measurements, we use Coumarin 481 at 2 g/liter, also in 1,4 dioxane. At these low pump powers, the dye is stationary, though standard recirculating dye cells can be used if higher powers are required.

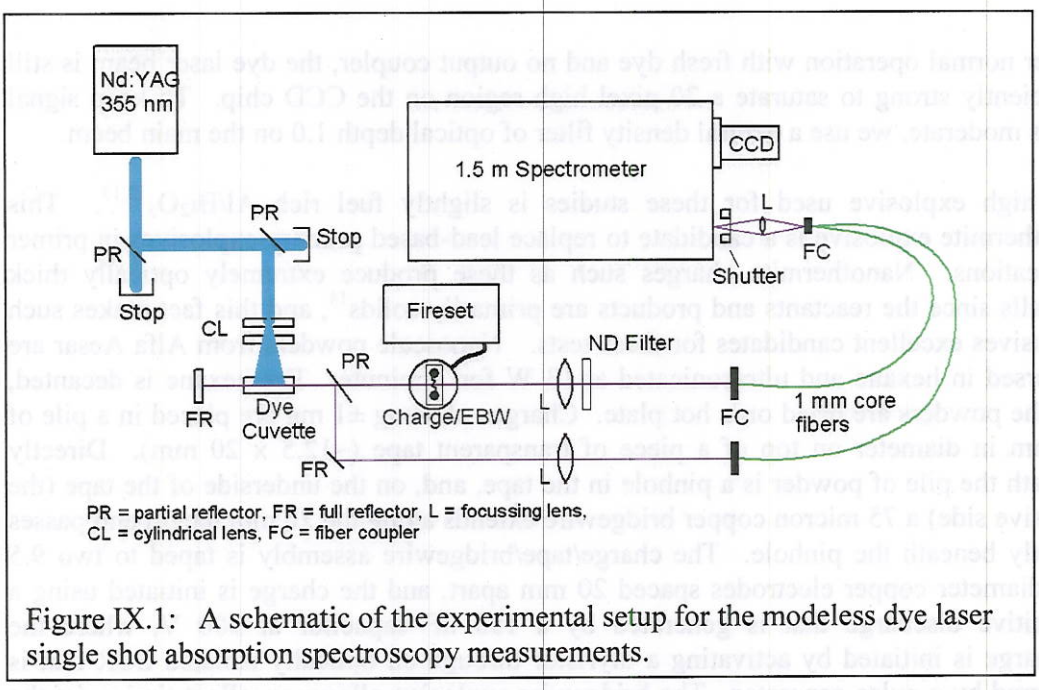

Figure IX.1: A schematic of the experimental setup for the modeless dye laser single shot absorption spectroscopy measurements.

The dye beam shows modest divergence (15 mrad) but is easily aligned through the optical setup. A beam sampler directs a small reflection from the output beam along a reference path, following an approach similar to that used in Reference 10 for normalization and compensation for inherent fluctuations in the spectral content of each pulse. The main beam is sent through the blast region, and both beams are then refocused using 500 mm focal length quartz lenses onto 1 mm silica core fibers. Fibers are routed to the spectrometer, which, in this case, is in the same room, though it could, in principle, be remotely located. The two fibers are re-imaged onto the entrance slit of the spectrometer so that they appear at the image plane in separate regions of the chip. Though much smaller fibers could be used, the large core fibers accommodate some steering, distortion, or defocusing of the beam due to index of refraction changes in the fireball, at the expense of signal that enters the spectrometer.

The spectrometer is a custom 1.52 meter Czerny-Turner instrument with a 3600 gr/mm grating, and a 9 degree deviation angle. Two 6" diameter spherical mirrors form the collimating and focusing elements. The longitudinal location of the 100 mm square grating with respect to the collimator and focuser is 85% of the collimator focal length to provide the flattest field at the focal plane, and the lateral position of the grating is adjustable to minimize coma for a specific wavelength[11]. The detector is an Andor iDus back thinned 256x1024 CCD array with peak quantum efficiency of greater than 90%. The pixel size is 26 microns, so that under these conditions, the dispersion is .003 nm/pixel, yielding a spectral range of 3.1 nm at 395 nm. At 485 nm, the dispersion is .002 nm/pixel for a range of 2.0 nm. With a 50 micron entrance slit, 2.5 pixel resolution (FWHM) is achieved (i.e. 0.0075 nm, R = 53,000 at 395 nm and .0050 nm, R = 97,000 at 485 nm). A fast shutter (Thorlabs Model SH05) allows light into the spectrometer for only one pulse, though the laser operates continuously at 10 Hz.

Under normal operation with fresh dye and no output coupler, the dye laser beam is still sufficiently strong to saturate a 20 pixel high region on the CCD chip. To keep signal levels moderate, we use a neutral density filter of optical depth 1.0 on the main beam.

The high explosive used for these studies is slightly fuel rich Al/Bi_2O_3[12,13]. This nanothermite explosive is a candidate to replace lead-based primary explosives in primer applications. Nanothermite charges such as these produce extremely optically thick fireballs since the reactants and products are primarily solids[14], and this fact makes such explosives excellent candidates for these tests. Nanoscale powders from Alfa Aesar are dispersed in hexane and ultrasonicated at 13 W for 1 minute. The hexane is decanted, and the powders are dried on a hot plate. Charges of 4 mg ±1 mg are placed in a pile of ~3 mm in diameter on top of a piece of transparent tape (~12.5 x 20 mm). Directly beneath the pile of powder is a pinhole in the tape, and, on the underside of the tape (the adhesive side) a 75 micron copper bridgewire extends along the 20 mm length and passes directly beneath the pinhole. The charge/tape/bridgewire assembly is taped to two 9.5 mm diameter copper electrodes spaced 20 mm apart, and the charge is initiated using a capacitive discharge that is generated by a 150 uF capacitor at 300 V, where the discharge is initiated by activating a thyristor through an optically isolated SCR that is triggered by a pulse generator. The bridgewire explosion allows excellent timing (at the microsecond level) of the initiation event, much more precise than hot wire methods that are commonly used for initiation.

In addition to explosive charges, exploding bridgewires of titanium and aluminum are placed across the electrodes and fired, producing dense atomic clouds that serve as an inexpensive test of timing and alignment. For all experiments, the dye laser beam is aligned to pass 1 cm over the initial bridgewire position, perpendicular to the wire. Visible luminosity from these clouds extends over a region of only a few centimeters in diameter.

Results and Analysis

The modeless dye laser does not produce an entirely smooth continuum, as is well known from prior works[5]. The spectral structure from a typical single shot is shown in Figure IX.2. The noise level is approximately 14% of the signal. Normalizing the main laser beam with the signal from the reference beam (bottom plot in Figure IX.2) shows a significant improvement to the 6% level. Typical integrated counts from the reference beam are approximately 40000 per pixel column, and thus the instrument noise should be dominated by photon statistics in the signal count which amounts to less than a 1% variation. The baseline noise level in the spectra varied significantly as the dye warmed and aged. The best spectra showed baseline noise at the 3% level. In the current setup, the noise level limits the (worst case) minimum absorption peak that can be resolved to approximately a 10% absorption from the baseline, or an equivalent width of 1.4 GHz (8 mÅ).

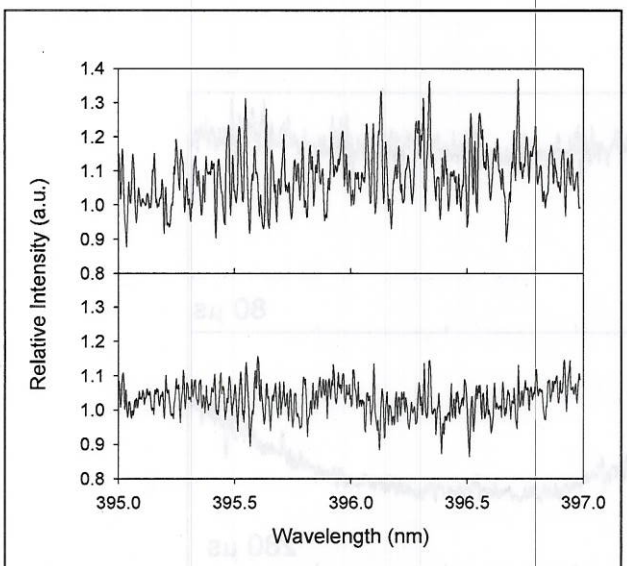

Figure IX.2: A typical plot of the single shot spectral intensity distribution of the laser before normalization (top) and after normalization with respect to the reference beam (bottom).

The initial proof-of-concept tests were performed in vapor clouds generated by aluminum and titanium exploding bridgewires (EBWs). For Al, we used 75 micron Al wire, and for Ti, we used 0.5 mm wide x 25 micron thick foil strips, cut by hand. Sequential tests were performed in which the laser pulse was delayed from the wire initiation time. Spectra were normalized by the reference beam and the resultant absorption spectra are shown in Figure IX.3. The EBWs produce fairly dense atomic clouds with broadband absorption of approximately 50%. The Al absorption lines ($^2P^\circ \rightarrow {}^2S$) are strong and easily resolved from the background. At peak Al absorbance, the lineshape is significantly broadened due to the large optical depth. These absorption lines persist for the first millisecond after the blast, though the bright luminous output lasts much less than 100 microseconds. Similar tests were performed on Ti strips which were 99.5% purity, and the major impurity is aluminum. In these clouds (as shown in Figure IX.4), both Ti ($^3F^\circ \rightarrow {}^3P^\circ$, $^3D^\circ$, $^3F^\circ$) and Al lines are clearly resolved in this small 3 nm spectral range. Equivalent widths of 1.4 GHz correspond to detection limits over a 10 cm path length of 190 ppb for Al and 160 ppb for Ti.

In addition to concentration measurements, temperature information can be generated from this set of lines since the absorptions originate from different lower energy states as referenced to the lowest ground state (0 and 112 cm^{-1} for Al; 0, 170, and 387 cm^{-1} for Ti). As such, the absorption spectrum probes the electronic state population distribution, and temperatures can be extracted assuming a Boltzmann distribution. Such "temperatures" are generated from line-of-sight averaged quantities, and thus may not be representative of any local or even average temperature. However, they do form an observable that is directly related to the temperature and concentration distributions within the fireball, and thus form a quantity that can be used to test and/or validate thermochemical fireball models. For the data shown in Figure IX.4, the six Ti lines were processed into estimated column densities and processed to yield the Boltzmann plot shown in Figure IX.5. It can be seen for this case that the data do not fall on a straight line that can be readily fit to a temperature. Points associated with multiple transitions from the same electronic state are widely spaced, suggesting that the population distribution in our experiment is not in equilibrium. Such a result would be consistent with a very short-

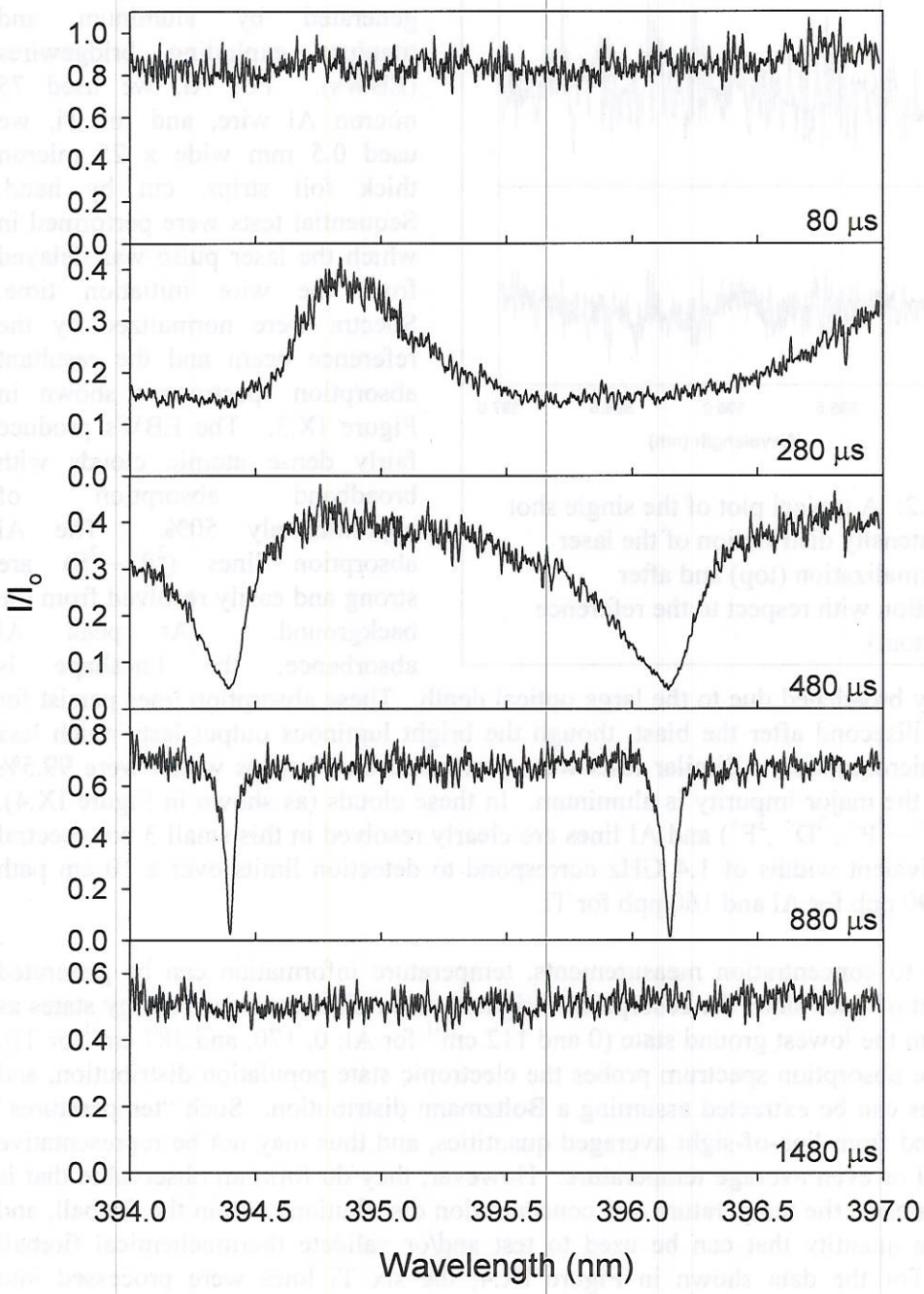

Figure IX.3: A temporal series of spectra from a 75 micron diameter exploding bridgewire cloud as probed by single shot absorption spectroscopy. Each spectrum is a different experiment with a different delay between wire ignition and the probe laser pulse.

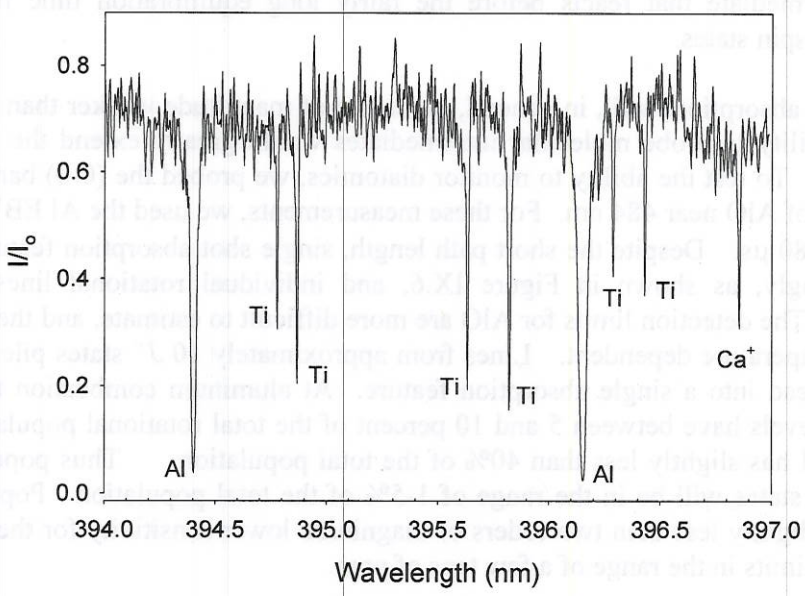

Figure IX.4: A single-shot absorption spectrum from an exploding foil of 98.5% pure Ti, showing Ti lines, as well as Al and Ca^+ impurities.

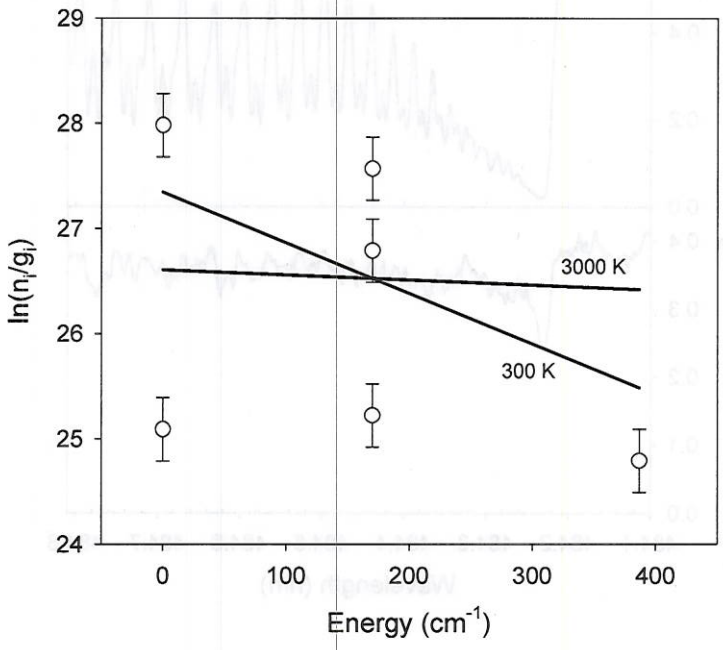

Figure IX.5: A Boltzmann plot of the Ti lines from the spectrum in Figure IX.4. Each data point is a single transition. The lines represent calculated slopes for 3000 K and 300 K. The results suggest a high degree of non-equilibrium in the state populations for this case.

lived intermediate that reacts before the fairly long equilibration time for the lower electronic spin states.

Molecular absorptions will, in general, be orders of magnitude weaker than atomic lines, but the ability to probe molecular intermediates would greatly extend the range of this technique. To test the ability to monitor diatomics, we probed the (0-0) band of the *B-X* transition of AlO near 484 nm. For these measurements, we used the Al EBW and a time delay of 280 μs. Despite the short path length, single shot absorption features appeared very strongly, as shown in Figure IX.6, and individual rotational lines are readily resolved. The detection limits for AlO are more difficult to estimate, and the limit will be highly temperature dependent. Lines from approximately 10 *J"* states pile up at the (0-0) band head into a single absorption feature. At aluminum combustion temperatures, these *J"* levels have between 5 and 10 percent of the total rotational population, and the *v"*=0 level has slightly less than 40% of the total population. Thus population in the absorbing states will be in the range of 1-5% of the total population. Population alone suggests slightly less than two orders of magnitude lower sensitivity for the diatomic, or detection limits in the range of a few tens of ppm.

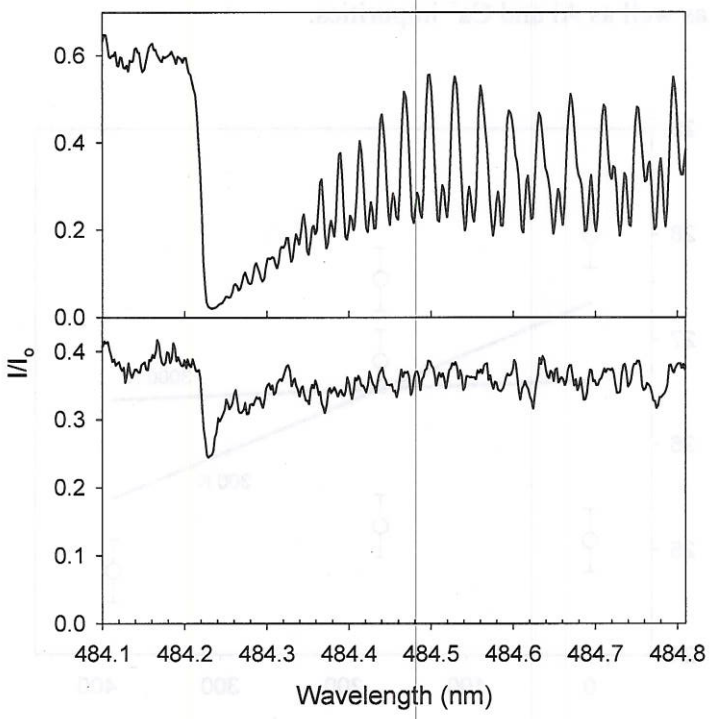

Figure IX.6: A single shot absorption spectrum of the bandhead region of the (0-0) band of the $B\,^2\Sigma^+ - X\,^2\Sigma^+$ transition of AlO in a cloud from an exploding 75 micron Al bridgewire, taken 280 μs after ignition (top) and at 300 us after ignition in an Al/Bi_2O_3 nanothermite explosion.

When applied to Al/Bi_2O_3 explosive charges, attenuation of the probe beam is significantly greater, as shown in Figure IX.7, which monitors transmitted signal from a 630 nm diode laser. During the first millisecond after ignition, the transmission of the beam drops quickly into the range of 20% and stays there for a few milliseconds, long after critical reactions are complete. Thus, this system represents a good test for this diagnostic of optically thick clouds. Note that the neutral density filter in the main beam line after the charge attenuates another 90%, so that the fraction of the probe beam that reaches the detector is only about 2% of the initial intensity.

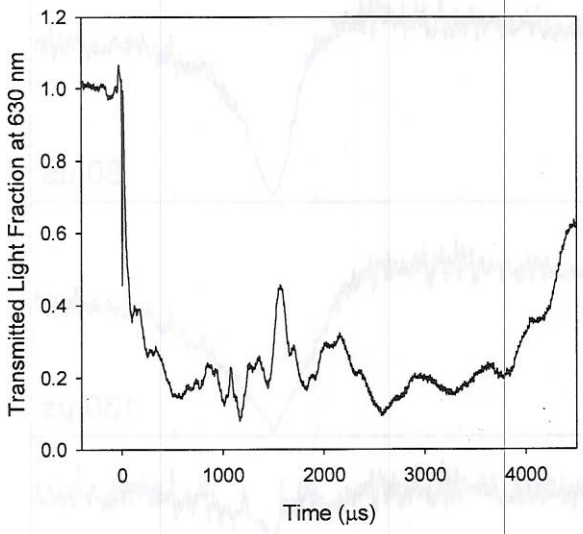

Figure IX.7: A single-shot photodiode trace showing attenuation of a 630 nm diode laser beam as a function of time for a 4 mg Al/Bi_2O_3 charge ignited by a Cu bridgewire.

The intense and bright fireball from the charge nevertheless produces fewer than 10 counts per pixel column, or less than 0.03% percent of the probe beam signal. This low amount is obtained without any attempt at spatial filtering or aperturing of the probe beam, and so further reductions are certainly possible if needed in the future - for example if the neutral density filter is removed to account for further beam attenuation.

The temporal evolution of Al absorption spectra in the fireball is shown in Figure IX.8, and the progression of equivalent width is shown in Table 1. The Al absorptions are again clearly resolved, despite the increased opacity. In these runs, Al appears earlier than in the EBW and does not persist as long. Time resolution of the Al absorption can be obtained in repeated trials with precisions of a few microseconds, limited by the variation in ignition timing from the Cu EBW ignitor. Equivalent widths obtained by such absorption methods can be processed into column-averaged number densities if an absorption path length is estimated. Conversion of number densities to mole fractions can be accomplished if a local pressure and temperature are known. For these fireballs, we do not know the temperature or pressure during the measurement, but the path length is readily estimated from visual observation of the luminous fireball, and we measure this at approximately 3 cm. Using this value, we also show estimated number densities for the relevant times in Table IX.I.

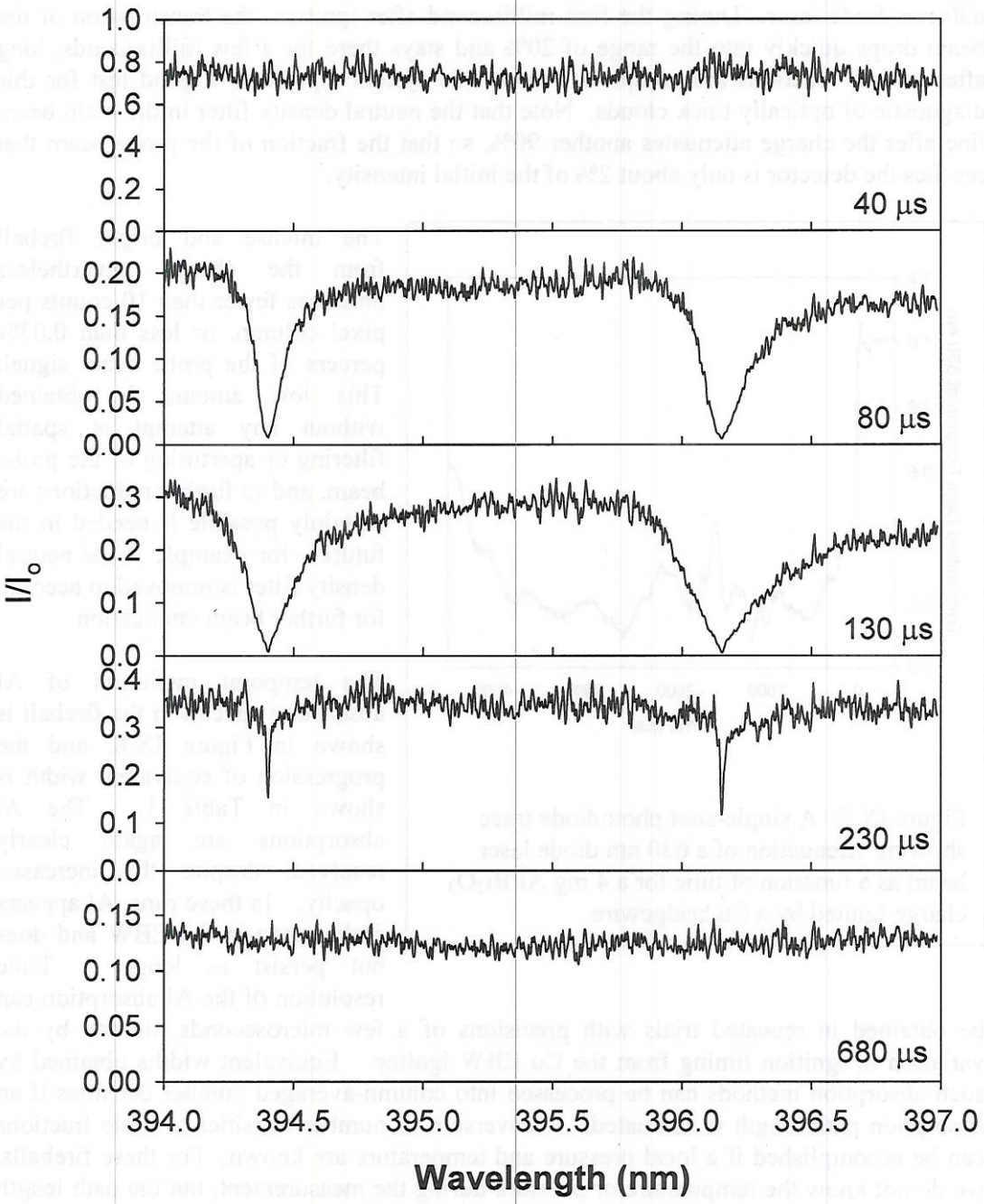

Figure IX.8: A temporal series of absorption spectra taken through the cloud generated by a 4 mg Al/Bi_2O_3 charges. Each spectrum represents a separate experiment.

Table IX.I: Equivalent width versus time for a sequence of single-shot measurements (one per test) of the 394.4 nm Al line in clouds produced by the explosion of 4 mg charges of Al/Bi_2O_3. Number density estimates assume a 3 cm path length.

Delay (us)	Equivalent Width (pm)	Number Density (cm^{-3})
40	0	0
80	151	4.4×10^{15}
130	286	1.7×10^{16}
230	17.3	5.4×10^{13}
330	2.8	7.9×10^{11}
480	2.3	6.0×10^{11}
680	0	0
780	0	0

Molecular AlO absorption was also observed in Al/Bi_2O_3 clouds, as shown in Figure IX.6, though the molecular signal peaks much later than the atomic signal. A peak absorption of approximately 40% was easily observed at 300 μs after ignition. Though features due to individual rotation lines are possibly resolved, the pileup of lines at the bandhead remains the most prominent feature.

Scale up of this technique to larger charges appears possible. In the current setup, the beam is attenuated 98% before entering the collection optics, and more than 10,000 counts of signal per pixel are achieved on the chip over a 20 pixel height. Without resorting to a larger pump laser, a factor of 125 can be gained in dye laser power by using full reflectors in the pump lines and an output coupler. Removing the current neutral density filter in the main beam path yields an increase in intensity at the spectrometer of another factor of 10. Suitable signal to noise ratios could be obtained with a 5x decrease in signal, and the intensity would still far exceed fireball illumination. Thus, usable signal levels at the detector could be maintained for fireballs attenuating 99.997% of the light. Assuming a characteristic attenuation length of 2 cm, 99.997% attenuation is achieved over a path length of 21 centimeters. In related work, we have measured luminous fireball diameters of 200 mg charges with 20% Al loading in PBX-9407 at roughly 5-10 cm during the early stages in which reactivity of aluminum is observed. Fireball diameter will scale as $m^{1/3}$, so a doubling of the fireball diameter requires an eightfold increase in charge mass (1.6 grams). Thus, the absorption-based technique presented here appears applicable without significant modification at least to the level of charges of a few grams of high explosive. Explosives with lighter Al loadings, or explosives with higher transparency (e.g. PETN) could be probed for even larger charges.

When applied to fireballs with optical density much greater than 1, this technique could involve damaging levels of light onto a CCD in the event of a misfire. Such effects could be mitigated by spreading the light over a larger portion of the chip using a negative cylindrical lens in front of the focal plane.

Spatial Resolution

Though the technique as described to this point offers excellent temporal and spatial resolution, only one measurement per test is possible. A simple extension of this technique to produce multiple spatial measurements in each shot was demonstrated, as shown in Figure IX.9, by splitting the main laser beam into four beams using beamsplitters, and directing three beams through separate parts of the fireball. For these measurements, we removed one of the partial reflectors from the 355 nm YAG beam to increase the power such that the power in each of the four beams was now greater than the power in the two beam arrangement discussed above. The beams were arranged at approximately 2.5 cm vertical separation, and all four beams were imaged onto the chip.

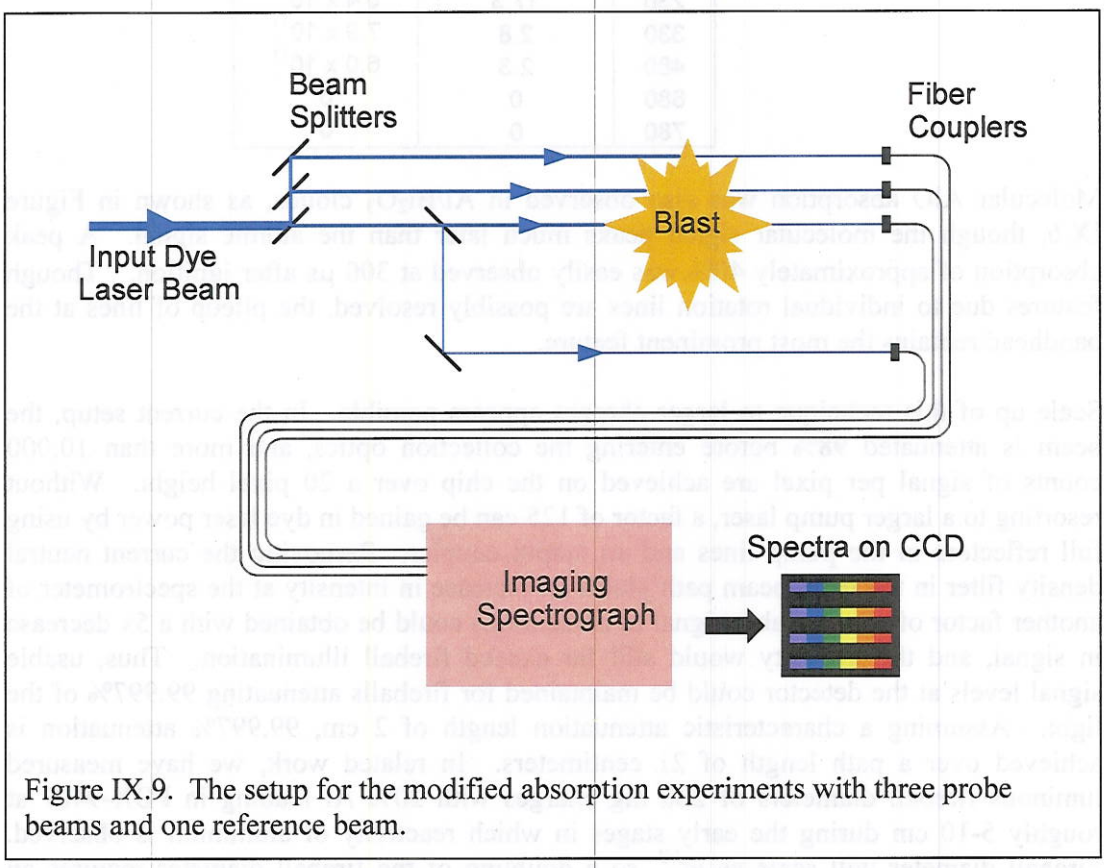

Figure IX.9. The setup for the modified absorption experiments with three probe beams and one reference beam.

The system on which we demonstrated this approach was a Metal Augmented Charge (MAC) where a standard RP-2 detonator formed the high explosive charge, and 5 mg of H-5 aluminum was placed on top of the charge. The charge disperses the powder towards the top of the fireball, generating a fireball with strong spatial variation in composition, which is an excellent test environment for this technique. The charge arrangement and results are shown in Figure IX.10.

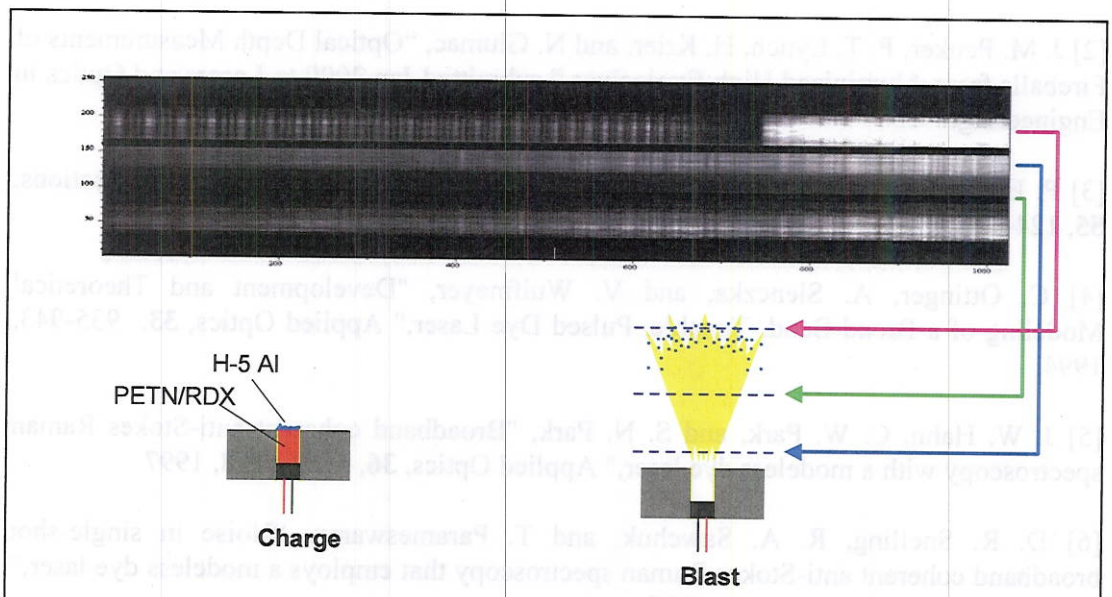

Figure IX.10. Charge configuration (bottom), and resultant spectra on the chip (top). AlO absorption is clearly shown in the top beam where the dispersed Al powder reacts with air and/or detonation products, while no AlO is seen in the middle or bottom portions of the fireball.

The results demonstrate clearly the utility of the technique for probing multiple locations in a single instant. Multiple timed shots would require significant extensions of this technique, but probing additional spatial locations would require only minor modification.

Conclusions

Time-resolved absorption spectroscopy through optically dense explosive fireballs has been demonstrated for the atomic species Al and molecular AlO in a nanothermite explosive. Despite strong attenuation of the probe beam, high signal levels across a 2-3 nm spectral range are maintained, allowing for high resolution absorption spectroscopy. Luminosity from the fireball is also strongly rejected. The detection limits for atomic species over 10 cm path lengths are less than 200 ppb, while limits for the diatomic are two to three orders of magnitude higher. Simultaneous measurements at multiple spatial locations have been demonstrated as a relatively simple extension of the technique. This absorption-based approach can be applied, without significant modification, to gram-scale high explosives experiments.

References

[1] J. R. Carney, J. S. Miller, J. C. Gump, and G. I. Pangilinan, "Time-resolved optical measurements of the post-detonation combustion of aluminized explosives," Review of Scientific Instruments, 77, 6, 063103, 2006.

[2] J. M. Peuker, P. T. Lynch, H. Krier, and N. Glumac, "Optical Depth Measurements of Fireballs from Aluminized High Explosives," submitted Jan 2009 to Lasers and Optics in Engineering.

[3] P. Ewart, "A modeless, variable bandwidth, tunable laser," Optics Communications, **55**, 124-126, 1985.

[4] C. Ottinger, A. Slenczka, and V. Wulfmeyer, "Development and Theoretical Modeling of a Broad-Band, Tunable, Pulsed Dye Laser," Applied Optics, **33**, 935-943, 1994.

[5] J. W. Hahn, C. W. Park, and S. N. Park, "Broadband coherent anti-Stokes Raman spectroscopy with a modeless dye laser," Applied Optics, **36**, 6722-6728, 1997

[6] D. R. Snelling, R. A. Sawchuk, and T. Parameswaran, "Noise in single-shot broadband coherent anti-Stokes Raman spectroscopy that employs a modeless dye laser," Applied Optics, **33**, 8295-8301, 1995.

[7] S. Roy, T. R. Meyer, and J. R. Gord, "Broadband coherent anti-Stokes Raman scattering spectroscopy of nitrogen using a picosecond modeless dye laser," Optics Letters, **30**, 3222-3224, 2005

[8] F. Vestin, M. Afzelius, and P. E. Bengtsson, "Improved temperature precision in rotational coherent anti-Stokes Raman spectroscopy with a modeless dye laser," Applied Optics, **45**, 744-747, 2006.

[9] P. Snowdon, S. M. Skippon, and P. Ewart, "Improved precision of single-shot temperature measurements by broadband CARS by use of a modeless laser," Applied Optics, **30**, 1008-1010, 1991.

[10] L. A. Huston, K. Iwata, W. L. Weaver, and T. L. Gustafson, "Broadband picosecond transient absorption spectroscopy at MHz repetition rates," Optics Communications, **88**, 105-109, 1992.

[11] M. V. R. K. Murty, "Theory and Principles of Monochromators, Spectrometers and Spectrographs," Optical Engineering, **13**, 23-39, 1974.

[12] S. Bhattacharya, Y. F. Gao, S. Apperson, S. Subramaniac, R. Shende, S, Gangopadhyay, E. Talantsev, "A novel on-chip diagnostic method to measure burn rates of energetic materials," Journal of Energetic Materials, **24**, 1-15, 2006.

[13] J. A. Puszynski, C. J. Bulian, and J. J. Swiatkiewicz, "Processing and ignition characteristics of aluminum-bismuth trioxide nanothermite system," Journal of Propulsion and Power, **23**, 698-706, 2007.

[14] D. S. Moore, S. F. Son, and B. W. Asay, "Time-Resolved Spectral Emission of Deflagrating Nano-Al and Nano-MoO3 Metastable Interstitial Composites," Propellants, Explosives, Pyrotechnics, **29**, 106-111, 2004.

X. Internal Fiber Probes for Fireball Spectroscopy and Pyrometry

Abstract

To address optical depth issues in aluminized fireballs, internal emission spectroscopy measurements were performed on aluminized charges using fiber optic probes and an imaging spectrometer with a high speed framing camera (HSFC) as the detector. This arrangement allowed simultaneous spatial, temporal, and spectral resolution of emissions within the fireball, as well as external to it. Fiber probes are robust and re-usable, and signal levels are strong enough such that microsecond level gates can be used while still achieving sub-nm spectral resolution. Initial results suggest that internal measurements yield significantly different temperature measurements than those obtained by an external probe, as might be expected from an optically thick medium.

Introduction

Significant questions have been raised about the interpretation of emission spectroscopy and pyrometry measurements that are obtained from outside the fireball. As our previous research has shown (see section VII), aluminized fireballs are extremely optically thick, and thus measurements made from the outside will observe light only from the outer regions of the fireball. There is significant reason to believe that such measurements may not be representative of the conditions throughout the fireball, as shown in Figure X.1.

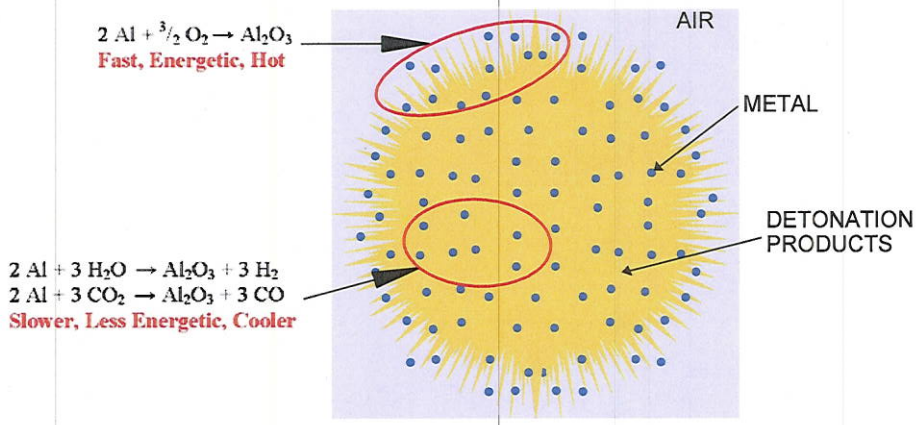

Figure X.I. A schematic of the cross-section of a fireball with hot detonation gases (orange) and solid reactive particles (blue), highlighting possible effects that may lead to non-uniform temperature and species distributions in the fireball.

Reactions of aluminum near the outer surface of the fireball will involve O_2, which generates hotter flames and no gaseous products. However, near the outer edge of the fireball, there is substantial heat loss to the cool ambient by conduction, convection, and radiation. Inside the fireball, the reactions generate less heat, but involve gaseous by

products, and there is no strong heat loss mechanism since these regions are surrounded by other hot zones. It is difficult to estimate a priori what the temperature and species distributions might look like. However, it may be reasonable to assume that temperatures in the fireball will be highest in the center and lower at the edges, due to heat transfer considerations. Since AlO is generated around the burning particles, and the hottest particles are at the edges, it may also be reasonable to assume there is more AlO at the edges of the fireball than in the center. At any rate, given the spatial variation in heat transfer and reaction conditions, it does appear unlikely that the fireball is highly homogeneous in terms of its thermo-chemical properties.

A simple means to probe the internal conditions in the fireball and compare to the results of measurements of an external probe is to simultaneous measure emission inside the fireball with fiber probes, and, at the same, time conduct an external measurement. The requirement of high temporal resolution makes this experiment challenging, but we were able to demonstrate this approach using our custom spectroscopic equipment and our HSFC.

Experimental

The general schematic for the fiber probe portion of the experiment is shown in Figure X.2. A charge is fired horizontally, and we image sample shots of the identical charge beforehand to know the spatial and temporal distribution of the fireball. Using this information, we position a series of fibers such that we can capture early and late stages of the fireball with moderate spatial resolution – limited by the optical depth of the fireball, which is about 2 cm. One fiber is placed outside the fireball and images along the firing axis from an external vantage point. This fiber then represents the commonly-used approach.

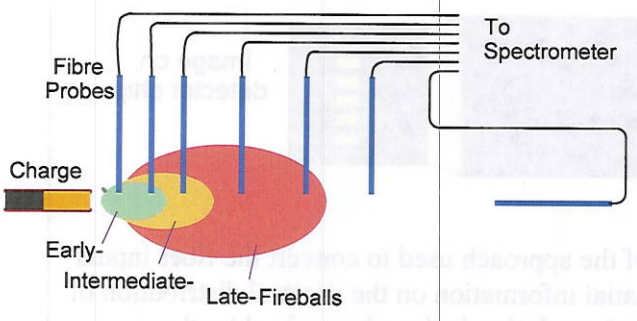

Figure X.2. A schematic of the general arrangement of the fiber probes with respect to fireball and charge locations.

Fibers were obtained from Edumund Scientific and were 1 mm plastic core, allowing good visible and near-IR transmission, with low cost. Fibers were protected in the fireball by using stainless steel sheaths made from 304 SS capillary tubes. The fiber tip is recessed inside the end of the tube such that an f/3 cone is allowed into the fiber, matching the inlet to the spectrometer (see below). A photograph of the experimental setup is shown in Figure X.3.

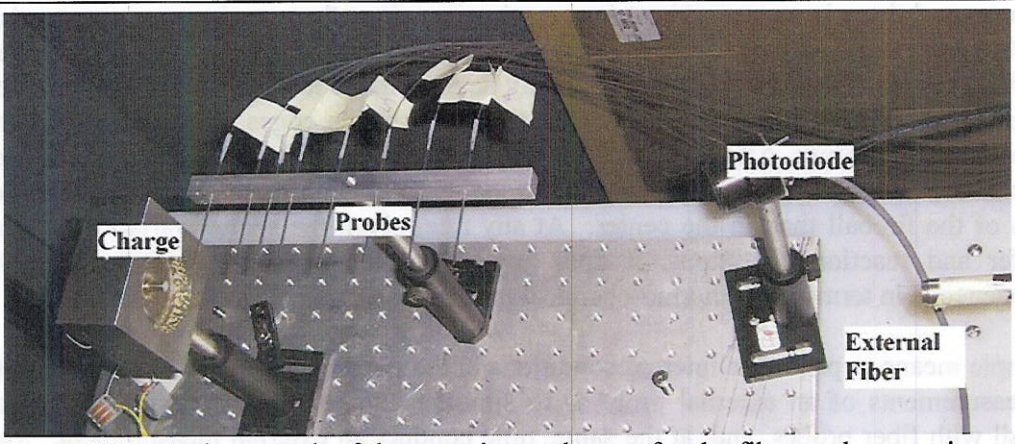

Figure X.3. A photograph of the experimental setup for the fiber probe experiments.

Fibers were aligned such that the probe tip was along the fireball central axis. A photodiode was used to verify timing in the experiments, and the charge was held in a stainless steel block with a recess to collect brass fragments from the casing. The charge was a modified RP-80 detonator with an output pellet that contained 20% aluminum powder in PBX-9407. Two powder sizes were tested: 3 um and 40 um. One charge with 50% of the 3 um powder was also tested. These are the same charges described in Chapter VI.

While collection of the light is relatively straightforward, collecting the spectral information with temporal and spectral resolution is more complicated. To achieve this goal, we apply the approach shown schematically in Figure X.4.

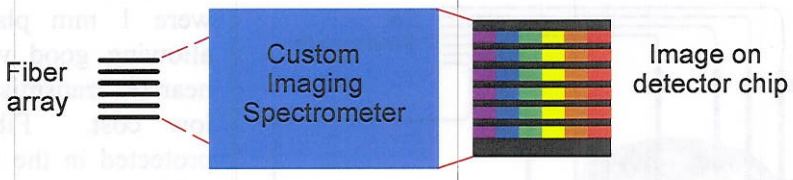

Figure X.4. A schematic of the approach used to convert the fiber inputs into images that contain spatial information on the spectral distribution of the light emission. Temporal resolution is then determined by the camera framing rate.

Central to this arrangement is the custom imaging spectrograph. We use a 135mm f/2.8 camera lens as an input collimator. At the focal plane of the camera lens, we arrange the fibers into a vertical column behind a 100 micron slit. The collimator generates a beam that is incident on a diffraction grating. We have used both transmission gratings (1200 gr/mm) and reflection gratings (1800 gr/mm). Light is dispersed by the grating and sent

to a focusing optic, which is also the input optic for the HSFC. In these tests, we used an f1.3 50mm camera lens. This arrangement allows us to achieve effectively an f/1.3 instrument, which is ultrafast, along with sub-nm resolution over a spectral range of several hundred nm. Resolution of this magnitude is sufficient to identify key atomic and molecular spectral features, as well as condensed phase temperatures from spectral continua. The high speed of the spectrometer system allows maximum utilization of the input light, enabling high signal-to-noise ratio spectra to be obtained with short exposures.

Results and Discussion

Five shots were fired in total, and each was successful. Initial results, shown in Figure X.5 for a 20% loading of 3 um Al used a 1200 gr/mm grating for resolution slightly less than 1 nm, and exposure times of 3 us for early times and 10 us for later times.

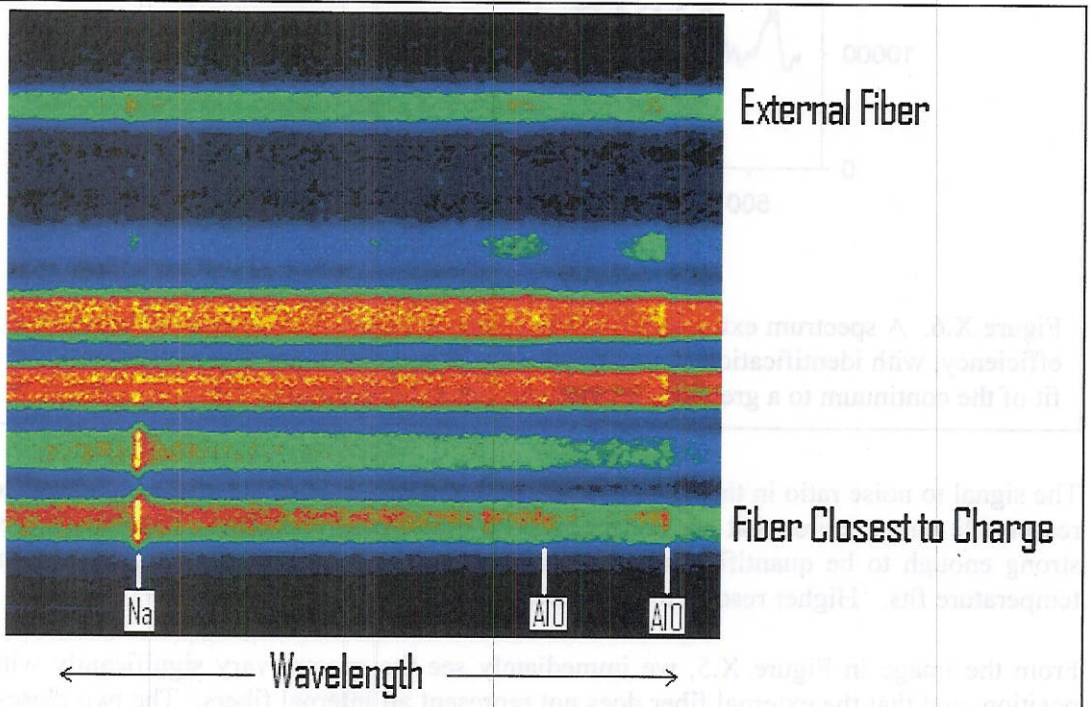

Figure X.5. False color image from the HSFC at 10 us after initiation of a 200 mg charge with 20% 3 um Al powder in PBX-9407. Each fiber spectrum represents a different position within the fireball. The exposure time is 3 us.

In general, the signal levels were good. Some saturation was observed in early time images, allowing us to switch to an 1800 gr/mm grating for the second set of shots and obtain greater spectral resolution (~0.6 nm) while maintaining high signal levels. AlO features were strongly seen, and the continuum emission was well resolved as well. Calibrations on wavelength and spectral efficiency allowed us to convert each image to a series of traces like that shown in Figure X.6, where we could fit the continuum to a greybody temperature.

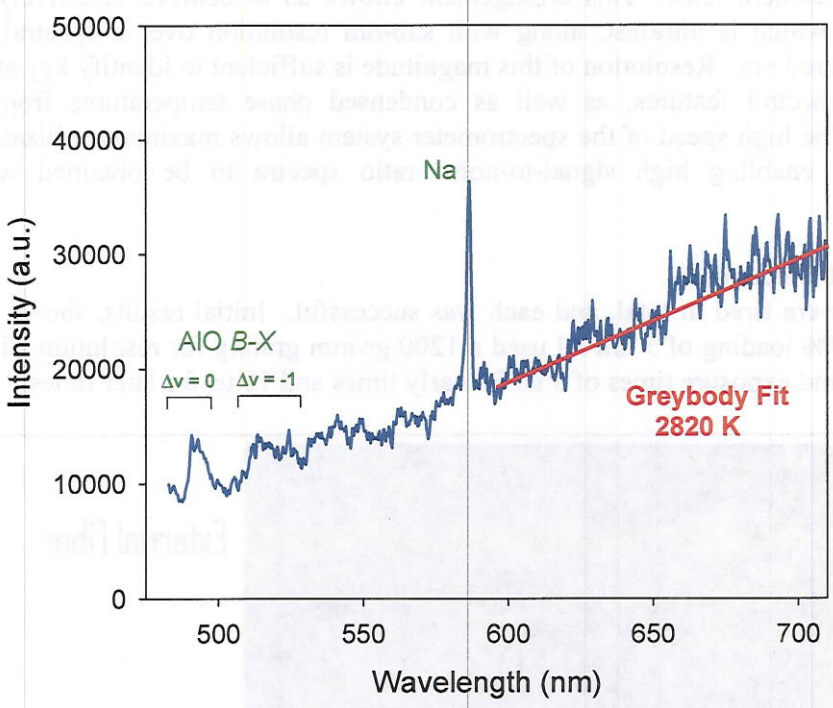

Figure X.6. A spectrum extracted from the image in Figure X.5, corrected for spectral efficiency, with identification of prominent atomic and molecular features, as well as a fit of the continuum to a greybody, condensed phase temperature.

The signal to noise ratio in the spectra is acceptable, and the fit of the continuum leads to reasonable temperatures that are consistent with other measurements. AlO features are strong enough to be quantified, though probably not well enough resolved to perform temperature fits. Higher resolution work would be required.

From the image in Figure X.5, we immediately see the spectra vary significantly with position, and that the external fiber does not represent all internal fibers. The two closest fibers (bottom two spectra) show strong Na emission, whereas the further fibers and external fiber show only a small peak. The fiber representing the front of the fireball (fifth from the bottom) shows the largest AlO signal relative to the background – i.e. weak background, strong AlO – whereas the other fibers, including the external fiber, show strong continuum and weak AlO on top of it. Clearly, there is a difference in the distribution of thermo-chemical properties within the fireball.

Processing the spectra in Figure X.5 to yield a temperature gives us the plot in Figure X.7 showing the condensed phase greybody temperature as a function of position in the fireball. In this case, the internal temperatures were higher than those observed at the outside edge of the fireball, and thus the externally measured greybody temperature is neither the average nor peak temperature of the fireball. Both "average" and "peak"

temperature estimates for external measurements are commonly used in the literature, but, according to these detailed measurements, neither is necessarily appropriate or accurate.

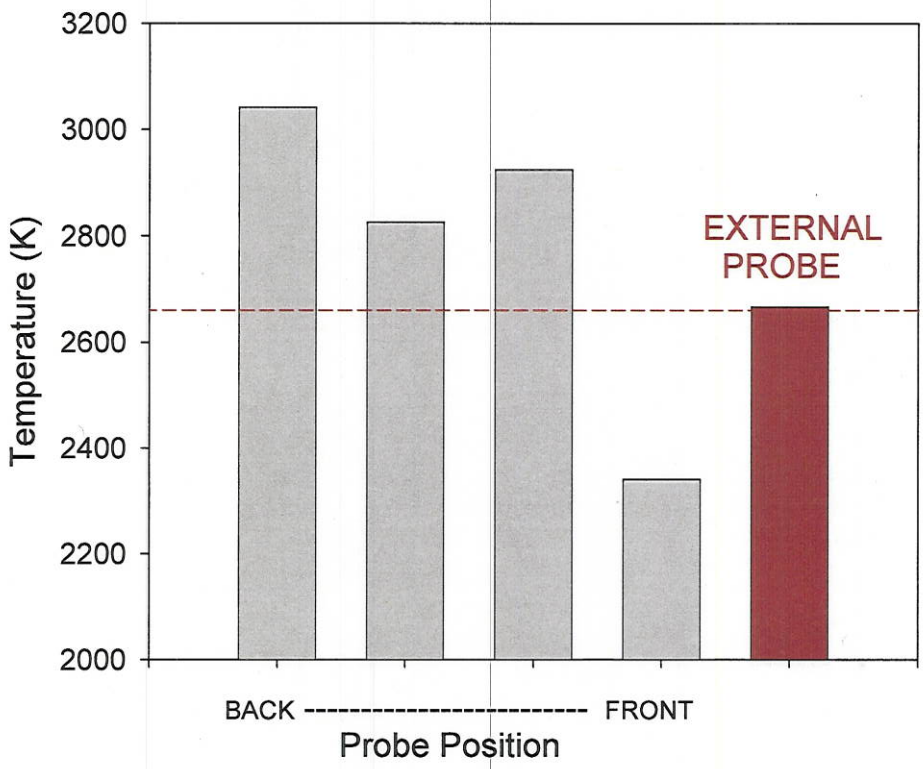

Figure X.7. Greybody temperatures from Figure X.5 showing the difference in measured temperature inside the fireball versus that measured by a probe external to the fireball.

Conclusions

Though this work remains preliminary and on-going, these measurements clearly demonstrate the ability to make internal emission spectroscopy measurements using simple fiber probes. The data also clearly show the spatial variation in thermo-chemical environment within the fireball, justifying the need to make these measurements, as opposed to relying on external measurements. There remains significant room for improvement, especially with regards to signal to noise ratio and uncertainty estimates, as well as detailed characterization of spatial uncertainties, but the critical elements of this measurement technology have been clearly demonstrated, and the potential for its use is quite promising.